Separation Control by Flow-Induced Oscillations of a Resonator

vorgelegt von
Diplom-Ingenieur
Frank Urzynicok
aus Berlin

von der Fakultät V – Verkehrs- und Maschinensysteme
der Technischen Universität Berlin
zur Erlangung des akademischen Grades

Doktor der Ingenieurwissenschaften
– Dr.-Ing. –

genehmigte Dissertation

Promotionsausschuß:

Vorsitzender:	Prof. Dr.-Ing. J. Thorbeck
Berichter:	Prof. Dr.-Ing. H.-H. Fernholz
Berichter:	Prof. Dr. rer. nat. Dr.-Ing. habil. A. Dillmann

Tag der wissenschaftlichen Aussprache: 4. Juli 2003

Berlin 2003
D 83

Acknowledgments

Now that the present thesis has come to a successful end, I would like to thank the many people who contributed to it in various ways.

In particular, it gives me great pleasure to thank Prof. H.-H. Fernholz for all his guidance and support throughout the years. In fact, it was his lecture on fluid mechanics that sparked my interest for this subject. I soon began working as a student assistant in his group, completed my diploma thesis under his auspices, and continued my career as a research associate investigating the present project. I am truly grateful to Prof. Fernholz for the technical knowledge I picked up, but also for the non-technical insight I gained during this long collaboration.

Besides my thesis supervisor, I further want to acknowledge the work of the thesis committee consisting of Prof. A. Dillmann and Prof. J. Thorbeck, who took on the role of the chairman.

I also wish to thank Prof. A. P. Dowling of the University of Cambridge who raised critical questions and helped to get the project off to a good start.

Throughout all my years at the Hermann-Föttinger-Institut, I enjoyed the interaction with my colleagues and former colleagues together with the outstanding atmosphere in what is known as the boundary-layer group: Frank Grewe, Karsten Knobloch, Rainer Sonnenberger, and Bruno Stefes as well as Sebastian Bake, André Huppertz, Gerd Janke, Maggie Kalter, Martin Schober, and Henri Siller. The casual framework of meeting for a cup of coffee every day after lunch was the source of very fruitful discussions and provided me with many valuable suggestions. My office mate Karsten deserves special mention, as he was invaluable in keeping up my spirit especially during those long, strenuous, and painful nights towards the end of this thesis.

As the successor of Patrick Erk, I benefited a lot from his excellent work on the previous project which led to the idea for the present investigation. Thanks are also due to Klaus Ehrenfried for making available his CFD code and providing his expertise on this subject. During the final phase of the measurements, I enjoyed the profitable cooperation with Maiko Garwon of the control group.

Furthermore, I am deeply indebted to my student co-workers who each put enormous effort into setting up experiments, performing measurements,

and evaluating data, often regardless of regular working hours: Michael Goetz, Harsimar-Singh Sahota, Marc Steinwand, Friedrich Bake, Michael Müller, and Liang Hauw Hartanto Darmadi. Their hard work brought about one directed study as well as five diploma theses.

No experiment would be possible without the people designing and manufacturing the apparatus. For the great care and precision in doing so, I would like to give thanks to the head of the workshop Bernd Barzantny and his team Axel Bendiks, Horst Mettchen, and Wilfried Postel. Just as important was the nursing of broken electronic equipment by Rainer Eschenhagen. Achim Leutz and Lilli Lindemann were of great help regarding administrative and financial matters.

Last, but definitely not least, I wish to thank my family. My wife Michelle put up with a long-distance transatlantic relationship for a number of years without too much complaint. I am very grateful that she made it work. My parents patiently supported me both in spirit and simply by running errands for me when measurements lasted until late into the night.

Again, I would like to express my warmest thanks to the people mentioned for their constant help and support!

Berlin, July 2003
Frank Urzynicok

Zusammenfassung

Strömungserregte akustische Resonatoren werden als adaptive passive Methode zur Beeinflussung von Ablösung untersucht. Passive Methoden benötigen keine Energiezufuhr von außen, um die Strömung zu verändern. In diesem Fall wird Fluid in einem Resonator durch Wechselwirkung mit einer Querströmung in Schwingung versetzt. An der Mündung entstehende Wirbel strukturieren die Strömung stromab so um, daß zusätzlicher Impuls in Wandnähe transportiert wird. Dadurch wird im zeitlichen Mittel ein Rückströmgebiet verkleinert oder ganz eliminiert. Die Kenngrößen der Beeinflussung (fluktuierender Impulsstrom in der Mündung und Frequenz der Schwingung) können über einen geschlossenen Regelkreis durch Veränderung der Resonatorgeometrie auf den Strömungszustand abgestimmt werden.

Um die Eigenfrequenzen und -moden zu bestimmen, wurden analytische, numerische und experimentelle Methoden angewendet. Eine Querströmung kann Resonanzschwingungen anregen, wenn die Frequenz, mit der sich im Resonatorhals Wirbel bilden, annähernd gleich einer dieser Eigenfrequenzen ist. Die Bildung der Wirbel wird durch die Geometrie der Resonatormündung bestimmt. Diese wurde so optimiert, daß die Wirbelstärke-Produktion erhöht wurde, verbunden mit einer verbesserten Wirkung auf ein stromab gelegenes Ablösegebiet.

Beim Einsatz mehrerer, in Spannweitenrichtung benachbarter Resonatoren bilden sich gegenphasige Schwingungszustände aus. Im Nachlauf der Schwingungsknoten entstehen alternierende Längswirbel, die die Wandschubspannung in diesem Bereich erhöhen und daher weiter zur Verringerung von Ablösegebieten beitragen. Gegenüber einem einzelnen Resonator ist der abgestrahlte Schalldruck um etwa eine Größenordnung verringert.

Die Methode wurde erfolgreich in zwei Strömungskonfigurationen eingesetzt: in einem Halbdiffusor mit 23° Öffnungswinkel und an einem gegenüber der Strömung stark angestellten Tragflügel mit FX 61-184-Profil ($\alpha = 23°$). In beiden Fällen befanden sich die Resonatoren kurz stromauf der Ablöselinie.

Im Diffusor wurde eine turbulent ablösende Grenzschicht durch in der Helmholtz-Mode schwingende Resonatoren beeinflußt. Das geschlossene Rückströmgebiet wurde verkleinert und der Druckrückgewinn mit einem Resonator um 13 % erhöht. Mit zwei gegenphasig schwingenden Resonatoren betrug die Verbesserung 18 %.

Um den Resonator an veränderliche Strömungsbedingungen anzupassen, wurde ein geschlossener Regelkreis eingesetzt, der auf einem Maximum-Such-Verfahren basierte. Als Stellgrößen dienten Schlitzweite und Höhe des Resonator-Hohlraumes, während der Schalldruck im Resonator und der Druckrückgewinn im Diffusor als Regelgrößen verwendet wurden. Der Regler konnte das globale Optimum beider Parameter unabhängig von den Anfangsbedingungen auffinden.

In den Experimenten am Tragflügel wurde die nahe der Vorderkante laminar ablösende Strömung durch einen Resonator beeinflußt, der in der ersten azimuthalen Hohlraum-Mode schwang. Die Länge des sich ursprünglich über die gesamte Saugseite des Profils erstreckenden Ablösegebietes wurde verringert. Stromab des Resonators gemessene Geschwindigkeitsprofile zeigten einen Impulszuwachs in Wandnähe. Die Saugspitze in der Druckverteilung wurde teilweise wiederhergestellt, woraus ein Auftriebsgewinn gegenüber dem unbeeinflußten Fall von bis zu 36 % resultierte.

Abstract

Flow-induced acoustic resonators are investigated as adaptive passive devices of separation control. Passive methods do not require an external energy input to manipulate the flow. In this case, fluid in a resonator oscillates by interaction with a cross-flow. Vortices generated at the orifice rearrange the flow downstream of the resonator so that additional momentum is transported into the near-wall region reducing or even eliminating reverse flow in the time-mean. The characteristic parameters of the control (fluctuating momentum flux in the orifice and frequency of the oscillation) can be adjusted to the flow conditions by changing the geometry of the resonator via an adaptive feed-back controller.

To determine the natural frequencies and modes of resonators, analytical, numerical, and experimental methods were applied. A cross-flow can trigger resonance, if the frequency at which vortices form in the resonator orifice is close to one of these natural frequencies. The formation of vortices is conditioned by the geometry of the resonator neck. It was optimized such that vorticity production was enhanced resulting in a greater impact on a downstream separation region.

Neighboring resonators exhibit a mode of anti-phase oscillation when arranged in spanwise direction. In the wake of the nodes of the oscillation, alternating longitudinal vortices form which increase the wall-shear stress in this region. Therefore, they contribute to a further reduction of a separation region. Compared with a single resonator, the radiated sound pressure is diminished by about an order of magnitude.

The method was successfully applied to two flow configurations: the flow in a half diffuser with expansion angle 23° and the flow around an airfoil with FX 61-184 profile at high angle of attack ($\alpha = 23°$). In both cases, resonators were located just upstream of the separation line. Microphone measurements as well as phase-locked LDA and PIV measurements of the velocity fields in the resonator necks and in their wakes were performed.

In the diffuser, a separating turbulent boundary layer was controlled by resonators of rectangular cross-section. The mode of oscillation was of the Helmholtz type. As a result, the extension of the closed reverse-flow region was reduced and the pressure recovery was increased by 13 % with one resonator, and by 18 % using two resonators that oscillated in anti-phase.

To adapt the resonator to changing flow conditions, a closed-loop control concept based on an extremum seeking strategy was employed. Manipulated variables were the slit width and the height of the resonator cavity, while controlled variables were the sound pressure in the resonator and the pressure recovery in the diffuser. The global optimum of both parameters was found by the controller independent of the initial conditions.

In the airfoil experiments, the laminar flow separating close to the leading edge of the wing section was manipulated by a resonator of circular cross-section oscillating in the first azimuthal cavity mode. The length of the separation region, which initially extended over the entire upper surface of the wing, was reduced. Velocity profiles measured downstream of the resonator showed an increase in momentum near the wall. Thereby, the suction peak in the pressure distribution was partially restored resulting in a lift gain of up to 36 % compared with the unforced case.

Contents

Chapter 1

Introduction

The phenomenon of flow separation is one of the major problems remaining for fluid dynamicists around the world. A flow separates from the surface of a body when the kinetic energy of its fluid particles closest to a bounding wall is not sufficient to overcome an adverse pressure gradient or when it grazes past a sharp edge.

In this chapter, problems associated with the occurrence of flow separation are discussed together with common strategies to avoid or at least to alleviate separation (section 1.1). In the context of this framework, the motivation and underlying idea of the control concept employed in the present study are introduced in section 1.2. Subsequently, a review is given of what has been achieved by other researchers in areas relevant to the present study and particularly in the field of separation control (section 1.3). At the end of this chapter, the path through the rest of this work is outlined (section 1.4).

1.1 The problem of flow separation and its control

A wide variety of engineering applications involving fluid dynamics suffers from the onset of flow separation under certain operating conditions equally pertaining to both internal and external flows. Examples of internal-flow configurations affected are pipe and duct systems, inlets, diffusers, valves, and turbomachines such as aircraft engines. External flows prone to separation occur, for instance, on constructions exposed to wind, such as buildings, suspension bridges, and wind turbines, as well as on all sorts of transport vehicles, ranging from submarines and motor vehicles or trains to military and commercial aircraft. Particular interest focuses on the flow around airfoils, as they constitute a key component in airplane, wind turbine, and turbomachinery aerodynamics often exhibiting regions of separated flow.

Circumstances under which flow separation is beneficial and, therefore, an integral part of the design are rare. One of the few examples are stall-controlled wind turbines where the pitch of the rotor blades is increased at

high wind speeds in order to evoke stall and, thus, prevent excessive rotational speeds and aerodynamic loads (e.g. Gasch, 1996). A second example are well-defined recirculating flow patterns in industrial burners, gas-turbine combustion chambers, or downstream of flame holders in afterburners. Here, the purpose is to ensure that the flow speed, which is typically an order of magnitude faster than the flame speed in a burning mixture, is reduced downstream of the fuel injector such that the flame is stabilized and not blown off. In the latter cases, the recirculation zones are induced either by a solid obstruction, a rapid area change of the flow duct, inlet swirl, or by directing jets into the combustion space (e.g. Turns, 1996; Cohen *et al.*, 1987; Mattingly *et al.*, 1987).

Consequences arising from flow separation are, among others, pressure losses, a deterioration of lift on airfoils, additional form drag, a change in heat transfer and mixing characteristics, and vibrations induced by the unsteadiness associated with separation or vortex shedding. Besides flow configurations where separation merely leads to comparatively slight deficiencies, considering, for instance, the increase in drag of an automobile and its impact on fuel consumption, there are a number of situations where avoiding separation is by all means critical in the operation of a device. This is illustrated by an abrupt breakdown of lift on airfoils as soon as the flow detaches from the leading edge (McCullough & Gault, 1951). Another example are violent aerodynamic pulsations associated with engine surge which occur as a consequence of rotating stall on compressor blades, and are a frequent cause for fatigue failures in gas turbines (Cohen *et al.*, 1987). Also, thromboembolic complications can arise that are linked to artificial heart valves, where a thrombus is likely to form, wherever the blood flow is stagnant (Timmel *et al.*, 2001). In summary, flow separation can drastically reduce performance, cause fatigue of material, and produce noise.

These highly undesirable effects have given rise to a variety of efforts aimed at avoiding separation and at eliminating the negative concomitant phenomena associated with it. A very successful approach has been the shape optimization, i.e. streamlining of bodies. Its purpose is to design the surface contour downstream of the line of minimum pressure in such a way that the steepness of the adverse pressure gradient is sufficiently reduced to prevent or postpone boundary layer separation (e.g. Gad-el-Hak & Bushnell, 1991). However, in many cases this method is limited by other design constraints, like weight and size requirements, so that separation cannot always be completely avoided. Thus, alternative approaches are needed.

In this context, flow control has received much attention lately. It is defined as manipulating the flow in order to make it behave differently than it would in the absence of control devices. Separation control, as a subsection of flow control dealing with the manipulation of separation regions and relying on similar control concepts, started with Prandtl (1905). He demonstrated that the flow around a circular cylinder could be kept attached as a result

of removing the boundary layer by suction through a spanwise slit.

Examples of common methods of separation control include many types of solid vortex generators embedded or submerged in a boundary layer (e.g. Pearcey, 1961; Lin, 1999), as well as vortex generator jets (e.g. Johnston & Nishi, 1990). Both introduce longitudinal (streamwise) vortices into the flow and, thus, enhance the transfer of high-momentum fluid from the outer flow to the near-wall region to keep the flow attached. Other control methods also intensify the wall-normal mixing to augment the boundary layer momentum, but rely on different physical mechanisms. These methods comprise, but are not limited to, inclined large-eddy breakup devices, often abbreviated as LEBUs (e.g. Lin *et al.*, 1990), steady blowing and suction through slits and holes (e.g. Park & Choi, 1999), pulsed jets (e.g. McManus *et al.*, 1994), as well as periodic excitation by acoustic or fluidic means (e.g. Ahuja & Burrin, 1984) and by mechanical actuators (e.g. Miau *et al.*, 1991). By contradistinction, there are methods that add momentum directly to the streamwise velocity profile in the vicinity of the wall by injecting fluid parallel to the surface. An example are mechanical devices of variable geometry in the form of leading-edge slats and slotted trailing-edge flaps on airfoils where the fluid discharge is driven by the pressure difference on the body itself (e.g. Gad-el-Hak & Bushnell, 1991).

A systematic comparison of the performance of various control methods in reducing a two-dimensional separation region downstream of a backward-facing ramp is given by Lin *et al.* (1990) and Lin (1999).

The wide variety of methods can be classified with regard to several different aspects:

- According to whether the energy needed for the manipulation of the flow is supplied by an external source or by the flow itself, one may differentiate between *active* and *passive* methods, respectively (e.g. Fiedler & Fernholz, 1990). Active methods require the use of actuators which are usually rather complex systems. Regarding their energy consumption, great care must be taken that it does not outweigh the benefits achieved by the control. They can be adjusted to changing flow conditions, if appropriate control schemes are implemented. Common passive devices such as solid vortex generators are comparatively simple, but tend to have detrimental effects, mostly by adding parasitic drag, under off-design conditions, i.e. in flow situations where stall suppression is not needed.

  Actuators associated with active control methods in general convert electric energy to some form of fluid motion or flap agitation. Among the fluidic actuator types are systems consisting of a cavity and an opening to the flow which are driven by loudspeakers, piezoelectric devices, or compressed air discharged by valves. A fluidic actuator concept that takes advantage of the resonant behavior of the driving mem-

brane is described by Rathnasingham & Breuer (1996). Mechanical actuator types are, for instance, oscillating flaps, fences, or microfabricated electro-mechanical systems, known as MEMS (e.g. McMichael, 1996).

- Another distinction can be made between *steady* and *periodic* actuation which in Fiedler & Fernholz (1990) is denoted as *static* and *dynamic* control. As proposed by Greenblatt & Wygnanski (2000), in this context the term *excitation* is defined as oscillatory, i.e. periodic actuation.

- With respect to the underlying physical process, Greenblatt & Wygnanski (2000) distinguish between methods that *add momentum* directly to the flow, for example, by steady blowing and those that *transfer* streamwise *momentum* from the free-stream. The latter can be achieved by removing the inner layer through suction, or by adding energy to it as a consequence of a mixing process, e.g. by vortex generators.

- Methods relying on the exchange of momentum between free-stream and near-wall region as a result of enhanced mixing can be further subdivided depending on the kind of vorticity generated by the control devices. Some generate *spanwise* vortices (e.g. certain types of oscillating flaps or fluidic excitation through slits), while others produce *longitudinal* vortices (e.g. vortex generators), or a combination thereof (e.g. adjacent fluidic or mechanical actuators operated out of phase (Seifert *et al.*, 1998)).

- With the use of acoustic means for flow control a distinction between *externally* and *internally* supplied excitation becomes necessary. External excitation is achieved by a sound source placed at a distance from the investigated body far from the separation region. Since the effectiveness of the control is biased by the acoustic properties of the wind tunnel, results are virtually not comparable. This method has no significance with regard to applicability, however, and is mentioned here for historical reasons only. Internal excitation, in contrast, supplies the perturbations through a slit or holes at a location where they have maximum impact on the separation region. In this case, the components of the actuator are usually contained in the wall.

  The designation of this method is not consistent in the literature. For instance, it is denoted as internal acoustic excitation by Ahuja & Burrin (1984), as hydrodynamic excitation by Greenblatt & Wygnanski (2000), and as fluidic excitation by Amitay *et al.* (2001). In the present investigation, the term *fluidic excitation* will be used, since a study by Erk (1997) in the near field of such a perturbation source revealed that

the fluid dynamic processes are responsible for manipulating the flow rather than the acoustic effects. Further details will be discussed in section 1.3.3.

- If the actuator properties (e.g. amplitude and, in some cases, also frequency of the perturbations generated by the actuator) can be adjusted to the flow conditions, the control method is denoted as *adaptive*.

- From the viewpoint of control theory, the various methods to adjust the actuator properties fall into three categories: *open-loop* control, *feed-forward* control, and *feed-back* or *closed-loop* control. To meet a certain target, an open-loop controller simply provides an input without regarding how the fluidic system responds to it. Information on the response can in principle be obtained by evaluation of a mathematical model, from a static map, or by measurements. A feed-forward controller predicts the response of the system to a known input based on a model and adjusts the input accordingly. This is an effective strategy as long as the input can be accurately quantified and the effect is known. The feed-back or closed-loop controller is the most useful control strategy for tackling unknown responses to an input. The system response is continuously monitored by measurement, and the input is adjusted accordingly.

Successful separation control has been demonstrated, for example, by Lin *et al.* (1990) on a ramp, by Huppertz (2001) on a backward-facing step, by Siller (1999) and Huppertz & Fernholz (2002) on a fence, by Obi *et al.* (1993) in a planar asymmetric diffuser, by Fernholz *et al.* (1993) on a wedge-like body, and by Ahuja *et al.* (1983), Ahuja & Burrin (1984), Erk (1997) and Siller & Fernholz (1999) on airfoils.

In spite of the enormous effort and abundance of work done within the past few years, the problem of separation is not yet solved. The majority of control methods mentioned are still far from technical application. Bearing in mind the potential benefits from manipulating separation regions, further research is worthwhile.

This investigation is one of sixteen sub-projects geared towards fundamental research in the field of flow control, and was financed by the DFG within the framework of the Collaborative Research Center - Sonderforschungsbereich (Sfb) - 557 entitled “Control of complex turbulent shear flows”.

1.2 The present approach to the problem

In this study, aerodynamically excited acoustic resonators were investigated as adaptive passive devices for separation control. The resonators consist of a cavity which is coupled to the ambient air by an opening (figure 1.1). If

during the flow-induced oscillations the pressure within a cavity cross-section is approximately uniform in space, the resonator is denoted a Helmholtz resonator. The corresponding mode of vibration is called the Helmholtz mode. When oscillating in a different mode, the resonator has no specific designation.

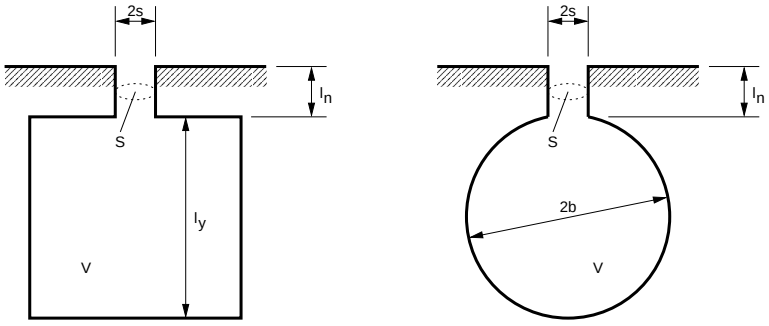

FIGURE 1.1: Notation of geometric quantities for both types of resonators used throughout this study. The circular opening areas are indicated for illustrative purposes only, as in the experiments the resonators exhibited slits. $2s$ denotes the slit width, l_n the neck length, S the opening area, V the cavity volume, l_y the height of a cavity with rectangular cross-section, and b the radius of a cavity with circular cross-section.

Passive methods do not require an external energy input to manipulate a separation region. In this case, fluid in an acoustic resonator is set oscillating by interaction with a grazing flow. The energy needed for the oscillations is thereby extracted from the flow itself and is returned to it almost entirely as periodic perturbations. As a result, spanwise vortices are generated at the slit. They reorganize the flow downstream of the resonator by transporting additional streamwise momentum from the free-stream into the near-wall region. The application of a spanwise array of resonators oscillating in anti-phase produces additional streamwise vorticity and further enhances the mixing process. As a consequence, a reverse-flow region can be reduced or even eliminated in the time-mean.

In contrast to common passive methods of flow control such as solid vortex generators, acoustic resonators offer the advantage of adaptivity. In this case, the characteristic parameters of the control (frequency and amplitude of the excitation) can be adjusted to varying flow conditions by changing the geometry of the resonator (volume of cavity and size of orifice). For this purpose, both open-loop and closed-loop control schemes are used in this investigation. In this context, a minor external energy input is needed to perform the necessary adjustments of the resonator geometry. An example of flow control by an adaptive acoustic resonator along with possibilities to adjust its geometry is shown schematically in figure 1.2.

In terms of the classification discussed in section 1.1, the characteristics of the present approach can be summarized as follows: An acoustic res-

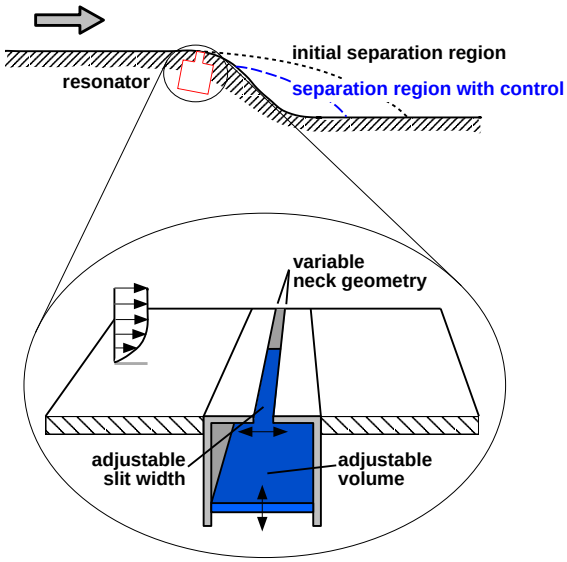

FIGURE 1.2: Schematic of an adaptive resonator employed to control a separation region.

onator is used as a *passively* driven fluidic actuator to supply *periodic* (or *dynamic*) forcing *internally*. As a consequence, either only *spanwise* vortices are generated or a combination of *spanwise and streamwise* vortices that *transfer momentum* from the free-stream to the near-wall region and, thus, control separation. The method becomes *adaptive* by employing *open-loop* and *closed-loop* control.

The present investigation is performed by primarily experimental means at low subsonic speeds.

1.3 Previous research in related fields

Since the Helmholtz resonator, functioning as actuator, is the key component of the present method of flow control, research done on it is presented here first along with a historical perspective. While section 1.3.1 discusses its acoustic properties, the phenomena occurring when induced by a grazing flow are addressed in section 1.3.2.

The remainder of this review is devoted to separation control issues such as the current understanding of the underlying principles, as well as a description of today's common methods of flow control (section 1.3.3). It is complemented by examples of separation control in the two configurations considered in this study, namely in diffusers (section 1.3.4) and on airfoils (section 1.3.5). To end this review the few attempts to use flow-induced resonators for the purpose of separation control are summarized in section 1.3.6.

1.3.1 Acoustic properties of Helmholtz resonators

A large amplitude response to excitation at the neck by small pressure fluctuations of certain frequencies, namely the resonance frequencies, is the characteristic of an acoustic resonator (Dowling & Ffowcs Williams, 1983). Apart from the Helmholtz resonator considered here, other types include single expansion-chamber silencers, organ pipe resonators, and resonant boxes.

Under resonant conditions, air flows through the orifice as a result of a difference of pressure on both sides, or due to its own inertia when such pressure has ceased (Rayleigh, 1896, § 303). The mass flow into and out of the cavity causes a change in density and pressure of the compressible air contained therein. In phase with the external disturbance, this in turn feeds the subsequent cycle of the velocity oscillation in the neck, such that the periodic process is sustained.

The adoption of resonators to enhance or attenuate sound fields dates as far back as ancient Greece, long before Helmholtz resonators were analyzed mathematically, where they were built into the walls under the seats in a number of open air amphitheaters. Ingard (1994) hypothesizes that the resonators were installed for their transient response, i.e. their reverberant properties.

Likewise, pipe organs, a somewhat related physical configuration, were part of the musical instruments known to Romans and Greeks nearly 2000 years ago (Fletcher & Rossing, 1991). During the 18th century, when the art of organ building had reached a technical peak, the resonances in organ pipes attracted the attention of numerous mathematicians to develop a theory for their description, among them Bernoulli and Euler as well as, later on, Lagrange and Poisson. However, it was not until Helmholtz (1860) investigated the problem, that the physics in the vicinity of the open end could be modeled correctly. In this region, the plane waves propagating within the pipe undergo a transition to continue their way as spherical waves in the free space. His solution was based on an analogy to potential functions used in electrical and magnetic science. By transferring the tools developed in this approach to the type of resonators that now bear his name (figure 1.3), Helmholtz (1860) became the first to provide a mathematical theory for them.

Prior to Helmholtz's analytical work, Sondhauss (1850*b*) conducted a series of systematic experiments to determine the natural frequency f_0 of resonators as a function of their dimensions when induced by heating or blowing across the opening. He found that the shape of the cavity had no effect on the oscillation frequency, but that it depended on other geometric parameters in the following way:

$$f_0 = C_1 \sqrt{\frac{S}{V l_n}}. \tag{1.1}$$

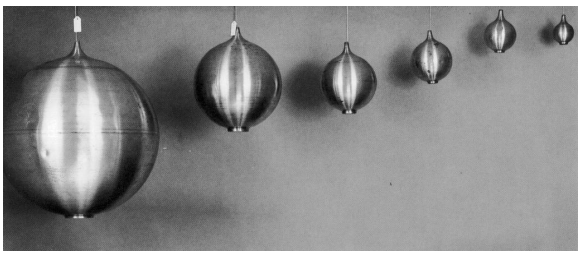

FIGURE 1.3: Historical resonators used by Helmholtz in his experiments. Taken from Hoffmann *et al.* (1997) with permission of the Hermann von Helmholtz-Gemeinschaft Deutscher Forschungszentren.

Herein S is the area of the resonator opening, V the volume of the cavity, and l_n the neck length (see figure 1.1). C_1 is a constant that Sondhauss determined as 52.200 m/s for resonators induced by heating and as 46.705 m/s when they were induced by blowing across the opening[1]. Apart from the failure to relate the constant C_1 to the speed of sound c, the result is remarkably close to the analytical solution (see equation (1.5)).

The outstanding contribution of Helmholtz (1860) is the theoretical derivation of an equation for the resonance frequency f_0 under the condition that all cavity and opening dimensions can be regarded as negligibly small compared to the wavelength, and that the area of the circular opening is negligibly small compared to the surface area of the cavity:

$$f_0 = \frac{c}{\sqrt{2}\sqrt[4]{\pi^5}} \frac{\sqrt[4]{S}}{\sqrt{V}}. \tag{1.2}$$

Strictly, this formula is only applicable to resonators without necks embedded in a flat, infinite surface. With appropriate values inserted, equation (1.2) yields

$$f_0 = 56.174\,\mathrm{m/s} \times \frac{\sqrt[4]{S}}{\sqrt{V}} \tag{1.3}$$

which agrees reasonably well with a result obtained earlier by Sondhauss (1850*a*). From experiments with humming tops, which correspond to spinning cavities with an opening on the side, he had derived an empirical formula for the frequency of the sound which is emitted when a stream of air is blown across the circular, quadratic, or rectangular opening of a resonator without neck[2]:

$$f_0 = 52.400\,\mathrm{m/s} \times \frac{\sqrt[4]{S}}{\sqrt{V}}. \tag{1.4}$$

[1] Originally, Sondhauss (1850*b*) used the notation of the French physicists resulting in values of the frequency twice as high (Helmholtz, 1860). Values have been converted and units have been added for dimensional consistency.

[2] As before, values have been converted and units have been added.

In anticipation of section 1.3.2, it is worth noting that tones were induced with both sharp and round edges at the opening. The agreement between theory and experiments improves, the smaller the ratio of the opening area to the surface area of the cavity (Helmholtz, 1860).

A simplified theory of the Helmholtz resonator was later presented by Rayleigh (1896, chap. 16). He based his analysis on the same assumptions as Helmholtz, namely uniform pressure in the interior of the cavity, and neglected losses due to friction. In analogy to a piston moving in a cylinder with one open end, he considered the kinetic and potential energies of the air in the resonator neck, applied Lagrange's method to obtain the differential equation of motion, and solved it for the period of vibration under the premise of harmonic motion. Including the influence of a long cylindrical neck of length l_n, he inferred the following expression for the resonance frequency:

$$f_0 = \frac{c}{2\pi}\sqrt{\frac{S}{V l_n}}. \tag{1.5}$$

A modern derivation was given by Dowling & Ffowcs Williams (1983) who obtained equation (1.5) from a momentum balance between both ends of the neck. Whereas equation (1.2) derived by Helmholtz is strictly valid only in the limit of vanishing neck length, Rayleigh's formula (1.5) is restricted to resonators with very long necks. Necks of practical length, however, render both equations inaccurate. Due to three-dimensional flow in the transition region of an opening with radius R, mass of the external fluid of the order of $\rho_0 R^3$ is accelerated in addition to the mass of air contained in the neck (Dowling & Ffowcs Williams, 1983). Since this makes the effective neck length slightly longer than the physical length, an end correction Δl_n is introduced for both sides of the open end denoted as Δl_{n_i} and Δl_{n_e} on the interior and exterior side, respectively (figure 1.4). The correction is taken into account by replacing the neck length l_n in equation (1.5) by an effective neck length (Rayleigh, 1896, § 307)

$$l_n^* = l_n + \Delta l_{n_i} + \Delta l_{n_e}. \tag{1.6}$$

The approximate theoretical determination is credited to Helmholtz (1860) who gave $\Delta l_n = \frac{\pi}{4} R$ as the correction for an open end of radius R in an infinite plane wall.

Similarly, Rayleigh (1896, § 304) introduced the concept of the conductivity from an electrical analogy to characterize various kinds of necks. The Rayleigh conductivity, denoted as K, relates the perturbation volume flux $\dot{V}$ through the aperture to the driving pressure difference $p_2 - p_1$ across it. For time harmonic pressures[3] p_1 and p_2 inside and outside the opening,

[3] All components of the acoustic field are proportional to $\mathrm{e}^{-\mathrm{i}\omega t}$. For convenience, the explicit dependence on this factor is suppressed here. p_1, p_2, v, and $\dot{V}$ are complex amplitudes containing phase and amplitude information.

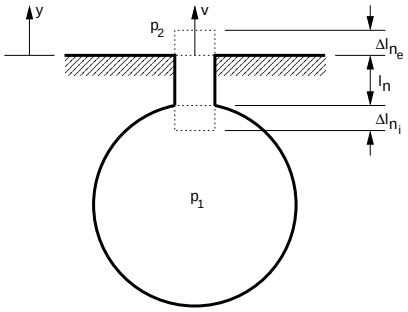

FIGURE 1.4: Notation of acoustic quantities associated with a resonator. p_1 and p_2 are the respective sound pressures inside and outside the cavity, and v is the perturbation velocity in direction of the coordinate y normal to the exit plane of the neck. Δl_{n_i} and Δl_{n_e} are the interior and exterior end corrections, respectively, applicable to the neck length l_n.

respectively, the Rayleigh conductivity is defined by the relation

$$K = \frac{\mathrm{i}\omega\rho_0\dot{V}}{p_2 - p_1} \tag{1.7}$$

where i is the imaginary unit, ω is the angular frequency, and ρ_0 is the mean mass density (figure 1.4). The conductivity is related to the specific acoustic impedance Z by the equation

$$Z = \frac{p_1 - p_2}{v} = -\mathrm{i}\omega\rho_0\frac{S}{K} \tag{1.8}$$

where v is the complex velocity amplitude normal to the exit plane of the aperture (e.g. Morse, 1948).

Besides the cylinder, there are very few forms of necks for which the conductivity can be determined accurately by analytical means. The resulting end correction Δl_n for one end of a cylindrical neck of length l_n and radius R with an unlimited flange lies in the range $\frac{\pi}{4}R \leq \Delta l_n < \frac{8}{3\pi}R$ (Rayleigh, 1896, § 307). The end correction coincides with the lower limit when l_n vanishes, increases with increasing neck length, but never attains the upper limit. For an unflanged termination experiments suggest a Δl_n between $0.54R$ and $0.60R$ (Skudrzyk, 1954). It can be shown that, among various forms of openings of given area, the circle has a minimum conductivity. For elliptical apertures, the conductivity increases slightly with increasing eccentricity. In general, the more the opening is elongated, the greater the conductivity for a given area and, as a consequence, the higher the resonance frequency.

Equation (1.5) is widely used in engineering practice. However, the choice of an appropriate value for the end correction Δl_n is crucial, depending on the details of the resonator geometry. An excellent compilation of tabulated values of Δl_n for a variety of opening shapes can be found, for example, in Heckl & Müller (1994, pp. 475–477).

Rayleigh (1896, § 310) also noted that, besides the mode of vibration discussed so far, often referred to as the Helmholtz mode and characterized by an oscillatory motion of air in the orifice, cavity modes may occur due to the formation of a standing wave pattern within the resonator volume. The "overtones" are not harmonically related to the Helmholtz resonance frequency and can be calculated theoretically only for a few cavity shapes. They will be investigated in greater detail in section 3.1.

So far, dissipation of acoustic energy has not been taken into account, which occurs mainly due to the radiation of sound into the ambient medium as well as due to viscous effects associated with the flow through the neck. While the natural frequency of a resonator is almost entirely independent of the rate of dissipation (Rayleigh, 1896, § 311), the peak response to external driving at the resonance frequencies is limited by damping (Dowling & Ffowcs Williams, 1983). A measure of the losses in a resonator is given by the quality factor Q. It represents the pressure amplification at resonance defined as the relation between the external driving pressure of an incident sound wave and the pressure amplitude within the cavity (e.g. Kinsler & Frey, 1962). The quality factor is also related to the exponential decay rate ε of a resonator subject to an incident pulse by the following equation where ω_0 is the angular resonance frequency:

$$Q = \frac{\omega_0}{2\varepsilon}. \tag{1.9}$$

To attenuate sound traveling along a duct, a Helmholtz resonator is connected to the side of it resulting in a maximum transmission loss at the resonance frequency (Dowling & Ffowcs Williams, 1983). Nowadays, Helmholtz resonators are commonly used as sound control devices in many situations, e.g. for noise attenuation in acoustic liners (Flynn & Panton, 1990) as they are integrated in the inlet duct of aircraft engines or applied to enhance the acoustics in reverberant rooms of buildings, in combustors (Flynn *et al.*, 1990), or in some types of car silencers (Dowling & Ffowcs Williams, 1983). Likewise, a passive Helmholtz resonator noise control system has been installed in the payload fairing of the Ariane-5 spacecraft, since structures exhibiting a plate-like vibration behavior, such as antennas and solar panels of satellites, are particularly susceptible to damage induced by the severe low-frequency noise produced by the rocket engines during launch (Eaton, 1997).

It is interesting to note that also the wave-induced oscillations in irregularly shaped harbors or bays of variable depth connected to the external sea by a narrow mouth or an entry channel can be modeled analytically according to the principles of Helmholtz resonators (e.g. Miles & Lee, 1975). The results are relevant to the frequency response to excitation by a tsunami, for example. The condition of uniform pressure within the resonator volume is, in this case, replaced by the assumption of homogeneous displacement of the

free surface throughout the harbor.

1.3.2 Flow-induced resonators

As a consequence of the coupling of acoustic resonance to some form of periodic flow disturbance, resonators can be excited by a cross-flow producing discrete frequency sound.

Although the first systematic experiments involving flow-induced resonators were conducted as early as 1850 by Sondhauss, interest did not focus on the details of the flow-induction mechanism itself until after World War II (Elder, 1978) when aerodynamically excited resonances had proven to cause undesirable effects on air and naval vehicles. As a deeper understanding was required to reduce or avoid the associated difficulties, flow-induced resonators have been studied extensively since then, primarily triggered by the intent to suppress the induced oscillations. Situations investigated occur, for example, in gas-transport pipe-systems with closed side branches (Bruggeman, 1987; Bruggeman *et al.*, 1989, 1991), on automobile sunroofs (Currle, 1990), and on air and naval vehicles (De Metz & Farabee, 1977) where aircraft landing gear wells and weapon bays have attracted particular attention (McGregor & White, 1970). In these configurations, the flow-induced periodic pressure fluctuations generate noise, structural vibration and fatigue problems (De Metz & Farabee, 1977). The oscillations were also noted to drastically increase mean drag (McGregor & White, 1970), and to significantly alter the heat transfer characteristics on the body housing the resonator in comparison to the non-resonating performance (Miles & Watson, 1971). For water flow past resonators and cavities, the strong induced pressure fluctuations were observed to be the source of cavitation damage (Rockwell & Naudascher, 1978).

In a variety of studies, the flow-induction of such resonators is attributed to a non-linear feed-back process which was first described by Rossiter (1964). As the approaching boundary layer passes the upstream edge of the resonator orifice, it forms into an unstable shear layer separating the stagnant fluid within the neck from the free-stream. Subsequently, this shear layer breaks down into discrete vortices which are shed at regular time intervals. They are then convected across the opening at a fraction of the free-stream velocity, while they rapidly grow in size. When the vortices eventually hit the downstream edge of the resonator neck, they generate pressure fluctuations and, thus, acoustic pulses. These pulses in turn feed back to the shear layer upstream, mainly via the air within the resonator volume, where they initiate the formation of further vortices. If the frequency of the vortex shedding lies within a close range of one of the natural frequencies of the resonator, the process can sustain itself and, as a consequence, resonance occurs. In this context, Miles & Watson (1971) report that a thin approaching boundary layer promotes both the occurrence and the intensity of resonance.

An alternative description is offered by Nelson *et al.* (1981, 1983). They explain the flow-acoustic interaction in the neck of an aerodynamically excited Helmholtz resonator in terms of a superposition of two flow fields and their corresponding pressure fields. One of the flow fields is associated with pressure and velocity fluctuations generated by the passage of vortices in the resonator neck, the other one with the reciprocating potential flow driven through the neck by the cavity pressure fluctuations as a consequence of the acoustic resonance. Both are linked by an unsteady Kutta condition implying that the flow separates tangentially at the upstream edge of the orifice. From momentum balances, a source and sink region of acoustic energy can be identified in which energy in the form of fluctuating momentum is extracted from and returned to the mean flow, respectively. The acoustic source is located near the downstream edge of the resonator opening, while the sink is in the proximity of the upstream edge. The power radiated into the acoustic far field and the power carried away by vortices, which are ejected from the opening, both result from an imbalance between source and sink of acoustic energy.

A similar viewpoint is adopted by Bruggeman *et al.* (1989). Their theory predicts sound absorption by vortex shedding at the upstream edge in the first half of a period of the acoustic oscillation. When a vortex approaches the downstream edge in the second half of the period, power is extracted from the flow to sustain the acoustic pulsations. The authors relate the strength of the acoustic source and sink and, therefore, the sound-pressure level to the shape of the neck. The local acoustic velocity increases with decreasing radius of curvature of the edges. As a result, a sharp upstream edge, or even more effective, a flat plate, enhances sound absorption. If the resonator features a rectangular opening, the character of the vortex shedding at the upstream edge is purely two-dimensional. The effects of various orifice geometries were also investigated by Panton (1990). He concluded that orifices that aid to direct the inflow into the neck aggravate the acoustic pulsations, whereas those that inhibit inflow have a negligible response.

Panton & Miller (1975*a*) experimented with a Helmholtz resonator with an opening comparable in size to the turbulent eddies in the approaching boundary layer. They concluded that the turbulent eddies are responsible for the excitation of the resonator. However, this hypothesis is untenable since the periodic fluctuations are also present when the boundary layer is laminar. A comparison of the Helmholtz and higher-order resonances induced by laminar and turbulent boundary layers, respectively, can be found in De Metz & Farabee (1977). They ascertained that the changes due to a transition from laminar to turbulent inflow conditions are minor. The most significant differences affect the convection velocity of the vortices in the opening and the application of appropriate scaling laws.

Due to the complexity of the processes involved and a lack of detailed understanding, no sufficiently accurate theoretical models are available to

compute the resonance frequency and amplitude of resonators when induced by a cross-flow. A compilation of resonance frequencies obtained from experiments and theory is shown in table 1.1.

Author	Resonance regime	Inflow	B. l. properties	Method
P. & M. '75	$St_{2s} = 0.19$–0.27	turb.	$2 < \frac{\delta}{2s} < 4$	exp.
D. & F. '77	$St_{\delta_2} = 0.022$	lam.	$0.02 < \frac{\delta_2}{2s} < 0.14$	exp.
D. & F. '77	$St_{2s} = 0.2$–0.4	turb.	$1 < \frac{\delta}{2s} \leq 17$	exp.
D. & F. '77	$St_{2s} = 0.2$	turb.	$17 < \frac{\delta}{2s} < 250$	exp.
E. '78	$St_{2s_n} = \frac{U_c}{U_\infty}(n + \frac{3}{4})$	lam./turb.	—	theor.
E. '78	$St_{2s} = 0.35$	turb.	$\frac{\delta}{2s} = 0.29$	exp.
N. *et al.* '81	$St_{2s} = 0.25$	—	—	—
B. '86	$St_{\delta_2} = 0.017$	lam.	$\frac{\delta}{2s} < 1$	theor.
B. '86	$St_{2s_n} = \frac{U_c}{U_\infty}(n + \frac{3}{4})$	lam./turb.	—	theor.
B. *et al.* '89	$St_{2s_n} = 0.4(n + 1)$	turb.	$\frac{\delta_2}{2s} = 0.005$	exp.
B. *et al.* '89	$St_{2s_n} = \frac{U_c}{U_\infty}(n + 1)$	lam./turb.	—	theor.
B. *et al.* '89	$St_{2s_n} = \frac{U_c}{U_\infty}(n + \frac{1}{3})$	lam./turb.	—	theor.
F. & P. '90	$St_{2s} = 0.24$	turb.	$\frac{\delta}{2s} = 2.72$	exp.
P. '90	$St_{2s} = 0.25$	turb.	$\frac{\delta}{2s} = 2.81$	exp.

TABLE 1.1: Overview of non-dimensional resonance frequencies induced by a cross-flow taken from literature. $St_{2s} = f_0 2s/U_\infty$, $St_{2s_n} = f_n 2s/U_\infty$, and $St_{\delta_2} = f_0 \delta_2/U_\infty$ are Strouhal numbers with f_n being the resonance frequency of order n ($n = 0, 1, 2, \ldots$), $2s$ the streamwise length of the opening, U_∞ the free-stream velocity, and δ_2 the boundary layer (b. l.) momentum thickness. U_c denotes the convection velocity of a vortex in the orifice and δ the boundary layer thickness.
P. & M. '75: Panton & Miller (1975*a*), D. & F. '77: De Metz & Farabee (1977), E. '78: Elder (1978), N. *et al.* '81: Nelson *et al.* (1981), B. '86: Blake (1986), B. *et al.* '89: Bruggeman *et al.* (1989), F. & P. '90: Flynn & Panton (1990), P. '90: Panton (1990).

Up to now, the details determining the amplitude of the oscillations are poorly understood. As the amplitude is limited by essentially non-linear effects, a mathematical treatment of the problem is rather complex (e.g. Howe, 1976). For instance, in the study by Bruggeman *et al.* (1989), theory and experiment differ by a factor of five in this respect. Blake (1986) hypothesized that the oscillation amplitude is limited by a ratio of rms-sound-pressure within the cavity to free-stream dynamic pressure of $p_{cav}/p_{dyn} < 1$. However, there is no obvious physical reason for this, and from the data of De Metz & Farabee (1977), and the data presented later in this work, it is evident that this assumption does not hold.

The interaction of resonators arranged in spanwise direction when excited by a turbulent boundary layer was investigated by Flynn & Panton (1990). They found that the oscillations between adjacent resonators were out of phase by 150 °–180 °. For close resonator spacings, the coherence be-

tween the pressure signals was high with values ranging from 0.95 to 1.00. Both frequency and amplitude of the oscillations were slightly altered as a consequence of the interaction. The effects observed were a function of the spacing between orifices and decreased as the separation distance became larger. Without specific reasoning, the authors suggested that the anti-phase behavior was due to a fluid-mechanic coupling as contrasted to an acoustic coupling.

To conclude this section, a problem closely related to aerodynamically excited resonators should be mentioned, namely the flow past a cavity. Unfortunately, notation is often sloppy in the literature such that cavities and resonators frequently get confused. In the present work, resonators are distinguished from cavities by their neck, i.e. by an opening that is small relative to the dimensions of the volume behind it. Similar to resonators, the flow-induced oscillations in cavities are generally undesired, and there have been a variety of efforts to avoid them in both passive (e.g. Franke & Carr, 1975; Heller & Bliss, 1975; Currle, 1990; Zhang *et al.*, 1999) and active ways (e.g. Lamp & Chokani, 1999; Raman *et al.*, 1999; Williams & Fabris, 2000; Kegerise *et al.*, 2002). The fluid dynamics differ from the motion present in a flow-induced Helmholtz resonator in that separation regions or a recirculating-flow field can form within the cavity (Rockwell & Naudascher, 1978). As a consequence, the geometry of the cavity, especially the ratio of streamwise length to depth, has a direct impact on the flow topology, whereas for the oscillations of Helmholtz resonators only the size of the cavity volume is important.

1.3.3 Principles of fluidic separation control

A number of extensive review articles have been published which provide an overview of separation control principles and methods. Work done in this field in the era of World War II and during the 15 years thereafter was summarized by Lachmann (1961*a*,*b*), while more recent reviews, focusing on fluidic control methods, were given by Fiedler & Fernholz (1990), Gad-el-Hak & Bushnell (1991), Wygnanski & Seifert (1994), Wygnanski (1997), and Greenblatt & Wygnanski (2000).

The reasons causing a flow to detach from a wall along with a variety of common control methods to reduce or prevent separation have already been discussed in section 1.1. The flow-induced Helmholtz resonator as the control method chosen in this investigation belongs to the class of fluidic control devices. Therefore, the present section is confined to aspects relevant mainly to this group of actuators. It is compiled from the aforementioned papers.

Fluidic separation control can be achieved by steady or oscillatory blowing and suction, or a combination thereof. As for other methods, the basic approach is to counteract the deficit in the streamwise velocity profile in the

near-wall region of a boundary layer on the verge of separation by energizing the inner layer. This can be accomplished by direct addition of momentum, for example by tangential blowing, or by transfer of momentum from the free-stream either as a result of removing the non-energetic part of the profile through suction or as a consequence of transverse mixing due to oscillatory actuation. If excitation is applied, it is commonly produced in active ways by internally mounted loudspeakers, pistons, valve systems or piezoelectric diaphragms and discharged into the flow through slits in the surface of the investigated body.

Oscillatory fluidic control has been shown to work effectively in both laminar and turbulent flows in a number of different configurations at low and high Reynolds and Mach numbers. In certain cases, excitation at proper frequency and amplitude restored a fully separated flow to a completely attached state. However, it remains to be seen how well this technique performs in practical applications. In general, the success of separation control by fluidic means depends on the location of the actuator where the excitation is introduced into the flow, the frequency and intensity of the oscillations, and the particular characteristics of the flow configuration considered. With respect to a variation of the individual control parameters, hysteresis was observed.

The optimum location of a fluidic actuator with respect to the separation line depends on the flow properties. The excitation should be introduced where the flow is receptive to it. If the boundary layer amplifies the imposed oscillations prior to detaching, an actuator location some distance upstream of the separation line might be beneficial. In the majority of cases, however, the effectiveness of the excitation decreases with increasing distance between actuator and separation location. If, under these circumstances, the actuator is placed too far upstream, the amplitude of the excitation decays before it reaches the separated flow region. Instead, fluidic separation control is usually most efficient when applied at, or close to, the natural separation line. Regarding the precise location, it seems advantageous to introduce the excitation slightly upstream of the separation line, rather than slightly downstream of it, although this might vary depending on the application.

The perception which processes in the near-field of fluidic actuators are responsible for bringing about the drastic changes in the flow downstream has changed over the past years. Initially, the effect of such actuators was attributed to emanating pressure waves or to vortical disturbances excited by sound through a receptivity process. However, it is now established that a purely fluidic mechanism is the key in this kind of separation control. Due to interaction of the cross-flow with the reciprocating motion of the fluid in the actuator neck driven by the excitation, large-scale vortices are produced which shed from the sharp edges of the slit (e.g. Erk, 1997, chap. 5). If the slit extends normal to the free-stream direction, two-dimensional, spanwise vortices are generated. Their dimension scales with the oscillation frequency of

the actuation. The vortices enhance the mixing rate downstream and, therefore, result in an effective transport of high-momentum fluid across the shear layer into the near-wall region. As a consequence, flow separation is delayed or even completely avoided in situations where an adverse pressure gradient prevails. In configurations where geometry-induced separation occurs, the spreading rate and entrainment of the shear layer forming downstream of the separation point are increased, resulting in a reduction of the reattachment length.

Reverse-flow regions feature a shedding-type instability and are bounded by a shear layer with a Kelvin-Helmholtz instability. In the context of the underlying physical principles of the control mechanism, there is dissent about the importance of these flow instabilities. This aspect is of practical relevance, because it is closely linked to the choice of an appropriate excitation frequency and to the amplitude required for the control. An unstable flow is particularly receptive to periodic disturbances of a certain frequency or frequency-band and amplifies them. Therefore, if a flow is excited at the frequency where it is most unstable, the actuation amplitude required to achieve a certain effect would be minimal. For active control devices, this means that external energy input need be minimal.

In view of the instability issue, the question which excitation frequency is the most effective for control is still a matter of discussion. The available data of various investigations are slightly contradictory. On the one hand, some authors (e.g. Wygnanski, 1997) claim that their fluidic control method exploits the instabilities inherent in the flow. In this regard, reduced frequencies St_L of the order $O(1)$ based on a characteristic length L of the problem have proven to work well in many configurations such as a deflected flap or an airfoil. On the other hand, although experimenting with very similar set-ups, other researchers (e.g. Erk, 1997) report no frequency selectivity but find a wide range of frequencies to be effective for flow control. Amitay *et al.* (2001) and Amitay & Glezer (2002) even suggest reduced frequencies St_L as high as $O(10)$ to yield optimum results.

Unfortunately, a straightforward comparison of data from the literature to clarify these contradictory statements is hampered by three factors: Firstly, a number of investigations fail to properly quantify the amplitude of the excitation applied. Often, the velocity perturbations at the actuator slit are determined using a single hot-wire probe which is, however, strongly biased by the cross-flow. A calibration in the absence of a grazing flow to circumvent this problem, in turn, changes the impedance of most excitation sources. Secondly, some fluidic actuators show three-dimensional behavior when driven at sufficiently high frequencies. This, of course, affects the success of the flow manipulation. Thirdly, the excitation frequencies are often reported as non-dimensional frequencies based on quantities that are, from a physical point of view, not relevant. For instance, in airfoil experiments the chord length c_w is a convenient length scale, but it is the length or height

of the separated flow region that dictate the parameters required for the control.

In general, a relatively low sensitivity of the flow to the reduced excitation frequency can be stated such that the suppression of separation seems to be a rather continuous function of St_L. Although for each configuration an optimum actuation frequency can be found and some frequencies even turn out to be detrimental, the physical reasons for this remain obscure. It is unclear if the effects can be attributed to the exploitation of a flow instability, or rather to a favorable match of the vortex dimensions and spacing to the extent of the separated flow region. It is also worth noting that the optimum excitation frequency is not significantly affected by the state of the upstream boundary layer (i.e. laminar, transitional, or turbulent).

Regarding the strength of the excitation, Poisson-Quinton & Lepage (1961) concluded from a variety of experiments on airfoils that separation control by steady blowing is governed by the momentum rather than the mass flux of the control device. Thus, in order to characterize the blowing intensity, they introduced the momentum coefficient c_μ in 1948. It is defined as the momentum flux $\dot{m}v_j$ due to the blowing relative to the free-stream dynamic pressure $\frac{1}{2}\rho U_\infty^2$ and wing area S_w:

$$c_\mu = \frac{\dot{m}v_j}{\frac{1}{2}\rho U_\infty^2 S_w} = \frac{4s}{c_w}\frac{v_j^2}{U_\infty^2}. \tag{1.10}$$

The jet velocity averaged across the slit of width $2s$ is represented by the parameter v_j. In the study of Poisson-Quinton & Lepage (1961), it was determined from the difference between driving pressure for blowing and ambient pressure under the assumption of isentropic conditions. $\dot{m}$ denotes the mass flux of fluid of density ρ out of the slit. The free-stream velocity is given by U_∞ and c_w is the chord length of the airfoil.

Seifert *et al.* (1993) extended the above definition of c_μ to oscillatory actuation by replacing the steady jet velocity v_j with the phase-averaged amplitude $\langle\hat{v}_j\rangle$ of the periodic flow in the slit. The corresponding quantity is called the oscillatory blowing momentum coefficient:

$$\langle c_\mu\rangle = \frac{4s}{c_w}\frac{\langle\hat{v}_j\rangle^2}{U_\infty^2}. \tag{1.11}$$

No data were presented, however, to substantiate that $\langle c_\mu\rangle$ is the appropriate quantity to characterize the intensity of zero net-mass-flux actuation producing alternating in- and outflow. Nevertheless, it is now extensively used for this purpose by various authors.

According to Wygnanski (1997), the delay of separation by periodic addition of momentum is attainable at levels of c_μ which are about two orders of magnitude lower than those necessary with steady blowing. To quantify the success resulting from the application of an active fluidic control method, the

net effect has to be considered, i.e. the balance between energy gain due to the actuation and energy expended for it. This aspect is frequently neglected in the literature. Experiments of separation control in diffusers by Kwong & Dowling (1994) and of airfoil stall control by Greenblatt & Wygnanski (2000) are exceptions in this respect. In both investigations, the net effect of excitation is reported to remain positive.

The general principles of fluidic separation control addressed in this section apply to a wide variety of flow situations including the flow in diffusers and around airfoils. These two configurations will be used as case studies in the present investigation to control a flow by means of acoustic resonators. Therefore, sections 1.3.4 and 1.3.5 will review examples of quantitative results for both cases.

1.3.4 Separation control in diffusers

Diffusers are diverging channels where a part of the kinetic energy of the flow is used to increase the static pressure difference Δp between the inlet and outlet. The diffuser performance is described by the pressure recovery coefficient $c_p = \Delta p/(\frac{1}{2}\rho U_\infty^2)$. Its upper limit is given by the corresponding c_p obtained from potential-flow theory as $c_{p_{\mathrm{pot}}} = 1 - (A_{\mathrm{in}}/A_{\mathrm{out}})^2$ where A_{in} and A_{out} are the cross-sectional areas of the diffuser inlet and outlet, respectively. At sufficiently high expansion angles, the adverse pressure gradient in streamwise direction causes the viscous flow to detach and the pressure recovery to drop. Although of fundamental and practical interest, investigations are comparatively scarce to control the separation region in planar diffusers and to enhance their performance.

In an experimental study, Obi *et al.* (1993) manipulated the pressure-induced separation region in an asymmetric planar diffuser with moderate expansion angle ($\beta = 10\,^\circ$). Inflow conditions were fully turbulent. Applying active excitation at a location 140 mm upstream of the separation line equivalent to a distance of 70 times the slit width of the actuator, the reverse-flow region was reduced or, at high momentum coefficients, eliminated. However, the manipulation was effective only within an optimum frequency range. For a reduced frequency $St_H = 0.11$ based on the diffuser height H, a maximum increase of the pressure recovery by 10 % was achieved. When forcing at $St_H = 0.52$, in contrast, the recirculation zone was even prolonged by 50 %. The relatively small improvement of the pressure recovery might be attributed to the large distance between actuator location and separation line in addition to the small dimensions of the separated flow region.

Another experimental investigation was performed by Kwong & Dowling (1994) aimed at enhancing the pressure recovery and diminishing the flow unsteadiness associated with separation in axisymmetric and planar diffusers. Steady blowing was effective in reducing the extent of the reverse-flow region and improving c_p, while zero net-mass-flux actuation via a feed-back loop

attenuated the flow unsteadiness. The energy net gain was positive when forcing the flow by steady blowing, but vanished for unsteady actuation. The combination of steady and unsteady blowing gave both a positive net gain owing to a good mean pressure recovery and reduced pressure oscillations.

Coller *et al.* (2000) tested a reduced-order model against measurements in a rapidly expanding half diffuser ($\beta = 23\,^\circ$) where the turbulent inflow detached at the sharp edge of the inlet. In contrast to the flow situation considered by Obi *et al.* (1993), the separation line was fixed changing from a weak to a strong reverse-flow pattern and causing the formation of an extensive recirculation zone. As a result, the diffuser exhibited extremely poor performance indicated by a pressure recovery of the baseline flow as low as 22 % of $c_{p_{\mathrm{pot}}}$. Excitation was introduced by a zero net-mass-flux actuator directly at the separation line. By application of an oscillatory momentum coefficient an order of magnitude less than in the investigation by Obi *et al.* (1993), the pressure recovery was greatly enhanced, but the performance remained significantly smaller than the potential flow value. In this context, Coller *et al.* (2000) pointed out that the velocity fluctuations due to the actuation are, on the one hand, a necessary prerequisite to enhance the mixing and promote the transversal momentum transfer, but on the other hand add to the pressure losses. This reduces the pressure recovery by about 10 % under forced conditions. Similarly to Obi *et al.* (1993), an optimum frequency range was found within which the pressure recovery was improved most. At the most effective reduced excitation frequency of $St_H = 0.24$, the flow responded to the actuation by forming pronounced vortical structures.

Author	Δc_p [%]	$c_{p_{\mathrm{base}}}$	$c_{p_{\mathrm{ctrl}}}$	$c_{p_{\mathrm{pot}}}$	β	St_H	$\langle c_\mu \rangle$
O. *et al.* '93	10	0.61	0.67	0.95	10°	0.11	1.21×10^{-2}
C. *et al.* '00	205	0.19	0.58	0.85	23°	0.24	1.26×10^{-3}

TABLE 1.2: Overview of flow control success and effective parameters in diffusers from experiments found in the literature. Δc_p describes the improvement in pressure recovery by comparison of the baseline and the controlled case represented by $c_{p_{\mathrm{base}}}$ and $c_{p_{\mathrm{ctrl}}}$, respectively. Both St_H and $\langle c_\mu \rangle$ are based on the difference H between outlet and inlet height of the diffuser.
O. *et al.* '93: Obi *et al.* (1993), C. *et al.* '00: Coller *et al.* (2000).

The aforementioned studies have in common that they achieve an improvement of the diffuser performance and a reduction of the separated flow region using flow-control mechanisms portrayed in section 1.3.3. A brief overview of related benchmark data is shown in table 1.2.

1.3.5 Separation control on airfoils

The scope of the present section is limited to types of separation on airfoils which are severely detrimental to lift. Flow scenarios of this kind are denoted

as stall and typically occur at high angles of attack when the airfoil operates near its maximum lift coefficient. According to McCullough & Gault (1951), three representative types of stall on airfoils can be distinguished: leading-edge stall, trailing-edge stall, and thin-airfoil stall. Leading-edge stall is characterized by an abrupt separation of the flow from the forward part of the airfoil accompanied by a drastic break-down of lift and a sharp rise in drag. Trailing-edge stall occurs, if the turbulent boundary layer detaches starting out from the aft of the suction side followed by a gradual upstream movement of the separation line with increasing angle of attack. Variations in lift and drag are smooth and continuous in this case. Thin-airfoil stall denotes a type of leading-edge stall marked by the formation of a separation bubble in the vicinity of the leading edge. With increasing angle of attack, the bubble grows in size until its reattachment line has eventually moved beyond the airfoil trailing-edge. Due to the distinct features of the three types of stall, an application of different control strategies is required.

We confine ourselves to the control applied to airfoils under post-stall conditions exhibiting flow separating from the leading edge. As this is the area of most active recent research, investigations of this kind are numerous (e.g. Ahuja & Burrin, 1984; Hsiao *et al.*, 1994; Wu *et al.*, 1998; Seifert & Pack, 1999). Examples of the control of trailing-edge stall are given by Huang *et al.* (1988), Siller & Fernholz (1999), and Goetz (2000). A thin-airfoil-stall scenario was investigated by Zhou *et al.* (1993).

Experiments on the fluidic control of leading-edge stall have in common that they employ actuators following identical design principles: oscillatory velocity perturbations are introduced into the flow near the separation line through a spanwise slit in the airfoil surface. The slit is connected by some kind of wave duct to a driver, e.g. a loudspeaker, piston, or piezoelectric element. Whereas the actuator location is fixed, the separation line shifts depending on the angle of attack.

This kind of separation control has been shown to be effective independent of the state of the upstream boundary layer, for swept and unswept wings, as well as on delta wings (Greenblatt & Wygnanski, 2000). Although most experiments were carried out on low-Reynolds-number airfoils, Seifert & Pack (1999) demonstrated recently that excitation produces similar results at chord Reynolds numbers as high as 3.8×10^7. As discussed earlier in section 1.3.3, the determination of the proper excitation frequency is still an unresolved issue. Greenblatt & Wygnanski (2000) report the most effective reduced frequencies to lie in the range of $0.3 \leq St_c \leq 4$. Amitay & Glezer (2002), in contrast, suggest $St_c \geq 10$. The oscillatory momentum addition $\langle c_\mu \rangle$ required varies between 1×10^{-4} and 3×10^{-2}.

In the post-stall regime, the effects of separation control on airfoils are most significant. The separated flow region can be greatly reduced resulting in an improvement of airfoil performance. The lift can be maintained at higher angles of attack, while leading-edge stall is delayed. However, there

is no or only a small beneficial effect on the maximum lift coefficient. Erk (1997) found that the increase in lift is coupled with a narrower wake and, therefore, reduced drag. He also noted the existence of a lower threshold of the excitation amplitude above which the control resulted in an increase of the lift coefficient. Above an upper threshold, the lift increase due to excitation saturates and in fact decreases with additional momentum input. In this case, the unsteady jet emanating from the actuator seems to block the oncoming boundary layer and promote separation.

The control technique described can also be applied in conjunction with high-lift systems, for example at the leading-edge of a trailing-edge flap. In this case, it is possible to enhance the circulation, and thus the lift, by a further increase of the excitation amplitude after separation control has reached saturation.

Several studies have been concerned with the control of a separation region forming under post-stall conditions on the wing section used in the present investigation. Details can be found in Béraud (1994), Clara (1996), Erk (1997), and Urzynicok (1997).

1.3.6 Separation control using flow-induced resonators

There exist very few studies which employ flow-induced oscillations of acoustic resonators for the purpose of flow control, or even more specific to manipulate separation regions. The only exceptions known to the author are represented by the work of Lin *et al.* (1990), the thesis of Erk (1997), and the report of Bader & Grosche (1999).

Flynn *et al.* (1990) were the first to suggest that a field of Helmholtz resonators (with circular orifices, in this case) driven by a grazing flow could modify a turbulent boundary layer. In a flow with zero pressure gradient, they observed a strong alteration of the turbulence structure in the boundary layer downstream of the resonators (logarithmic law, Reynolds stresses). In the vicinity of the orifice, the turbulent fluctuations normal to the free-stream increased by 300 % and at 20 orifice diameters downstream the turbulence level was still 3 % higher.

Lin *et al.* (1990) comparing several methods to control turbulent separation downstream of a ramp found that a row of passive resonators with circular orifices had no effect on the separation region, although they produced high acoustic disturbances in case of resonance. Most likely, however, the resonators were placed too far upstream of the separation line (3.5δ) due to experimental constraints. Furthermore, it is unknown, whether resonance frequency and amplitude were suitable to match the properties of the separated flow region.

In contrast to this, Erk (1997) found that on a wing section under post-stall conditions the spanwise cavity-slot system near the leading edge, designed to be actively driven by loudspeakers, acted as a flow-induced res-

onator when the energy input was turned off. As a result, pressure fluctuations in the cavity were high and lift was up by 9 % compared with the unforced flow.

With a similar configuration, Bader & Grosche (1999) delayed leading-edge separation on an airfoil towards higher angles of attack by 2 ° due to flow-induced pressure fluctuations in their cavity-slot system.

1.4 Outline of the following chapters

In the investigation of separation control by flow-induced acoustic resonators two partial aspects can be identified that can be looked at independently: on the one hand resonator-related issues such as their acoustic properties and how resonance is induced by a cross-flow, on the other hand how a separation region can be controlled by fluidic methods. This leads to two principal questions, the first one being how to provide excitation of a defined frequency and amplitude by means of a resonator, and the second which frequency and amplitude are most effective in manipulating a separation region. After a presentation of the experimental facilities and techniques (chapter 2), the first problem is addressed for single Helmholtz resonators in chapter 3 and for systems of adjacent resonators in chapter 4. The second problem is discussed in chapter 5. Finally, both problem areas are merged in chapter 6, which demonstrates the success of separation control by acoustic resonators based on examples of two different flow configurations: The first set-up incorporates a resonator upstream of a rapidly expanding planar asymmetric diffuser applied to reduce the evolving reverse-flow region. In the second case, a flow-induced resonator is used to manipulate the laminar flow separating from the leading edge of an airfoil at high angle of attack. Both configurations differ in the characteristics of the boundary layer grazing past the resonator and in the location of the Helmholtz resonator with respect to the separation line. Chapter 7 is devoted to a closed-loop control strategy that approaches both problems at the same time.

Although great care has been taken to keep the notation as consistent as possible, each chapter is followed by its own table of symbols to avoid confusion in the abundance of different physical quantities.

List of symbols

A_{in}	cross-sectional area of the diffuser inlet
A_{out}	cross-sectional area of the diffuser outlet
b	radius of a circular pipe
c	speed of sound ($\approx 343\,\text{m/s}$ in air at room temperature)
c_p	pressure coefficient ($= \Delta p/(\frac{1}{2}\rho U_\infty^2)$)
$c_{p_{\text{base}}}$	pressure coefficient associated with baseline flow conditions

$c_{p_{\mathrm{ctrl}}}$	pressure coefficient associated with manipulated flow conditions
$c_{p_{\mathrm{pot}}}$	pressure coefficient obtained from potential flow theory
c_w	airfoil chord length
c_μ	momentum coefficient
$\langle c_\mu \rangle$	oscillatory blowing momentum coefficient
C_1	constant
f_0	resonance frequency
f_n	resonance frequency of order n
H	diffuser height
i	imaginary unit ($= \sqrt{-1}$)
K	Rayleigh conductivity
L	characteristic length
l_n	neck length of a resonator
l_n^*	effective neck length of a resonator
l_y	height of the resonator cavity
$\dot{m}$	mass flux
n	order of resonance ($= 0, 1, 2, \ldots$)
p_1	sound pressure inside the resonator cavity
p_2	sound pressure outside the resonator neck
p	static pressure
p_{cav}	rms sound-pressure within the resonator cavity
p_{dyn}	free-stream dynamic pressure
Q	quality factor of resonator
R	radius of opening
s	half-slit width of the resonator neck
S	cross-sectional area of the resonator orifice
S_w	wing area
St_{2s}	Strouhal number based on streamwise length of resonator neck
St_{2s_n}	Strouhal number based on $2s$ and f_n
St_c	Strouhal number based on airfoil chord length
St_H	Strouhal number based on diffuser height H
St_L	Strouhal number based on characteristic length L
St_{δ_2}	Strouhal number based on boundary layer momentum thickness
t	time
U_c	convection velocity of a vortex in the resonator opening
U_∞	free-stream velocity
v	perturbation velocity in y-direction
v_j	velocity in the actuator slit averaged across the width
$\langle \hat{v}_j \rangle$	phase-averaged amplitude of v_j
V	volume of the resonator cavity
$\dot{V}$	perturbation volume flux
y	wall-normal coordinate originating at the wall
Z	specific acoustic impedance
β	diffuser expansion angle

δ	boundary-layer thickness
δ_2	momentum thickness of the boundary layer
Δc_p	variation of pressure coefficient due to excitation
Δl_n	end correction
Δl_{n_e}	end correction on exterior side of neck
Δl_{n_i}	end correction on interior side of neck
Δp	static pressure rise in diffuser
ε	exponential decay rate
ρ	mass density of fluid
ρ_0	mean mass density of fluid
ω	angular frequency
ω_0	angular resonance frequency

Chapter 2

Experimental apparatus and methods

The present investigation addresses a wide variety of aspects associated with flow control by aerodynamically excited resonators. The scope ranges from purely acoustic measurements of a resonator's frequency response to the documentation of the effect of separation control on the flow field in two sample configurations. In this chapter, after a portrayal of the two types of resonator models used as fluidic actuators (section 2.1), the wind tunnels the experiments were conducted in will be described (section 2.2), along with the measurement techniques applied (section 2.3). A detailed discussion of the various set-ups that were considered throughout this study is postponed to later chapters, and will be presented in the context of the respective experimental results to prevent confusion.

2.1 Resonator models

Two different types of resonators were employed in the course of these experiments. A resonator with rectangular cavity cross-section was investigated to gain further insight into the details of the flow-induction process and to optimize the aerodynamic excitation with respect to the use as fluidic actuator. Subsequently, this resonator was adopted to manipulate the reverse-flow region in a planar asymmetric diffuser. On the other hand, the flow separating from the leading edge of an airfoil under high angle of attack was controlled by a resonator with circular cross-section.

2.1.1 Resonator with rectangular cross-section

A two-dimensional resonator with a cavity of rectangular cross-section as shown schematically in figure 2.1 was employed in experiments carried out in the open-return wind-tunnel that will be described in section 2.2.1. In

these studies, the resonator neck was mounted flush with the surface and spanned the entire tunnel width of 400 mm. The internal dimensions of the cavity measured $l_x = 140\,\text{mm}$ in streamwise and $l_z = 387.3\,\text{mm}$ in spanwise direction, while the neck had a length of $l_n = 9.35\,\text{mm}$. All resonator walls were acoustically rigid.

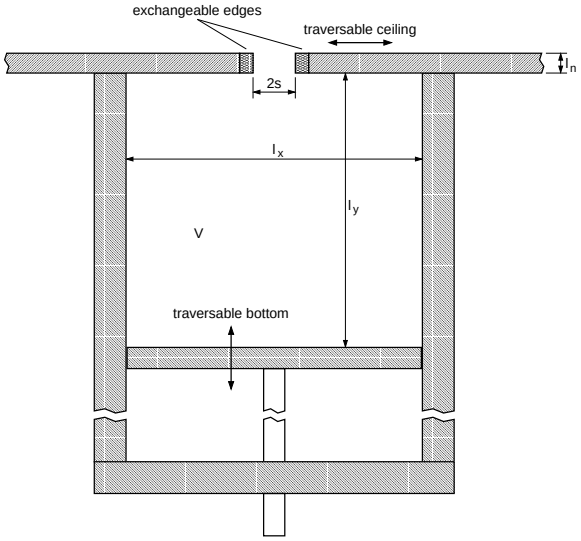

FIGURE 2.1: Resonator of rectangular cross-section with variable slit width $2s$ and variable cavity height l_y. l_x denotes the streamwise cavity length, l_n the neck length, and V the cavity volume.

The volume height l_y could be varied by traversing the bottom plate of the resonator cavity between 0 and 430 mm with a resolution of $3.2 \times 10^{-1}\,\mu\text{m}$. Between the bottom plate and the casing a 0.5 mm wide gap was left and sealed with a lubricated felt gasket. Similarly, the slit width $2s$ could be altered between 0 and 30 mm by moving one of the two plates forming the cavity ceiling. In this case, the positioning accuracy was $2.1 \times 10^{-2}\,\mu\text{m}$. Both traversing gears were operated by a PID-controller connected to a microcomputer.

By variation of l_y and $2s$, the cavity volume and the cross-sectional area of the orifice could be modified. According to equation (1.5), the resonance frequency is a function of both quantities such that the resonator could be tuned within a wide band of frequencies. If subject to acoustic excitation, strong resonance occurred at frequencies between 60 and 1000 Hz with an appropriate choice of these parameters. However, the range of frequencies induced in the presence of a grazing flow was smaller than this, as will be seen in section 3.2.5.

To study the influence of the neck shape on the intensity of the flow-induced oscillations, the orifice edges could be exchanged (see figure 2.1). Details of the various neck geometries will be shown in section 3.2.6 in con-

junction with the respective results.

The single resonator could be converted into a system of two to five adjacent resonators of identical dimensions arranged in spanwise direction. To this end, a corresponding number of rigid dividing walls of 5 mm thickness were installed in the cavity. As a result, the volume height was fixed at $l_y = 125\,\mathrm{mm}$, while slit width and neck geometry could be varied in the manner described before.

Optionally, for the experiments of chapter 5 determining the characteristic quantity of fluidic actuator output, the bottom plate including the traversing mechanism could be exchanged for an immovable plate holding loudspeakers as active actuators. In this case, the cavity height was fixed at $l_y = 50$ or $150\,\mathrm{mm}$, respectively.

2.1.2 Resonator with circular cross-section

In order to manipulate the separated flow on an airfoil, a two-dimensional resonator with circular cavity cross-section was used. It extended along the entire span of 900 mm. The orifice was flush with the wall on the suction side of the airfoil and was located near the leading edge at a chordwise position of $x/c = 1.9\,\%$ (figure 2.2). A neck of length $l_n = 5.3\,\mathrm{mm}$ connected the cavity to the ambient flow. As before, all resonator walls were acoustically rigid. A small fraction of the inside of the walls was lined with partially embedded steel tubes of diameter 2 mm which were required for the measurement of the static pressure distribution around the wing model.

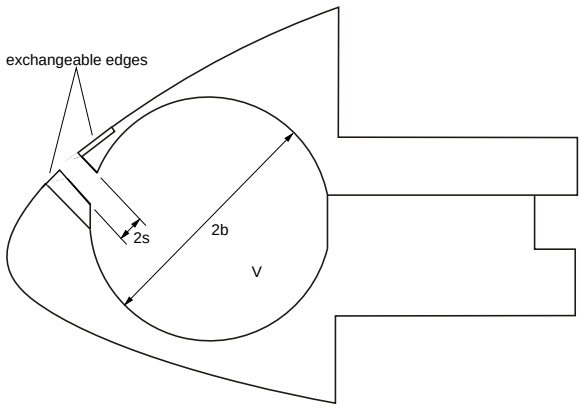

FIGURE 2.2: Nose section of the airfoil housing the resonator of circular cavity cross-section. $2s$ represents the slit width, b the radius of the cavity, and V its volume.

The resonator featured a slit whose width $2s$ could be varied in discrete steps between 1.6, 2.6, and 4.6 mm backed by a cavity of diameter $2b = 28\,\mathrm{mm}$. Unlike for the resonator with rectangular cross-section, the goal of varying the slit width was not to adjust the resonance frequency, but to maximize the resonator output. Since higher-mode oscillations were

dominant when controlling the flow in this case, the resonance frequency was independent of the slit width as it was entirely determined by the cavity dimensions. This will be shown in section 3.1.1.

Similar to the cuboidal resonator, the neck geometry could be modified by exchanging the upstream and downstream edges to optimize the oscillation amplitude. Details of the different geometries will be presented in section 6.5.1.

Alternatively, the resonator cavity could be equipped with a set of dividing walls of thickness 5 mm that were equally spaced in spanwise direction. As a result, systems of nine or ten adjacent resonators were obtained.

In experiments to measure the baseline flow properties, where excitation was undesired, masking tape was placed over the slit.

2.2 Wind tunnels

The success of flow control by acoustic resonators was demonstrated using two fundamentally different flow configurations (see sections 6.4 and 6.5) requiring the use of separate wind tunnels. This section reviews the characteristics of the tunnels.

2.2.1 Open-return wind-tunnel

The wind tunnel employed in the experiments investigating details of the flow-induction process of resonators and controlling the separated flow in a planar asymmetric diffuser is of the low-speed, open-circuit type (figure 2.3). It provides a maximum flow speed of about 28 m/s at turbulence levels less than 0.15 % throughout the entire velocity range (see figure A.1).

The flow is driven by a centrifugal fan with 12 backward-curved blades powered by a 3 kW motor. The downstream diffuser is decoupled from the fan in order to avoid vibrations and has an expansion ratio of 2.18. Together with the cylindrical settling chamber, it features a total of five screens and two filter mats to avoid separation and to minimize the turbulence level. A $6.25:1$ contraction provides the link to the test section of length 2325 mm with a rectangular cross-section of 280 mm $\times$ 400 mm. The 1800 mm long upstream portion of the side walls consists of a combination of acrylic and crystal glass to allow access to optical measurement techniques such as flow visualizations, Laser Doppler Anemometry (LDA), Particle Image Velocimetry (PIV), and oil-film interferometry. For the same reason, the entire top of the test section is made from acrylic glass. Due to spatial constraints, the tunnel ends into a compact, radial diffuser with an opening ratio of 5.46. It reduces repercussive effects that might occur in the test section as a consequence of vortex shedding due to the exiting jet.

The flow conditions in the measurement section of the wind tunnel are discussed in appendix A.

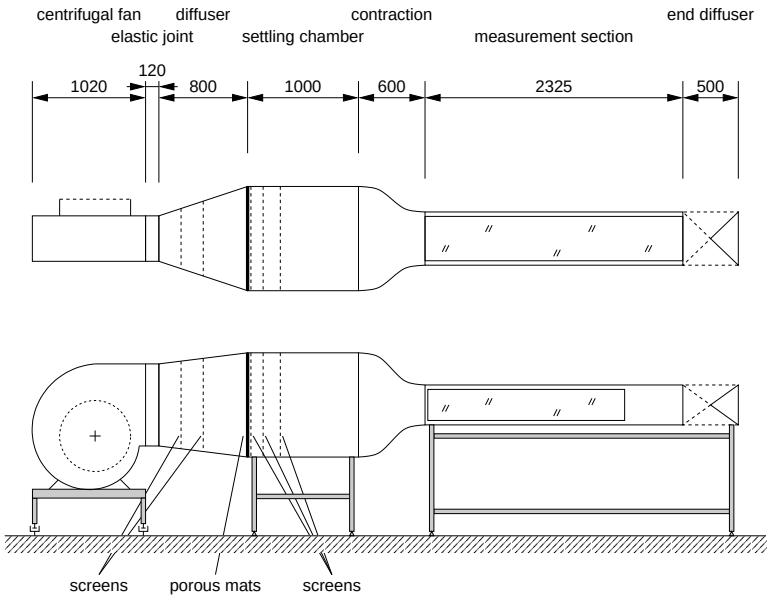

FIGURE 2.3: Top and side view of the open-return wind-tunnel utilized for resonator and diffuser studies.

2.2.2 Closed-return wind-tunnel

The measurements concerned with separation control on a wing section by means of an acoustic resonator were conducted in the large wind tunnel of the Hermann-Föttinger-Institut. The tunnel was operated in closed-return configuration and provides flow speeds up to 40 m/s in the test section (figure 2.4). The turbulence level is less than 0.23 % over the entire range of the free-stream velocities with the incidence of the fan blades set to 30 % (Jaroch & Dengel, 1983).

The single-stage axial fan is powered by a 500 kW motor and features adjustable blades. Among the particular characteristics of the tunnel are sound absorbers upstream and downstream of the fan, turning vanes in the corners, and a set of screens and filters in the settling chamber aiming at reducing the turbulence level. The settling chamber is followed by a 6.25 : 1 contraction. The subsequent test section consists of four interchangeable boxes with a cross-section of 2000 mm × 1400 mm measuring 10000 mm in total length. The first box is equipped with a six-component mechanical balance accessible through the wind-tunnel floor. Windows in the roof and the side walls allow for the observation of flow visualizations or the application of optical measurement devices.

A detailed assessment of the flow conditions in this wind tunnel was provided by Jaroch & Dengel (1983).

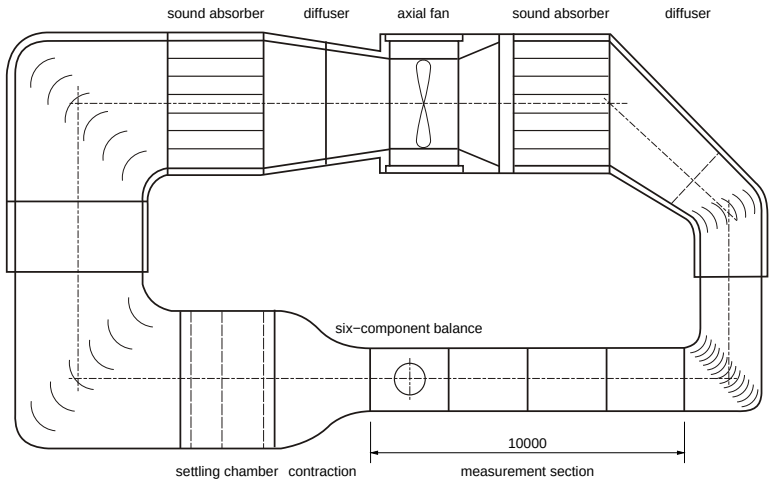

FIGURE 2.4: Top view of the large closed-return wind-tunnel of the Hermann-Föttinger-Institut utilized for airfoil studies.

2.3 Measurement techniques

In this section, the measurement techniques applied are presented. They are discussed in the context of the wind tunnel they were used in. As a consequence, a few measurement techniques may be mentioned twice. In these cases, the differences regarding settings and equipment involved will be pointed out depending on the wind tunnel.

2.3.1 Measurement techniques in open-return wind-tunnel

The measurements performed in the open-return wind-tunnel comprised flow visualizations along with the determination of acoustic quantities, static and dynamic pressures, wall shear-stresses as well as mean and fluctuating components of the velocity vector throughout the flow field. The techniques were applied to study resonator oscillations induced by a zero pressure-gradient flow and the effect of flow control in a diffuser.

Flow-visualization techniques

The flow topology along the wall in the wake of various systems of adjacent resonators was visualized by applying the oil-film technique. To this end, the wall consisting of a blackened glass surface was coated with a thin layer of a mixture of petroleum, oleic acid, and finely powdered white pigments of titanium dioxide. As the flow acted on the coating, the petroleum evaporated and left behind dry pigments on the surface. The remaining pattern gave a time-averaged picture of the flow direction close to the wall. Further details on this technique can be found, for example, in Merzkirch (1987).

To determine the separation line on the inclined wall of the diffuser configuration, the application of the oil-film technique was impractical. The coating would have been strongly biased by gravitational forces such that an array of tufts was used instead to visualize the flow field. Orienting the tufts in streamwise direction, one end was attached to the surface using tape. The choice of nylon yarn with diameter 0.1 mm as tuft material was determined by a balance of indicating behavior, stiffness, intrusiveness, and the tendency to tangle. A comprehensive overview of flow visualizations involving tufts is given by Crowder (1989).

All flow patterns visualized were captured with a 1.5 megapixel digital camera of type Kodak DC260 with an 8–24 mm zoom lens. Inherent to both visualization techniques is that there might be a slight error resulting from the disturbance of the flow close to the wall by the presence of either the oil-film or the tufts. Therefore, during flow visualizations no data were collected by other measurement techniques.

Microphone measurements

Microphone probes of 0.25 in (6.35 mm) diameter were used to record pressure spectra within the cavities of aerodynamically excited resonators. When investigating systems of adjacent resonators, a probe mounted flush with one of the side walls was embedded in each of the cavities. From the spectra, the peak response frequency as well as the corresponding sound pressure were determined.

The condenser microphones consisted of capsules (Brüel & Kjær 4136) in conjunction with Brüel & Kjær 2670 preamplifiers. In the range between 20 Hz and 10 kHz, their frequency response was flat within ± 0.25 dB. The upper limit of their dynamic range was 172 dB below which the distortion of the sound pressure was less than 3 %. The microphone signal was fed into a measuring amplifier (Brüel & Kjær 2610) and then processed by a Hewlett Packard 35670A Dynamic Signal Analyzer or by a Hewlett Packard 34970A digital voltmeter. Typically, a number of 10 spectra were averaged, each of which had a bandwidth of 800 Hz and a frequency resolution of 0.5 Hz.

In order to determine the sound pressure radiated into the ambient medium by a flow-induced resonator, a microphone probe fitted with a Brüel & Kjær streamlining nose cone (UA 0385) was placed in the free-stream. It was positioned near the end of the test section at a distance 1573 mm downstream of the resonator orifice ($x = 2230$ mm). As the probe was mounted on a y-z-traversing gear, the sound pressure could be measured throughout the entire tunnel cross-section in case a standing wave pattern occurred.

The absolute calibration of the microphones was accomplished via a pistonphone (Brüel & Kjær 4228) taking into account a correction for variations in the ambient static pressure. The resulting uncertainty was less than 0.15 dB. For the measurement of phase differences between the oscillations

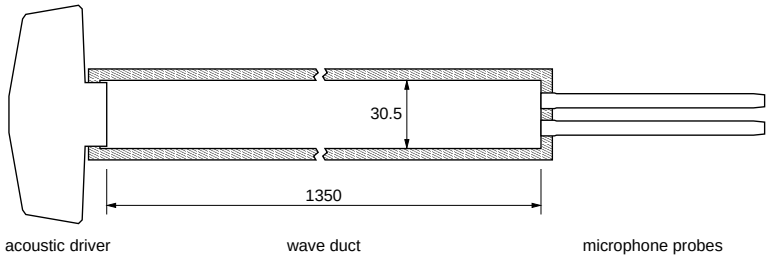

FIGURE 2.5: Schematic of the test rig used for relative calibration of four microphones at a time.

of adjacent resonators, a relative or phase calibration was performed in a special calibration rig (figure 2.5). It featured a cylindrical wave duct of length 1350 mm with a loudspeaker attached to one end and a set of four microphones mounted at the other end. The probes were flush with the terminating wall at an exact equal distance from the acoustic source. The tube diameter was 30.5 mm such that only plane waves could propagate at frequencies below the cut-off frequency of 6591 Hz. This ensured that sound waves arriving at the microphones were characterized by the same phase throughout the entire cross-section. White noise in the frequency range from 20 Hz to 5 kHz was applied during the calibration. Relative to each other, all Brüel & Kjær microphones exhibited phase deviations which were less than $\pm 1\,^\circ$ in this band of frequencies.

Measurement of dynamic and static pressure

The free-stream dynamic pressure was monitored by means of a Prandtl probe extended from the tunnel ceiling 218 mm downstream of the entrance to the test section. The probe was mounted at an off-center position ($z = -100$ mm), 67.5 mm underneath the ceiling. In the zero pressure-gradient set-up, this was equivalent to a wall distance of $y = 182.5$ mm while in the diffuser configuration $y = 67.5$ mm.

To assess the pressure recovery produced by the half diffuser, the difference in static pressure between the Prandtl tube upstream and a static pressure probe (see Vagt & Fernholz, 1977) downstream of the diverging section was measured. For this purpose, the latter probe was placed as far as possible downstream of the separation region at $x = 2125$ mm on the tunnel centerline. At this location, the transverse distribution of the static pressure coefficient was back to being approximately homogeneous. In the most unfavorable case, however, variations were still as high as $\pm 8.7\,\%$. Therefore, a wall distance was chosen where the vertical gradient was negligible such that c_p was not significantly affected by the inhomogeneities ($y = 40$ mm).

The differential pressure transducers were MKS Baratron 220 CD and 120 AD with an accuracy of $\pm 0.15\,\%$ and $\pm 0.12\,\%$ of the reading, respec-

tively. Their output voltage was averaged by an HP 34970A multimeter over periods of 20 s for the Prandtl tube and 200 s for the static pressure probe.

Wall shear-stress measurement techniques

Preston tube In order to determine the wall shear-stress in zero pressure-gradient flow, Preston tubes of diameters $d = 1$, 1.5, and 2 mm were used. The corresponding static pressure was measured by a static pressure probe at the exact same streamwise position with a wall distance of $y = 25$ mm and a spanwise offset of $\Delta z = 100$ mm. From the pressure difference, the wall shear-stress was calculated making use of calibration curves according to Patel (1965). In boundary layer scaling, the Preston tube diameters $d^+ = du_\tau/\nu$ were between 25 and 150 which was well within the range of the calibration. Herein, u_τ denotes the friction velocity and ν the kinematic viscosity. The pressure signals were measured and processed in the same way as described before in the context of other pressure probes. Averaging times were from 120 to 200 s.

Wall pulsed-wire anemometry Wall pulsed-wire anemometry was applied to determine the wall shear-stress and the reverse-flow factor as measures of the success of separation control by resonators. The reverse-flow factor represents the number of samples indicating flow in the upstream direction with respect to the total amount of samples taken. Details of this measurement technique are described in a survey by Fernholz *et al.* (1996).

In the half-diffuser configuration, the probe was mounted on a segment that was inserted flush with the wall into a groove of length 1088 mm along the centerline of the test section. By interchanging the segments which filled the groove, the measurement location could be adapted.

Both the wall pulsed-wire anemometer and the probes were built in-house. In order to generate a sufficiently large heat tracer in the highly turbulent flow, the probes featured a pulsed wire of diameter 9 µm with a length of 4 mm. Depending on the probe, the distance between pulsed and sensor wires was 0.5 and 0.7 mm. The sensor wires had a diameter of 2.5 µm and an active length of 2 mm. Their clearance to the wall measured 70 µm.

The probes were calibrated against a Preston tube of diameter 1.5 mm in a turbulent boundary layer with zero pressure-gradient. For the collection of calibration and measurement data, the probes were pulsed at a frequency of 25 Hz for a total of 5000 and 7500 samples, respectively. The overall accuracy of this method is estimated by Fernholz *et al.* (1996) to be ±4 %.

Hot-wire anemometry

As a measurement technique with high temporal resolution, hot-wire anemometry was performed to gather spectra of the velocity fluctuations. At

the spanwise center of the entrance to the empty measurement section ($x = 0\,\text{mm}$, $y = 60\,\text{mm}$, $z = 0\,\text{mm}$), it was used to assess the turbulence level of the wind tunnel. In the planar diffuser, power spectra of the flow were taken to determine the frequency of instabilities in the shear layer separating at the diffuser inlet. In this case, the measurement location was 375 mm downstream of the entrance to the expanding portion.

The probes were manufactured in-house made of a 5 µm platinum-coated tungsten wire with gold-plated ends and an active length of 1.2 mm. They were operated with an overheat ratio of 60 %. The anemometer bridge (DLR HDA III F) provided a linearized signal after calibration. The output signal was then processed by an FFT analyzer (HP 35670A) to determine power spectra and rms-fluctuations. Due to use of the AC mode involving a 1 Hz high-pass filter, all spectra were limited to the range above this cut-off frequency. Typically, a total of 250 spectra were averaged, with a frequency resolution of 0.25 Hz.

The hot-wire probes were calibrated versus a Prandtl tube in the free stream. The linearization of the calibration chart was based on King's law.

Laser Doppler Anemometry

A two-component Dantec FiberFlow system based on the color separation method was used for non-intrusive LDA flow measurements in backscatter mode. It served to measure cross-sections of the velocity fields within the resonator slit and the diffuser, velocity profiles of the boundary layers up- and downstream of the resonator, and the reverse-flow factor in a plane parallel to the inclined diffuser wall.

A 300 mW air-cooled argon-ion laser of type Ion Laser Technology 5500A-00 delivered coherent light to a transmitter box (60X41) with four fiber manipulators (60X24). Connected to them by a glass fiber cable (60X30), the fiber optic transducer was a 60 mm probe of type 60X63. To reduce the size of the measuring volume, a beam expander 55X12 was attached to the probe. Most of the experiments were performed using optics with a focal length of 600 mm giving a measurement volume of the shape of a spheroid with diameter 88 µm and length 1.40 mm. High-accuracy boundary layer profiles were determined with a focal length of 310 mm resulting in a corresponding measurement volume of 46 µm in diameter and 0.38 mm in length (see table 2.1). The transmitting optics were mounted on a three-dimensional traversing gear outside the test section. Usually, a number of 1×10^5 bursts were requested within a permitted time frame of 60 s. To improve accuracy even further, these values were increased to 2.5×10^5 bursts and 120 s for the measurements of sections 6.3 and A.4. Typical data rates were around 2 kHz. Bursts collected were processed by two burst spectrum analyzers (57N10 and 57N25) before the data were evaluated by software implemented in-house.

Focal length	[mm]	310	600	1000
Diameter of measurement volume	[mm]	0.046	0.088	0.150
Length of measurement volume	[mm]	0.38	1.40	4.00

TABLE 2.1: Size of LDA measurement volume depending on focal length of the optics. Experiments with 310 and 600 mm focal length were performed in the open-return wind-tunnel, the 1000 mm lens was used in the closed-return tunnel.

By measurements in the near field of a fluidic excitation source operated at frequencies up to 2 kHz, Sonnenberger (1997) demonstrated that LDA can temporally resolve the associated periodic flow fields. He found that diethylhexylsebacat (DEHS) particles of diameter 1 µm or less showed superior properties over other seeding materials in following high-frequency fluctuations. With equations taken from Ruck (1990), he computed the minimum amplitude accuracy as 99 % for fluid fluctuations of frequencies up to 7.4 kHz resolved by this type of seeding particles. The accuracy drops to 97 %, if frequencies as high as 12.1 kHz occur.

In the present experiments, DEHS was introduced into the flow in front of the fan inlet by a cyclone seeder (Palas AGF 10.0). For measurements within the slit of the resonator, a small amount of additional material was fed into the cavity through one of the microphone holes by an AGF 2.0 seeder. According to the manufacturer's specifications, both types of seeders ensured that the maximum particle size did not exceed 1 µm.

When periodic processes were measured, such as the oscillating flow field in the resonator neck, a trigger signal was recorded together with the bursts allowing for a phase-averaged evaluation of the data later on.

LDA biases Much like other measurement techniques, LDA is subject to systematic errors, a detailed discussion of which can be found, for example, in DeGraaff (1999). The biases associated with the LDA system described above have been addressed by Siller (1999), Huppertz (2001), and Kalter (2001). The subsequent sources of error have been recognized as being most severe: fringe bias, validation or filter bias, velocity bias, velocity gradient bias, and the influence of scattered light in the proximity of a wall.

Fringe bias occurs, if a particle does not cross enough fringes on its way through the measurement volume to be validated. Since the LDA system used in the present experiments applies a frequency shift of 40 MHz to either one of the laser beams of each color, the fringe pattern moves relative to the flow. Thus, fringe bias is completely avoided.

Validation bias is due to deviations from a flat validation response over the possible range of velocity measurements. The magnitude of this bias is difficult to quantify as it is highly dependent on the LDA system and its settings. The resulting error becomes insignificant, if the velocity is less than 45 % of the ratio of measurement volume diameter and record interval.

Therefore, parameters were set accordingly where possible.

Velocity bias stems from the fact that, in an evenly seeded flow, the amount of particles crossing the measurement volume is proportional to their velocity. This causes a significant source of error in measurements taken in burst mode where each particle triggers one measurement. This bias is drastically reduced, however, if the LDA system operates in continuous mode where particles trigger measurements as long as they travel through the measurement volume. Therefore, this mode was employed in the present investigation.

Velocity gradient bias is a consequence of spatial velocity differences within the measurement volume. As long as the mean velocity varies linearly across the volume diameter, only fluctuating velocity components will be biased while the measured mean value will still be determined correctly. From experiments in a turbulent boundary layer with a measurement volume of comparable size, DeGraaff (1999) reports that, except for $\overline{u'^2}$, the velocity gradient bias was considerably less than 1 %. During the experiments presented here, the gradient error was minimized by using the smallest possible measurement volume in each situation.

Finally, light that is scattered near a wall adds noise to the burst signals recorded. If the signal-to-noise ratio becomes too unfavorable, bursts might be undetectable which in turn causes a significant error. In this study, walls were made of crystal glass blackened at the back. This ensured a highly reflective surface allowing for unbiased measurements even at wall distances as close as 0.05 mm (see appendix B).

Particle Image Velocimetry

Digital Particle Image Velocimetry (DPIV) was applied to measure instantaneous two-dimensional velocity fields in wall-normal cross-sections of the actuator slit and of the diffuser. In contrast to the remainder of the present investigation, these experiments involved *active* actuation (see chapter 5). They served to determine the characteristic physical quantity describing the output of a fluidic actuator.

The two-component DPIV system consisted of two pulsed Nd:YAG lasers (Continuum Minilite II) providing 25 mJ pulse energy within 3–5 ns, an arrangement of lenses on an optical bench, a PCO SensiCam 12-bit digital camera with a 1280×1024 pixel CCD chip, and a TC412 synchronizer manufactured by OFS. The measurements were triggered and evaluated by OFS VidPIV software installed on a personal computer. Like in the LDA experiments, the seeding material DEHS was introduced into the flow by a cyclone seeder of type Palas AGF 10.0.

Lasers and optics were mounted above the test section. By expanding the laser beam with a cylindrical lens, a light sheet of thickness 1 mm was generated in the x,y-plane along the tunnel centerline. As a result, the

dimensions of the investigated areas were about 35 mm × 28 mm for the slit and 369 mm × 296 mm for the diffuser cross-section. The camera was equipped with lenses of 135 and 28 mm focal length in the respective cases and placed normal to the measurement plane. Picture pairs were taken at a rate of 2 Hz with a time lag between both pictures set depending on the velocities measured. Delay times ranged from 5 to 50 µs for the measurement in the slit plane and from 150 to 300 µs when capturing the entire diffuser cross-section. Accordingly, velocity fields calculated from a number of 100 and 150 picture pairs were averaged.

Due to the limited rate at which picture pairs could be recorded, it was not possible to temporally resolve the dynamics of the flow. In order to allow for phase-averaging of the instantaneous velocity fields, the PIV measurement was triggered on the basis of the phase of the actuator signal. For this purpose, the phase of maximum outflow from the slit was determined beforehand by hot-wire anemometry in the absence of a cross-flow as a function of excitation frequency and amplitude.

The image pairs were evaluated applying the cross-correlation method with an interrogation size of 64 × 64 pixels and a 25 % overlap. To detect outliers, the computed velocity vectors were first passed through a global window filter before they were processed by a local median filter over 3 × 3 neighboring points. Subsequently, eliminated outliers were interpolated. The results could be improved by applying an adaptive cross-correlation with 32 × 32 pixels interrogation size and 50 % overlap in an iterative second step. Before averaging, the vector fields were filtered and interpolated again analogous to the first cycle.

Data acquisition

A personal computer (PC) was used as the core component to control the measurements, the acquisition of data, and their subsequent processing. For this purpose, it was equipped with parallel ports, an IEEE interface, and a 12-bit analog-to-digital (AD) converter (WIN 30DS) with an accuracy of ±0.06 %. The parallel ports handled the communication with the TLX motion controllers of the traversing gears as well as the data acquisition of the pulsed-wire anemometry. The IEEE bus connected the PC to peripheral devices such as the dynamic signal analyzer and both multimeters. Hot-wire anemometry involved sampling data via the AD converter.

During LDA measurements, a separate PC controlled the burst spectrum analyzers via IEEE bus and the three-axes ISEL traverse positioning the laser probe via a serial port.

In addition to permanently monitoring the temperature in the test section, two HP 34970A multimeters equipped with 20-channel multiplexers each were employed to read the output voltages of several pressure transducers and microphone amplifiers. At the same time, microphone signals

were processed by the four-channel FFT analyzer that also served to determine hot-wire spectra. Oscilloscopes were used to monitor signals of the PIV synchronizing unit as well as of LDA bursts, microphones, hot-wire and pulsed-wire probes.

2.3.2 Measurement techniques in closed-return wind-tunnel

As mentioned earlier, the experiments associated with the control of separation on an airfoil were performed in a closed-return wind-tunnel. The effects of the manipulation were documented by flow visualizations, measurements of static pressure distributions, of the velocity field, of the reverse-flow factor along the surface, and of lift and drag forces acting on the airfoil. Besides, acoustic quantities and the fluctuating velocity field in the slit were determined to characterize the flow-induced oscillations of the resonator.

Monitoring of angle of attack

The angle of attack of the airfoil was monitored by a rotary encoder (Hengstler RI 36) coupled to the axis of rotation at the quarter-chord position. The encoder allowed the wing to be adjusted with an accuracy of 0.025 °. Beforehand, the device had been calibrated at zero angle of attack by a high-precision spirit-level resolving 0.017 °.

Measurement of free-stream dynamic pressure

A Prandtl tube of diameter 10 mm extending from the roof of the test box served to determine the free-stream dynamic pressure. The probe was located 800 mm upstream of the leading edge of the airfoil where the flow field was unaltered by the presence of the wing model. As before, differential pressure transducers and multimeters were used to gage and subsequently process the pressure signals.

Flow-visualization techniques

To visualize the effect of fluidic excitation on the flow topology along the suction side of the airfoil, tuft and oil-film techniques have been applied in a similar fashion to the experiments carried out in the open-return tunnel. For this purpose, the surface of the airfoil model was covered with self-adhesive black foil such that the static pressure taps were protected.

Regarding the interpretation of the results, one has to be aware that the separated flow over the airfoil is highly unsteady. While the dynamics of the flow are captured well by the tuft technique, oil-film visualizations merely reflect an averaged flow picture. This applies especially to the location of the separation line. At high angles of attack, the oil-film might also be slightly biased by the influence of gravity. The resolution of tuft visualizations, in

turn, is limited such that small-scale features of the flow can be resolved only down to the tuft spacing dimension.

Microphone measurements

As a reference, the resonator accommodated a microphone probe at the center of the cavity mounted approximately flush with the curved wall. Due to spatial constraints, a 0.25 in (6.35 mm) precision microphone of the compact type G.R.A.S. 40BP was used in conjunction with a preamplifier 26AC. Maximum deviations from the flat frequency response were at most ± 1 dB for frequencies between 10 Hz and 25 kHz. As long as sound-pressure levels did not exceed 170 dB, representing the upper limit of the dynamic range, the distortion was less than 3 %. After amplification by a Brüel & Kjær 2610, the microphone signal was processed by a Tektronix 2642A FFT analyzer. Typically, 100 spectra were averaged which were characterized by a frequency resolution of 12.5 Hz and a bandwidth ranging from 0 to 20 kHz. The absolute calibration was performed by means of a pistonphone.

In flow control experiments involving a system of adjacent resonators, miniature electret condenser microphones of diameter 10 mm were placed in each of the individual cavities. Their main purpose was to provide phase information on the induced pressure oscillations. Before the tests, they had been calibrated relative to the reference microphone in the rig described earlier in this section (see figure 2.5).

Six-component wind-tunnel balance

The airfoil model was held by three streamlined supports accessing the six-component wind-tunnel balance through the floor of the test box. Care was taken to avoid any contact between parts of the balance set-up and the test section as this would have biased the measurement. Equipped with six strain gages, the balance was capable of assessing all six aerodynamic forces and moments that acted on the investigated body.

Before each run, the static loading due to the model and support weight was compensated by determining the offset under no-flow conditions to ensure an accurate measurement of the lift. Because the supports were exposed to the flow, they contributed an unknown but significant portion to the total drag measured. Therefore, all data on drag were discarded. As evidence of the symmetry of the flow around the airfoil, the roll moment was considered. Asymmetric flow conditions indicated by large values of the roll moment were related to untrustworthy lift data.

The output of the six strain gages was read by integrating voltmeters (Prema 6040) that were set to average over periods of 20 s. According to Meyer (2000), the balance was calibrated for lift forces up to 3 kN with an error of less than 0.23 %.

Measurement of the pressure distribution

For the measurement of the pressure distribution along the surface, the airfoil was equipped with 35 pressure taps of 0.6 mm diameter. Due to design constraints, they were located off the centerline at a position of $z/s_w \approx \pm 0.12$, where z represents the spanwise coordinate and s_w the wing span. Figure 2.6 shows the chordwise tap positions. Their spacing is closer near the leading edge, where the largest pressure gradients occur, and where the effects of the flow control are presumably most pronounced.

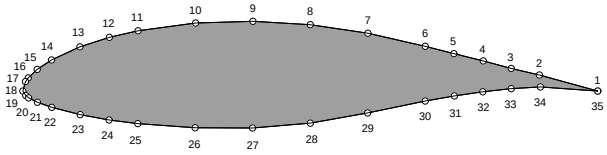

FIGURE 2.6: Location of pressure taps along the contour of the FX 61-184 airfoil.

All taps were connected to the ports of a Scanivalve PDCR23D rotary pressure scanner valve. It was followed by a differential pressure transducer (MKS Baratron 220 CD) with an accuracy of $\pm 0.15\,\%$ of the reading, the output of which was processed by a multimeter. To allow for the pressure to homogenize in the coupling tube after switching ports, there was a waiting period of 20 s between consecutive measurements. 500 samples were averaged per tap ensuring a reproducibility of the results within 1 %.

By integration of the measured pressure distribution along the airfoil contour, the total pressure force acting on the wing was computed. Its components parallel and normal to the free-stream direction represent the pressure drag and lift, respectively. Both were non-dimensionalized to yield the corresponding coefficients. Regarding the interpretation of the results, one has to bear in mind that the pressure distributions determined at one spanwise cross-section cannot account for three-dimensional effects of the flow field.

Laser Doppler Anemometry

LDA was applied to determine the velocity field on the suction side of the airfoil and to perform phase-locked measurements of the oscillating flow within the resonator neck. The apparatus used for this purpose was almost identical with the LDA equipment described in the context of the open-return wind-tunnel. Solely, the optics of the laser head were different. In order to carry out measurements in the vicinity of the centerline of the wing, a focal length of 1000 mm was required, because the laser head was mounted on a two-dimensional traversing gear outside the 2000 mm wide test section. As a consequence of a small tilt of the probe, which was necessary when acquiring data near the airfoil surface, the measurement cross-section

was slightly off center ($z/s_w = 4.7\,\%$ for the global velocity field and $2.6\,\%$ during measurements within the slit). The dimensions of the measurement volume associated with a focal length of 1000 mm were 150 µm in diameter and 4.00 mm in length (see table 2.1).

When investigating the global flow field, the seeding material was introduced directly downstream of the porous mat in the settling chamber on the streamline under consideration. For the study of the unsteady flow through the slit exit plane, the seeding was brought into the flow through the resonator cavity at a very low rate such that the additional volume flux did not alter the resonance properties. In the first case, 5×10^4 bursts were requested within a time frame of 150 s. Corresponding data rates were around 1 kHz. In contrast, the slit measurements were supposed to be phase-averaged and, thus, a trigger signal obtained from the reference microphone was recorded in addition to the velocity data. Therefore, 2×10^6 of both trigger and velocity samples were requested during a time period of 300 s in this case. Typically, 2×10^5 of them were velocity samples. The large number of trigger samples is owed to the high resonance frequency of approximately 7.35 kHz compared to the low data rate which was around 100 Hz.

As pointed out before, the amplitude accuracy of LDA measurements in view of the high-frequency oscillations of the seeded flow was 99 %. However, because of the length of the record interval required, the phase could only be resolved down to 15 °. The earlier discussion of LDA biases applies in the same way to both cases presented in this section. Although the quality of the airfoil surface is inferior to the one of blackened glass, no problems due to scattered light were encountered, because measurements at wall distances of less than 0.5 mm were avoided.

Wall pulsed-wire anemometry

The reverse-flow factor at the wall along the centerline on the suction side of the airfoil was measured by wall pulsed-wire anemometry. For the determination of this quantity, no calibration was required. However, trigger levels and other probe settings had to be chosen with great care.

Probes and anemometer were identical with the equipment described in section 2.3.1. Mounted on a traversable belt at midspan, one pulsed-wire probe could be moved in streamwise direction between $x/c = 18.3$ and $73.3\,\%$. Due to the limited range of the belt traverse, a second probe was installed at a fixed position ($x/c = 6.9\,\%$) shortly downstream of the resonator neck. This region was of particular interest regarding a comparison between baseline and controlled flow conditions. During the measurements, 7500 samples were taken at a rate of 25 Hz.

Data acquisition

The data acquisition system of the airfoil experiments resembled the one described at the end of section 2.3.1. In addition, the voltmeters reading the wind-tunnel balance transfered their data via IEEE bus to the PC. The computer also controlled the switching of ports on the rotary pressure scanner.

List of symbols

b	radius of a circular pipe
c	airfoil chord length
c_p	pressure coefficient ($= \Delta p/(\frac{1}{2}\rho U_\infty^2)$)
d	Preston tube diameter
d^+	Preston tube diameter in inner-law scaling
l_n	neck length of a resonator
l_x	width of the resonator cavity
l_y	height of the resonator cavity
l_z	span of the resonator cavity
s	half-slit width of the resonator neck
s_w	wing span
u'	fluctuating streamwise velocity
u_τ	skin-friction velocity
V	volume of the resonator cavity
x	streamwise coordinate originating at entrance of test section; airfoil: chordwise coordinate originating at nose
y	wall-normal coordinate originating at the wall
z	spanwise coordinate originating at centerline of test section or resonator
Δ	variation of a quantity
ν	kinematic viscosity of the fluid

Chapter 3

Single acoustic resonators

In preparation for the use of acoustic resonators as flow-control devices, this chapter studies their acoustic properties and their induction by a grazing flow with a scope limited to single resonators only. More precisely, it investigates how sound of a specific frequency can be generated by a resonator when a cross-flow is present, and how the amplitude of the induced pressure fluctuations at this frequency can be made as large as possible. Both aspects are of particular interest. The exact predictability of the resonance frequency is required during the design process of a resonator to adapt it for the application in a specific flow situation. The optimization of the amplitude of the flow-induced oscillations aims at providing types of resonators that have a maximum effect on a separation region.

The frequencies at which a flow-induced resonator oscillates essentially depend on its purely acoustic properties. Therefore, section 3.1 discusses the acoustic response of resonators in the absence of a cross-flow. Subsequently, section 3.2 deals with resonators that are induced by a grazing flow.

3.1 Acoustic response

In order to obtain tools for the design of quasi two-dimensional resonators, analytical and numerical methods to determine their natural frequencies and modes in the absence of a cross-flow were tested (sections 3.1.1 and 3.1.2, respectively) and then checked experimentally (section 3.1.3).

During the experiments of this study, resonators with cylindrical and cuboidal cavities were used, and are discussed in this section. The investigation is kept as general as possible. However, where explicit values of resonance frequencies, cycle durations, or the pressure field are given, the computations are based on resonators with the dimensions listed in table 3.1.

Cross-section		Rectangular	Circular
Cavity radius	b [mm]	—	14.0
Cavity length	l_x [mm]	140.0	—
	l_y [mm]	129.6	—
	l_z [mm]	387.3	900.0
Slit width	$2s$ [mm]	9.0	1.6
Neck length	l_n [mm]	9.35	5.27

TABLE 3.1: Dimensions of both sample resonators investigated throughout section 3.1. l_x, l_y, and l_z are the respective cavity dimensions in x-, y-, and z-direction.

3.1.1 Analytical computations

The analytical approach to assess the natural frequencies and modes of resonators in the case without cross-flow is facilitated by differentiating between a low- and a high-frequency regime. In the low-frequency regime, the air within the neck is essential for resonance and the corresponding mode of oscillation is called Helmholtz mode. In the high-frequency regime, the influence of the neck can be neglected and only modes of the resonator cavity are excited. The higher modes of resonators are, therefore, determined by the shape of their volume. These modes can be cylinder or channel modes, for example, if the cavity cross-section is circular or rectangular, respectively, as in the present cases.

The computations of this section follow a suggestion by Dowling (1998). The details are elaborated in Urzynicok & Dowling (1999).

Helmholtz-Mode

Some approaches to compute the resonance frequency of the Helmholtz mode were discussed in section 1.3.1. The applicability of equation (1.5) given there was based on the assumption that the pressure is uniform throughout the resonator. This implies that all cavity and opening dimensions can be regarded as negligibly small compared to the wavelength of the sound. Panton & Miller (1975*b*) showed that as soon as one of the resonator dimensions exceeds 1/16 of a wavelength, equation (1.5) begins to become less accurate. For both resonators considered here, this is clearly the case, since the spanwise cavity length l_z of the resonator with rectangular and with circular cross-section amounts to 387 and 900 mm, respectively. At a frequency of, say, $f = 1\,\mathrm{kHz}$ this is of the same order of magnitude as the corresponding wavelength of the sound being $\lambda = 343\,\mathrm{mm}$. Thus, an equation to compute the Helmholtz resonance frequency of two-dimensional resonators had to be developed that also accounts for possible standing waves in spanwise direction. In the following, the derivation is sketched briefly.

Spanwise sound-pressure distribution in a 2D-resonator For the spanwise distribution of the sound pressure p_1 in a slitted circular wave duct Neise (1975) gives the following differential equation that can be obtained from applying the continuity equation to an infinitesimally short spanwise element of the resonator and making use of a momentum balance within the cavity[1]:

$$\frac{\mathrm{d}^2 p_1}{\mathrm{d}z^2} + p_1 \left(\frac{\omega^2}{c^2} + \frac{\mathrm{i}\omega\rho_0 2s}{A Z_s} \right) = 0. \tag{3.1}$$

Herein, z denotes the spanwise coordinate, ω the angular frequency, c the speed of sound, i the imaginary unit, ρ_0 the mean density, A the area of the cross-section of the resonator cavity, and Z_s the specific acoustic impedance of the slit of width $2s$. It can be shown that equation (3.1) is also valid for slitted pipes of arbitrary, but in spanwise direction constant shape of the cross-section. It can, therefore, be applied to both resonator types investigated here.

Specific acoustic impedance of the slit A major difficulty in applying equation (3.1) is to determine an appropriate expression for the slit impedance Z_s. In this section, a relation will be derived that takes into account both the neck length l_n of the resonator and a spanwise pressure distribution $p_1(z)$.

The transmission characteristics of a slit were already studied by Rayleigh (1896) and Lamb (1932). Based on the results of Lamb (1932, § 305), Hughes (1988) derived an equation for the Rayleigh conductivity of a slit of width $2s$ and infinite length in an infinitesimally thin rigid plate. After cancelation of a term that represents a mean flow through the slit, the Rayleigh conductivity K per unit length of the slit reads:

$$\frac{K}{l_z} = -\frac{\frac{\pi}{2}}{\ln\frac{h}{4} + \mathrm{C} - \mathrm{i}\frac{\pi}{2}}. \tag{3.2}$$

Here, $h = k_r s$ is the Helmholtz number, $k_r = \omega/c$ is the wave number of the acoustic pressure normal to the slit centerline, and $\mathrm{C} = 0.5772\cdots$ is the Euler constant. The conductivity is related to the specific acoustic impedance by equation (1.8). To include the influence of the neck length l_n into the expression for the impedance, a momentum balance per unit length across the opening of the resonator is taken. Using in addition a relation between the perturbation volume flux through an aperture and the incident sound pressure (Hughes, 1988, eq. 2.61), an equation for the slit impedance Z_s is obtained that accounts for the length of the resonator neck:

$$Z_s = -\rho_0 \mathrm{i}\omega \left\{ l_n + \frac{4s}{\pi} \left(-\ln\frac{h}{4} - \mathrm{C} + \mathrm{i}\frac{\pi}{2} \right) \right\}. \tag{3.3}$$

[1] Like in section 1.3.1, all components of the acoustic field are proportional to $\mathrm{e}^{-\mathrm{i}\omega t}$. For convenience, the explicit dependence on this factor is suppressed here.

The first term on the right-hand side represents the specific acoustic impedance of the mass in the resonator neck (Morse, 1948, p. 234). The second term can be regarded as an end correction for the neck length l_n similar to the concept reviewed in section 1.3.1.

To include pressure variations in spanwise direction, the expression for the slit impedance has to be extended. The extension is done by comparing the results of the wave equation for a sound wave propagating outward from the slit exit plane in two cases, one being independent of and one being dependent on z.

In the first case, the pressure p_2 outside the resonator is constant along the span and only a function of the radial coordinate r. Therefore, the one-dimensional wave equation in cylindrical coordinates can be applied:

$$-\frac{1}{c^2}\frac{\partial^2 p_2}{\partial t^2}+\frac{1}{r}\frac{\partial p_2}{\partial r}+\frac{\partial^2 p_2}{\partial r^2}=0. \tag{3.4}$$

It is solved by Bessel functions of the first and second kind of the order $m = 0$, J_0 and Y_0, and by the Hankel function $H_0^{(1)} = J_0 + \mathrm{i}Y_0$. Since their arguments are small versus unity in the vicinity of the slit, they can be approximated by developing them into a series and neglecting terms of higher order. As a result, the expression for the outward propagating wave can be written as follows where $\hat{p}_2$ is the amplitude of the pressure:

$$p_2=\hat{p}_2\,\mathrm{i}\frac{2}{\pi}\left\{\ln\left(\frac{1}{2}k_r s\right)+\mathrm{C}-\mathrm{i}\frac{\pi}{2}\right\}\mathrm{e}^{-\mathrm{i}\omega t}. \tag{3.5}$$

In the second case, when the pressure p_2 exhibits spanwise variations and, therefore, depends on both r and z, the two-dimensional wave equation can be used:

$$-\frac{1}{c^2}\frac{\partial^2 p_2}{\partial t^2}+\frac{\partial^2 p_2}{\partial z^2}+\frac{1}{r}\frac{\partial p_2}{\partial r}+\frac{\partial^2 p_2}{\partial r^2}=0. \tag{3.6}$$

Again, it is solved by the same types of functions and, thus, the subsequent approximation is done in analogy to the previous case. An additional factor $\cos(k_z z)$ is introduced to account for the spanwise pressure variation with an associated wave number k_z. Then, the outward propagating pressure wave has the form:

$$p_2=\hat{p}_2\cos(k_z z)\mathrm{i}\frac{2}{\pi}\left\{\ln\left[\frac{1}{2}\left(\frac{\omega^2}{c^2}-k_z^2\right)^{\frac{1}{2}}s\right]+\mathrm{C}-\mathrm{i}\frac{\pi}{2}\right\}\mathrm{e}^{-\mathrm{i}\omega t}. \tag{3.7}$$

The comparison of equations (3.5) and (3.7) representing outward propagating waves in cases with constant and variable pressure along the span, respectively, suggests to modify a term in the expression derived for the slit impedance in order to account for the spanwise distribution of the pressure. In equation (3.3), the Helmholtz number $h = k_r s$ is, therefore, replaced by

the term $\zeta = \left(\frac{\omega^2}{c^2} - k_z^2\right)^{1/2} s$, where the abbreviation ζ was introduced for convenience. As a result, the specific acoustic impedance of the slit now reads:

$$Z_s = -\rho_0 \mathrm{i}\omega \left\{ l_n + \frac{4s}{\pi} \left(-\ln \frac{\zeta}{4} - \mathrm{C} + \mathrm{i}\frac{\pi}{2} \right) \right\}. \tag{3.8}$$

Again, the second term on the right-hand side can be regarded as an end correction for the neck length l_n. It accounts for the spanwise variation of the pressure, since ζ is, by definition, a function of the spanwise wave number k_z. When no spanwise standing waves are present ($k_z = 0$), ζ just equals the Helmholtz number h such that equation (3.8) reduces to equation (3.3), as would be expected.

Helmholtz resonance frequency In the low-frequency regime, the pressure inside the resonator cavity is only a function of the spanwise coordinate z and can be written in the form $p_1 = \hat{p}_1 \mathrm{e}^{\mathrm{i}k_z z}$. Applying this relation in combination with equations (3.1) and (3.8) yields an implicit representation of the resonance frequencies that occur due to a superposition of the Helmholtz resonance with spanwise standing waves:

$$\omega^2 = c^2 k_z^2 + c^2 \frac{2s}{A} \frac{1}{l_n + \frac{4s}{\pi} \left(-\ln \frac{\zeta}{4} - \mathrm{C} + \mathrm{i}\frac{\pi}{2} \right)}. \tag{3.9}$$

Since ζ is a function of the angular frequency ω, the resonance frequencies have to be evaluated by iteration.

To allow for the formation of standing waves in the duct, the wall-normal derivative of the pressure has to vanish at the rigid ends ($z = \pm l_z/2$). These boundary conditions are satisfied for:

$$k_z = \frac{q_z \pi}{l_z}, \tag{3.10}$$

where q_z is the amount of nodes in the spanwise pressure distribution. It should be noted that both terms on the right-hand side in equation (3.9) are functions of k_z because of $\zeta = \zeta(k_z)$.

For homogeneous pressure along the span ($q_z = 0$), the Helmholtz resonance frequency of the resonator with rectangular cross-section is $f_0 =$

	q_z					
Cross-section	0	1	2	3	4	5
Rectangular	194 Hz	483 Hz	906 Hz	1342 Hz	1782 Hz	2222 Hz
Circular	848 Hz	869 Hz	929 Hz	1022 Hz	1139 Hz	1274 Hz

TABLE 3.2: Resonance frequencies resulting from superposition of Helmholtz mode and spanwise standing waves in the resonator cavity depending on the amount of nodes q_z.

194 Hz, while in the circular case it is $f_0 = 848$ Hz. Results for Helmholtz modes with spanwise standing waves superimposed are shown in table 3.2. A comparison with numerical and experimental data is given in section 3.1.4.

When can the slit be neglected? The result of the previous section can be used to estimate the error that occurs in the subsequent computations of resonances in the high-frequency regime when the slit is neglected.

In equation (3.9), which allows for the computation of Helmholtz resonance frequencies, the first term on the right-hand side accounts for the duct modes, while the second, complex one represents the contribution of the neck:

$$\omega^2 = \underbrace{\left(c\frac{q_z\pi}{l_z}\right)^2}_{\text{duct term}} + \underbrace{c^2\frac{2s}{A}\left\{\dots\right\}}_{\text{slit term}}.$$

Due to the iterative character of equation (3.9), however, no explicit term that describes the error due to the approximation can be solved for.

Since the influence of spanwise standing waves on the slit term is negligible (Urzynicok & Dowling, 1999), ζ is set equal to the Helmholtz number h. Then, the alteration of the frequency due to the slit term is independent of the mode considered. The iteration can be performed replacing the duct term by the frequency of interest with and without the slit term. The resulting deviation Δf depending on the frequency f is shown in figure 3.1 for both resonators.

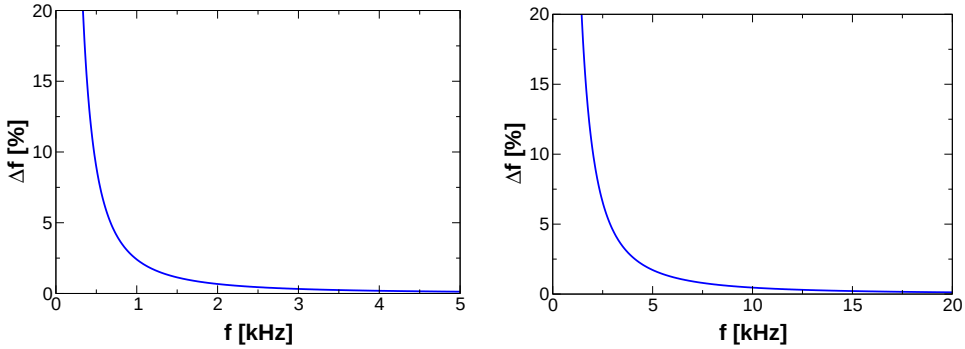

FIGURE 3.1: Error in the computed resonance frequency due to neglect of the slit for a resonator of rectangular (left) and of circular cross-section (right). Results based on resonator dimensions as shown in table 3.1 on page 46.

With increasing frequency, the error Δf due to the neglect of the slit decreases rapidly. The presence of the slit becomes less and less significant at high frequencies.

As a worst case, therefore, the error at the lowest frequency of interest in the high-frequency regime is determined. It is associated with the first cavity mode which occurs at 1225 and 7179 Hz in the cavity of rectangular

and circular cross-section, respectively. The corresponding error resulting from neglect of the slit in both cases is 1.65 % and 0.86 %. At higher cavity modes, it is even less than that. The resonance frequencies of the higher modes can be found in tables 3.3 and 3.4. They have been used here in anticipation of the results of the following analytics.

Higher modes

As mentioned before, the slit is neglected for the computations in the high-frequency regime. According to the shape of the resonator volume the determination of the higher or cavity modes and their corresponding natural frequencies is done in different coordinate systems. For consistency, resonators with cuboidal and cylindrical cavities are considered.

Higher modes of a cuboidal resonator cavity The natural frequencies ω of the cavity modes in all three directions (x, y, z) in a rectangular duct with rigid ends can be calculated from the three-dimensional wave equation in Cartesian coordinates. It has the form:

$$\frac{\partial^2 p_1}{\partial x^2} + \frac{\partial^2 p_1}{\partial y^2} + \frac{\partial^2 p_1}{\partial z^2} = \frac{1}{c^2}\frac{\partial^2 p_1}{\partial t^2}. \tag{3.11}$$

In each dimension, the standing-wave solution consists of a superposition of two waves moving in opposite direction with different amplitudes. Therefore, the general solution can be written as:

$$p_1(x,y,z,t) = \mathrm{e}^{\mathrm{i}\omega t}\left(A_1\mathrm{e}^{\mathrm{i}k_x x}+A_2\mathrm{e}^{-\mathrm{i}k_x x}\right)\left(B_1\mathrm{e}^{\mathrm{i}k_y y}+B_2\mathrm{e}^{-\mathrm{i}k_y y}\right)\left(C_1\mathrm{e}^{\mathrm{i}k_z z}+C_2\mathrm{e}^{-\mathrm{i}k_z z}\right)$$

A_1, A_2, B_1, B_2, C_1, and C_2 are constants representing amplitudes of individual waves. k_x, k_y, and k_z denote the respective wave numbers in direction of the three coordinates x, y, and z.

Assuming that the boundaries are perfectly rigid, the wall-normal derivative of the pressure p_1 within the cavity has to vanish at all walls. With this choice of boundary conditions, ω can be determined from the equation:

$$\omega = c\left\{\left(\frac{q_x\pi}{l_x}\right)^2 + \left(\frac{q_y\pi}{l_y}\right)^2 + \left(\frac{q_z\pi}{l_z}\right)^2\right\}^{\frac{1}{2}}, \tag{3.12}$$

where q_x, q_y, and q_z denote the modes, i.e. the amount of nodes in the pressure distribution, in x-, y-, and z-direction.

Various acoustic modes (q_x, q_y) confined to a cross-section of a rectangular duct are shown schematically in figure 3.2. The results relevant to this study are contained in table 3.3 on page 67 where they are also compared with numerical and experimental data.

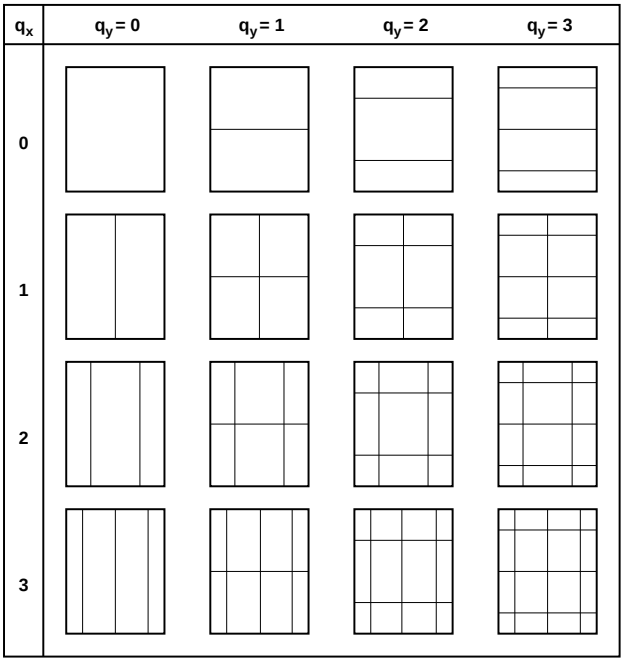

FIGURE 3.2: Scheme of nodal lines of various transverse acoustic modes (q_x,q_y) in a rectangular duct.

Higher modes of a cylindrical resonator cavity The natural frequencies ω of the higher modes for a cylindrical resonator volume are obtained in analogy to the previous case from the three-dimensional wave equation. In cylindrical coordinates, r, ϑ, and z, this equation reads:

$$\frac{\partial^2 p_1}{\partial r^2} + \frac{1}{r}\frac{\partial p_1}{\partial r} + \frac{1}{r^2}\frac{\partial^2 p_1}{\partial \vartheta^2} + \frac{\partial^2 p_1}{\partial z^2} = \frac{1}{c^2}\frac{\partial^2 p_1}{\partial t^2}. \tag{3.13}$$

We are looking for fundamental standing-wave solutions, each of which corresponds to a distinct mode of vibration. Therefore, the general solution has the form:

$$p_1(r,\vartheta,z,t) = \mathrm{e}^{\mathrm{i}\omega t} J_m(k_r r)\left(C_1 \mathrm{e}^{\mathrm{i}k_z z} + C_2 \mathrm{e}^{-\mathrm{i}k_z z}\right)\mathrm{e}^{\mathrm{i}m\vartheta}. \tag{3.14}$$

Here, m is the order of the Bessel function $J_m(g)$ with g being a real variable.

Again, appropriate boundary conditions are that the wall-normal derivative of p_1 vanishes at the walls. Then, the resonance frequencies in a closed cylinder with rigid ends can be determined depending on the azimuthal (m), radial (n), and axial (q_z) modes:

$$\omega = c\left\{\left(\frac{j'_{m,n}}{b}\right)^2 + \left(\frac{q_z \pi}{l_z}\right)^2\right\}^{\frac{1}{2}}. \tag{3.15}$$

Thereby[2], $j'_{m,n}$ is the $(n+1)$st positive zero of $J'_m(g)$. Values of $j'_{m,n}$ are given in figure 3.3 for a number of modes. The order m of the Bessel function corresponds to the number of pressure nodal lines in radial direction, while n equals the number of pressure nodal lines in circumferential direction.

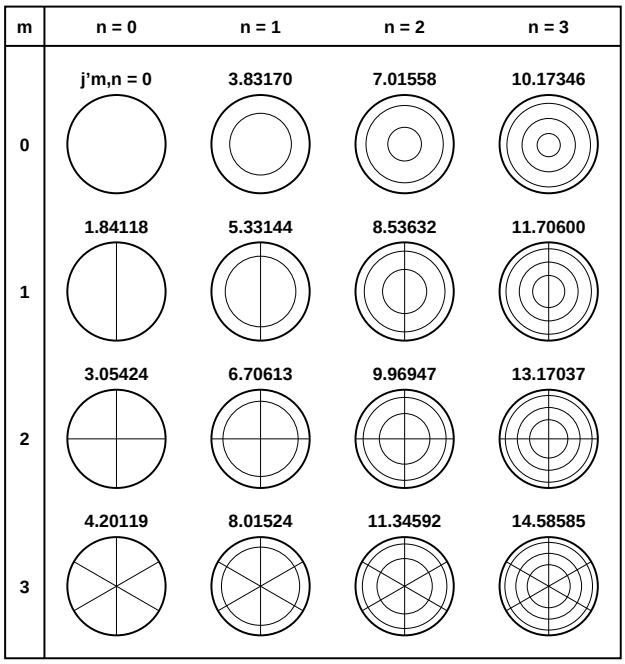

FIGURE 3.3: Scheme of nodal lines of various transverse acoustic modes (m,n) in a circular duct. Values for $j'_{m,n}$ from Abramowitz & Stegun (1965).

The various acoustic modes (m, n) in a cross-section of a circular duct are shown schematically in figure 3.3. Results needed in the discussion of subsequent sections can be found in table 3.4 along with a comparison to numerical and experimental data.

3.1.2 Numerical computations

The underlying idea of the numerical computations was to determine the natural frequencies of the resonators from their respective impulse response. Similar to mechanical structures, which respond to a mechanical impulse with all their natural modes and frequencies, the natural oscillations of an acoustic resonator can be excited by a pressure impulse. In the compu-

[2]The notation follows the suggestions of Eriksson (1980) because of its close analogy to that used in rectangular ducts. The plane wave mode is represented by $m = 0$, $n = 0$. The trivial or zero solution is not included in the proposed scheme (see figure 3.3).
In contrast to this, Abramowitz & Stegun (1965) introduce n as the number of the zero of $J'_m(g)$ which simply increases all of its values by one. In addition, several other labeling approaches can be found in the literature.

tations, this impulse was prompted by abruptly relaxing an initial excess pressure within the resonator with respect to the surrounding (+10 %). As a consequence, the cavity pressure underwent a damped vibration that excited all resonance frequencies. By investigation of the pressure time-signal at an appropriate point in the resonator cavity with suitable methods, the frequencies of the occurring natural modes could be determined.

The computations were performed for cross-sections of both a rectangular and a circular type consistent with the resonators discussed before. Deviating from the dimensions given in table 3.1, the resonators were assumed to be of infinite length l_z in spanwise direction. In this way, the 2D-Helmholtz mode as well as higher two-dimensional modes could be analyzed. However, modes involving spanwise oscillations, which are assumed to be of little or no importance in this investigation[3], could not be determined due to the two-dimensionality of the computations.

Numerical method

A finite volume method was employed to solve the two-dimensional unsteady Euler equations. It was optimized with respect to an accurate description of vortices and acoustic perturbations, and features a reduced numeric viscosity which is achieved by a particular spatial interpolation of higher order. The code was developed and made available by Ehrenfried & Meier (1995), where the reader is referred to for further details.

The computations were carried out over 120,000 time steps for the rectangular cross-section and over 95,000 time steps for the circular one.

Boundary conditions

Reflecting boundary conditions were prescribed at points located on rigid walls, i.e. on the walls inside the resonator, the resonator neck, and along the wall which the resonator is integrated in. To ensure an unperturbed computation of the sound waves in the ambient air, non-reflecting boundary conditions were implemented at the outer three boundaries of the computational domain.

Computational grids

The spatial discretization was performed using unstructured triangular grids. They were created by a so-called front generator, which inserts grid points along a front line starting out from a surrounding curve along all inner and outer boundaries. With advancing front, the grid grows from the edges until it comprises the entire surrounded region. In doing so, the generator strives to abide by given target distances between grid points. In an iterative

[3] This will be substantiated, for example, in section 3.2.4.

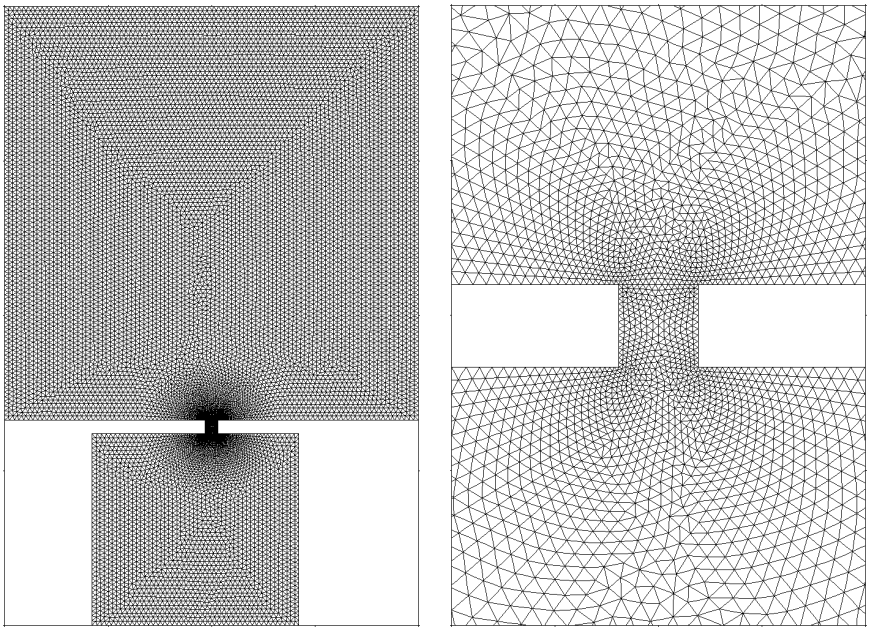

FIGURE 3.4: 2D computational grid for the resonator of rectangular cross-section. Resonator dimensions as shown in table 3.1 on page 46. The resonator is located in the lower half of the picture, shown above are the orifice and the ambient air. On the right, the refinement of the grid in the vicinity of the resonator neck is depicted.

post-process local irregularities are removed in order to obtain a grid with preferably equiangular triangles.

The triangular grids used in the computations of the two subsequent sample cases consisted of 13,402 grid points for the rectangular resonator cross-section (figure 3.4) and 10,700 grid points for the circular cross-section (figure 3.5). Their mesh density was increased in the vicinity of convex edges occurring at the resonator neck (see respective right-hand sides in both figures). For the front generator, the target values of the distances between grid points were reduced by a factor 6.7 at these edges compared to the inner points of the computational domain. The distances in the transitional region in between were specified by linear interpolation.

Computed pressure fields

Figures 3.6 and 3.7 visualize a part of the result of the computations for a resonator of rectangular and of circular cross-section, respectively. The pressure throughout the computational domain is shown as the third dimension in the graphs. The height of the cylinder, therefore, represents the pressure in the resonator cavity.

It should be noted that the first cycle of Helmholtz-mode oscillation shown in both figures is biased by transient phenomena. Therefore, the

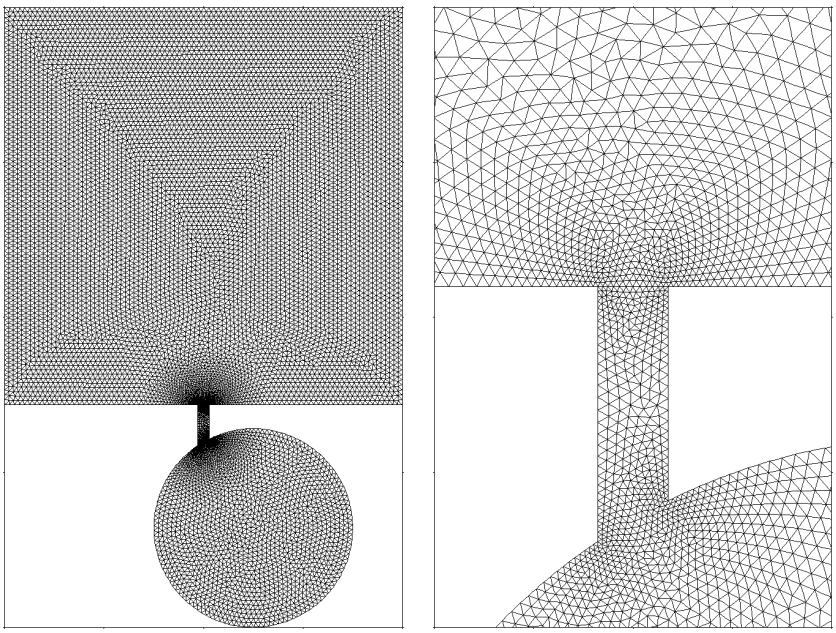

FIGURE 3.5: 2D computational grid for the resonator of circular cross-section. Resonator dimensions as shown in table 3.1 on page 46. The resonator is located in the lower half of the picture, shown above are the orifice and the ambient air. On the right, the refinement of the grid in the vicinity of the resonator neck is depicted.

cycle durations and the resulting resonance frequencies given are valid for this first cycle only and are not the actual result of the computation yet.

Both cases investigated exhibit a similar qualitative behavior. As the excess pressure is released from the resonator, a pressure wave emanates from its orifice. Subsequently, with rapidly dropping pressure within the cavity, the pressure field associated with the formation of a vortex pair at the orifice appears. With time it convects away from the opening. The up and down movement of the pressure within the cavity stems from the Helmholtz mode, the wavy pattern in it is due to a superposition of higher modes. The fundamental oscillation is strongly damped as can bee seen from the relatively low pressure within the cavity after the completion of the first cycle.

Computed pressure time-signals

From the numerically computed temporal development of the pressure field, the pressure time-signal can be extracted at an arbitrary point in order to determine the natural frequencies of the resonator via a frequency analysis. In the choice of a specific point care was taken that it was not located on one of the nodal lines associated with one of the modes. Otherwise, the corresponding mode would not contribute to the pressure signal in this point

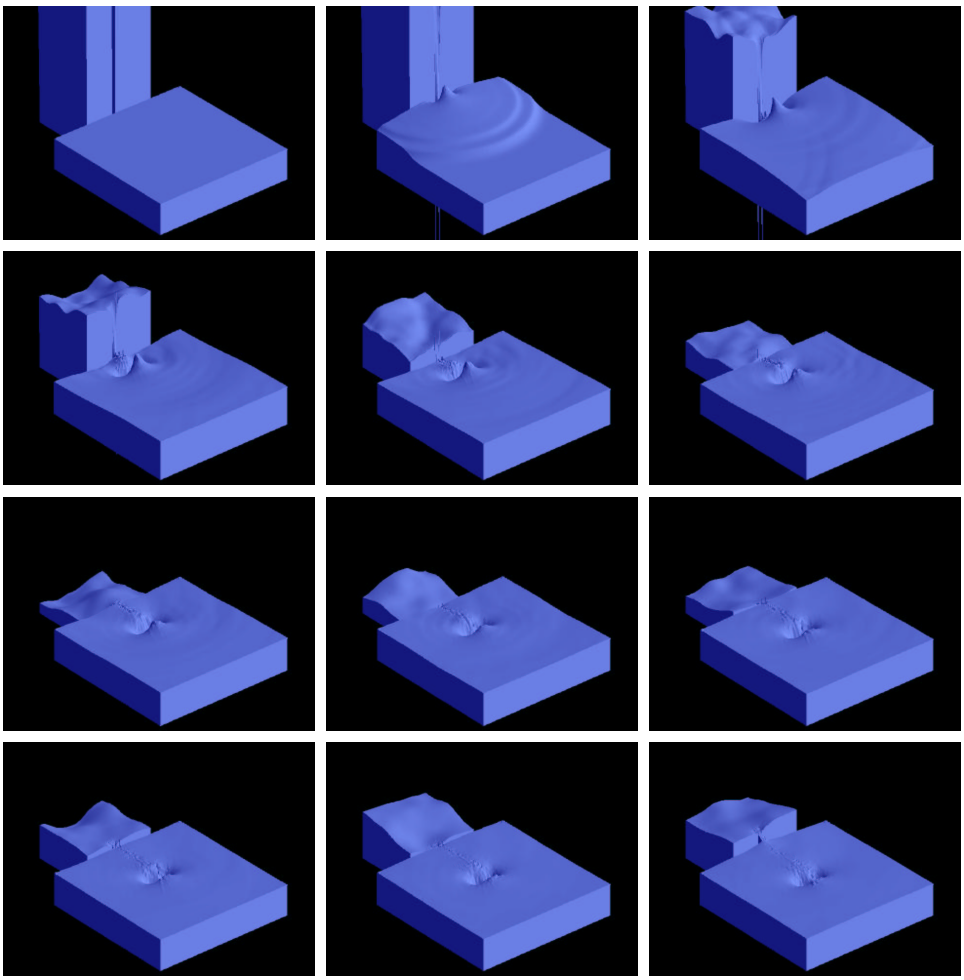

FIGURE 3.6: Visualization of the pressure field during the first cycle of Helmholtz-mode oscillation from computation with a resonator of rectangular cross-section. Resonator dimensions as shown in table 3.1 on page 46. Time increment between pictures $\Delta t = 0.473\,\text{ms}$, cycle duration $T = 5.206\,\text{ms}$ equivalent to a resonance frequency of $f_0 = 192\,\text{Hz}$.

and could, therefore, not be detected by a frequency analysis.

For both sample cases, the time traces of the pressure p_1 at a fixed location within the resonator cavity in principle show identical behavior (figure 3.8). They can be interpreted by taking into account the results of the analytical computations and by bearing in mind the three-dimensional representation of the pressure field. The pressure inside the cavity performs a strongly damped oscillation in the Helmholtz mode with cavity modes superimposed that cannot be further distinguished at a first glance. Quantitatively, however, the respective cycle durations and the corresponding resonance frequencies are substantially different. To gain further insight, a detailed frequency analysis is required. Three methods serving this purpose

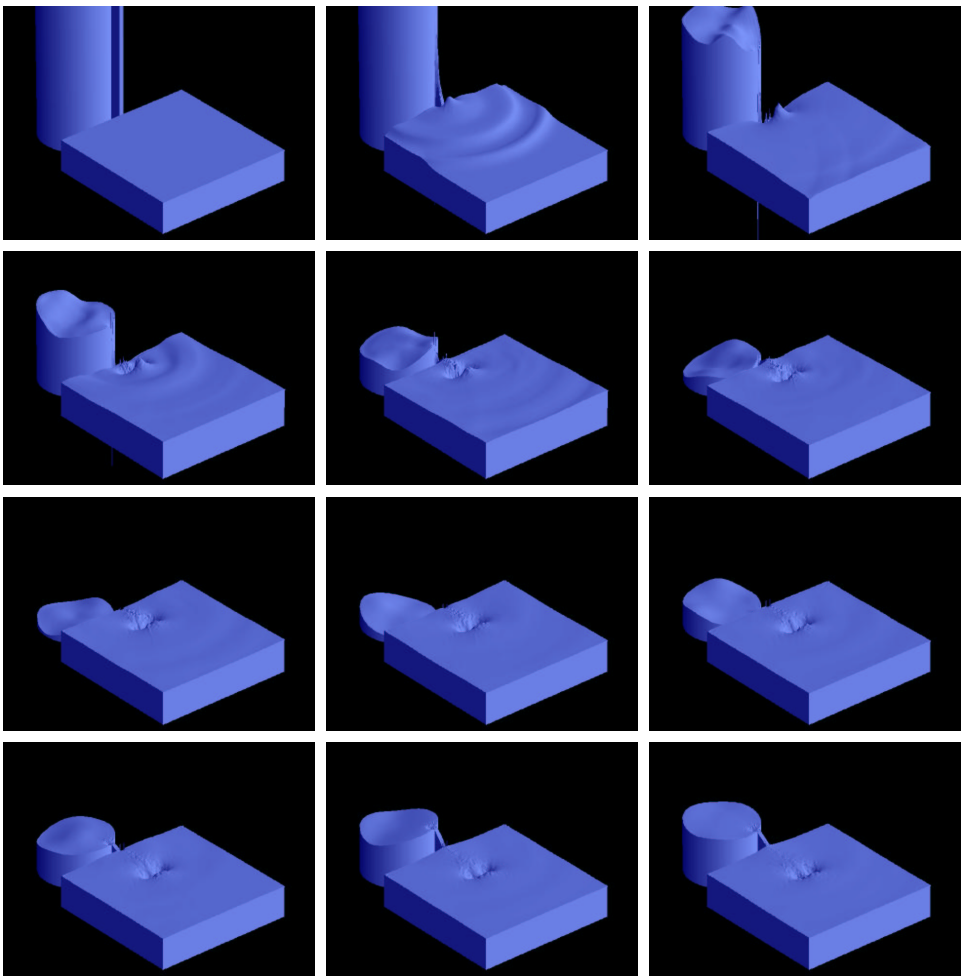

FIGURE 3.7: Visualization of the pressure field during one cycle of Helmholtz-mode oscillation from computation with a resonator of circular cross-section. Resonator dimensions as shown in table 3.1 on page 46. Time increment between pictures $\Delta t = 0.108\,\text{ms}$, cycle duration $T = 1.190\,\text{ms}$ equivalent to a resonance frequency of $f_0 = 840\,\text{Hz}$.

are discussed in the following, namely a curve-fit technique as well as DFT and wavelet analyses.

Curve fit of the pressure time-signal The discrete pressure time-signal consisting of values w_i was approximated in a least-squares sense by points f_i of a fit function. To this end, function e accounting for the deviation between time trace and fit was minimized by iteration[4]:

$$e = \sum_i (f_i - w_i)^2 \,. \tag{3.16}$$

[4]The program performing the curve fit was part of the software provided by Ehrenfried & Meier (1995).

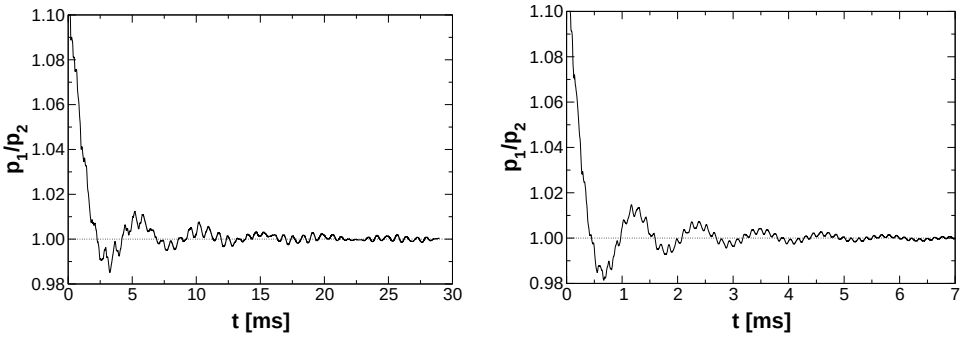

FIGURE 3.8: Pressure time-signals from CFD at fixed locations within the resonator cavity. Resonator of rectangular cross-section (left) and of circular cross-section (right). Resonator dimensions as shown in table 3.1 on page 46.

The coefficients f_i were obtained from a fit function of the following form, which is apt to describe a damped oscillation with offset, phase shift, and a linear element:

$$f_i = L + M\,\mathrm{e}^{-\varepsilon t_i}\cos\left(\omega_0 t_i + \varphi\right) + N t_i. \tag{3.17}$$

Hereby, ω_0 represents the unknown angular frequency, t_i are discrete points in time, L, M, and N are coefficients, ε is a constant of decay, and φ a phase offset.

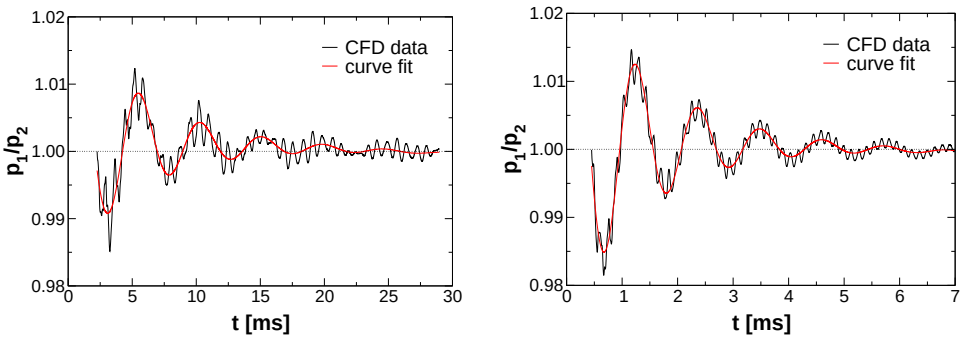

FIGURE 3.9: Curve fit for resonators of rectangular (left) and of circular cross-section (right) yielding the frequencies of the Helmholtz resonance at 209 and 891 Hz, respectively. Resonator dimensions as shown in table 3.1 on page 46.

For a better fit, the transient phase between $t = 0\,\mathrm{ms}$ and the first crossing of unity by the time signal of p_1/p_2 was excluded from the fit procedure. Results of the curve fit are shown in figure 3.9 and are given in tables 3.3 and 3.4. They imply that the fundamental oscillation was captured very well by this method. However, since the fit function f_i in equation (3.17) does not account for any higher modes, this technique was confined to the determination of the natural frequency ω_0 of the 2D Helmholtz mode. Because of

the vast amount of cavity modes an appropriate extension of this approach would have resulted in an extremely complex fit function and, thus, did not appear worthwhile. In addition, the frequency resolution of the curve fit as a measure of its quality in relation to other methods of frequency analysis remained obscure.

DFT analysis of the pressure time-signal The discrete Fourier transform (DFT) is a common algorithm to obtain frequency information from a time signal. In both cases investigated, however, the application of the DFT has two disadvantages: On the one hand, the frequency resolution of short time signals is relatively coarse. If Δt denotes the overall duration of the signal, the frequency resolution is $\Delta f = 1/\Delta t$ (e.g. Bendat & Piersol, 1993). On the other hand, the non-periodicity of the signal requires the use of a window function. It attenuates the data near the edges of the interval to be analyzed and, thus, reduces edge effects occurring when the time series is finite. In the present cases, however, this virtually eliminates a vital portion of the signal, namely the outset of the damped vibration.

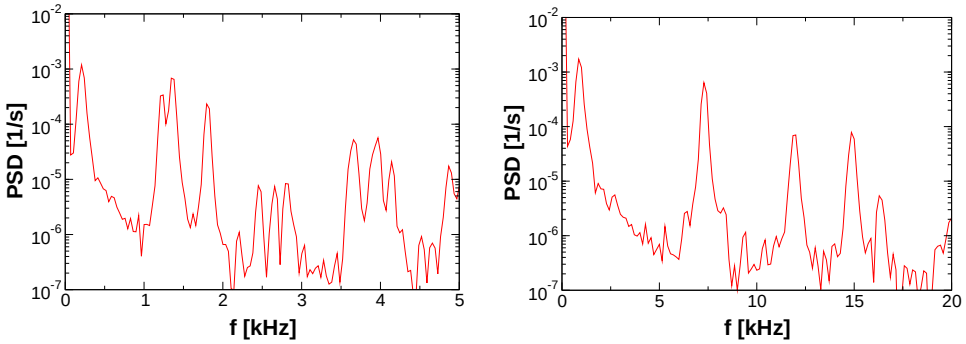

FIGURE 3.10: Fourier transform of the pressure time-signal for resonators of rectangular (left) and of circular cross-section (right). Resonator dimensions as shown in table 3.1 on page 46.

The results of the DFT presented in figure 3.10 were computed applying a Hanning window to the data. For the pressure time-signal of the rectangular resonator cross-section with an overall duration of $\Delta t = 29.0\,\text{ms}$, the frequency could be resolved with an accuracy of $\Delta f = 34.5\,\text{Hz}$. With respect to the identification of the Helmholtz resonance frequency at $f_0 = 207\,\text{Hz}$, the resulting uncertainty is $\pm 8.3\,\%$. Due to the rapid sequence of the physical process, Δt is merely 7.0 ms in the case of the resonator with circular cross-section. This yields a frequency resolution of the DFT of $\Delta f = 142.9\,\text{Hz}$. Regarding the Helmholtz resonance frequency at $f_0 = 857\,\text{Hz}$, this implies a maximum uncertainty of $\pm 7.9\,\%$.

In contradistinction to the curve fit, the resonance frequencies of higher modes could be determined as well (see figure 3.10). However, they suffer

from the same poor frequency resolution Δf found already for the detection of the Helmholtz resonance frequency. For a complete overview of the DFT results, the reader is referred to tables 3.3 and 3.4.

Wavelet analysis of the pressure time-signal Wavelet analysis allows to circumvent the shortcomings of the DFT. Generally, it offers advantages over conventional Fourier methods in cases where a signal under investigation contains discontinuities, sharp peaks, or non-stationary power at many different frequencies. Similarly to how arbitrary functions can be represented by superposing sines and cosines in traditional Fourier methods, superposed wavelets can be used instead for the approximation. Wavelets are mathematical functions which decompose a time series into various frequency components and then analyze each component with a resolution according to its scale (Graps, 1995). As a result, a one-dimensional time series is transformed to a two-dimensional time-frequency image such that both the dominant modes and how those modes vary in time can be determined (Torrence & Compo, 1998).

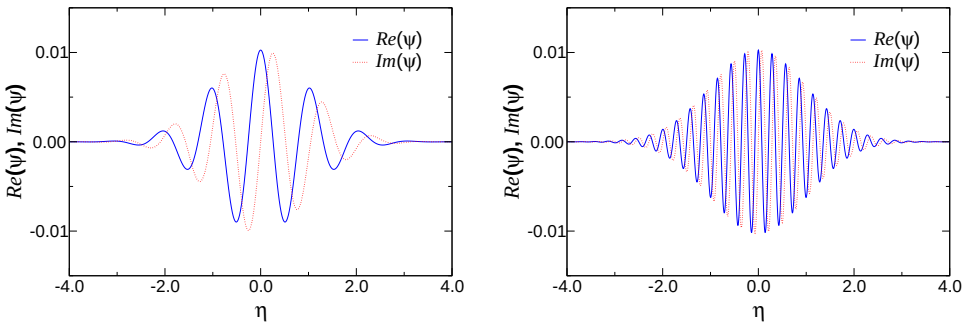

FIGURE 3.11: Real and imaginary part of two Morlet wavelets ψ used in the analysis of the pressure time-signal obtained from CFD. Left: $\omega_w = 6$, right: $\omega_w = 22$.

A wavelet function $\psi(\eta)$ must satisfy certain mathematical requirements, for example it must have zero mean and be localized in both time and frequency space. It is a function of the nondimensional time η which is the time t normalized by the scale T_w. By scaling a so-called mother wavelet, basis functions ranging from short high-frequency ones to long low-frequency ones can be generated. Short wavelets are required to isolate signal discontinuities, while long ones are used to obtain detailed frequency analysis. Torrence & Compo (1998) recommend considering several factors in the choice of an appropriate wavelet function. For the analysis of time series, where smooth, continuous variations in wavelet amplitude are expected, the non-orthogonal transform has advantages over the orthogonal one. To capture oscillatory behavior, a complex wavelet function is regarded as the preferred choice. The width and, therefore, the scale of a wavelet function has to be chosen as a compromise between desired time and frequency resolution. Finally, the

shape of the wavelet function should in general reflect the type of features present in the time series.

To analyze the pressure time-signal wavelets of the Morlet type were chosen as basis functions which are both non-orthogonal and complex. They consist of a plane wave modulated by a Gaussian, where ω_w represents a nondimensional frequency (Torrence & Compo, 1998):

$$\psi(\eta) = \pi^{-1/4} \mathrm{e}^{\mathrm{i}\omega_w \eta} \mathrm{e}^{-\eta^2/2} \tag{3.18}$$

For two wavelet frequencies used in the present analysis, $\omega_w = 6$ and 22, the Morlet wavelet functions are shown in figure 3.11. Additionally, wavelets with $\omega_w = 100$ were used in the evaluation. The choice of the wavelet parameter ω_w was determined by a compromise: While Morlet wavelets with high ω_w provide enhanced resolution of high-frequency components in the signal, they tend to cause oscillations in the low frequency regime of the calculated spectrum (see figure 3.12). Three values were, therefore, chosen to cover the frequency range of interest in the analysis.

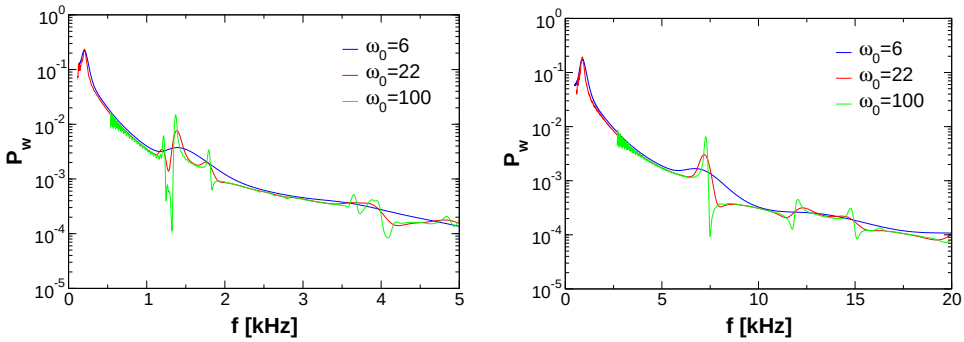

FIGURE 3.12: Global wavelet spectra of the pressure time-signal for a resonator of rectangular (left) and of circular cross-section (right). Resonator dimensions as shown in table 3.1 on page 46. P_w is the nondimensional wavelet power.

The wavelet software employed to analyze the data computed numerically was provided by C. Torrence and G. Compo, University of Colorado, Boulder[5]. As a result wavelet spectra were obtained that are local in time. The average over all the local wavelet spectra gives the global wavelet spectrum. It is shown for both resonator types in figure 3.12 using three different analyzing functions. Inherently, the spectra differ from the corresponding Fourier spectra (see figure 3.10). The Helmholtz resonance frequency can easily be identified at 202 Hz for resonators of rectangular cross-section and at 886 Hz, if the cross-section is circular in shape. The resonance frequencies of the cavity modes are listed in tables 3.3 and 3.4. The frequency resolution in the determination of resonances was in all cases better than $\Delta f = 1$ Hz.

[5]The software is available at URL `http://paos.colorado.edu/research/wavelets/`. Accessed last on February 12th, 2003.

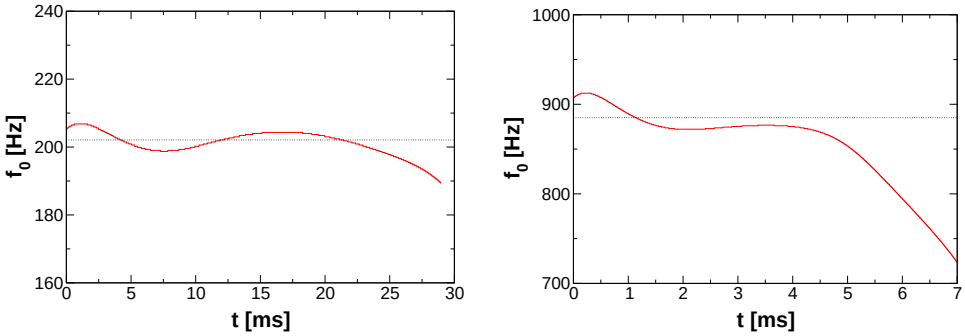

FIGURE 3.13: Helmholtz resonance frequency f_0 as a function of time as determined using the Morlet ($\omega_w = 6$) wavelet. The result of the global wavelet spectrum is indicated by the dotted line. Resonator of rectangular (left) and of circular cross-section (right). Resonator dimensions as shown in table 3.1 on page 46.

The uncertainty in the Helmholtz resonance frequency was, therefore, better than $\pm 0.5\,\%$ for the resonator with rectangular cross-section and less than $\pm 0.06\,\%$ for the circular one. In general, higher-frequency peaks are smaller than the lower-frequency peaks. This is due to the width of the wavelet filter in Fourier space. At small wavelet scales (high frequency), the wavelet is very broad in frequency, therefore any peaks in the spectrum get smoothed out. At large wavelet scales, the wavelet is more narrow in frequency, therefore the peaks are sharper and have a larger amplitude. Some mathematical background on how wavelet spectra compare to Fourier spectra is given, for example, by Perrier *et al.* (1995).

It should be noted that the results of the wavelet transformation provided in tables 3.3 and 3.4 are time averages. However, the process of releasing the excess pressure from the resonators in the CFD calculations is unsteady. Therefore, the resonances excited by the accompanying pressure impulse are not precisely constant in time. To illustrate how the transformation resolves the variation of single frequency components of the signal with time, the change of the Helmholtz resonance frequency is shown for both sample cases in figure 3.13.

3.1.3 Experimental investigation

In order to judge the quality of the analytical and numerical computations, the transfer functions of both resonators were determined experimentally. To this end, the resonators were excited by an incident sound wave. The results served to identify occurring resonances and to assess their natural frequencies. Similar measurements had been performed, for example, by Nelson *et al.* (1981).

The experimental investigation was conducted in an anechoic chamber without cross-flow present. The transfer function was measured between a

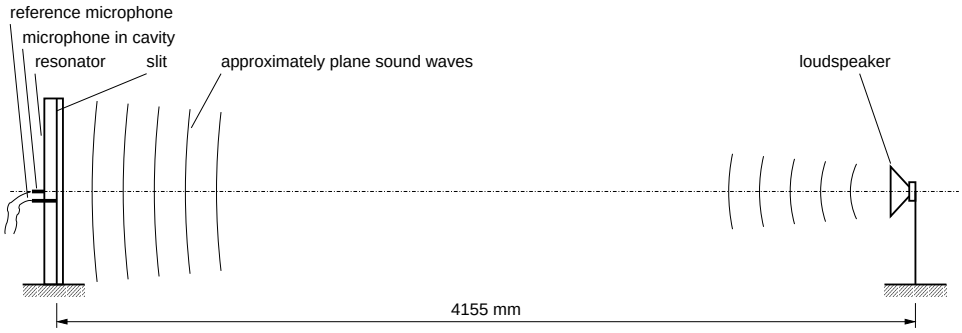

FIGURE 3.14: Schematic of experimental set-up in anechoic chamber. Shown to scale with the cylindrical resonator used in the airfoil model.

microphone of diameter 6.35 mm at midspan of the resonator cavity and an identical, second microphone outside the resonator that provided a reference for the oncoming sound. The diaphragm of the cavity microphone was mounted flush with the inner surface of the resonator. The reference microphone was embedded in a non-reflecting wall consisting of foamed material. At a distance of 4155 mm, the sound source was located sufficiently far from the resonator model such that it was stimulated by an approximately plane wave along its entire span (figure 3.14). The maximum retardation between the resonator center and its outer edges was 4.8 mm for the cuboidal and 24.3 mm for the cylindrical resonator. At a frequency of 1 kHz, for example, this corresponded to a maximum difference in phase of 5.0 ° and 25.5 ° along the span, respectively.

The sound pressure at the reference microphone was kept constant as the sound emitted by the loudspeaker was swept through the frequencies. In this way, a wide range from 10 Hz to 5 kHz and from 300 Hz to 20 kHz could be covered in the respective experiments. The resulting accuracy in the measurement of the Helmholtz resonance frequency was ±0.1 Hz, while higher modes were determined within ±1.6 Hz or ±12.3 Hz depending on the sweep range.

It was suspected that non-linearities might occur, for instance, due to the formation of small vortices at the sharp edges of the slit as the flow enters or leaves the resonator. The influence of non-linearities, however, is an essential aspect in judging the validity of the mathematical methods applied. Therefore, measurements were performed at different reference sound-pressure levels ranging from 22 to 92 dB. Since the resulting frequency-response functions remained unaffected, especially regarding magnitude and frequency of the Helmholtz resonance, it was concluded that no significant non-linearities occurred.

As the spanwise dimensions of all resonator models investigated in principle allowed for the formation of axial standing waves, it was checked, whether these were in fact excited. For this purpose, the phase difference between

two microphones located in the resonator cavity was measured, while one of them was traversed along the span. It was shown that in the frequency band of the Helmholtz resonance no standing waves formed in spanwise direction. Therefore, only the 2D-mode of the Helmholtz resonance was excited.

For both sample resonators, the measured frequency responses are shown in figures 3.15 and 3.16 where they are contrasted with the outcome of the analytical and numerical computations. An overview of the corresponding resonance frequencies can be found in tables 3.3 and 3.4.

3.1.4 Synopsis of results

A synopsis of the results of the analytical and numerical computations in comparison with the experimental data is given in figure 3.15 for a resonator with rectangular cavity cross-section and in figure 3.16 for one with circular cross-section. The maxima in the measured transfer functions correspond to the resonances. In general, these are reflected by both types of computations with very good accuracy. On the basis of these computations, the first resonance peak could be identified as the Helmholtz mode in both cases, whereas the other peaks are associated with the respective higher modes of the cuboidal and cylindrical cavities. The resonances are related more precisely to the modes of oscillation in tables 3.3 and 3.4.

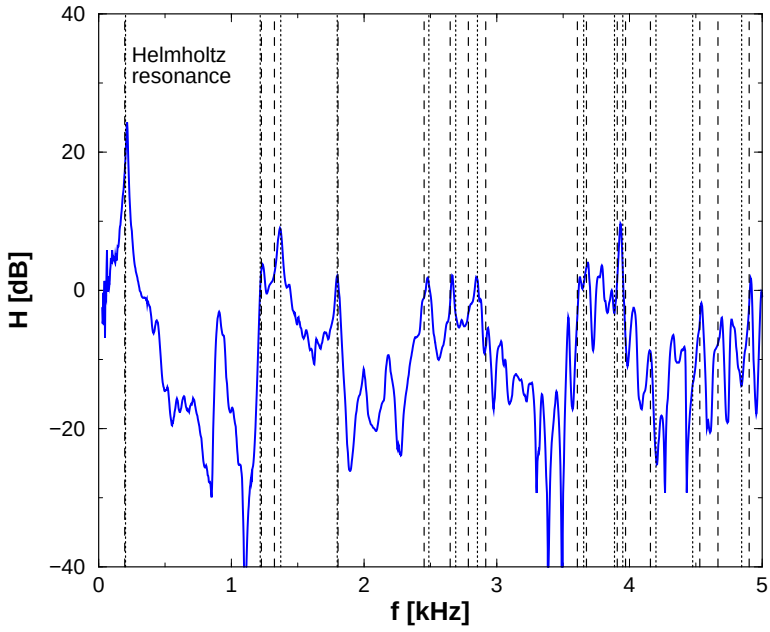

FIGURE 3.15: Measured transfer function H of a resonator with cuboidal cavity (solid blue line). The vertical lines show the resonances determined analytically (dashed lines) and numerically (dotted lines). Resonator dimensions as shown in table 3.1 on page 46.

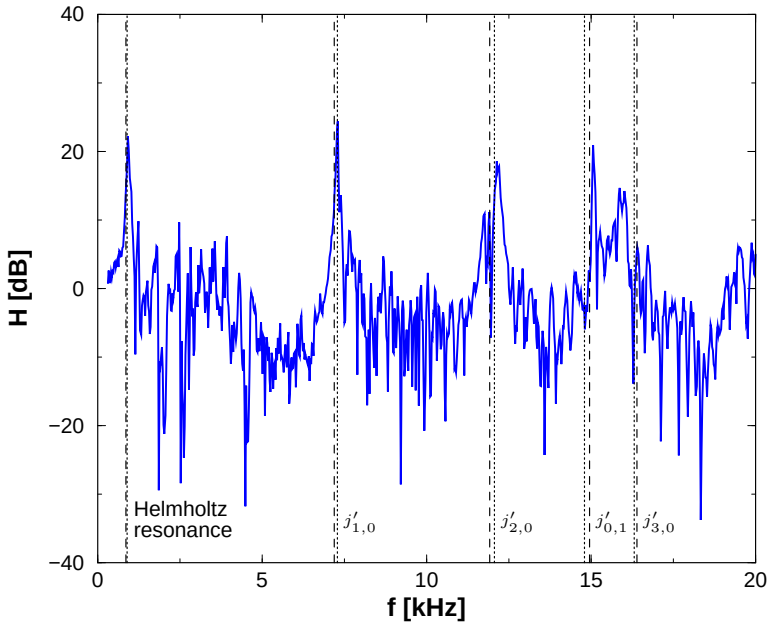

FIGURE 3.16: Measured transfer function H of a resonator with cylindrical cavity (solid blue line). The vertical lines show the resonances determined analytically (dashed lines) and numerically (dotted lines) and indicate which mode of vibration occurs in each case. Resonator dimensions as shown in table 3.1 on page 46.

In the transfer function of the cuboidal resonator (figure 3.15), the Helmholtz mode is clearly dominant. Most of the higher modes, that can theoretically propagate within the cavity, in fact occur in the experiment, but at a much lower amplitude. Among them, the first vertical mode ($q_x = 0$, $q_y = 1$) is relatively pronounced, which appears to be a consequence of the excitation promoting oscillations in the direction of the cavity height. However, no explicit preference can be observed regarding which types of modes tend to get strongly excited, and which ones weakly or not at all.

In contrast to this, all modes of the cylindrical resonator including both Helmholtz and higher modes have about equal magnitude in the frequency-response function (figure 3.16). The intense excitation of higher modes is most likely due to the off-center location of the resonator neck. It is worth noting that, in this case, all modes are detected by both types of computations as well as in the measurements.

How the outcome of the analytical, numerical, and experimental methods differs for changing resonator dimensions, is compared in figure 3.17. The agreement regarding the Helmholtz resonance frequency of a resonator with rectangular cavity cross-section is shown when the slit width is varied between 1 and 20 mm. As before, the results collapse with good accuracy. However, the precision of the analytical computations slightly decreases at

Mode	Experiment	Analytics	Numerics		
			Fit	DFT	Wavelet
	f [Hz]	f [Hz]	f [Hz]	f [Hz]	f [Hz]
Helmholtz	212	194	209	207	202
$q_x = 1,\ q_y = 0$	1233	1225	—	1242	1217
$q_x = 0,\ q_y = 1$	1364	1323	—	1346	1371
$q_x = 1,\ q_y = 1$	1797	1803	—	1795	1796
$q_x = 2,\ q_y = 0$	2477	2450	—	2450	2487
$q_x = 0,\ q_y = 2$	2661	2647	—	2657	2688
$q_x = 2,\ q_y = 1$	2845	2785	—	2795	2853
$q_x = 1,\ q_y = 2$	—	2916	—	—	—
$q_x = 2,\ q_y = 2$	3625	3607	—	—	—
$q_x = 3,\ q_y = 0$	3687	3675	—	3658	3652
$q_x = 3,\ q_y = 1$	3930	3906	—	—	3884
$q_x = 0,\ q_y = 3$	—	3970	—	3969	3949
$q_x = 1,\ q_y = 3$	—	4155	—	4141	4198
$q_x = 3,\ q_y = 2$	—	4529	—	4521	4475
$q_x = 2,\ q_y = 3$	—	4665	—	4659	—
$q_x = 4,\ q_y = 0$	4913	4900	—	4866	4845

TABLE 3.3: Comparison of the natural frequencies found experimentally, analytically, and numerically for a resonator with rectangular cross-section. Resonator dimensions as shown in table 3.1 on page 46.

Mode	Experiment	Analytics	Numerics		
			Fit	DFT	Wavelet
	f [Hz]	f [Hz]	f [Hz]	f [Hz]	f [Hz]
Helmholtz	908	848	891	857	886
$j'_{1,0}$, 1st azimuthal	7294	7179	—	7286	7277
$j'_{2,0}$, 2nd azimuthal	12120	11909	—	12000	12053
$j'_{0,1}$, 1st radial	15050	14941	—	14858	14788
$j'_{3,0}$, 3rd azimuthal	16011	16382	—	16286	16307

TABLE 3.4: Comparison of the natural frequencies found experimentally, analytically, and numerically for a resonator with circular cross-section. Resonator dimensions as shown in table 3.1 on page 46.

large slit widths.

In the experiments, it was shown that in both cases no spanwise standing waves occurred in the vicinity of the Helmholtz resonance frequency. Thus, although the numerical computations were restricted to two dimensions, one can expect physically valid results from using a 2D-Euler solver.

The excellent overall agreement in the above comparisons implies that

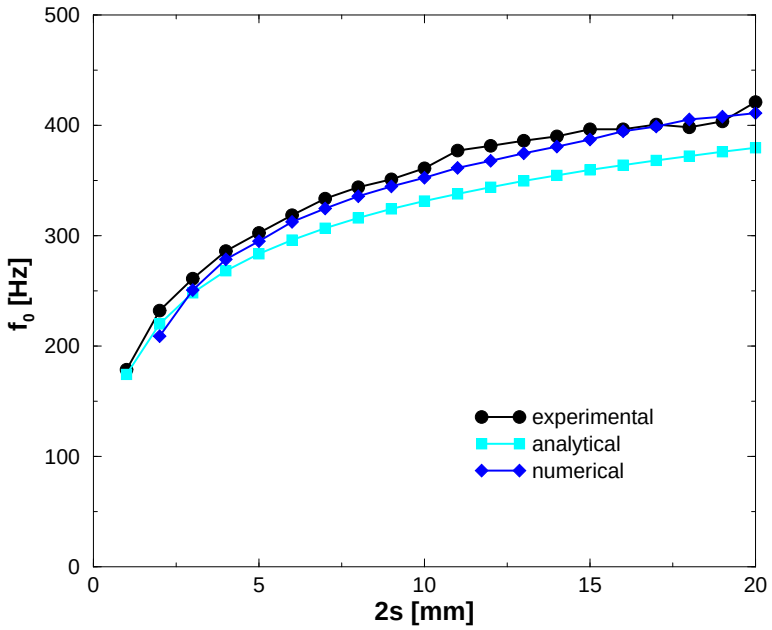

FIGURE 3.17: Comparison of results obtained by experimental, analytical, and numerical methods to determine the Helmholtz resonance frequency f_0 depending on the slit width $2s$ for a resonator with rectangular cavity cross-section. $l_y = 50\,\text{mm}$, other dimensions as shown in table 3.1 on page 46.

both the analytical and the numerical method are well capable of predicting the natural frequencies of a resonator with sufficient accuracy. These methods can, therefore, be employed to design resonators with acoustic properties suitable for specific applications.

3.2 Response to aerodynamic excitation

In contrast to the previous section, which focused on resonators induced by incident sound waves, this section addresses the properties of single acoustic resonators which are set oscillating by an incompressible, steady, two-dimensional grazing flow. For the remainder of this chapter, the scope is limited to the excitation of the Helmholtz mode such that the shape of the cavity is not significant. It will be seen later (see section 6.5) that the results can readily be transferred to oscillations of higher modes.

First, a parameter study elaborates on the relevant variables of the aerodynamic excitation (section 3.2.1). After a presentation of the experimental set-up in section 3.2.2, the mechanism of the flow induction is investigated (section 3.2.3) followed by a discussion of the influence of each parameter determined in the parameter study (section 3.2.5 to 3.2.9). Other aspects of importance such as two-dimensionality (section 3.2.4) and hysteresis effects

(section 3.2.10) will also be addressed.

3.2.1 Parameter study

In the investigation of an aerodynamically excited resonator, the frequency f_0 and the rms-value p_{cav} of the induced pressure oscillations in the cavity are of particular interest. Both parameters depend on the properties of the grazing flow and on the resonator geometry.

When a two-dimensional resonator of the kind presented in figure 1.1 oscillates in the Helmholtz mode, f_0 and p_{cav} are functions[6] $\mathcal{F}$ of the free-stream velocity U_∞, the fluid density ρ, the kinematic viscosity of the fluid ν, the boundary-layer momentum-thickness δ_2, the state of the boundary layer, the slit width $2s$, the neck length l_n, the cross-sectional area of the cavity A, and the shape of the resonator neck:

$$\left.\begin{matrix} p_{cav} \\ f_0 \end{matrix}\right\} = \mathcal{F}(\underbrace{U_\infty, \rho, \nu, \delta_2, \text{laminar/turbulent}}_{\text{flow properties}}, \underbrace{2s, l_n, A, \text{neck shape}}_{\text{resonator geometry}}) \quad (3.19)$$

In order to consider higher modes of oscillation as well, the shape of the cavity would have to be included also in the above relevance list. By means of dimensional analysis, the amount of independent variables can be reduced from nine to six yielding the following, most general, dimensionally homogeneous relation of the relevant parameters:

$$\left.\begin{matrix} \frac{p_{cav}}{p_{dyn}} \\ St_{2s} \end{matrix}\right\} = \mathcal{F}(Re_{2s}, \frac{\delta_2}{2s}, \text{laminar/turbulent}, \frac{l_n}{2s}, \frac{A}{4s^2}, \text{neck shape}) \quad (3.20)$$

Herein, p_{cav}/p_{dyn} quantifies the magnitude of the flow-induced pressure oscillations with respect to the free-stream dynamic pressure $p_{dyn} = \frac{1}{2}\rho U_\infty^2$, $St_{2s} = f_0 2s/U_\infty$ is the reduced frequency of oscillation, and $Re_{2s} = U_\infty 2s/\nu$ the Reynolds number with both latter quantities based on the slit width $2s$. The influence of the parameters on the right-hand side on magnitude and frequency of the resonator oscillations will now be investigated.

3.2.2 Experimental set-up

Fundamental properties of flow-induced resonators and the impact of their oscillations on the turbulent boundary layer downstream were investigated in a flow with nominally zero pressure gradient ($\mathrm{d}c_p/\mathrm{d}x = -6.58 \times 10^{-2}\,/\mathrm{m}$). The experiments were conducted in the open-return wind-tunnel presented above (section 2.2.1). For this purpose, a resonator of the type described in section 2.1.1 was mounted flush with the wall in a flat plate (figure 3.18).

[6] The symbol $\mathcal{F}$ indicates a relation between variables, but denotes a different function in each equation of this section.

Cavity volume and slit width of the cuboidal resonator could be adjusted via two computer-controlled traversing gears whereas the neck geometry could be varied by exchanging the edge pieces (see figures 3.25 and 3.26).

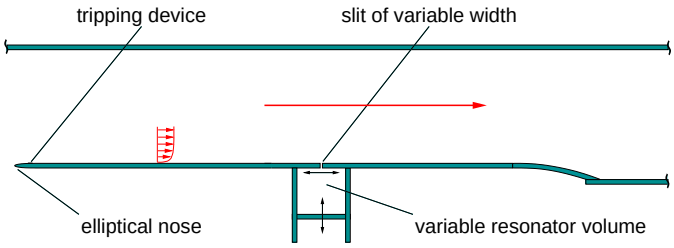

FIGURE 3.18: Schematic view of the experimental set-up for the investigation of aerodynamically excited resonators.

The boundary layer of the contraction upstream was removed by a bypass at the entrance of the measurement section ($x = 0\,\text{mm}$) to eliminate any influence of upstream history on the test boundary layer. The bypass featured an adjustable outlet vane that combined tuning the pressure gradient to approximately zero and fixing the stagnation point at the leading edge of the flat plate. To facilitate this, the exit blockage of the terminating diffuser could also be adjusted. Both means ensured clearly defined initial conditions for the boundary layer along the plate. The leading edge of the plate was located at $x = 0\,\text{mm}$ and had an elliptical nose with an aspect ratio of $1:5$ shaped according to Hancock (1980). At flow velocities exceeding $10\,\text{m/s}$, the laminar boundary layer was artificially tripped 52 mm downstream of the leading edge by two rows of Dymo tape with letters "V" imprinted pointing in downstream direction. The streamwise distance between both rows was 25 mm while each row had a width of 9.4 mm and a height of 0.6 mm.

For the use of optical measurement techniques such as LDA or PIV, the flat plate had been coated with glass that was blackened on the back to make it highly reflective. As a result, the measurements could be performed with extremely low noise levels even in the close vicinity of the wall (see Huppertz, 2001). The height of the measurement section above the plate was 250 mm. The resonator orifice was situated at a streamwise distance of 657 mm from the leading edge.

For the investigation of the resonators, a Cartesian right-handed coordinate system (x, y, z) was used: x originated at the entrance of the measurement section pointing in free-stream direction, y represented the component normal to the lower wall, and z denoted the spanwise component originating at the centerline of the test section.

Great care was taken in the design of the wind tunnel and set-up to ensure high-quality initial conditions, especially regarding the two-dimensionality of the flow. For a detailed discussion of the flow characteristics, refer to appendix A.

3.2.3 Mechanism of the flow-induction process of a resonator

Phase-averaged LDA measurements of the flow field in the resonator neck were taken within a cross-section of 31 mm × 20 mm (figure 3.19). In both x- and y-direction, the points of the measurement grid were spaced 0.5 mm apart. The shape of the neck (denoted as R0/K0) was of the conventional type featuring right-angled corners at the upstream (R0) and downstream (K0) edge. Figure 3.20 shows the corresponding vorticity field during one cycle of the resonator oscillations as a function of phase.

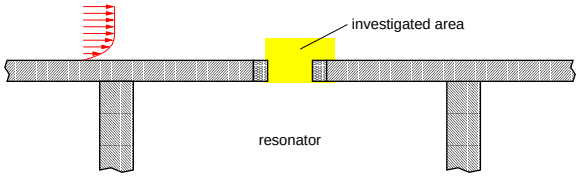

FIGURE 3.19: Illustration of the area investigated by phase-averaged LDA measurements (yellow). Dimensions to scale.

The vorticity plots imply that one oscillation cycle is characterized by the following sequence of processes: At the upstream edge of the resonator orifice, the approaching boundary layer forms into a free shear layer, which is inherently unstable. Since the flow leaves the upper surface tangentially, it appears that the Kutta condition is satisfied at the edge. The shear layer protrudes about halfway into the neck, where it is displaced due to interaction with the reciprocating flow field associated with the cavity pressure fluctuations. As a consequence of this displacement, the break-down of the shear layer into a large-scale spanwise vortex seems to get triggered. During the second half of the cycle, this vortex grows in size while it is convected across the opening. Eventually, it hits the downstream edge of the neck in a way that most of its vorticity stays contained within the orifice.

The above measurements confirm the common ideas of the flow-induction process of acoustic resonators as they were discussed in section 1.3.2. The features of the periodic flow field as described, for example, by Rossiter (1964) can be recognized in the LDA results, which agree also well with unsteady flow visualizations by Nelson *et al.* (1981). However, on the basis of the vorticity plots alone, induced pressure fluctuations or the acoustic feed-back path cannot be inferred.

3.2.4 Spanwise dependence of the resonator oscillations

To assess the two-dimensionality of the vortex-shedding process and of the induced oscillations within the resonator neck, a phase-averaged LDA measurement in spanwise direction was performed. For one cycle of oscillation, the result is shown in figure 3.21 in terms of the vertical velocity component v along the spanwise centerline in the slit exit plane.

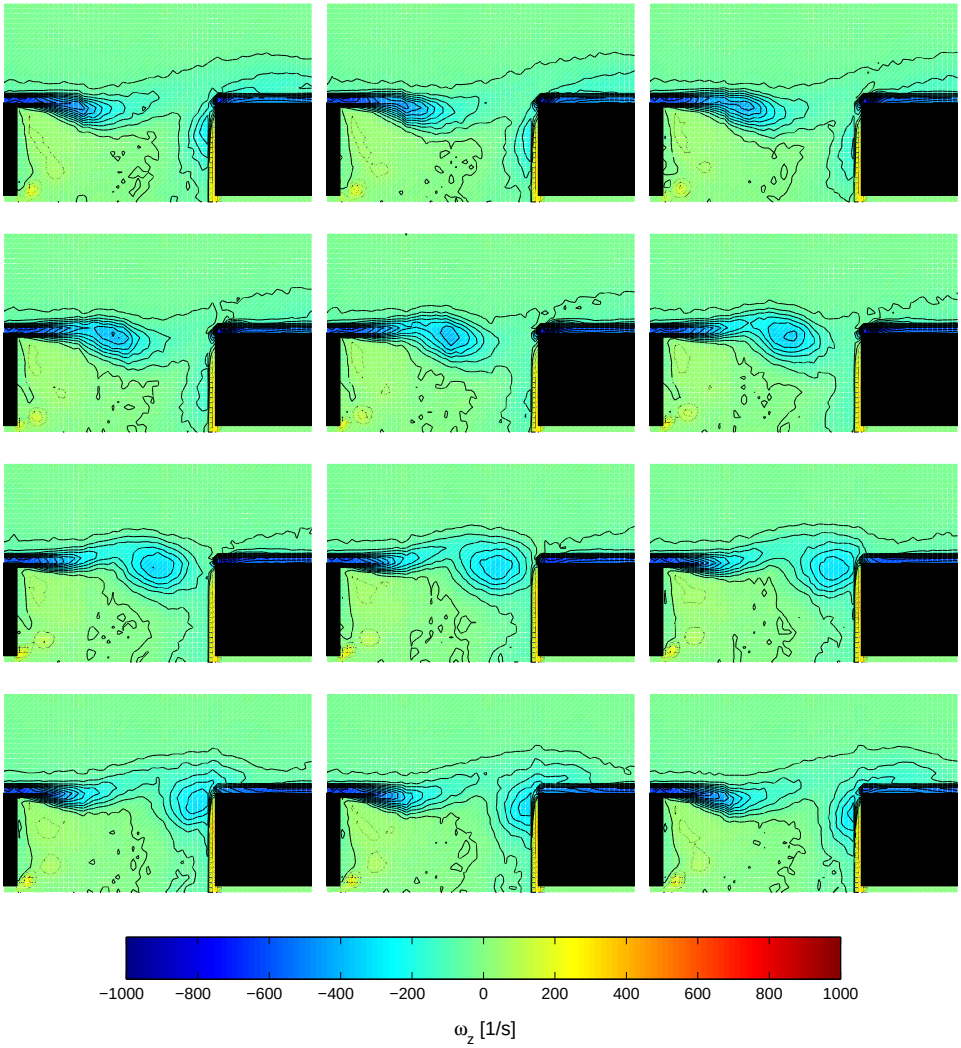

FIGURE 3.20: Phase-averaged LDA measurement in the resonator neck with conventional geometry (R0/K0) at different phase angles (successive phase shifts at increments of $\Delta\varphi = 30\,^{\circ}$, color scale and contours correspond to vorticity ω_z). $Re_u = 1.5 \times 10^6$, slit width 20 mm, resonance frequency 450 Hz, cavity height 50 mm.

The vertical velocity component results from the superposition of the vortically induced flow field in the orifice and the sound particle velocity driven by the acoustic resonance. This component is correlated along the entire span of the resonator neck confirming that the flow can be considered as two-dimensional. This agrees with Bruggeman *et al.* (1989) who report that the vortex shedding at the upstream edge is purely two-dimensional, if the opening is rectangular. Therefore, measurements taken at midspan suffice to adequately represent the properties of the flow. For $z/W > 40\,\%$,

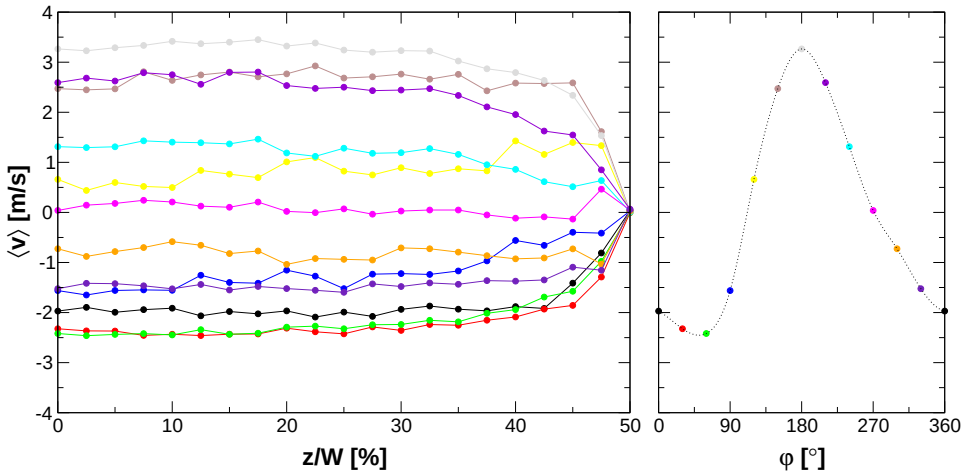

FIGURE 3.21: Phase-averaged vertical velocity component $\langle v \rangle$ along the half span of the resonator neck (left) together with phase angle at midspan in relation to cavity pressure (right). Data from LDA measurement. W denotes the width of the measurement section. $Re_u = 1.5 \times 10^6$, $2s = 20\,\text{mm}$, neck geometry R0/K0, $f_0 = 450\,\text{Hz}$, $l_y = 50\,\text{mm}$, $x - x_{LE} = 10\,\text{mm}$ with x_{LE} representing the streamwise location of the leading edge of the neck, $y = 0\,\text{mm}$.

the velocity data deviate from a homogeneous distribution as a consequence of the corner flow in the test section. This effect is closely related to the spanwise distribution of the wall shear-stress upstream, which exhibits a similar behavior (see appendix A.3). The decreasing wall shear-stress within the respective outer 10 % of the wind-tunnel width indicates a lack of energy in the near-wall region, which is responsible for the reduced aerodynamic excitation of the resonator towards both edges.

3.2.5 Influence of cross-flow on natural frequencies

When induced by a grazing flow, the response of a resonator is a "clean" sine wave with steady frequency. Figure 3.22 shows a typical spectrum of the sound pressure in the cavity of an aerodynamically excited resonator. The peak of the Helmholtz resonance frequency at 203 Hz is very narrow and lies more than 50 dB above the background noise. Although higher harmonics do occur, their small amplitude, which is more than 40 dB less than that of the fundamental oscillation, renders them insignificant. These characteristics imply that the resonance is well focused and very stable.

An example of how the Helmholtz resonance frequency of the acoustic response, discussed in section 3.1, is related to the natural frequency of the flow-induced oscillations, is given in figure 3.23. It shows resonance frequencies and amplitudes in the resonator cavity as a function of the slit width. Whereas the values of the acoustic case were obtained from analytical computations, the data associated with the aerodynamic excitation stem

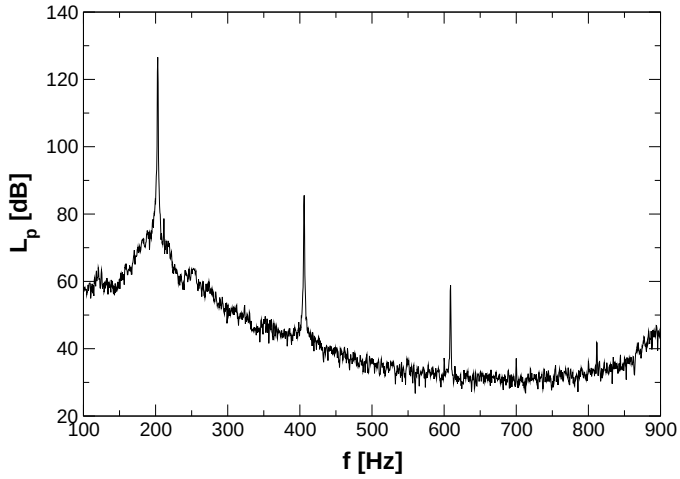

FIGURE 3.22: Typical spectrum of the flow-induced sound-pressure level L_p within the resonator cavity. $Re_u = 6.5 \times 10^5$, $2s = 9\,\text{mm}$, neck geometry A30/K5 (see section 3.2.6), $f_0 = 203\,\text{Hz}$, $l_y = 129.6\,\text{mm}$.

from microphone measurements. As a criterion for the occurrence of flow-induced resonance, the ratio of rms sound-pressure in the cavity p_{cav} to free-stream dynamic pressure p_{dyn} was considered. Distinct oscillations are present when p_{cav}/p_{dyn} exceeds 1 % such as in the range of slit widths from 7 to 14 mm. For these cases, it is possible to determine the according frequency of the sound produced. The maximum amplitude of the flow-induced sound

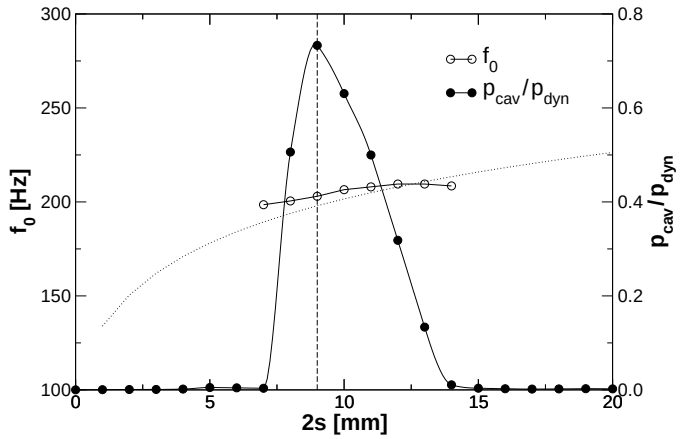

FIGURE 3.23: Rms-value of the sound pressure p_{cav} in the resonator cavity with respect to the dynamic pressure p_{dyn} of the oncoming flow as well as corresponding Helmholtz resonance frequency depending on the slit width. The vertical line marks the case of resonance, where p_{cav}/p_{dyn} is maximal. The dotted line represents the values of the resonance frequency obtained analytically according to section 3.1.1. $Re_u = 6.5 \times 10^5$, neck geometry A30/K5 (see section 3.2.6), $l_y = 129.6\,\text{mm}$.

pressure is obtained at $2s = 9\,\text{mm}$ indicating that, under these conditions, the frequency of the vortex shedding is most suitable to excite the Helmholtz-mode oscillations. In this situation, the resonance frequency induced by the flow is approximately identical with the corresponding value for purely acoustic excitation. Presumably, the slight remaining difference between the two is a consequence of the influence of the grazing flow or is owed to the mathematical model. It will be seen later (see section 6.5) that the result might be generalized such that flow-induced resonance can occur whenever the vortex shedding frequency is approximately equal to *any* of the natural frequencies of the resonator.

The close connection between acoustic and flow-induced resonance frequencies confirms that the methods developed in section 3.1 for the acoustic case can also be applied in the design of aerodynamically excited resonators.

The above results agree with those of Flynn & Panton (1990), who report that Helmholtz resonators respond only to a certain frequency band of fluctuations in the flow. They conclude that strong resonance is limited to circumstances where a natural frequency of the resonator coincides with the dominant frequency provided by the shear layer in the opening. According to Panton & Miller (1975*a*), the interaction between turbulence and acoustic motion in the orifice causes a slight shift in the natural frequency of resonators induced by a turbulent cross-flow compared to resonators excited acoustically.

Similar to the previous measurements, the Helmholtz resonance frequency was investigated for a wide variety of combinations of slit width and Reynolds number. For this purpose, the slit width $2s$ was varied between 1 and 20 mm,

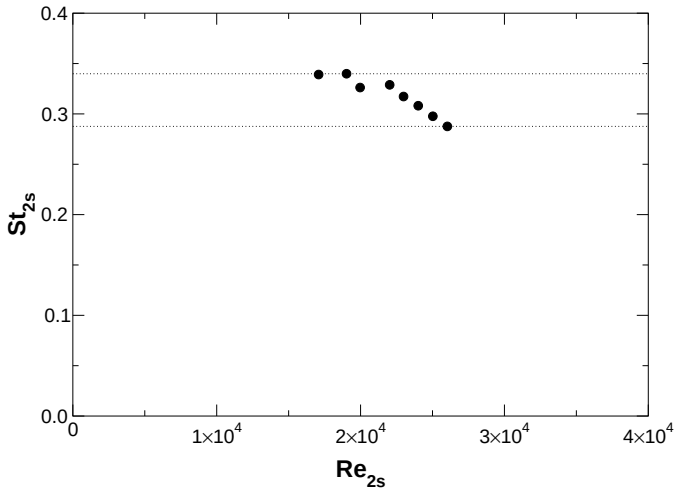

FIGURE 3.24: Nondimensional Helmholtz resonance frequencies St_{2s} for resonators with various slit widths as a function of the Reynolds number Re_{2s} (neck geometry R0/K0). The horizontal lines indicate the Strouhal-number range of the oscillations.

while Reynolds numbers Re_u based on unit length ranged from 2.0×10^5 to 1.75×10^6. Resonances are summarized in figure 3.24 in terms of reduced frequencies St_{2s} versus Reynolds number Re_{2s}. In the graph, both nondimensional parameters are based on the slit width $2s$. If the oscillation amplitude p_{cav}/p_{dyn} exceeded 1 % for more than one value of the slit width at a specific Reynolds number, only the respective maximum was considered.

Under all flow conditions, the reduced Helmholtz resonance frequency lies between $St_{2s} = 0.29$ and 0.34. This is well within the range of values found in the literature given in table 1.1 on page 15, which vary between $St_{2s} = 0.19$ and 0.40. According to De Metz & Farabee (1977), the resonator is oscillating in the fundamental mode in these cases, where at any time there is only one vortex formed by the shear layer present in the resonator opening.

3.2.6 Influence of neck geometry on the flow induction

An effective induction by the cross-flow is the most essential prerequisite for the applicability of a resonator as a flow-control device. In order to improve the aerodynamic excitation, the resonator-neck geometry was, therefore, modified. The optimization had two specific goals: On the one hand, the amplitude of the induced pressure oscillations should be maximized. In this way, the vorticity production at the resonator orifice would be enhanced resulting in a maximum effect on a separation region. On the other hand, the range of Reynolds numbers, where resonance occurs, should be enlarged in order to extend the scope of possible flow situations that could be controlled. Since Helmholtz resonators have almost exclusively been applied as sound absorbers in the past, the above goals are contrary to previous investigations.

Neck geometries considered

Nevertheless, it seems worthwhile to consider earlier work in order to derive guidelines, in which direction modifications of the neck geometry might be beneficial for the purpose of flow control. With the focus confined to the influence of the shape of the orifice on the response of flow-induced resonators, the literature review given in section 1.3.2 is briefly extended here.

In an explorative study, the effect of the geometry of circular openings was investigated by Panton (1990) on the basis of thirteen samples. He found that resonators with an opening slanted towards the oncoming flow responded with high oscillation amplitudes, whereas those with an opening slanted the other direction had a negligible response. This agrees with observations by Franke & Carr (1975) and Heller & Bliss (1975) who report that inclined trailing edges had proven to be very effective in reducing cavity oscillations. An investigation by Bruggeman *et al.* (1991) to suppress pulsations in gas transport systems embraces a theoretical model for the acoustic energy absorbed or generated by a vortex traveling across the open-

ing. According to this model, the formation of a vortex at the upstream edge absorbs acoustic energy, whereas sound production occurs when the vortex approaches the downstream edge of the orifice after half an oscillation period. The strength of the acoustic source and sink is determined by the local acoustic velocities which, in turn, depend on the shape, i.e. the sharpness of the resonator neck.

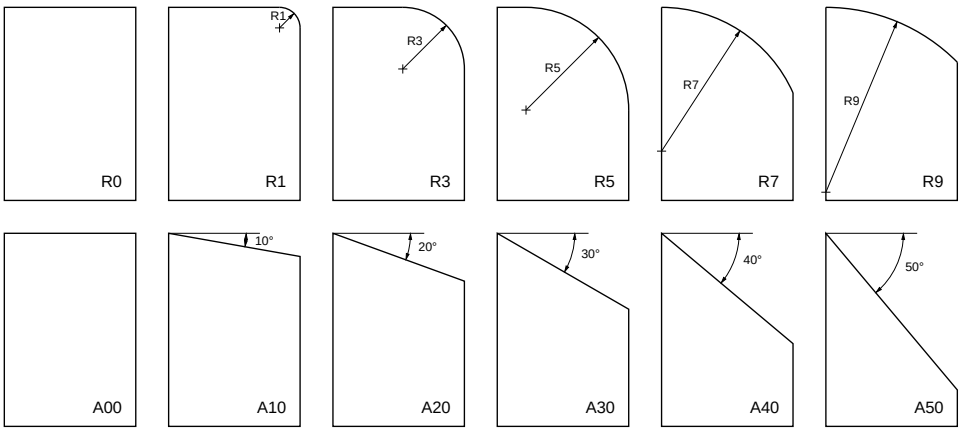

FIGURE 3.25: Resonator-neck geometries implemented at the upstream edge. R_{LE} denotes the radius of curvature of the leading-edge corner (top row), γ_{LE} represents the expansion angle of the leading edge (bottom row). The edges were mounted flush with the wall. When built in, flow was from left to right.

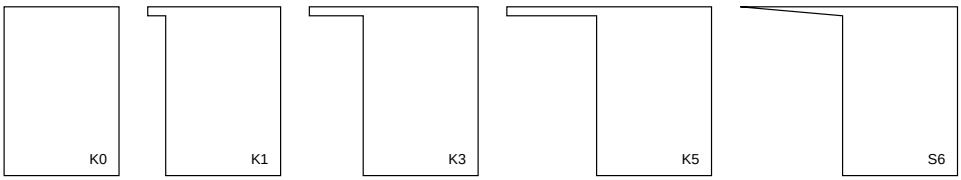

FIGURE 3.26: Resonator-neck geometries implemented at the downstream edge. The edges were mounted flush with the wall. When built in, flow was from left to right.

As a consequence, the resonator geometries investigated were aimed at minimizing the acoustic absorption at the upstream edge while maximizing the acoustic production at the downstream edge. This required small sound particle velocities near the leading edge such that it was rounded off or inclined as depicted in figure 3.25. In contrast, several types of horizontal blades pointing towards the oncoming flow were installed at the trailing edge to increase the acoustic velocities in this region (figure 3.26).

At a later stage in the investigation, the neck geometry was further improved (denoted by an asterisk) by inserting a fence directly upstream of the leading edge and by changing the vertical position of the downstream blade (figure 3.27). The fence was variable in height. The underlying idea of

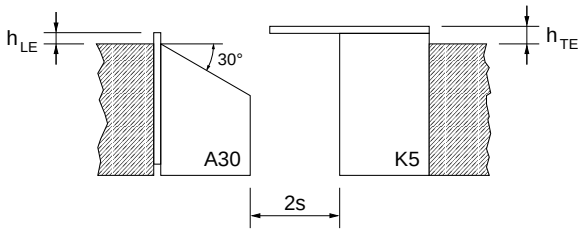

FIGURE 3.27: Neck geometry A30*/K5* with a fence of height h_{LE} inserted upstream of the leading edge, and with a horizontal blade installed at a distance h_{TE} above the wall.

having a fence protrude into the grazing flow was to involve more energetic regions of the boundary layer in the shear-layer roll-up process and, thus, to direct more energy into the resonator to feed the oscillations.

Influence of neck geometry on oscillation amplitude

The influence of variations in the neck geometry on both the pressure oscillations induced in the resonator cavity, and the Reynolds number range where resonance occurred, was considerable. Figures 3.28 and 3.29 illustrate the effects of the systematic modification of the upstream edge. The results are given as a field representation of the sound-pressure level L_p produced by the resonator in the space spanned by slit width and unit Reynolds number. Deviating from the result of the parameter study, the oscillation amplitude was characterized by L_p in these graphs because of its logarithmic properties.

The conventional neck geometry denoted as R0/K0 or A00/K0 shows a very limited range of Reynolds numbers ($1.0 \times 10^6 \leq Re_u \leq 1.3 \times 10^6$) where resonance at only moderate oscillation amplitudes ($p_{cav}/p_{dyn} = 14\,\%$, $L_p = 122.2\,\mathrm{dB}$) is induced. When no pulsations are excited within the resonator, the sound-pressure level is between 60 and 100 dB ($p_{cav}/p_{dyn} < 1\,\%$) depending on the free-stream velocity. This represents the background noise caused by the flow in the wind tunnel.

With increasing radius of curvature at the upstream edge, however, this scenario gradually improves in both respects (figure 3.28). The best results are obtained with a leading-edge radius of $R_{LE} = 7\,\mathrm{mm}$. In this case, the relative sound pressure is as high as $p_{cav}/p_{dyn} = 45\,\%$ ($L_p = 139.6\,\mathrm{dB}$), and resonance is present for Reynolds numbers above 1.25×10^6 until the measurement range of 1.75×10^6 is exceeded. Although the Reynolds number range is slightly larger in the case with $R_{LE} = 5\,\mathrm{mm}$, the oscillations are not quite as pronounced. A further increase of the radius beyond 7 mm appears to be detrimental.

Variations in the inclination angle γ_{LE} of the upstream edge produce results superior to the ones before (figure 3.29) with the only exception of the case with $\gamma_{LE} = 10\,^\circ$, where virtually no resonance can be induced. In contrast, leading edges slanted at greater angles promote resonances associ-

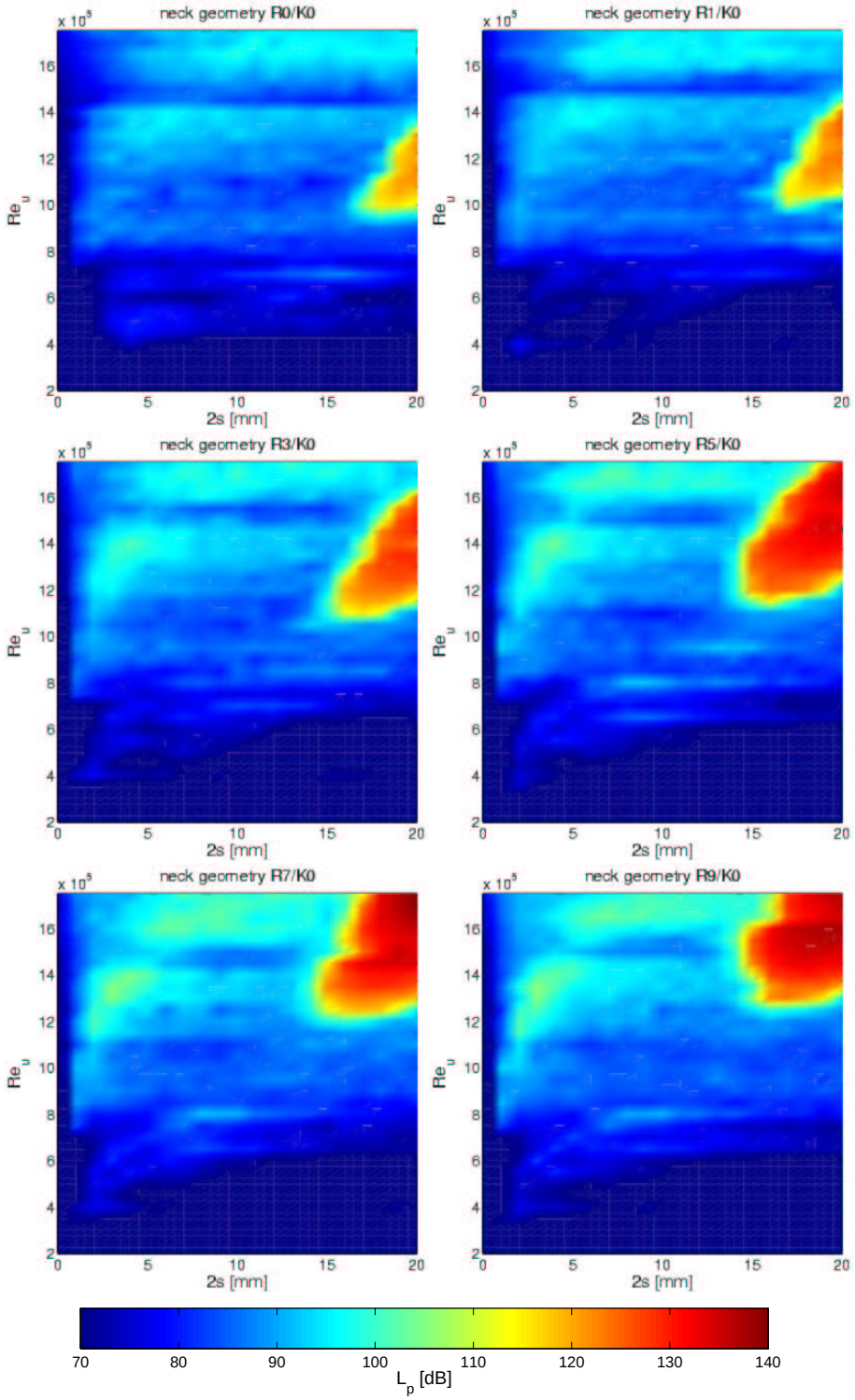

FIGURE 3.28: Sound-pressure level (see color scale) of the resonance peaks depending on Reynolds number and slit width: Neck geometries differ by radius of curvature R_{LE} of the leading edge ranging from 0 to 9 mm. $l_y = 129.6$ mm.

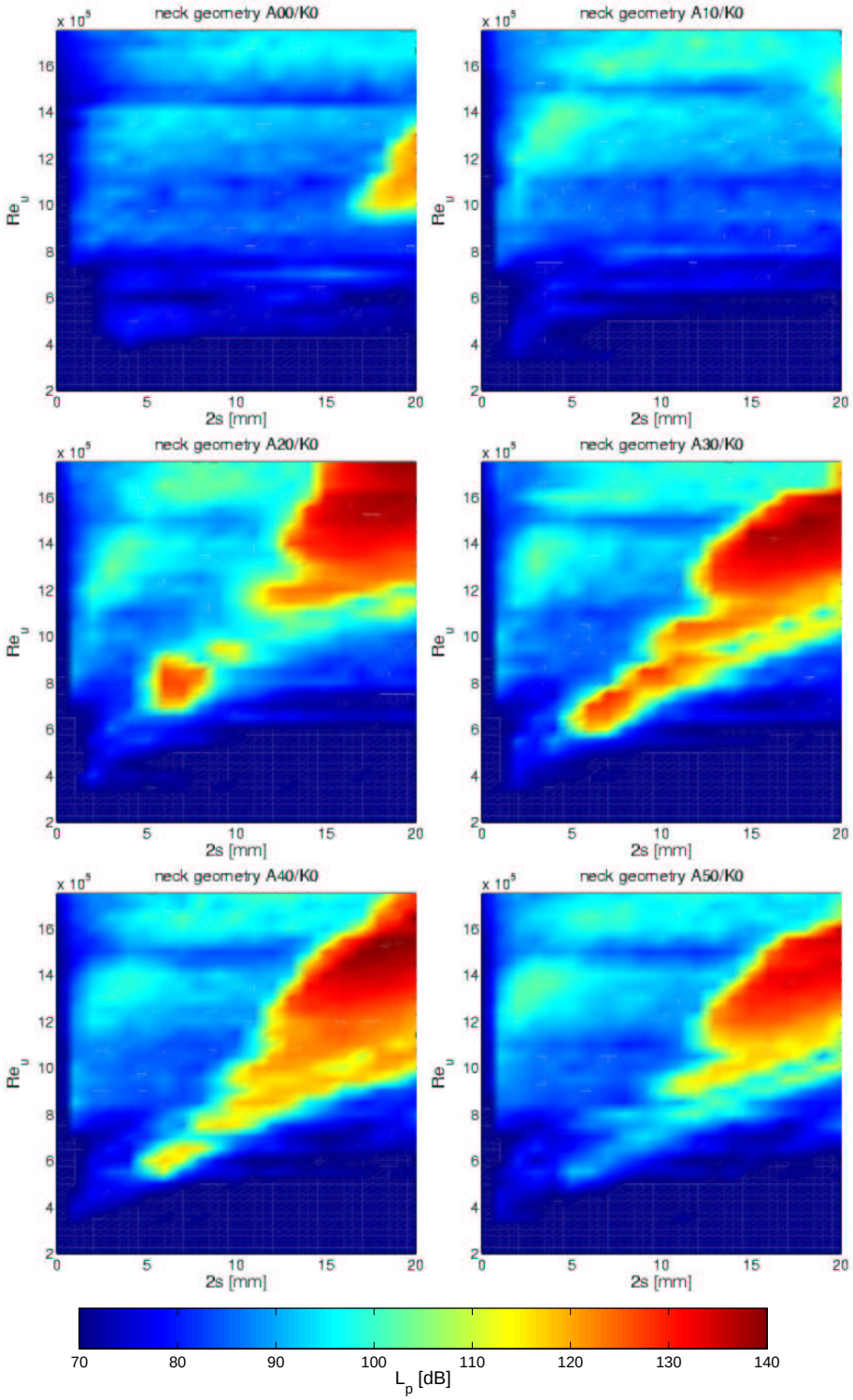

FIGURE 3.29: Sound-pressure level (see color scale) of the resonance peaks depending on Reynolds number and slit width: Neck geometries differ by angle γ_{LE} of the leading edge ranging from $0\,^\circ$ to $50\,^\circ$. $l_y = 129.6\,\mathrm{mm}$.

ated with high oscillation amplitudes. An inclination of 30 ° can be regarded as the optimum as values of p_{cav}/p_{dyn} as high as 74 % are achieved in this case. Furthermore, resonant conditions are provided within a wide band of Reynolds numbers Re_u ranging from 0.6×10^6 up to 1.75×10^6. These favorable effects diminish once the angle is increased beyond the optimum value of 30 °.

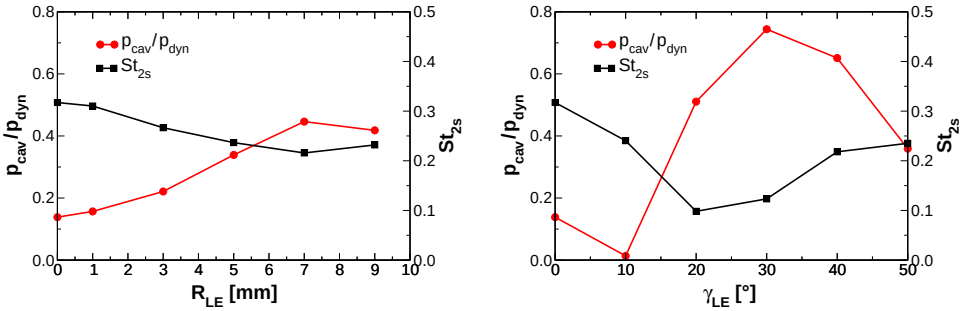

FIGURE 3.30: Nondimensional maximum sound pressure and corresponding resonance frequency of flow-induced resonators with eleven different neck geometries (microphone measurement). Starting out from configuration R0/K0 or A00/K0, the acoustic absorption was reduced by rounding (left) or inclining (right) the upstream edge. R_{LE} and γ_{LE} denote radius or angle of the leading edge of the orifice, respectively. Re_u and $2s$ variable, $l_y = 129.6$ mm.

For each neck configuration discussed before in the context of figures 3.28 and 3.29, the most favorable cases of resonance characterized by a maximum relative sound pressure are summarized in figure 3.30. The effect of systematically varying the radius R_{LE} of the leading edge on both the induced oscillation amplitude in terms of p_{cav}/p_{dyn} and the reduced frequency St_{2s} is seen to be gradual and relatively moderate. In contrast, a change in the inclination angle γ_{LE} causes pronounced differences regarding both parameters. In addition to the improvement of the sound pressure, it is interesting to note that the Strouhal number varies within a wide range from 0.10 to 0.32 in this case.

Similarly, the influence of the downstream edge geometry was studied on the basis of the configuration with optimum leading edge (A30/K0). Best results were obtained by the installation of a horizontal blade protruding 5 mm into the orifice in the upstream direction. In figure 3.31, the generated sound-pressure level for the resulting edge configuration (A30/K5) is contrasted with the original neck geometry (R0/K0). As a consequence of the modifications, the domain of Helmholtz resonance expanded towards smaller slit widths (from 18 down to 8 mm) covering a wider range of Reynolds numbers Re_u from 0.55×10^6 to 1.70×10^6. Besides, the induced rms pressure-fluctuations in the cavity increased up to a maximum of $p_{cav}/p_{dyn} = 81\,\%$.

In a final modification, a fence was inserted upstream of the leading edge, and the vertical position of the trailing edge was varied (see figure 3.27).

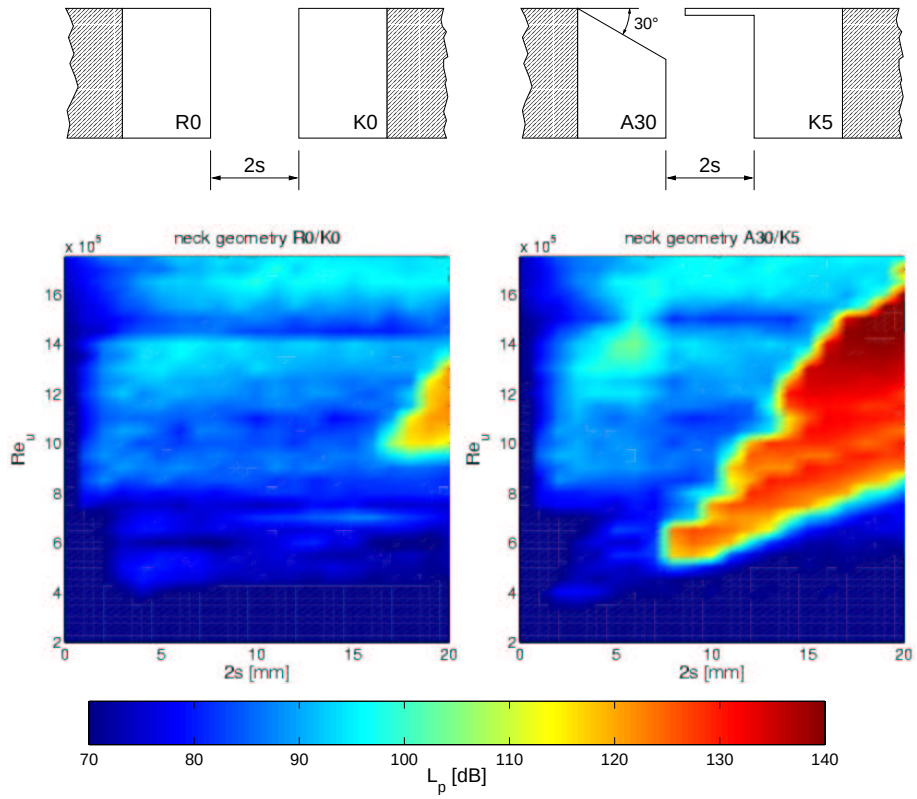

FIGURE 3.31: Sound-pressure level (see color scale) of the resonance peaks for two different neck geometries depending on Reynolds number and slit width: Conventional neck geometry R0/K0 (left), neck geometry A30/K5 with optimized leading and trailing edges (right). $l_y = 129.6\,\text{mm}$, $l_n = 9.35\,\text{mm}$.

Optimum values for the fence height and the location of the horizontal blade above the wall were $h_{LE} = 0.8\,\text{mm}$ and $h_{TE} = 1.25\,\text{mm}$, respectively. The resulting ratio of rms cavity-pressure to free-stream dynamic pressure was as high as 108 %, which is in contrast to Blake (1986) who postulated $p_{cav}/p_{dyn} < 100\,\%$. Due to its outstanding response level, this resonator configuration denoted as A30*/K5* was eventually applied for flow-control purposes. An according plot of the resonance domain will be shown later in the context of separation control in a diffuser (figure 6.18 in section 6.4.5). In conclusion, it can be stated that both optimization goals have been met by the modification of the neck geometry.

Influence of neck geometry on resonance frequencies

In the same manner as in figure 3.24, the Helmholtz resonance frequency was investigated for twelve additional neck geometries. The combinations of slit width and Reynolds number considered were identical to before. As a result, figure 3.32 shows the reduced frequencies of the Helmholtz resonance

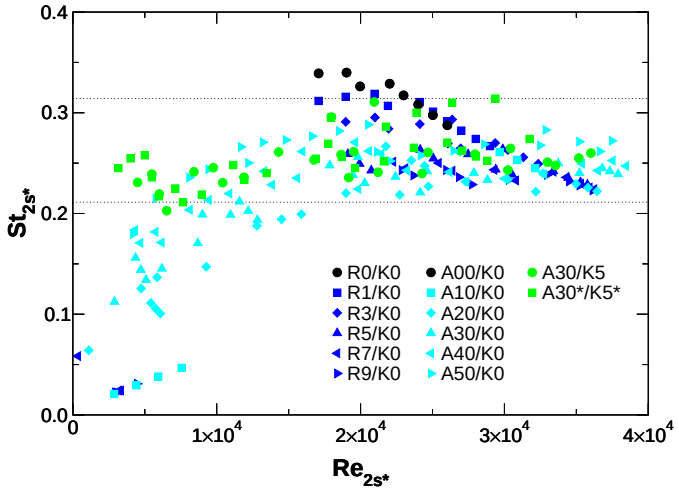

FIGURE 3.32: Nondimensional Helmholtz resonance frequencies St_{2s^*} for resonators with various slit widths and slit geometries (for explanation see figures 3.25 and 3.26) as a function of the Reynolds number Re_{2s^*}. The horizontal lines indicate the Strouhal-number range of the oscillations associated with the optimum neck geometry A30*/K5*.

for cases, where the rms sound-pressure measured inside the resonator cavity exceeded 1 % of the free-stream dynamic pressure.

Although having nominally the same slit width, the resonator necks comprised slightly different volumes of air depending on their orifice geometry (see definition of slit width in figure 3.31). This caused a small variation in the Helmholtz resonance frequency. In order to compensate for this effect, an equivalent slit width denoted as $2s^*$ was introduced. It represents the slit width that a comparable resonator with identical neck volume, but rectangular edges (configuration R0/K0 in figures 3.25 and 3.26) would have. In the plot, both the Strouhal and Reynolds numbers St_{2s^*} and Re_{2s^*}, respectively, are based on this equivalent slit width $2s^*$.

Figure 3.32 illustrates that due to the various neck configurations, oscillations are excited in a wide range of reduced frequencies extending from 0.02 to 0.34. The resonances between $St_{2s^*} = 0.02$ and 0.20, however, are limited to Reynolds numbers below 1.5×10^4 while for higher Re_{2s^*}, all resonances lie in the frequency band between 0.20 and 0.34. Strouhal numbers less than 0.10 are associated with very low oscillation amplitudes ($1.0\,\% \leq p_{cav}/p_{dyn} \leq 1.2\,\%$) such that the relevant Strouhal numbers are confined to the range 0.10 to 0.34. It should be noted that all resonances within this domain occur under fully turbulent inflow conditions and exhibit relatively large oscillation amplitudes. Comparable values of St_{2s^*} found in the literature cover the range between 0.19 and 0.40 (see table 1.1). Since in the present case the smallest values are obtained solely with the configurations A20/K0 and A30/K0, it is implied that the occurrence of such

exceptionally low Strouhal numbers is closely related to the neck geometry.

A change of the radius of curvature R_{LE} at the upstream edge has only a minor influence on the Strouhal number of the induced oscillations. For $Re_{2s^*} > 0.5 \times 10^4$, the nondimensional Helmholtz resonance frequencies associated with the corresponding configurations (cases R0/K0 through R9/K0) lie in the range from $St_{2s^*} = 0.20$ to 0.34. The reduced frequencies slightly decrease with increasing radius of curvature while fluctuating less with Re_{2s^*}.

A variation of the inclination angle γ_{LE} of the leading edge, in contrast, has a strong impact on both the Reynolds- and the Strouhal-number range of the resonances. At small values of γ_{LE}, the resonance frequencies are low and increase with the Reynolds number. If γ_{LE} is enlarged, the Strouhal numbers tend to augment and to be on one level with respect to Re_{2s^*} (see cases A00/K0 through A50/K0).

Both configurations with modified trailing edges, A30/K5 and A30*/K5*, are characterized by relatively constant resonance frequencies throughout the entire range of Reynolds numbers. In the final configuration (A30*/K5*), the Strouhal numbers vary between 0.21 and 0.31.

Influence of neck geometry on vortex dynamics

The influence of the neck geometry on the dynamics of the vortices generated in the resonator orifice was studied on the basis of one sample case. For this purpose, a resonator with neck geometry A30/K5 was chosen and set off against the conventional configuration R0/K0 investigated before (see figure 3.20). Apart from the cavity height, all parameters were equal to the previous LDA measurement. The dimensions of the area examined during the experiment were 37.5 mm × 20 mm, similar to the region depicted in figure 3.19.

The basic sequence of processes during one cycle of oscillation is much the same as in the description of the conventional case (see section 3.2.3). In the plots of the phase-averaged vorticity field, however, a few relevant differences regarding the flow topology are apparent which result from the modified shape of the orifice (figure 3.33). In contrast to configuration R0/K0, the displacement of the shear layer due to the inclined edge is stronger and takes place further upstream causing the discrete vortex to form much earlier. Subsequently, while it is convected across the opening, the vortex has more time to grow before it hits the downstream edge and is, therefore, larger in size (diameter 9.8 mm as opposed to 6.9 mm). In view of the use of the resonator as a flow-control device, the most important difference occurs towards the end of the oscillation cycle, when virtually the entire vortex is pushed out of the orifice and *lifted above* the downstream edge before being convected away. This enhances the mixing further downstream and has, therefore, important consequences for the flow field in the wake of the resonator, which will be the topic of chapter 6.

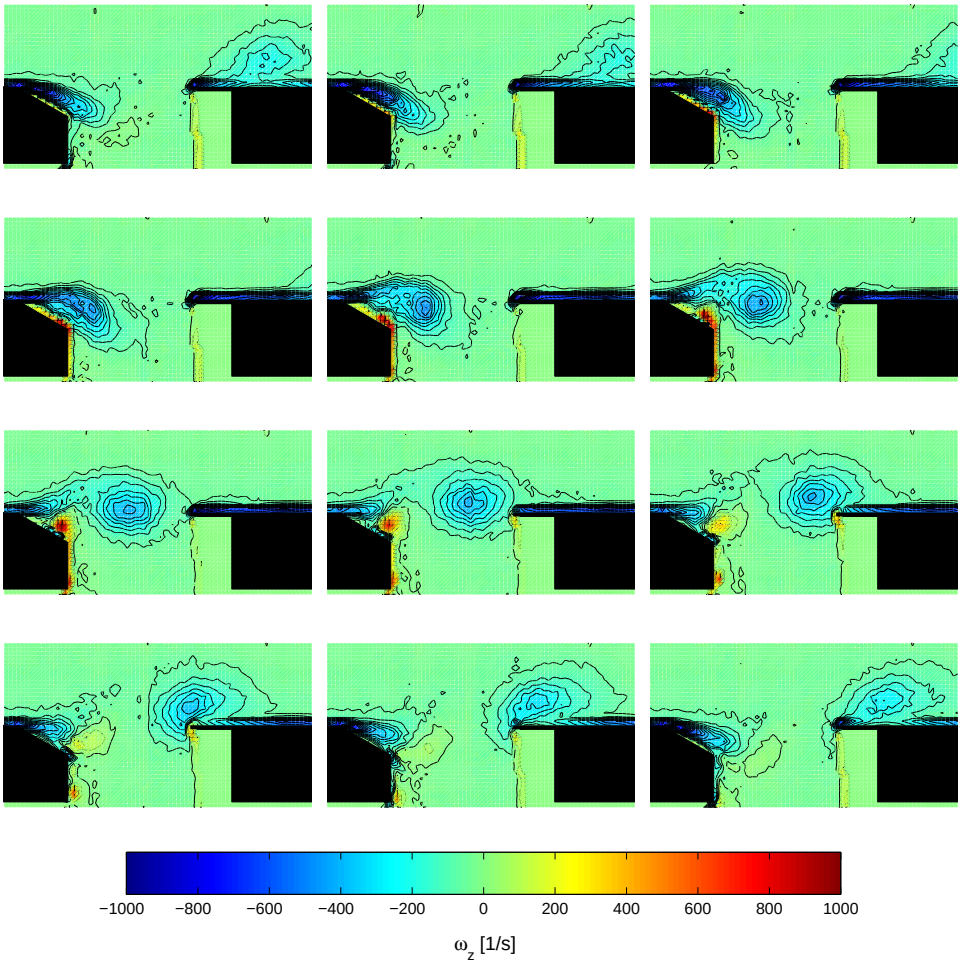

FIGURE 3.33: Phase-averaged LDA measurement in the resonator neck with improved geometry (A30/K5) at different phase angles ($\Delta\varphi = 30°$, color scale and contours correspond to vorticity ω_z and are identical to figure 3.20). $Re_u = 1.5 \times 10^6$, slit width 20 mm, resonance frequency 290 Hz, cavity height 108 mm.

3.2.7 Influence of resonator volume on the flow induction

Besides a variation of the resonance frequency, a change of the cavity volume has implications for the intensity of the induced pressure oscillations and for the Reynolds-number range of their occurrence. This is illustrated in figure 3.34, where the size of the resonator volume has been varied by changing the cavity height l_y between 50 and 370 mm.

For the smallest cavity investigated ($l_y = 50$ mm), Helmholtz resonance occurs at unit Reynolds numbers ranging from 0.85×10^6 to above 1.75×10^6. When the cavity height is increased, this resonance regime becomes narrower, and shifts towards lower Reynolds numbers. Starting at $l_y = 282$ mm, a

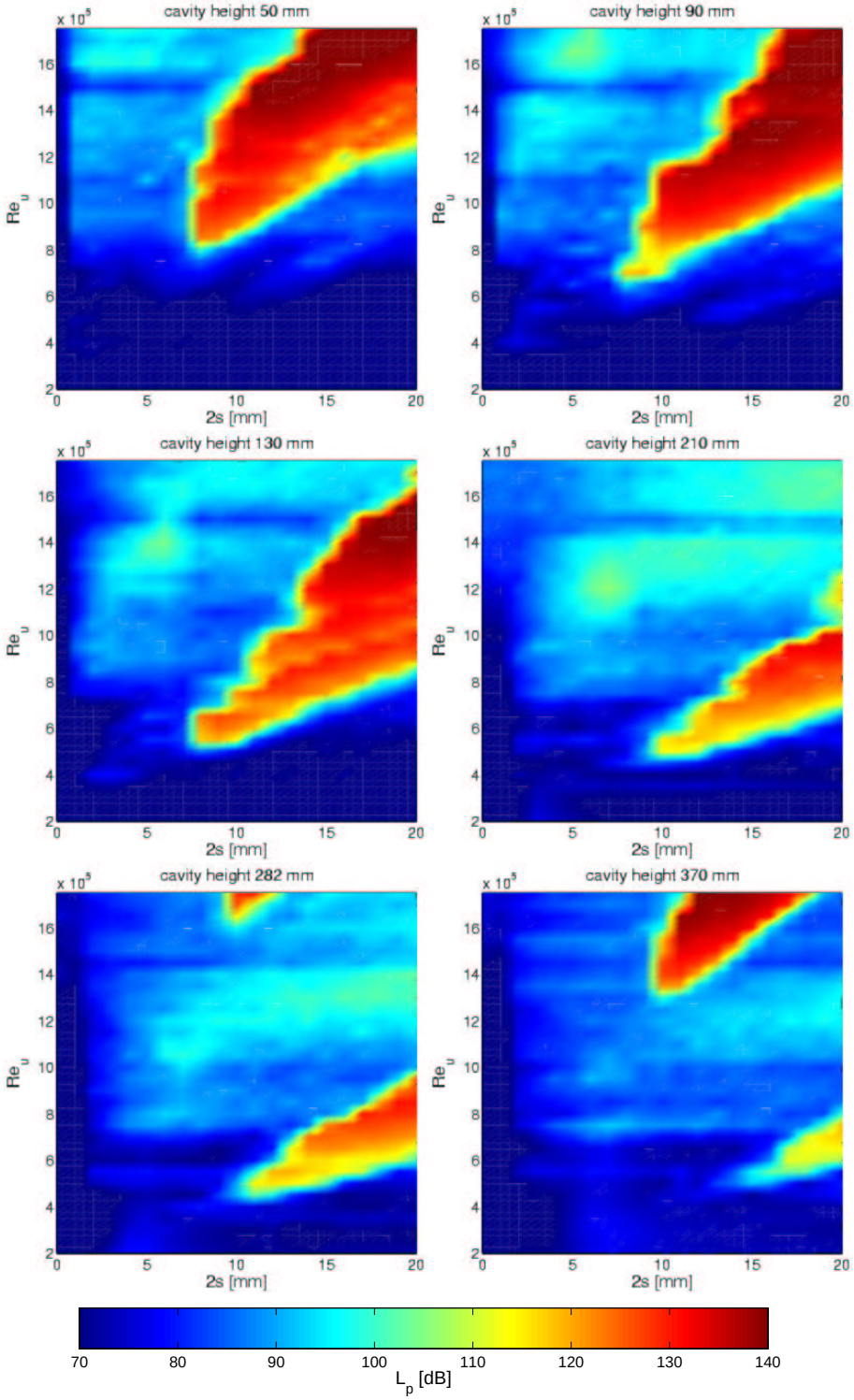

FIGURE 3.34: Sound-pressure level (see color scale) of the resonance peaks depending on Reynolds number and slit width: Cavity height l_y varies from 50 to 370 mm. Neck geometry A30/K5.

separate domain evolves at high Reynolds numbers ($Re_u \geq 1.65 \times 10^6$), in which resonant conditions are present. This second domain is associated with the first vertical cavity mode. While the intensity of the Helmholtz-mode excitation deteriorates when the cavity is enlarged even further, the first higher mode becomes dominant and expands in terms of the Reynolds-number range. The attenuation of the Helmholtz mode appears to be caused by the fact that the pressure is no longer homogeneous throughout the entire cavity as a consequence of its large dimensions. The homogeneity of pressure, however, is an essential characteristic of the Helmholtz mode.

According to Panton (1990), the response level for different modes is a smaller fraction of the free-stream dynamic pressure, the higher the mode. This applies to the two modes observed in the present experiment.

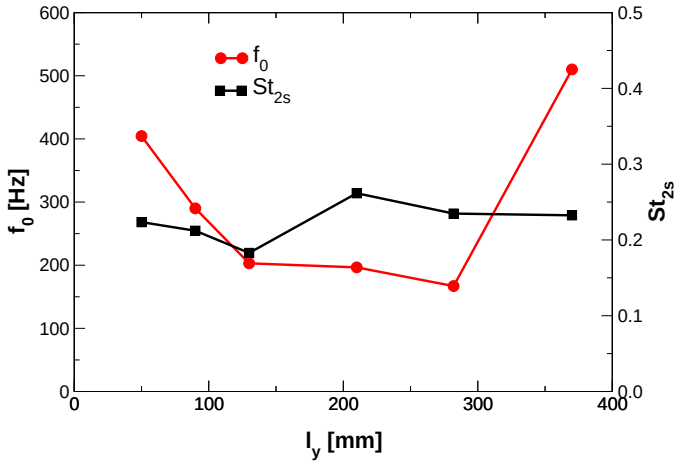

FIGURE 3.35: Dimensional and nondimensional frequencies of the resonance peaks depending on cavity height l_y. Re_u and $2s$ variable, neck geometry A30/K5.

Corresponding to the above cases, figure 3.35 compares the dimensional and nondimensional resonance frequencies depending on the cavity height. Since St_{2s} stays relatively unaffected by the variation of the resonator volume, it can be concluded that the fluid dynamics in the orifice responsible for the excitation remain identical. The trend of f_0, in contrast, reveals the switch of the oscillation mode: Whereas the initial drop in the natural frequency is due to a decreasing Helmholtz resonance frequency as a consequence of an enlarging volume, the sudden rise at high l_y clearly indicates a change in the mode.

3.2.8 Influence of neck length on the flow induction

As another option to vary the Helmholtz resonance frequency, modifications of the neck length l_n were investigated regarding their impact on intensity and conditions of aerodynamic excitation. To this end, resonators with necks

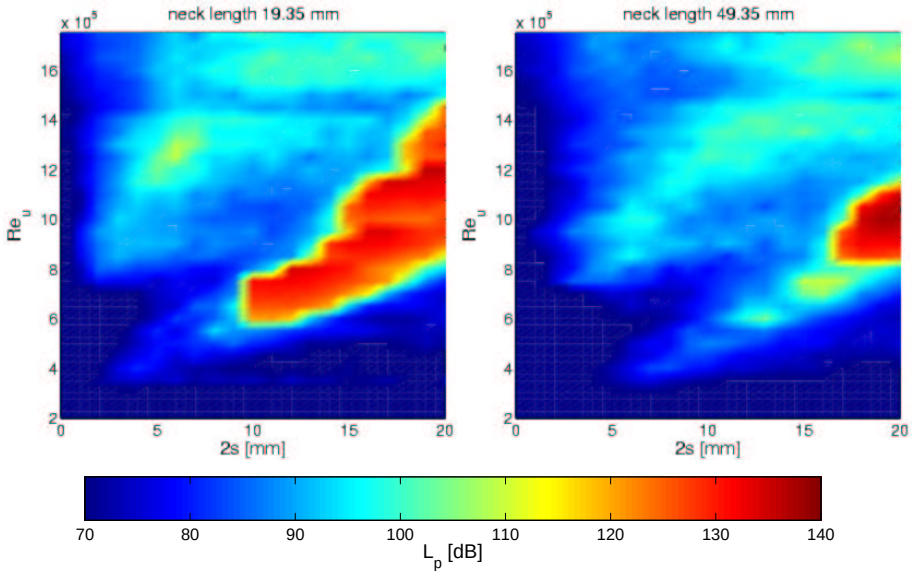

FIGURE 3.36: Sound-pressure level (see color scale) of the resonance peaks depending on Reynolds number and slit width: Neck length l_n varies from 19.35 to 49.35 mm. Neck geometry A30/K5, $l_y = 129.3$ mm.

of different length were manufactured by mounting miscellaneous extension parts to the cavity ceiling, flush with the leading and trailing edges of the slit.

As a consequence of increasing l_n, the resonance frequency was in fact reduced. However, a comparison of a resonator with $l_n = 9.35$ mm (right-hand plot of figure 3.31) to resonators with necks of length 19.35 and 49.35 mm (figure 3.36) revealed adverse concomitant effects on the flow induction: Although the domain where resonances occurred did not shift, its Reynolds-number range became very narrow. While the original configuration ($l_n = 9.35$ mm) showed oscillations induced in a range $0.55 \times 10^6 \leq Re_u \leq 1.70 \times 10^6$, this range was limited to Reynolds numbers between 0.60×10^6 and 1.45×10^6 when the neck length was 19.35 mm, and was reduced to $0.85 \times 10^6 \leq Re_u \leq 1.15 \times 10^6$ for $l_n = 49.35$ mm. Against this background, it is somewhat surprising that the maximum oscillation amplitude remained largely unaffected and reached values around $p_{cav}/p_{dyn} = 110\,\%$ with both latter configurations.

Nevertheless, the limited Reynolds-number range of aerodynamic excitation renders resonators with long necks impractical as control devices. The neck length for all experiments involving resonators of rectangular cross-section was, therefore, chosen as $l_n = 9.35$ mm.

3.2.9 Influence of momentum thickness on the flow induction

To investigate the influence of the momentum thickness δ_2 on the flow induction of resonators, the properties of the approaching boundary layer were altered by tripping it in various ways. Strips of different streamwise extension made of Dymo tape, Velcro tape, and sandpaper were applied as tripping devices (Steinwand, 2002). The corresponding boundary-layer profiles were measured as close as 1.0 mm upstream of the inclined leading-edge piece (A30) of the orifice ($x - x_{LE} = -7.35$ mm), while the resonator was oscillating.

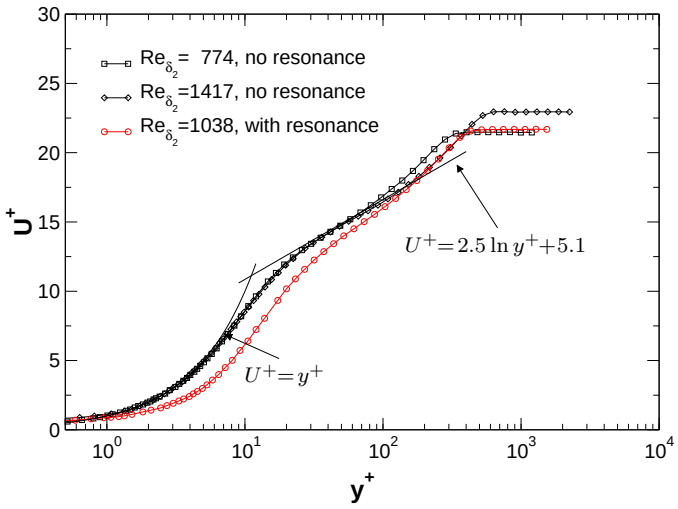

FIGURE 3.37: Influence of resonator oscillations on the mean velocity profile of the boundary layer upstream of the resonator. All boundary layers were tripped by the same device. Cases without resonance: Data taken from appendix A.4. $x - x_{LE} = -26.35$ mm, $2s = 0$ mm. Case with resonance: $x - x_{LE} = -7.35$ mm, $2s = 9$ mm, $l_y = 130$ mm, neck geometry A30/K5.

To isolate the effect of the resonator oscillations from the effect of the different tripping devices, figures 3.37 and 3.38 show a comparison between velocity profiles measured with and without resonance. $U^+ = U/u_\tau$, u'_{rms}/u_τ, and $y^+ = yu_\tau/\nu$ denote the mean and fluctuating streamwise velocity component and the distance normal to the wall in inner-law scaling. All three boundary layers presented were tripped in the same way by two rows of Dymo tape (see section 3.2.2).

When the resonator is not oscillating, the mean velocity data measured upstream of its neck collapse with both linear and logarithmic laws of the wall, and show excellent agreement with data compiled by Fernholz & Finley (1996). Apart from values beyond $y^+ = 100$, a variation of Re_{δ_2} from 774 to 1417 has no effect on the unperturbed profiles. In contrast, the data of the case biased by the resonator oscillations ($Re_{\delta_2} = 1038$) lie well below the inner law throughout the region $0.8 \leq y^+ \leq 120$. Since the Reynolds

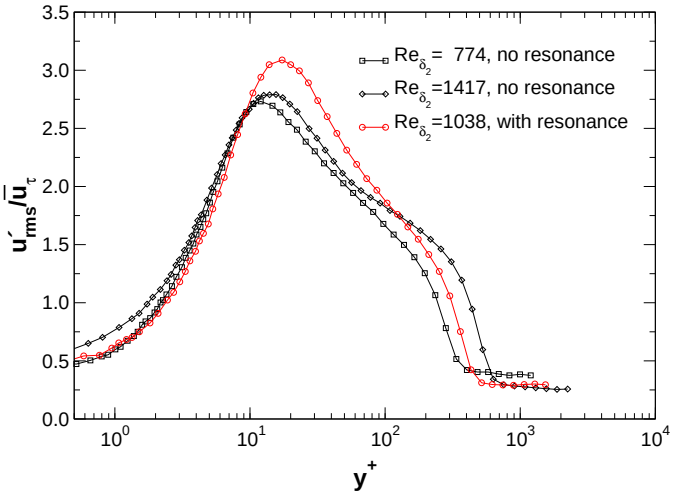

FIGURE 3.38: Influence of resonator oscillations on the profile of u'_{rms} upstream of the resonator. All boundary layers were tripped by the same device. Cases without resonance: Data taken from appendix A.4. $x - x_{LE} = -26.35\,\text{mm}$, $2s = 0\,\text{mm}$. Case with resonance: $x - x_{LE} = -7.35\,\text{mm}$, $2s = 9\,\text{mm}$, $l_y = 130\,\text{mm}$, neck geometry A30/K5.

numbers are comparable, this implies that the deviations must entirely be attributed to the velocity fluctuations induced in the resonator orifice directly downstream.

As for the mean velocity, the agreement of the u'_{rms} profiles associated with the baseline flow conditions to the data available in Fernholz & Finley (1996) is very good. This applies in particular to the maximum of u'_{rms}/u_τ at 2.75 and its location at $y^+ \approx 15$. A minor influence of Re_{δ_2} can be observed for wall distances exceeding $y^+ = 10$ causing u'_{rms}/u_τ to increase slightly with the Reynolds number. In the presence of strong resonator oscillations, however, the profiles differ clearly from the ones discussed before throughout the range $10 \leq y^+ \leq 120$. For instance, the maximum value of u'_{rms}/u_τ is as high as 3.1, in this case.

On the basis of the previous results, the influence of diverse tripping devices on the boundary-layer characteristics can be derived by considering the changes relative to the perturbed velocity profiles at $Re_{\delta_2} = 1038$. An overview of the associated parameters is given in table 3.5. Corresponding profiles of the mean and fluctuating streamwise velocities are presented in figures 3.39 and 3.40, respectively.

These data show that, besides δ_2, other properties of the boundary layer are affected as well by the variation of the tripping device. All profiles of the mean streamwise velocity exhibit a velocity deficit similar to the one observed before. This behavior is most pronounced for $\delta_2/2s = 0.176$, where the amplitude of the resonator oscillations has a maximum (see figure 3.41), and becomes less distinctive with increasing momentum thickness when the

Re_{δ_2} [−]	$\delta_2/2s$ [−]	δ_{99} [mm]	δ_1 [mm]	δ_2 [mm]	H_{12} [−]	c_f [−]	p_{cav}/p_{dyn} [−]
1038	0.176	13.92	2.45	1.58	1.55	4.25×10^{-3}	0.94
1107	0.188	14.82	2.57	1.69	1.52	4.20×10^{-3}	0.84
1235	0.209	15.81	2.88	1.88	1.53	3.93×10^{-3}	0.78
1299	0.219	19.09	2.88	1.97	1.46	4.06×10^{-3}	0.77
1557	0.265	20.89	3.46	2.39	1.45	3.80×10^{-3}	0.64
1936	0.330	22.66	4.50	2.97	1.52	3.34×10^{-3}	0.43
2098	0.359	23.46	5.14	3.23	1.59	3.00×10^{-3}	0.08

TABLE 3.5: Properties of the boundary layer upstream of the oscillating resonator ($x - x_{LE} = -7.35\,\text{mm}$) depending on the tripping device. $Re_u = 6.5 \times 10^5$, $2s = 9\,\text{mm}$, $l_y = 130\,\text{mm}$, neck geometry A30/K5. Data refer to figures 3.37 to 3.41.

induced sound pressure deteriorates. From the above discussion it is clear that the discrepancies in the velocity profile are not a consequence of variations in Re_{δ_2} (also see figure A.4), but that they are caused by the changing amplitude of the oscillations in the nearby orifice of the flow-induced resonator.

For $\delta_2/2s \geq 0.330$, additional differences occur in the region of the buffer layer and the logarithmic law, which can be understood in conjunction with the distributions of the fluctuating velocity component (figure 3.40). In these cases, u'_{rms} exhibits large deviations in the range $10 \leq y^+ \leq 800$ including the decrease of the peak value of the fluctuations at $y^+ \approx 16$, and the formation of a second maximum at $y^+ \approx 200$. Again, a comparison with

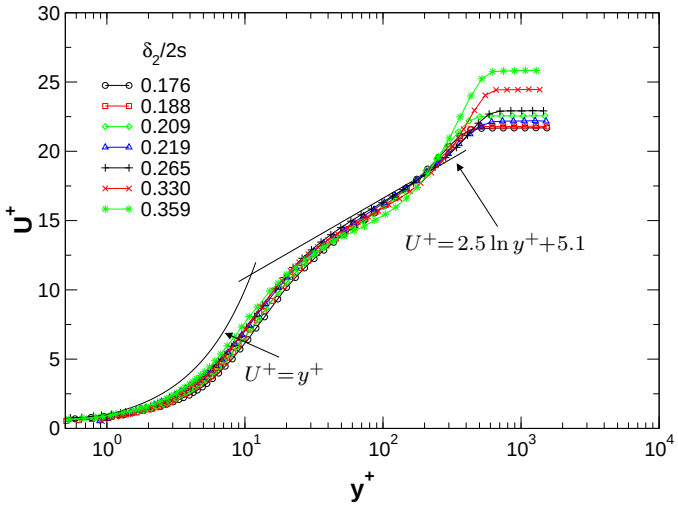

FIGURE 3.39: Mean velocity profiles of the boundary layer upstream of the oscillating resonator ($x - x_{LE} = -7.35\,\text{mm}$) depending on the tripping device. $Re_u = 6.5 \times 10^5$, $2s = 9\,\text{mm}$, $l_y = 130\,\text{mm}$, neck geometry A30/K5.

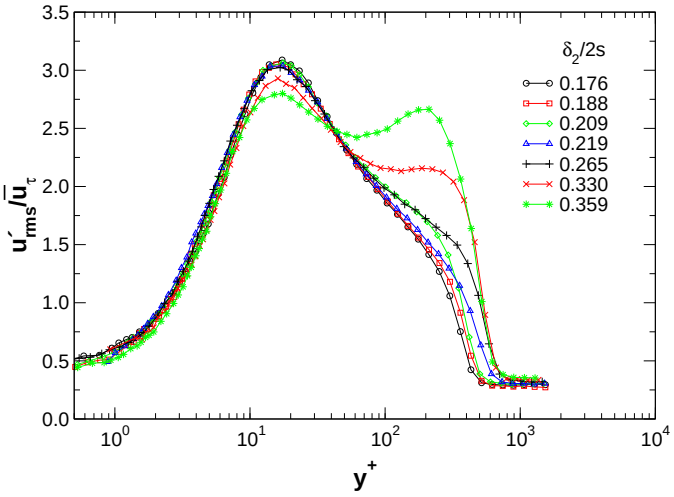

FIGURE 3.40: Profiles of u'_{rms} upstream of the oscillating resonator ($x-x_{LE} = -7.35\,\mathrm{mm}$) depending on the tripping device. $Re_u = 6.5 \times 10^5$, $2s = 9\,\mathrm{mm}$, $l_y = 130\,\mathrm{mm}$, neck geometry A30/K5.

the unperturbed data (see figures 3.38 and A.5) demonstrates that this is not a Re_{δ_2}-effect. The agreement with data presented in Fernholz & Finley (1996) becomes better, the smaller $\delta_2/2s$. This indicates that the boundary layers associated with large momentum thicknesses did not reach a state of equilibrium yet, after being tripped. Most likely, this was a consequence of the short streamwise distance to the trailing edge of the tripping devices used in these cases. It can be hypothesized that a small separation region formed downstream of the trips, because the u'_{rms} data exhibit characteristics of typical relaxation profiles (see, for example, Kalter & Fernholz, 2001). To substantiate this, figure 3.41 shows a slightly raised level in the form parameter H_{12} with values in the range between 1.45 and 1.59, as opposed to typical values found in the literature from 1.41 to 1.47 at these Reynolds numbers (Fernholz & Finley, 1996).

In conclusion, it can be inferred that at low $\delta_2/2s$, the velocity profiles are biased by the presence of strong resonance, whereas at high momentum thickness, the tripping devices alter the boundary-layer characteristics.

In spite of this note of caution, the impact of the momentum thickness on the amplitude of the flow-induced oscillations, as seen in figure 3.41, appears very clear such that the aforementioned differences do not seem to affect the result significantly. The aerodynamically excited sound pressure decays rapidly with increasing δ_2. This will become important in the context of choosing an adequate streamwise resonator location upstream of a separation region such that the induced oscillations are strong enough to manipulate the flow.

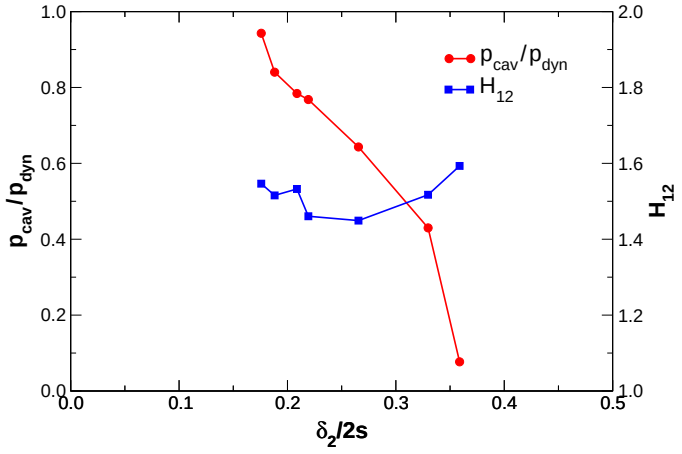

FIGURE 3.41: Influence of the nondimensional boundary-layer momentum-thickness $\delta_2/2s$ on the oscillation amplitude p_{cav}/p_{dyn} of flow-induced resonance. As an indication for the state of the boundary layer, the corresponding form parameter H_{12} is shown with the data. $Re_u = 6.5 \times 10^5$, $2s = 9\,\text{mm}$, $l_y = 130\,\text{mm}$, neck geometry A30/K5.

3.2.10 Hysteresis of the flow induction

It is worth noting that hysteresis effects of the flow-induction of resonators occur when the slit width, the cavity volume, or the unit Reynolds number are varied. This is exemplified in figure 3.42 for the most significant case by measurements of the oscillation amplitude when traversing the slit width in the direction from a closed to an open state and vice versa.

The apparent hysteresis loop is particularly pronounced in the vicinity

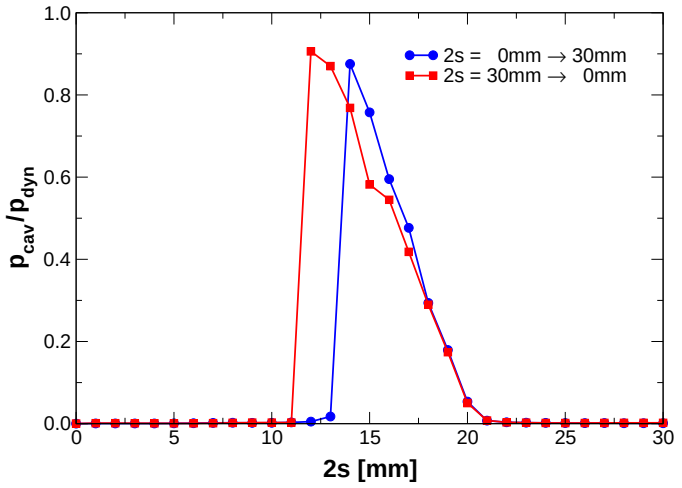

FIGURE 3.42: Hysteresis effect in the oscillation amplitude p_{cav}/p_{dyn} of a flow-induced resonator due to variation of the slit width $2s$. $Re_u = 7.0 \times 10^5$, $l_y = 129.6\,\text{mm}$, neck geometry A30*/K5*.

of the peak resonance. Whereas the relative sound pressure amounts to $p_{cav}/p_{dyn} = 88\,\%$ in the process of opening the slit, the oscillation amplitude rises as high as 91 % when traversing the slit towards a closed state. In addition, the location of the maximum with respect to the associated slit width changes: In the first case, the optimum slit width is 14 mm, while in the second case it is 12 mm.

This aspect will become relevant in the context of the closed-loop control-scheme presented in chapter 7.

3.2.11 Concluding remarks on single resonators

This chapter was intended to lay the basis for a fundamental understanding of the important parameters governing the flow-induction process of acoustic resonators. Therefore, it seems adequate to sum up some key results at this point:

- The natural frequencies of the purely acoustic response of a resonator coincide approximately with the resonant frequencies excited by a grazing flow.
- The natural frequencies of the acoustic response can be computed both analytically and numerically with equally good accuracy.
- The shape of the resonator neck plays an important role in determining the intensity of the flow induction.
- The neck geometry was optimized with respect to p_{cav}/p_{dyn} yielding values as high as 108 % with configuration A30*/K5*.
- The amplitudes of the induced pressure oscillations increase with decreasing boundary-layer momentum-thickness.
- For a specific Reynolds number, the maximum relative sound pressure can be achieved by a variation of cavity height l_y and slit width $2s$.
- A hysteresis loop regarding the oscillation amplitude occurs when geometric parameters or the Reynolds number are varied.

List of symbols

A	cross-sectional area of the resonator cavity
A_1	constant amplitude of a wave in x-direction
A_2	constant amplitude of a wave in x-direction
b	radius of a circular pipe
B_1	constant amplitude of a wave in y-direction
B_2	constant amplitude of a wave in y-direction

c	speed of sound ($\approx 343\,\mathrm{m/s}$ in air at room temperature)
c_f	skin-friction coefficient
c_p	pressure coefficient ($= \Delta p/(\frac{1}{2}\rho U_\infty^2)$)
C	Euler constant ($= 0.5772\cdots$)
C_1	constant amplitude of a wave in z-direction
C_2	constant amplitude of a wave in z-direction
e	deviation between discretized function and its curve fit
f	frequency
f_0	resonance frequency
f_i	discrete values of fit function
$\mathcal{F}$	arbitrary function
g	real variable
h	Helmholtz number
h_{LE}	height of fence upstream of the leading edge of the resonator neck
h_{TE}	wall distance of horizontal blade installed at the trailing edge of the resonator neck
H	acoustic transfer function
H_{12}	velocity-profile form-parameter
$H_m^{(1)}(g)$	Bessel function of the third kind of order m (Hankel function)
i	index denoting points of discretized functions
i	imaginary unit ($= \sqrt{-1}$)
$j'_{m,n}$	$(n+1)$st positive zero of $J'_m(g)$
$J_m(g)$	Bessel function of the first kind of order m
$J'_m(g)$	derivative of the Bessel function with respect to g
k_r	wave number of the acoustic pressure in radial direction
k_x	wave number of the acoustic pressure in x-direction
k_y	wave number of the acoustic pressure in y-direction
k_z	wave number of the acoustic pressure in spanwise direction
K	Rayleigh conductivity
L	fit coefficient
L_p	sound-pressure level
l_n	neck length of a resonator
l_x	width of the resonator cavity
l_y	height of the resonator cavity
l_z	span of the resonator cavity
m	number of pressure nodal lines in radial direction, equals order of Bessel function
M	fit coefficient
n	number of pressure nodal lines in circumferential direction
N	fit coefficient
p_1	sound pressure inside the resonator cavity
$\hat{p}_1$	amplitude of sound pressure p_1
p_2	sound pressure outside the resonator neck

$\hat{p}_2$	amplitude of sound pressure p_2
p_{cav}	rms sound-pressure within the resonator cavity
p_{dyn}	free-stream dynamic pressure
P_w	nondimensional wavelet power
q_x	amount of pressure nodes in x-direction
q_y	amount of pressure nodes in y-direction
q_z	amount of nodes of the spanwise pressure distribution
r	radial coordinate
R_{LE}	radius of curvature of the leading edge of the resonator neck
Re_{2s}	Reynolds number based on streamwise length of resonator neck
Re_{2s^*}	Reynolds number based on equivalent slit width $2s^*$
Re_u	Reynolds number based on unit length (1 m)
Re_{δ_2}	Reynolds number based on boundary-layer momentum-thickness
s	half-slit width of the resonator neck
s^*	equivalent half-slit width of the resonator neck
St_{2s}	Strouhal number based on streamwise length of resonator neck
St_{2s^*}	Strouhal number based on equivalent slit width $2s^*$
t	time
t_i	discrete values in time
T	cycle duration
T_w	wavelet scale
u'_{rms}	rms-value of the fluctuating streamwise velocity
u_τ	skin-friction velocity
U	time-averaged streamwise velocity component
U_∞	free-stream velocity
U^+	streamwise velocity component in inner-law scaling
v	velocity component in y-direction
w_i	discrete values of pressure-time signal
W	width of the measurement section
x	streamwise coordinate originating at entrance of test section
x_{LE}	streamwise location of the leading edge of the resonator neck
y	wall-normal coordinate originating at the wall
y^+	distance from wall in inner-law scaling
$Y_m(g)$	Bessel function of the second kind of order m (Weber function)
z	spanwise coordinate originating at centerline of test section or resonator
Z_s	specific acoustic impedance of the slit
γ_{LE}	inclination angle of the leading edge of the resonator neck
δ_1	displacement thickness of the boundary layer
δ_2	momentum thickness of the boundary layer
δ_{99}	99 %-thickness of the boundary layer
Δ	variation of a quantity
ε	exponential decay rate

ζ	abbreviation for $s\left(\frac{\omega^2}{c^2}-k_z^2\right)^{1/2}$
η	nondimensional time
ϑ	circumferential coordinate
λ	wavelength of sound
ν	kinematic viscosity of the fluid
ρ	mass density of fluid
ρ_0	mean mass density of fluid
φ	phase
ψ	wavelet function
ω	angular frequency
ω_0	angular resonance frequency
ω_w	nondimensional frequency of a Morlet wavelet
ω_z	z-component of the vorticity vector
$\overline{\quad}$	time-averaged value of a quantity
$\langle\ \rangle$	phase-averaged value of a quantity

Chapter 4

Systems of adjacent acoustic resonators

This chapter is devoted to the oscillatory behavior of systems of adjacent acoustic resonators, their induction by a grazing flow, and their influence on the radiated sound pressure and the flow topology downstream.

To describe the natural frequencies and modes of resonator systems, a theoretical model is derived, which neglects effects due to a cross-flow. The results are then compared to experimental data that were obtained with flow-induced resonators. Subsequently, the domain, in which the resonators can be set oscillating by the flow, is discussed with respect to Reynolds number, slit width, and mode. The last two sections deal with the impact of out-of-phase oscillations of the flow-induced resonator systems on the radiated sound pressure and on the wall-shear stress in their wake.

4.1 Acoustic response of resonator systems

In the first section of this chapter, a mechanical analog for systems of adjacent acoustic resonators without cross-flow will be derived, their equations of motion will be set up, and the corresponding natural frequencies and modes will be calculated. The frequencies and modes considered in this chapter have to be clearly distinguished from those of single acoustic resonators discussed in section 3.1.1. The following investigation is confined to situations in which each resonator oscillates in its Helmholtz mode. Depending on the phase relation between interacting resonators, different modes of the resonator system can occur. The equations of motion characterizing this type of system are coupled differential equations, and will be derived in sections 4.1.3 to 4.1.5. The concept of modal analysis is introduced to decouple and solve such equations, and then mechanical analogs for two types of systems are discussed.

4.1.1 Modal analysis of oscillatory systems

An oscillatory system is fully described by its equations of motion. For a linear, undamped mechanical system of n degrees of freedom, they can be written in the form

$$\underline{\underline{m}}\,\underline{\ddot{y}}(t) + \underline{\underline{k}}\,\underline{y}(t) = \underline{0} \tag{4.1}$$

where $\underline{y}(t)$ is the displacement vector, and $\underline{\underline{m}}$ and $\underline{\underline{k}}$ are the mass and stiffness matrices, respectively. Both are symmetric, but usually not diagonal. A non-diagonal mass matrix is a consequence of inertial coupling in the system, whereas a non-diagonal stiffness matrix results from coupling through the elastically restoring forces. The differential equations for $\underline{y}(t)$ can be decoupled by an appropriate linear coordinate transformation, which yields a system of independent differential equations of motion. This procedure is referred to as modal analysis (Meirovitch, 1986).

For this purpose, the displacement $\underline{y}(t)$ is separated into a space and a time component $\underline{u}$ and $f(t)$, respectively, where $\underline{u}$ is assumed to be a constant amplitude and $f(t)$ a time-harmonic solution of frequency ω:

$$\begin{aligned} \underline{y}(t) &= \underline{u} f(t) \\ &= \underline{u} \mathrm{e}^{\mathrm{i}\omega t} \end{aligned} \tag{4.2}$$

Inserting this expression into equation (4.1) leads to a generalized eigenvalue problem. In the physical domain, the mathematical eigenvalues correspond to natural frequencies of the free vibration:

$$\Big(\underbrace{\underline{\underline{k}} - \omega^2 \underline{\underline{m}}}_{\underline{\underline{a}}} \Big) \underline{u} = \underline{0} \tag{4.3}$$

For $\underline{u}$ to give non-trivial solutions, the determinant of $\underline{\underline{a}}$ must be zero:

$$\det(\underline{\underline{a}}) = \det(\underline{\underline{k}} - \omega^2 \underline{\underline{m}}) = 0 \tag{4.4}$$

The evaluation of the determinant yields a polynomial of order n in ω^2. It has $2n$ zeros, which reduce to n solutions for ω, since the resonance frequencies are positive quantities and, therefore, only positive roots of ω^2 are considered.

In order to compute the mode shapes, which allow for the description of any possible motion of the system, the eigenvectors have to be determined. The eigenvectors $\underline{u}_i$ $(i = 1, \ldots, n)$ corresponding to the natural frequencies ω_i are obtained from solving the following n systems of equations:

$$\left(\underline{\underline{k}} - \omega_i^2 \underline{\underline{m}} \right) \underline{u}_i = \underline{0} \qquad i = 1, \ldots, n \tag{4.5}$$

However, the resulting $\underline{u}_i$ are not unique, and only the ratios of their components are fixed. The eigenvectors contain a constant factor α, which can

be different for every single vector. It is common to choose α such that the respective first component equals unity.

On the basis of the eigenvectors, the general solution for a general motion of the system can be written as the result of a superposition of the different modes of vibration:

$$\underline{y}(t) = \sum_{i=1}^{n} A_i \cos(\omega_i t - \varphi_i)\underline{u}_i \tag{4.6}$$

The constants A_i and φ_i denote the amplitude and phase of the mode i, respectively. These $2n$ parameters have to be determined from the initial conditions.

4.1.2 Mechanical analogy of a Helmholtz resonator

In a mechanical analogy, a single Helmholtz resonator is often modeled as an undamped spring-mass system with one degree of freedom (e.g. Kinsler & Frey, 1962, chap. 8). The fluid in the orifice of the resonator thereby acts as the oscillating mass m, while the compressible fluid in the resonator cavity features a spring stiffness k (figure 4.1). When only small deformations are considered, nonlinear effects can be neglected. The resonance frequency ω of such an oscillator is

$$\omega = \sqrt{\frac{k}{m}}. \tag{4.7}$$

For a Helmholtz resonator, the mass of fluid in the orifice is $m = \rho l_n S$, where ρ is the fluid density, l_n the neck length, and S the cross-sectional area of the orifice. The spring stiffness of the fluid in the cavity underneath is $k = \rho c^2 S^2 / V$. Herein, c is the speed of sound, and V the volume of the cavity. Inserted into equation (4.7), the well-known expression for the natural frequency of a resonator derived by Rayleigh (1896) is obtained (see equation (1.5)):

$$\omega = c\sqrt{\frac{S}{V l_n}}. \tag{4.8}$$

Note that neither the derivation of Helmholtz (1860) nor the one of Rayleigh (1896) made use of the mechanical analogy (see section 1.3.1).

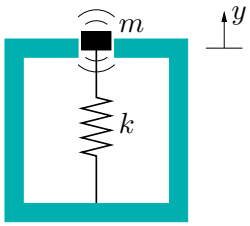

FIGURE 4.1: Mechanical analog of a single Helmholtz resonator. The mass of fluid in the orifice is depicted in a non-equilibrium position.

4.1.3 Two adjacent Helmholtz resonators

On the basis of the mechanical analogy for a single Helmholtz resonator, a system of two adjacent resonators can be represented in terms of two coupled oscillators with one degree of freedom each. The coupling of both masses of fluid in the orifices is specified by the spring stiffness k_3 (figure 4.2). As in the case of just one degree of freedom, the oscillations are assumed to be linear and undamped.

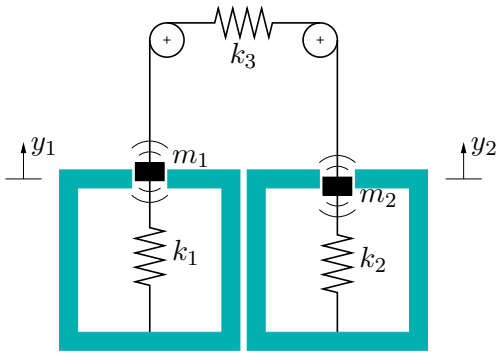

FIGURE 4.2: Mechanical analog of two coupled Helmholtz resonators. The masses of fluid in the respective orifices are depicted in non-equilibrium positions.

Considering the associated free-body diagram and applying Newton's second law, the following differential equations of motion are derived for the system with two degrees of freedom described above (e.g. Meirovitch, 1986):

$$m_1\ddot{y}_1(t) + (k_1 + k_3)y_1(t) + k_3y_2(t) = 0 \tag{4.9}$$

$$m_2\ddot{y}_2(t) + k_3y_1(t) + (k_3 + k_2)y_2(t) = 0 \tag{4.10}$$

Both resonators are supposed to have identical geometric dimensions such that their symmetry can be exploited by substituting

$$m_1 = m_2 \qquad k_1 = k_2. \tag{4.11}$$

As a result, both natural frequencies of the system are obtained by performing a modal analysis as discussed in section 4.1.1:

$$\omega_1 = \sqrt{\frac{k_1}{m_1}} \tag{4.12}$$

$$\omega_2 = \sqrt{\frac{k_1 + 2k_3}{m_1}}. \tag{4.13}$$

It is interesting to note that ω_1 is identical to the Helmholtz frequency of a single resonator. Since it is rather difficult to give an accurate estimate for the spring stiffness k_3, a specific value of ω_2 cannot easily be predicted. Obviously, however, the frequency ω_2 must be greater than ω_1.

To characterize the motion of the system, the natural modes are readily determined by computing the eigenvectors $\underline{u}_i$ $(i = 1, 2)$. Each of them is associated with the corresponding natural frequency ω_i:

$$\underline{u}_1 = [1, -1] \tag{4.14}$$
$$\underline{u}_2 = [1, 1] \tag{4.15}$$

In the fundamental mode represented by $\underline{u}_1$, both resonators oscillate with equal amplitude at the Helmholtz frequency ω_1, but diametrically *out of phase*. In contrast, when oscillating at the frequency ω_2 in the higher mode denoted by $\underline{u}_2$, the motions in both resonators are *in phase*. Again, they have equal amplitude. Both modes are illustrated in figure 4.3.

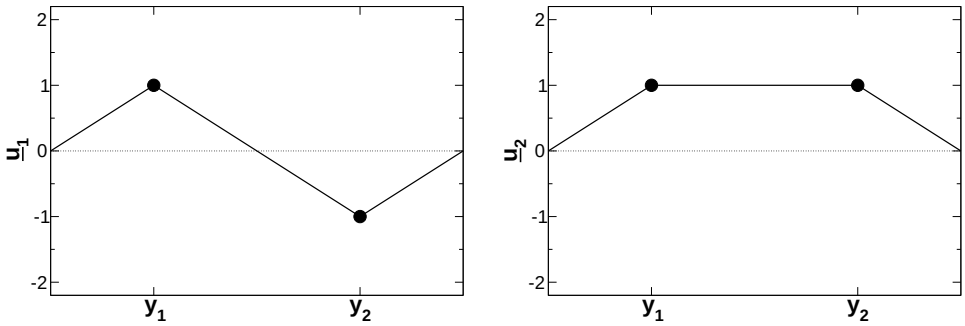

FIGURE 4.3: Synchronous amplitudes $\underline{u}_1$ and $\underline{u}_2$ of both modes when oscillating with frequencies ω_1 and ω_2, respectively. y_1 and y_2 designate the resonators.

4.1.4 Three adjacent Helmholtz resonators

The model representing three adjacent Helmholtz resonators is set up in analogy to the previous case. It comprises three coupled oscillators with one degree of freedom each. As a significant difference to the system with two degrees of freedom, there is not only an elastic coupling to the respective adjacent resonator, but also a coupling between both external ones, since all resonators interact with each other. The different ways of coupling of the fluid masses in the orifices are described by the three spring constants k_4, k_5, and k_6 (figure 4.4). All other assumptions made previously still apply.

For the three-degree-of-freedom system, the equations of motion are derived in the same way as before yielding three coupled differential equations:

$$m_1\ddot{y}_1(t) + (k_1 + k_4 + k_6)y_1(t) + k_4y_2(t) + k_6y_3(t) = 0 \tag{4.16}$$
$$m_2\ddot{y}_2(t) + k_4y_1(t) + (k_2 + k_4 + k_5)y_2(t) + k_5y_3(t) = 0 \tag{4.17}$$
$$m_3\ddot{y}_3(t) + k_6y_1(t) + k_5y_2(t) + (k_3 + k_5 + k_6)y_3(t) = 0 \tag{4.18}$$

By means of modal analysis (see section 4.1.1), the system of equations is

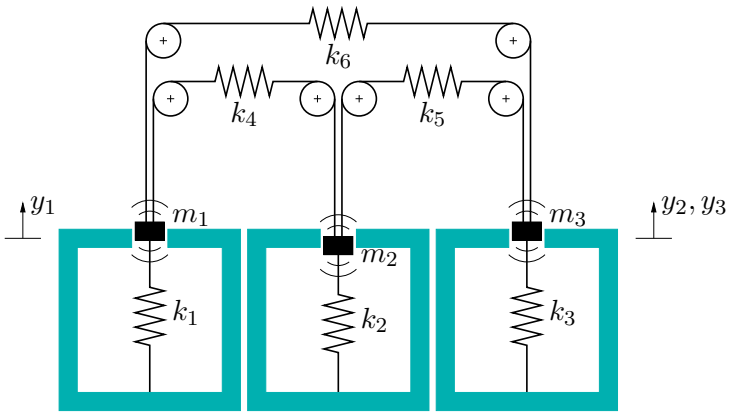

FIGURE 4.4: Mechanical analog of three coupled Helmholtz resonators. The masses of fluid in the respective orifices are depicted in non-equilibrium positions.

decoupled and solved for the natural frequencies ω_i $(i = 1, \ldots, 3)$. For simplification, it is assumed again that all resonators have identical dimensions:

$$\omega_1 = \sqrt{\frac{k_1 + k_4}{m_1}} \tag{4.19}$$

$$\omega_2 = \sqrt{\frac{k_6 + k_1 + \frac{3}{2}k_4 - \frac{1}{2}\sqrt{4k_6^2 - 4k_4k_6 + 9k_4^2}}{m_1}} \tag{4.20}$$

$$\omega_3 = \sqrt{\frac{k_6 + k_1 + \frac{3}{2}k_4 + \frac{1}{2}\sqrt{4k_6^2 - 4k_4k_6 + 9k_4^2}}{m_1}} \tag{4.21}$$

After computing the eigenvectors and choosing the constant α such that the first component of each vector equals unity, the following representation of the occurring modes is obtained:

$$\underline{u}_1 = [1, 0, -1] \tag{4.22}$$

$$\underline{u}_2 = \left[1, \frac{1}{2}\frac{k_4 - 2k_6 - \sqrt{4k_6^2 - 4k_4k_6 + 9k_4^2}}{k_4}, 1\right] \tag{4.23}$$

$$\underline{u}_3 = \left[1, \frac{1}{2}\frac{k_4 - 2k_6 + \sqrt{4k_6^2 - 4k_4k_6 + 9k_4^2}}{k_4}, 1\right] \tag{4.24}$$

To visualize the second and third mode, an approximate value for the spring stiffness k_6 has to be estimated. Presumably, according to the mechanical model in figure 4.4, k_6 is of the same order of magnitude as the spring stiffness k_4 or k_5, which describe the coupling of two directly adjacent resonators.

Thus, setting $k_6 = k_4$ in equations (4.23) and (4.24), the eigenvectors have the form:

$$\underline{u}_1(k_6 = k_4) = [1, 0, -1] \tag{4.25}$$
$$\underline{u}_2(k_6 = k_4) = [1, -2, 1] \tag{4.26}$$
$$\underline{u}_3(k_6 = k_4) = [1, 1, 1] \tag{4.27}$$

The resulting mode shapes based on these values are shown in figure 4.5. In the fundamental mode associated with $\underline{u}_1$, both outer resonators oscillate *in anti-phase* at equal amplitude with the frequency ω_1, while the center resonator stays at rest. In the next higher mode corresponding to the eigenvector $\underline{u}_2$, all resonators oscillate with the frequency ω_2. Thereby, both outer resonators oscillate *in phase* at equal amplitude. The air in the inner one, however, moves *in anti-phase* to them, and is displaced approximately twice as much. The exact value of the amplitude ratio of the inner resonator with respect to the outer ones depends on the actual value of the spring stiffness k_6. Finally, in the highest mode represented by $\underline{u}_3$, all three resonators oscillate *in phase* with frequency ω_3, and exhibit identical amplitudes. Again, the displacement of the center resonator may vary with k_6.

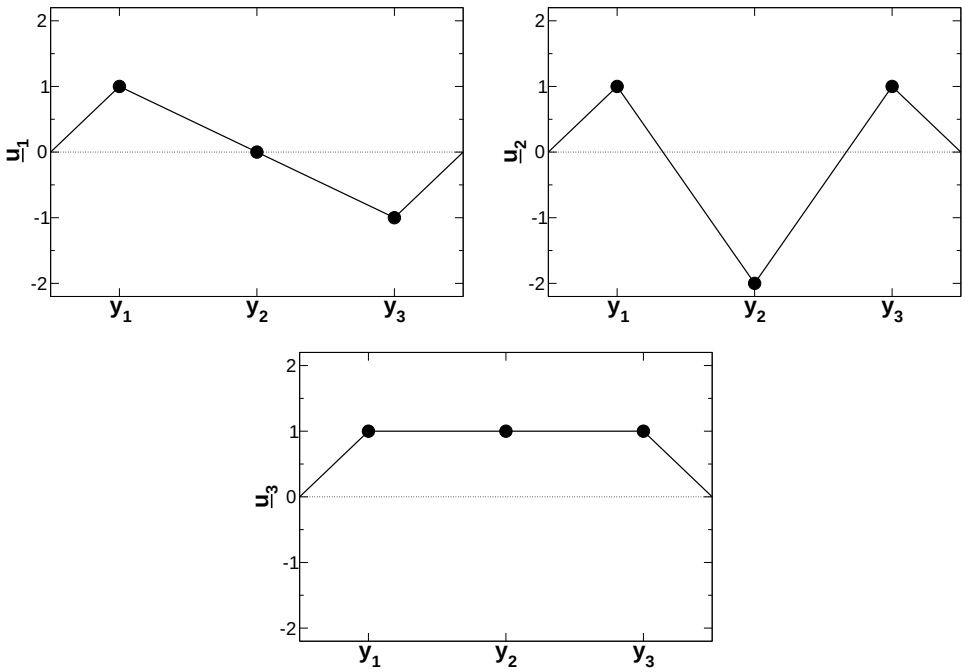

FIGURE 4.5: Synchronous amplitudes $\underline{u}_i$ of the modes when oscillating with frequencies ω_i $(i = 1, \ldots, 3)$. The resonators are designated by y_i.

4.1.5 General systems of adjacent Helmholtz resonators

Much like in the previous sections, the mechanical analog can easily be extended to describe systems of higher numbers of adjacent resonators. For a system of n resonators, the elastic coupling between them is represented by $n(n-1)/2$ spring elements. Although the associated equations of motion can be set up, the resulting coupled differential equations cannot be solved in a closed form by analytical means, if n exceeds four. In these cases, a solution has to be obtained numerically. In addition, a corresponding number of assumptions for the respective values of the spring stiffness has to be made.

4.2 Response of resonator systems to aerodynamic excitation

Results of the aerodynamic excitation of single resonators were presented in section 3.2. In this context, the parameters affecting oscillation amplitude and frequency were discussed extensively. The scope of the present section is, therefore, limited to effects that arise from the coupling between the resonators of a system. Interest will especially focus on the phase difference between the oscillations in the individual cavities. On this basis, the pressure fluctuations excited by the cross-flow can be attributed to the modes computed in section 4.1. Since the calculations were performed for two and three adjacent resonators, these cases will continue to serve as examples.

4.2.1 Experimental set-up

To investigate aerodynamically excited systems of resonators, the experimental set-up described in section 3.2.2 was slightly modified: The resonator cavity was divided into adjacent resonators of identical dimensions by inserting various numbers of rigid walls (see section 2.1.1). As a consequence, the cavity height was fixed at $l_y = 125\,\mathrm{mm}$, while slit width and neck geometry could be changed as before. Throughout the experiments presented here, only the neck configuration A30/K5 was used. Each cavity was equipped with a microphone probe to monitor the respective sound pressure and phase.

4.2.2 Two adjacent Helmholtz resonators

The results of microphone measurements in the cavity of two flow-induced adjacent resonators are illustrated in figure 4.6 in terms of resonance frequency, amplitude, and phase difference between both resonators. Although this graph represents only one sample case, it characterizes well the typical behavior of such systems.

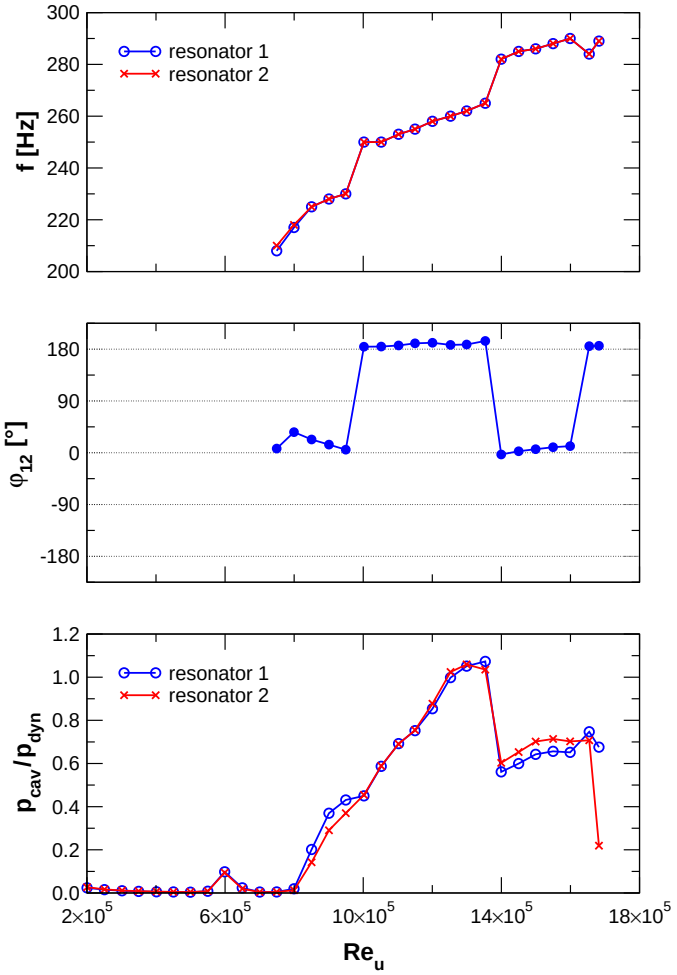

FIGURE 4.6: Experimental results of two adjacent Helmholtz resonators: measured resonance frequencies f, phase difference φ_{12} between both resonators, and ratio of induced sound pressure p_{cav} to dynamic pressure of the free-stream p_{dyn}. $2s = 18\,\mathrm{mm}$, $l_y = 125\,\mathrm{mm}$, neck geometry A30/K5.

Resonance occurred at Reynolds numbers starting from $Re_u = 7.5 \times 10^5$ and persisted until the measurement was limited by the maximum speed of the wind tunnel at $Re_u = 16.8 \times 10^5$. Regarding the phase difference φ_{12} between the oscillations in both resonator cavities, four domains with respect to the Reynolds number can be distinguished:

- A domain of *in-phase* oscillations occurred at Reynolds numbers between $Re_u = 7.5 \times 10^5$ and 9.5×10^5. In this range, only moderate resonance was excited, as the relative sound pressure did not exceed a value of $p_{cav}/p_{dyn} = 43\,\%$, after starting from $0.5\,\%$. It can be speculated that this amplitude did not provide a strong enough elastic coupling between both resonators to trigger the anti-phase oscillation associated

with the first mode (see equation (4.14)). Instead, the pressure in both resonators seemed to fluctuate independently without noticeable interaction. Another indication for this uncoupled behavior was the slight difference between the resonance frequencies at low Re_u as well as the differing sound pressures. A similar response could also be observed at other slit widths when $p_{cav}/p_{dyn} \leq 45\,\%$.

- At Reynolds numbers between $Re_u = 10.0 \times 10^5$ and 13.5×10^5, both resonators oscillated *in anti-phase*. This case corresponded to the fundamental mode $\underline{u}_1$ computed in section 4.1.3 (equation (4.14)). Depending on Re_u, the resonance frequency f_1 lay between 250 and 265 Hz. An important result regarding the application of the resonator system as flow-control device is that with $p_{cav}/p_{dyn} = 107\,\%$, the highest relative sound pressure was produced in this mode shape.

- Both resonators oscillated *in phase* in the subsequent Reynolds-number range between $Re_u = 14.0 \times 10^5$ and 16.0×10^5. This situation was related to the higher mode $\underline{u}_2$ computed in section 4.1.3 (equation (4.15)). At the same time when the mode switched from the fundamental to the higher one, the resonance frequency jumped up to values between $f_2 = 282$ and 290 Hz. On the basis of the natural frequencies of both modes $\underline{u}_1$ and $\underline{u}_2$, an estimate for the spring stiffness k_3 relative to k_1 can be calculated from equations (4.12) and (4.13). The resulting ratio is a measure for the strength of the elastic coupling between both resonators, and has a value of $k_3/k_1 = 0.122$.

- At even higher Reynolds numbers beyond $Re_u = 16.5 \times 10^5$, another domain of *anti-phase* oscillations occurred. As indicated by the abrupt drop in the sound pressure, however, resonance was about to cease under these flow conditions. Although the system of resonators oscillated once again in its fundamental mode, this state appeared to have merely transitional character.

4.2.3 Three adjacent Helmholtz resonators

Similar to the previous section, experimental results obtained from microphone measurements in the cavities of three flow-induced adjacent resonators are presented in figures 4.7 to 4.9. The numbering of the resonators is according to figure 4.4. Again, the discussion is based on one representative configuration.

In this sample case, resonant conditions prevailed for Reynolds numbers ranging from $Re_u = 7.0 \times 10^5$ to 14.6×10^5, as implied by the course of p_{cav}/p_{dyn} in figure 4.9. In contrast to the case with two resonators, the oscillatory behavior of the present system did not change within this domain.

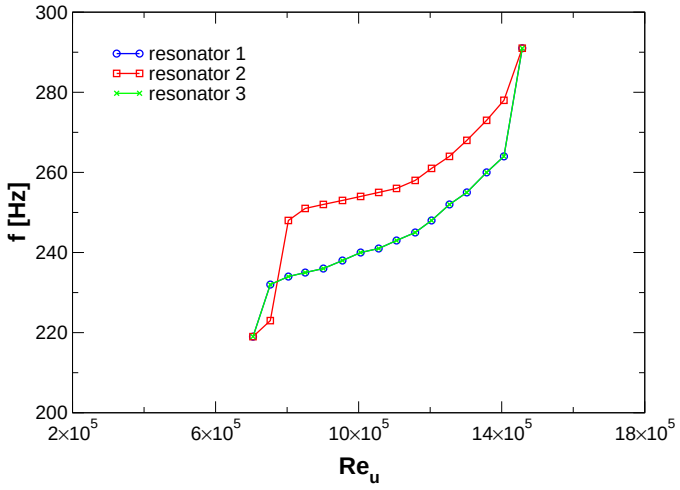

FIGURE 4.7: Measured resonance frequencies f of three flow-induced adjacent Helmholtz resonators as a function of the unit Reynolds-number Re_u. $2s = 14\,\text{mm}$, $l_y = 125\,\text{mm}$, neck geometry A30/K5.

Figure 4.7 shows that the resonance frequencies induced by the cross-flow increased with Re_u, which was a consequence of maintaining an approximately constant Strouhal number. Under all flow conditions, both outer resonators denoted as 1 and 3 oscillated at identical frequencies. The fluid motion inside the center resonator 2, however, was characterized by a slightly higher frequency, with the exception of the first two and the last data point. In the latter situations, the oscillation amplitudes were very small (see figure 4.9) such that the coupling between the resonators was rather weak. The difference in the natural frequencies of resonators with equal dimensions under identical free-stream conditions is a result of the interaction when arranged in a system. The fact that distinct frequencies are present simultaneously in the various resonator cavities indicates that two modes of oscillation are involved.

Details of how these modes superimpose, can be derived from the synopsis of the sound-pressure spectra of all three resonators depicted in figure 4.8. In the case of maximum oscillation amplitude shown (i.e. for maximum p_{cav}/p_{dyn}), the spectra feature two pronounced resonance peaks. They occur at both natural frequencies present in figure 4.7 at the corresponding Reynolds number of $Re_u = 11.1 \times 10^5$. Depending on the resonator, though, the amplitudes vary widely: While both outer resonators 1 and 3 generate their maximum sound pressure at $f_1 = 243\,\text{Hz}$, the peak of the center resonator 2 occurs at $f_2 = 256\,\text{Hz}$. However, all spectra exhibit a second, much smaller peak at the resonance frequencies of the respective other resonators. This is a clear indication of the interaction with one another.

These mutual dependencies are illustrated more systematically in fig-

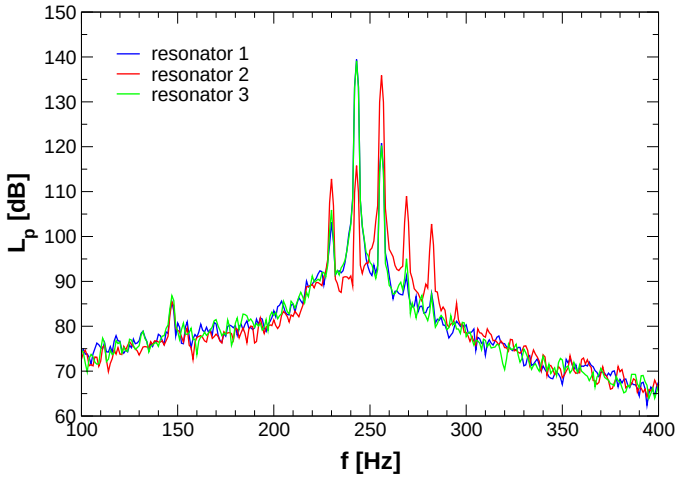

FIGURE 4.8: Spectra of the sound-pressure level in three adjacent Helmholtz resonators at maximum amplitude ($p_{cav}/p_{dyn} = 112$, 75, and 108 % in resonators 1, 2, and 3, respectively). Resonators 1 and 3 oscillate at $f_1 = 243$ Hz, while resonator 2 has a resonance frequency of $f_2 = 256$ Hz. $Re_u = 11.1 \times 10^5$, $2s = 14$ mm, $l_y = 125$ mm, neck geometry A30/K5.

ure 4.9 in terms of phase differences between the resonators and amplitudes of the induced sound pressure. Figures 4.9 a+c and 4.9 b+d show these parameters for either one of the two superimposing modes corresponding to the resonance frequency of both outer resonators (f_1) and to the one of the center resonator (f_2), respectively. Figures 4.9 a+b depict the phase angle between the periodic motion of the respective frequency component in two resonators. The amplitude of the relative sound pressure associated with each frequency component is shown in figures 4.9 c+d for all three resonators. Regarding both occurring modes of oscillation, the graphs imply:

- At the natural frequency f_1, the outer resonators 1 and 3 oscillate *in anti-phase* at an equally large amplitude. The much smaller sound pressure in resonator 2 indicates that this frequency component does virtually not contribute to the fluid motion in the center cavity (figure 4.9 c). Because of that, the phase difference φ_{12} between the resonators 1 and 2 behaves irregularly (figure 4.9 a). This mode of vibration can be identified as the fundamental mode $\underline{u}_1$ (see figure 4.5), where only the outer resonators are involved in the vibration at frequency f_1.

- At the natural frequency f_2 of the next higher mode $\underline{u}_2$ (see figure 4.5), the center resonator 2 oscillates at a large amplitude *in anti-phase* to both outer resonators 1 and 3 (figure 4.9 b) which perform a periodic motion of comparatively small amplitude (figure 4.9 d). The spring

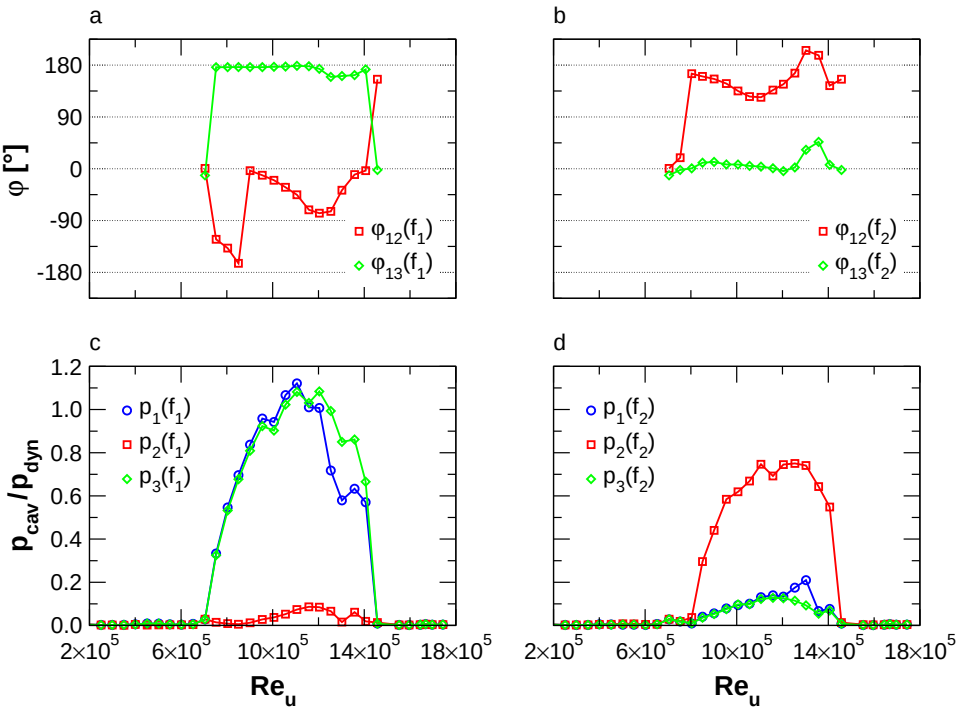

FIGURE 4.9: Experimental results of three flow-induced adjacent Helmholtz resonators: Phase difference φ_{12} and φ_{13} between the resonators and generated sound pressure p_{cav} relative to the free-stream dynamic pressure p_{dyn}. In the legend, p_j denotes p_{cav}/p_{dyn} in resonator j. All quantities are shown for the frequencies f_1 (a+c) and f_2 (b+d) related to both superimposing modes $\underline{u}_1$ and $\underline{u}_2$. $2s = 14\,\text{mm}$, $l_y = 125\,\text{mm}$, neck geometry A30/K5.

stiffness k_6 can be determined from the amplitude ratios by means of equation (4.23) resulting in $k_6 = 3.175k_4$. Inserting this value into equation (4.20), the natural frequency f_2 is obtained with $f_2 > f_1$. This result is consistent with the behavior of the resonance frequencies observed in figure 4.7.

Figures 4.8 and 4.9 illustrate that both the first and second mode are excited by the cross flow at the same time. They superimpose as described by equation (4.6). The highest mode $\underline{u}_3$ is not induced under the present flow conditions and with the resonator geometries investigated.

4.2.4 General systems of adjacent Helmholtz resonators

The previous results and additional experiments with systems of four and five resonators imply that there is a fundamental difference in the behavior of systems with an even number and those with an odd number of resonators.

The oscillations of even-numbered systems are confined to the presence of one mode at a time. Although different modes might occur depending on the flow conditions, the preferred mode of vibration is characterized by an

anti-phase relation between the fluid motion in the resonators. This can be observed, for example, in figure 4.11.

The oscillations of an odd number of adjacent resonators involve several simultaneous modes, which superimpose. A mode distinguished by a large-amplitude, *anti-phase* oscillation of the outer resonators is dominant. In this situation, however, the center resonator is left in an indifferent state. As a consequence, it oscillates in its own mode, in which the surrounding resonators are involved only to a small extent. The induced sound-pressure amplitude of the center resonator is generally lower than that of resonators located at off-center positions (see, for example, figure 4.12).

4.3 Resonance regime of flow-induced resonator systems

For systems of two and three adjacent resonators, the regime, where resonance was induced by a cross-flow, is illustrated in figures 4.10 to 4.12 with respect to Reynolds number and slit width. Apart from the sound pressure produced within this domain, the phase relations between the resonators involved were of particular interest. The results were obtained by simultaneous microphone measurements in each of the individual resonator cavities of a configuration.

According to figure 4.10, both resonators in a system of two behave virtually identical regarding their resonance regime and intensity. Under all flow

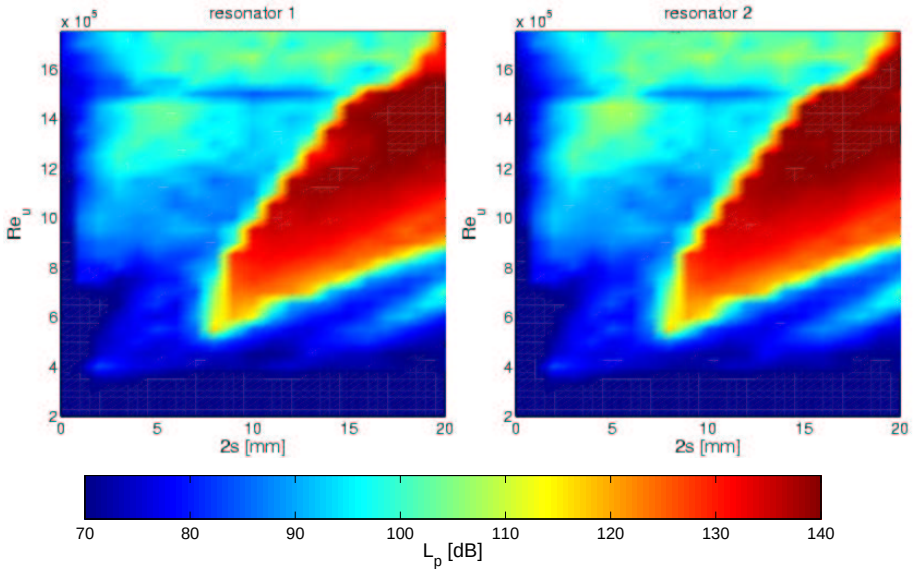

FIGURE 4.10: Sound-pressure level (see color scale) of the resonance peaks in two adjacent resonators depending on Reynolds number and slit width. Neck geometry A30/K5, $l_y = 125$ mm.

conditions investigated, they oscillated at exactly equal amplitude. Compared to the corresponding resonance domain of a similar single resonator (see right-hand side in figure 3.31), resonant conditions extended over a slightly larger range of Reynolds numbers and slit widths. In addition, the oscillation amplitudes were generally higher.

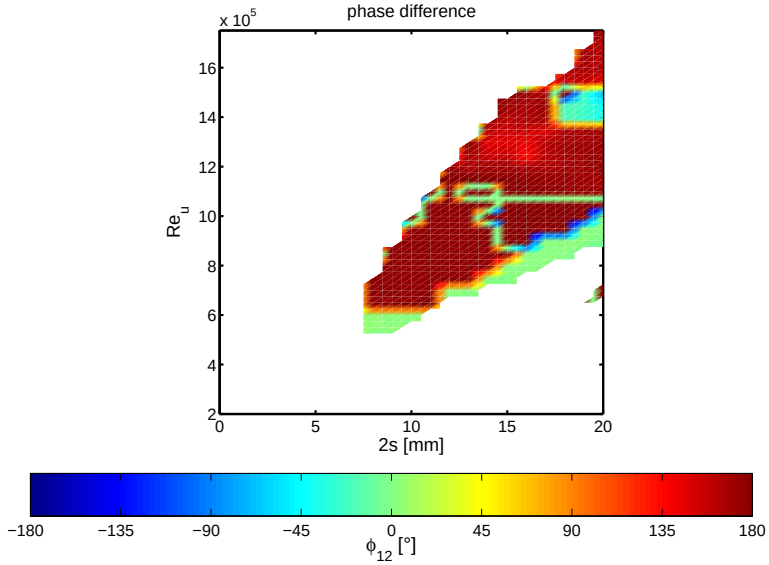

FIGURE 4.11: Phase difference (see color scale) between the oscillations in two adjacent resonators depending on Reynolds number and slit width. Cases without resonant conditions ($p_{cav}/p_{dyn} < 1\,\%$) are left blank. Neck geometry A30/K5, $l_y = 125\,\mathrm{mm}$.

The phase relation between the oscillations in both resonators is shown in figure 4.11. Areas left blank indicate that no phase angle could be specified in situations where $p_{cav}/p_{dyn} < 1\,\%$. Under resonant conditions, however, phase differences of about 180 ° were clearly dominant. This implies a preference for the fundamental mode associated with *anti-phase* oscillations. Flow conditions that triggered *in-phase* oscillations were rare, and practically no phase angles in the range $0\,° < \varphi_{12} < 180\,°$ occurred. In combination with figure 4.10, it can be inferred that the sound-pressure levels produced had a maximum when both resonators oscillated *in anti-phase*.

For the case of three adjacent resonators, only the amplitude within the resonance regime is shown (figure 4.12), because the superposition of two modes renders other representations impractical. The domain providing resonant conditions in both outer resonators resembles in its extensions the one for the system of two resonators discussed before. In comparison to a single resonator (see right-hand side in figure 3.31), the resonance regime enlarged and featured higher amplitudes. While the behavior of both outer resonators 1 and 3 was identical, the properties of the center resonator 2 differed: The extension of the corresponding resonance regime was smaller than that of the outer resonators regarding both the Reynolds-number range

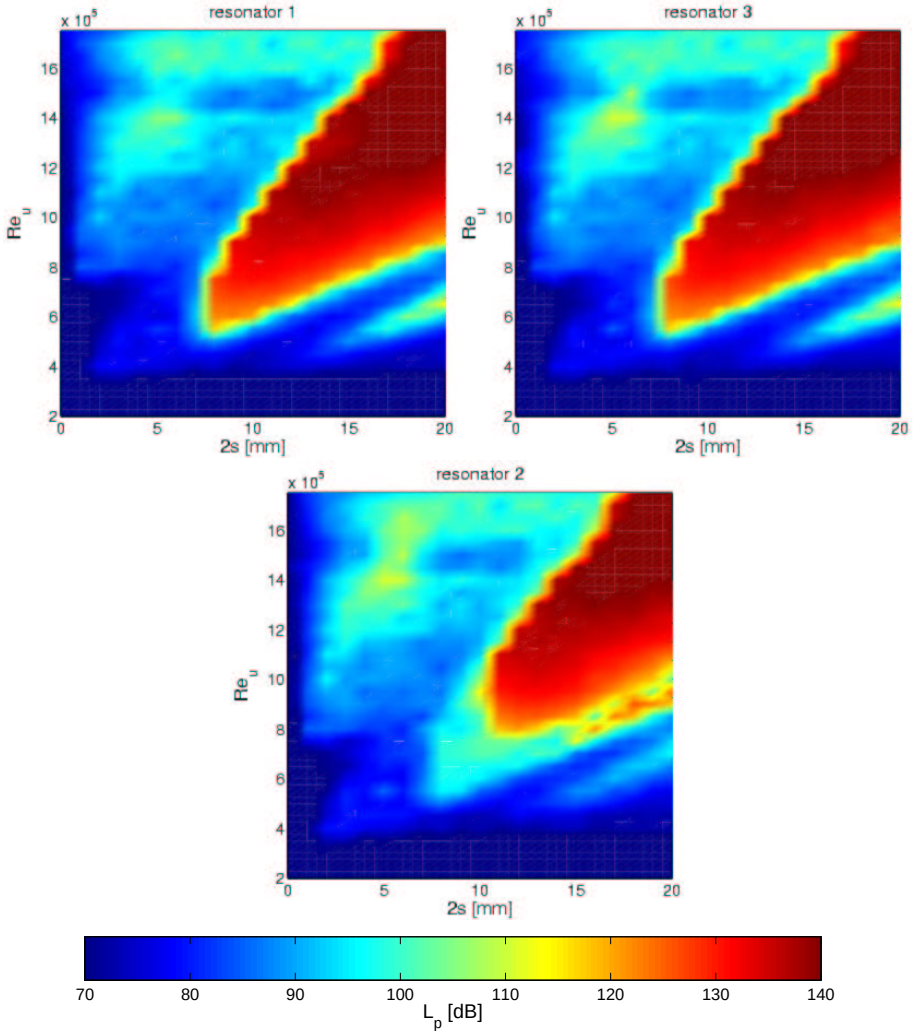

FIGURE 4.12: Sound-pressure level (see color scale) of the resonance peaks in three adjacent resonators depending on Reynolds number and slit width. Neck geometry A30/K5, $l_y = 125\,\text{mm}$.

and the slit widths. In addition, the induced oscillations were confined to lower amplitudes.

4.4 Radiated sound pressure of flow-induced resonator systems

In addition to the oscillation amplitude within each cavity of the flow-induced Helmholtz resonators, the sound pressure radiated into the ambient fluid was measured at a location 1573 mm downstream of the orifices. The goal was to investigate the influence of the oscillation mode on the intensity of the

n_z [–]	Re_u [–]	$2s$ [mm]	Mode	p_{cav}/p_{dyn} [%]	p_{rad}/p_{dyn} [%]	p_{rad}/p_{cav} [%]
1	0.65×10^6	9	Helmholtz	68	11	16
2	0.92×10^6	18	in-phase	38	8	20
2	0.95×10^6	18	anti-phase	41	1	3
2	1.34×10^6	18	anti-phase	110	3	3
3	0.95×10^6	20	in-phase	20	4	19
3	1.40×10^6	20	superposition	103	3	3
4	0.96×10^6	20	in-phase	25	5	19
4	1.40×10^6	20	anti-phase	92	3	3
5	0.84×10^6	19	in-phase	17	3	17
5	1.35×10^6	19	superposition	92	4	4

TABLE 4.1: Sound pressure produced by systems of one to five flow-induced resonators depending on their mode of vibration. n_z is the number of resonators in the system, p_{dyn} the free-stream dynamic pressure, p_{cav} the rms sound-pressure in the cavities, and p_{rad} the radiated rms sound-pressure at a distance 1573 mm downstream. Neck geometry A30/K5, $l_y = 125$ mm. The case $n_z = 2$ is illustrated in figure 4.6. For $n_z = 3$, a similar case is shown in figure 4.9, which differs regarding the values of $2s$ and Re_u from the data of this table.

radiated sound. In this context, the term "out of phase" will be used in the following to denote both anti-phase oscillations and the superposition of several modes.

Table 4.1 lists the results for numbers n_z of one to five adjacent resonators. Each case with more than one resonator was investigated under various flow conditions necessary to excite different modes of oscillation. The quantity p_{cav} represents the average of the rms sound-pressures inside the individual cavities of a configuration. The radiated sound pressure p_{rad} was determined at 280 points of a measurement grid throughout the entire wind-tunnel cross-section (see section 2.3.1), and averaged. In fact, the sound-pressure level was nearly homogeneous in this plane, with variations of less than ±1 dB. The actual result is described by the amplitude ratio p_{rad}/p_{cav} between the radiated sound pressure and the one prevailing inside the resonator cavities.

The data in table 4.1 imply that the mode shape of the oscillations had a strong effect on the sound pressure radiated by the systems of resonators. While the sound-pressure ratio p_{rad}/p_{cav} associated with in-phase oscillations lay in the range between 16 and 20 %, this ratio was as low as 3 to 4 % when the resonators oscillated out of phase. This behavior was identical independent of the number of resonators in the system. Even when the relative oscillation amplitude p_{cav}/p_{dyn} inside the cavities was as high as 100 %, p_{rad}/p_{cav} was reduced by about an order of magnitude in cases with out-of-phase oscillations. Neither variations of the Reynolds number Re_u

nor of the oscillation amplitude p_{cav}/p_{dyn} seemed to affect the reduction of the radiated sound pressure. This can be observed by comparing both cases with $n_z = 2$ that exhibit anti-phase behavior. With the same resonator system, a slight increase in the Reynolds number from 9.2×10^5 to 9.5×10^5 was accompanied by a change of the mode from in-phase to anti-phase oscillations. Obviously, the resulting drastic drop in the radiated sound pressure was solely caused by the transition of the oscillation mode.

In conclusion, the large reduction of the radiated sound pressure as a consequence of out-of-phase oscillations can be attributed to the interference of the sound waves emanating from the resonator orifices at different phase angles. It should be noted that the aforementioned results can easily be transferred to the characteristics of *active* actuators operated in anti-phase.

4.5 Wake of flow-induced adjacent resonators

Changes in the wake downstream of flow-induced resonator systems were studied by oil-film visualizations and measurements of the wall-shear stress distribution depending on the mode of oscillation. As before, results obtained with sample configurations of two and three resonators will be shown (figures 4.13 and 4.14, respectively).

4.5.1 Oil-film visualization

For both systems, the oil-film visualizations showed footprints of alternating longitudinal vortices forming in the wake of the dividing walls when out-of-phase oscillations were excited by the flow (right-hand sides in figures 4.13 and 4.14). This effect did not simply stem from the presence of a separating wall between the resonators, as can be seen from the visualizations of modes associated with in-phase oscillations. In this case, the wake remained completely homogeneous (left-hand sides in both figures).

While single flow-induced resonators generate spanwise vortices at their opening (see section 3.2.3), systems of adjacent resonators operating in the appropriate mode form longitudinal vortices in addition. This is evidently caused by the fact that, in this case, the location of the separating walls coincides with nodes of the spanwise distribution of the sound particle velocity. A similar vortex pattern was observed by Seifert *et al.* (1998) who experimented with piezoelectric flaps driven in anti-phase to control the separated flow region on a wing section.

4.5.2 Wall-shear stress distribution

The spanwise distributions of the wall-shear stress in the wake of both configurations of adjacent resonators show a marked increase in c_f downstream of a separating wall, when the resonators oscillate out of phase. The peaks in the

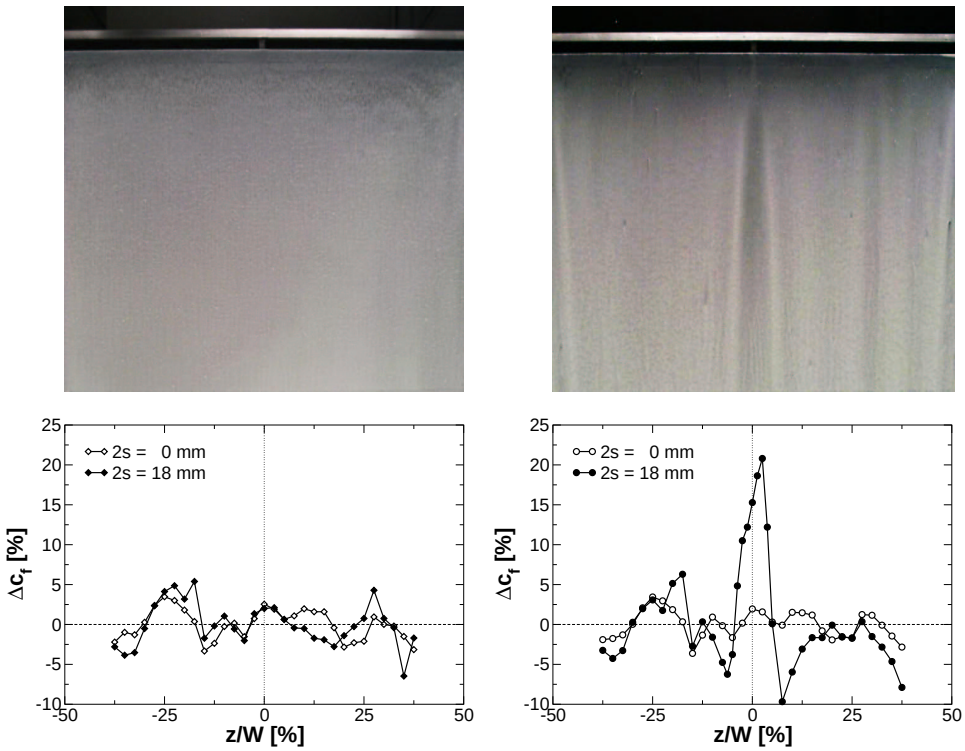

FIGURE 4.13: Wake of two adjacent resonators oscillating *in phase* at $Re_u = 9.2 \times 10^5$ (left), and *in anti-phase* at $Re_u = 1.3 \times 10^6$ (right). $2s = 18\,\text{mm}$, $l_y = 125\,\text{mm}$, neck geometry A30/K5.
Top: Oil-film visualization. The upstream edge of the resonator neck is seen as the shiny horizontal part. At the center of the slit just below, the separating wall between both resonators is visible. Flow is from top to bottom.
Bottom: Spanwise variation of the skin-friction coefficient downstream of the resonators ($x - x_{LE} = 200\,\text{mm}$). The dotted vertical line indicates the spanwise location of the separating wall.

wall-shear stress correspond well with the locations of the vortex footprints observed during the flow visualizations. At a position 200 mm downstream of the system of two resonators, a 20 % increase in the skin-friction coefficient c_f was measured. With three adjacent resonators, the increase was around 10 %. However, the local increase in c_f is at the expense of the shear stress in neighboring regions (right-hand sides in figures 4.13 and 4.14).

In contrast, when in-phase oscillations are induced, the skin-friction distribution is not altered compared to the baseline-flow case obtained with a closed resonator (left-hand sides in both figures).

With respect to flow control, the local increase of the wall-shear stress as a consequence of out-of-phase oscillations of adjacent resonators is likely to further reduce separation regions. This result might be expected to apply to *active* actuators driven in anti-phase as well.

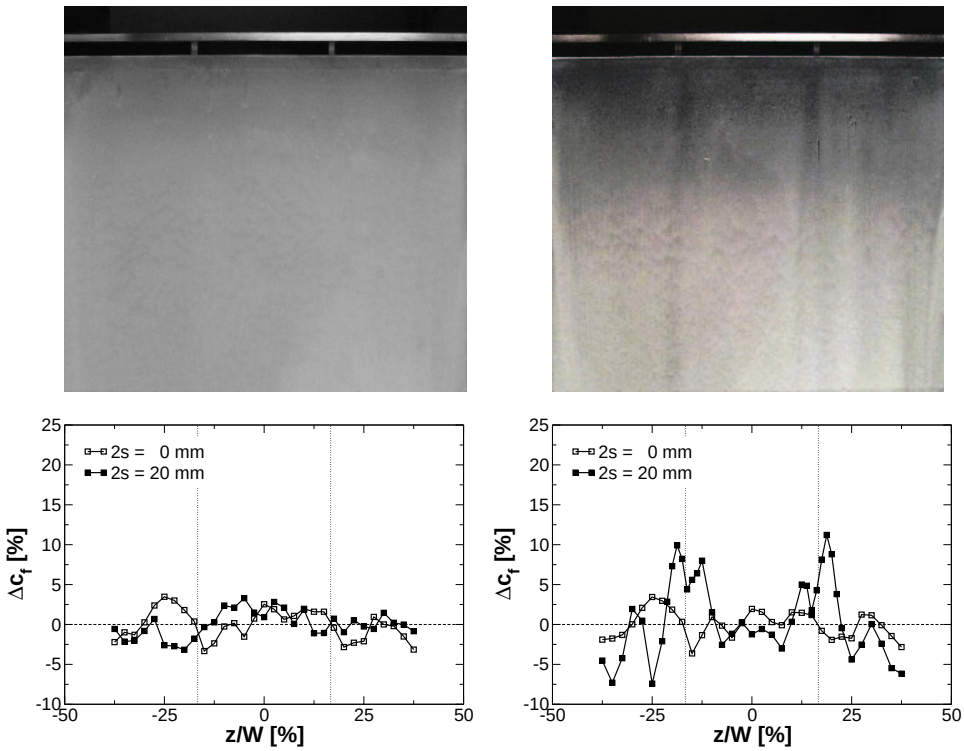

FIGURE 4.14: Wake of three adjacent resonators oscillating *in phase* at $Re_u = 9.5 \times 10^5$ (left), and *out of phase* at $Re_u = 1.4 \times 10^6$ (right). $2s = 20\,\text{mm}$, $l_y = 125\,\text{mm}$, neck geometry A30/K5.
Top: Oil-film visualization. The upstream edge of the resonator neck is seen as the shiny horizontal part. Within the slit just below, both separating walls between the three resonators are visible. Flow is from top to bottom.
Bottom: Spanwise variation of the skin-friction coefficient downstream of the resonators ($x - x_{LE} = 200\,\text{mm}$). The dotted vertical lines indicate the spanwise location of the separating walls.

4.6 Concluding remarks on resonator systems

The results of this chapter which are relevant to a later application in the context of separation control can be briefly summarized as follows:

- A model of purely acoustic coupling between adjacent resonators captures the occurring oscillation modes. This is in contradiction to Flynn & Panton (1990) who attribute the interaction within a system of resonators to a flow phenomenon that is not further specified.
- Flow-induced systems with an even number of resonators oscillate in one mode at a time, depending on the Reynolds number, with a preference for anti-phase behavior.
- The motion of flow-induced systems with an odd number of resonators

is the result of a superposition of several modes.

- The sound radiated by a system of resonators oscillating out of phase is about an order of magnitude less than that radiated when oscillating in-phase at a comparable amplitude.
- Resonator systems operated out of phase generate alternating streamwise vortices in their wake increasing c_f in these regions. This is favorable for flow control.
- The benefits of out-of-phase oscillations for the radiated sound pressure and the skin friction downstream might also be expected when applying active actuators.

List of symbols

$\underline{\underline{a}}$	abbreviation for $\underline{\underline{k}} - \omega^2 \underline{\underline{m}}$
A	amplitude of a mode
c	speed of sound ($\approx 343\,\mathrm{m/s}$ in air at room temperature)
c_f	skin-friction coefficient
f_0	resonance frequency
$f(t)$	time component of the displacement vector
i	index denoting the mode
i	imaginary unit ($= \sqrt{-1}$)
k	spring stiffness of compressible fluid
$\underline{\underline{k}}$	stiffness matrix
L_p	sound-pressure level
l_n	neck length of a resonator
l_y	height of the resonator cavity
m	mass of fluid in the resonator orifice
$\underline{\underline{m}}$	mass matrix
n	degrees of freedom
n_z	number of adjacent resonators
p_{cav}	rms sound-pressure within the resonator cavity
p_{dyn}	free-stream dynamic pressure
p_{rad}	radiated rms sound-pressure
Re_u	Reynolds number based on unit length (1 m)
s	half-slit width of the resonator neck
S	cross-sectional area of the resonator orifice
t	time
$\underline{u}$	constant amplitude of the displacement vector
V	volume of the resonator cavity
W	width of the measurement section
x	streamwise coordinate originating at entrance of test section

x_{LE}	streamwise location of the leading edge of the resonator neck
y	displacement of fluid mass in the resonator orifice
$\ddot{y}$	acceleration of fluid mass in the resonator orifice
$\underline{y}(t)$	displacement vector of a system
z	spanwise coordinate originating at centerline of test section or resonator
α	arbitrary, but constant factor
Δ	variation of a quantity
ρ	mass density of fluid
φ	phase
ω	angular frequency

Chapter 5

General aspects of flow control by fluidic actuators

This chapter discusses two aspects associated with the manipulation of separation regions by fluidic actuators: Firstly, it will be investigated which physical quantity is most appropriate to characterize the strength of the excitation produced by a fluidic actuator (section 5.2). As pointed out in section 1.3.3, it cannot be concluded from the literature, whether the effect of zero net-mass-flux actuation is governed by the addition of unsteady momentum, or rather by a different parameter. Secondly, the properties of the flow field downstream of the actuator are examined in order to illustrate the mechanism responsible for the manipulation of a separated flow region (section 5.3).

In contrast to all other investigations of this project, *active* actuation via loudspeakers was used instead of passive control by a resonator. In this way, a wide range of excitation parameters was tested that could be set with the loudspeakers more flexibly than by adjusting a flow-induced resonator. Most important, individual parameters such as frequency and amplitude could be varied independently.

Since both active and passive fluidic actuators rely on the generation of spanwise vortices to manipulate a flow, the fluid-mechanical processes induced downstream of the perturbation source are identical. The results of this chapter can, therefore, be transferred to the case of separation control by aerodynamically excited resonators.

5.1 Experimental set-up

The experiments were conducted in a planar asymmetric diffuser which expanded the tunnel height from 135 to 280 mm, as illustrated in figure 5.1. For this purpose, the diffuser was installed in the test section of the open-return wind-tunnel (see section 2.2.1). A flexible joint connected the inlet

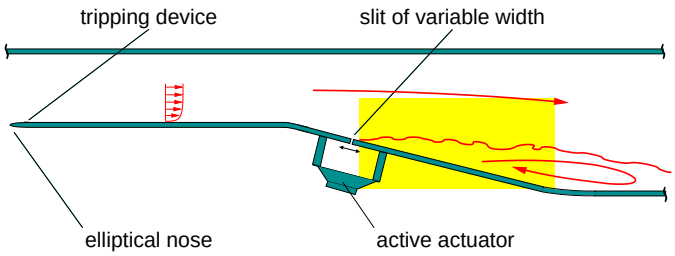

FIGURE 5.1: Schematic of the experimental set-up to control the separated flow in a planar asymmetric diffuser by active actuation. The area investigated by the PIV measurements of section 5.3 is shaded in yellow.

channel of length 605 mm to the diverging section. This allowed the diffuser expansion-angle to be varied in the range from 0 ° to 20 °. In the present investigation, it was adjusted to 18 °. The actuator slit was mounted flush with the inclined bottom wall at a distance of 165 mm downstream of the diffuser entrance. All other details such as the tripping devices or the bypass were identical to the set-up presented in section 3.2.2. After some modification, the diffuser was also used in the flow-control experiments of section 6.4.

Flow separation occurred directly downstream of the actuator. The three-dimensionality of the reverse-flow region developing in the half diffuser was reduced by a vortex generator in either corner of the measurement section upstream of the diverging part. Flow visualization showed that the separation line was two-dimensional along the inner 50 % of the bottom wall.

The actuator was driven by a set of three loudspeakers, and featured a conventional orifice geometry (R0/K0, see figures 3.25 and 3.26). The actuator dimensions were identical to those of the resonator in section 2.1.1. While the slit width was variable, the cavity height remained fixed at $l_y = 50\,\text{mm}$.

The measurement techniques included pressure probes, microphones, hot-wire anemometry, as well as time- and phase-averaged DPIV.

5.2 Characteristic physical quantity of fluidic actuator output

In this section, a parameter will be determined, which characterizes the strength of fluidic excitation and which is, at the same time, uniquely correlated with the effect on the separation region. This quantity has to be independent of the geometrical shape of the excitation source. On the basis of this parameter, results obtained from flow-control experiments with different types of actuators and with varying amplitudes or frequencies are comparable. In addition, this parameter allows to investigate the properties of excitation sources independent of a separation region. An issue mainly

of importance to experiments involving *active* flow control is the necessity to differentiate between the receptivity of the manipulated shear layer and the transfer characteristics of the fluidic actuator when operating at various frequencies. Both effects can only be properly distinguished, if the characteristic quantity of the excitation is held constant.

Throughout the experiments, the reduced actuation frequency St_{2s} based on the slit width $2s$ was kept constant to ensure that the local flow processes in the vicinity of the slit scale equally. To this end, the frequency was adjusted accordingly, while the slit width was varied between 1 and 20 mm at increments of 1 mm. Cases of two different Strouhal numbers were considered, namely $St_{2s} = 0.02$ and 0.05. Care was taken to manipulate the shear layer only at frequencies in a range where the receptivity was high. All measurements were performed at a unit Reynolds number of $Re_u = 6.5 \times 10^5$.

To describe the output of the actuator, the velocity field in its orifice was measured by phase-averaged PIV. Different key parameters such as the fluctuating mass and momentum flux through the actuator slit were calculated from the data, and then correlated with the pressure recovery coefficient c_p in the half diffuser. In this context, c_p was a measure of the effectiveness of the flow control and, thus, of the extension of the separation region. For our purposes, c_p is given as a fraction of its possible upper limit, i.e. of the corresponding pressure coefficient $c_{p_{\mathrm{pot}}}$ obtained from potential-flow theory (see section 1.3.4). Details regarding the measurement of c_p were explained in section 2.3.1.

For a slit of width $2s$ and spanwise length l_z, the area of the exit plane is $2s \times l_z$. Then, the steady convective mass and momentum flux, $\dot{m}$ and $\dot{I}$ respectively, per slit length l_z out of a region bounded by the surface $2s \times l_z$ can be written in integral form (e.g. Batchelor, 1967, sec. 2.2 and 3.2):

$$\frac{\dot{m}}{l_z} = \rho \int_{x=0}^{x=2s} \underline{u}(x) \cdot \underline{n}\, dx \tag{5.1}$$

$$\frac{\dot{I}}{l_z} = \rho \int_{x=0}^{x=2s} \underline{u}(x)\underline{u}(x) \cdot \underline{n}\, dx \tag{5.2}$$

Herein ρ denotes the fluid density, and $\underline{u}(x) = (u(x), v(x), w(x))$ the velocity vector of the fluid emanating from the slit as a function of the streamwise coordinate x across the slit. $\underline{n}$ is the unit outward normal pointing in positive y-direction, i.e. perpendicular to the mean flow. Both equations assume homogeneity in spanwise direction, but account for the fact that in- and outflow can occur at the same time at different streamwise positions across the slit.

For a velocity field fluctuating periodically in time, equations (5.1) and (5.2) can be rewritten to yield the net rate at which mass and momentum

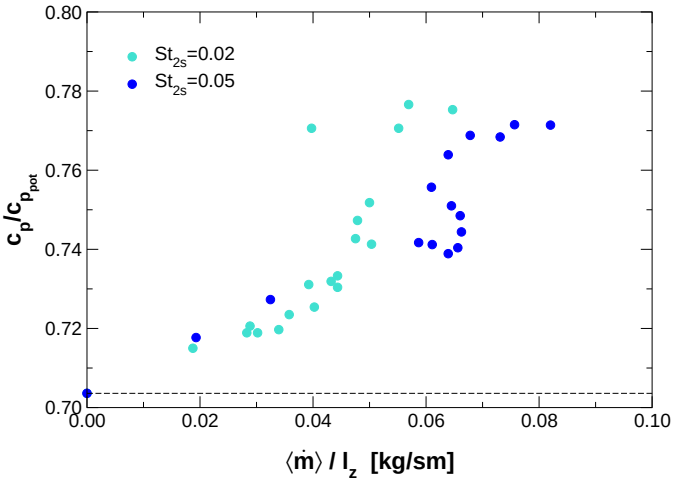

FIGURE 5.2: Pressure recovery in the half diffuser given as ratio of actual and theoretically possible value from potential-flow theory as a function of the fluctuating mass flux of the actuator. The dashed line corresponds to the baseline case. $Re_u = 6.5 \times 10^5$.

per unit span are flowing across the slit exit plane:

$$\frac{\langle \dot{m} \rangle}{l_z} = \frac{\rho}{T} \int_{t=0}^{t=T} \left| \int_{x=0}^{x=2s} \langle \underline{u}(x,t) \rangle \cdot \underline{n} \, dx \right| dt \tag{5.3}$$

$$\frac{\langle \dot{I} \rangle}{l_z} = \frac{\rho}{T} \int_{t=0}^{t=T} \left| \int_{x=0}^{x=2s} \langle \underline{u}(x,t) \rangle \langle \underline{u}(x,t) \rangle \cdot \underline{n} \, dx \right| dt \tag{5.4}$$

T represents the period, t the time, and $\langle \underline{u}(x,t) \rangle$ the phase-locked velocity vector of the flow through the slit of the actuator.

Figures 5.2 and 5.3 show the relative pressure coefficient $c_p/c_{p_{\text{pot}}}$ of the half diffuser as a function of the fluctuating mass and momentum flux through the slit, as calculated from equations (5.3) and (5.4), respectively. While the graphic representation of $c_p/c_{p_{\text{pot}}}$ versus the mass flux does not yield a unique relation, pressure recovery and momentum flux exhibit a functional dependence: The pressure recovery in the half diffuser increases monotonic with the momentum flux until saturation occurs. In this case, the data sets obtained with the two different Strouhal numbers collapse.

These results imply that the fluctuating momentum flux through the slit, or a non-dimensional equivalent, is the appropriate quantity to characterize the output of a fluidic actuator. This might, at first, not be surprising, but it could not be predicted from the available literature.

As seen before, the momentum flux cannot be measured easily. Its accurate determination is laborious, since it requires the measurement of the velocity distribution across the slit, and the application of phase-averaging methods in the post-processing.

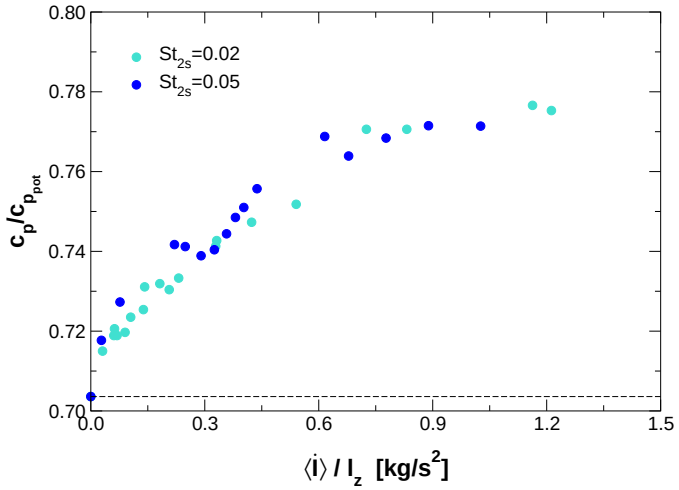

FIGURE 5.3: Pressure recovery in the half diffuser given as ratio of actual and theoretically possible value from potential-flow theory as a function of the fluctuating momentum flux of the actuator. The dashed line corresponds to the baseline case. $Re_u = 6.5 \times 10^5$.

In anticipation of the parameter study of section 6.1, the momentum flux is usually non-dimensionalized. The new quantity is referred to as the oscillatory momentum coefficient $\langle c_\mu \rangle$:

$$\langle c_\mu \rangle = \frac{2\langle \dot{I} \rangle}{l_z L \rho U_\infty^2} \tag{5.5}$$

where L is a characteristic length of the problem, and U_∞ the free-stream velocity. Throughout the present study, $\langle c_\mu \rangle$ will be based on L as the streamwise length of the reverse-flow region.

5.3 Mechanism of fluidic separation control

The experiments in this section complement measurements of the flow in the near field of an actively driven fluidic actuator by Erk (1997), who showed that such a perturbation source acts as a "vortex pump": The spanwise vortices ejected from the orifice (figure 5.4) intensify the mixing across the shear layer downstream as they are convected along. In this way, they transport energetic fluid into the near-wall region such that the flow can negotiate an adverse pressure gradient and overcome separation more easily.

Figures 5.5 and 5.6 present a more global view regarding the interaction of the spanwise vortices with a separation region. They show a cross-section of the flow field in the half diffuser starting from the trailing edge of the actuator, and extending 90 slit widths downstream. The investigated area is illustrated in figure 5.1.

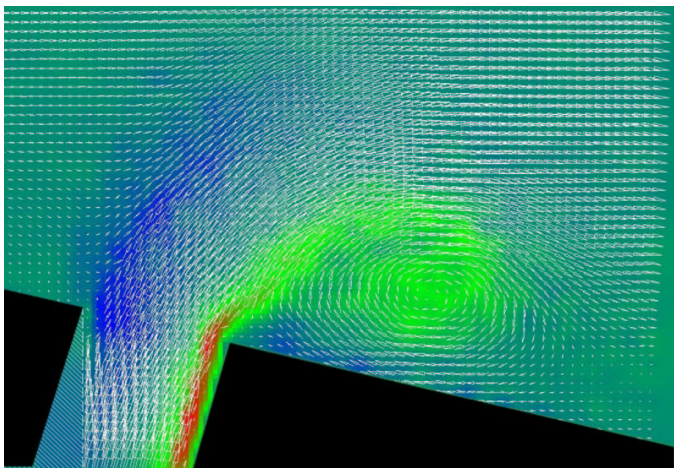

FIGURE 5.4: Phase-averaged PIV measurement showing the formation of a spanwise vortex at the orifice of the fluidic actuator in terms of the velocity vectors and the vorticity field (color scale) at maximum outflow. $Re_u = 6.5 \times 10^5$, $2s = 7\,\mathrm{mm}$, $St_{2s} = 0.02$, $\langle c_\mu \rangle = 1.07 \times 10^{-2}$.

The vorticity fields in figure 5.5 are computed from time-averaged PIV measurements. They demonstrate the success of the active flow control: In the baseline case shown on the left-hand side of the figure, a large-scale reverse-flow region forms in the diffuser. It is bounded by a separated shear layer, which is marked by a high concentration of vorticity. In contrast, the separation region almost entirely disappears when fluidic excitation is applied. This is seen on the right-hand side, where the vorticity is spread out even up close to the wall indicating that a strong mixing process is acting on the flow. As a result, the pressure recovery increased from $c_p/c_{p_{\mathrm{pot}}} = 0.70$ to 0.78.

The phase-averaged PIV measurements of the vorticity in figure 5.6 show that the coherent vortical structures generated at the orifice of the perturbation source persist until far downstream. While they are convected away

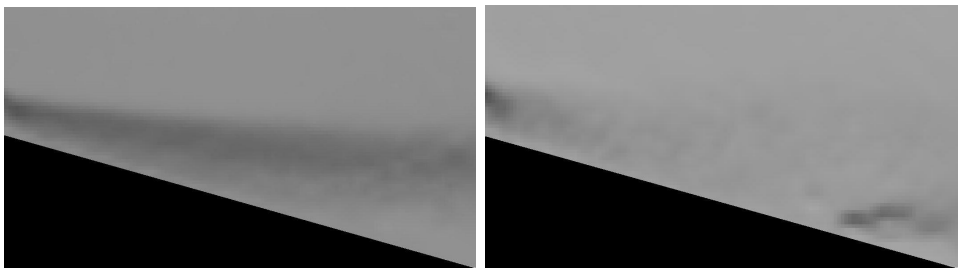

FIGURE 5.5: Time-averaged PIV measurement of the vorticity field in a half diffuser without (left) and with (right) active flow control. $c_p/c_{p_{pot}} = 0.70$ (left) and 0.78 (right), $Re_u = 6.5 \times 10^5$. Controlled case: $2s = 4\,\mathrm{mm}$, $St_{2s} = 0.02$, $\langle c_\mu \rangle = 3.29 \times 10^{-2}$.

from the actuator by the cross-flow, they increase in size. At any phase angle of the imposed excitation signal, three vortices are simultaneously present within the investigated section of the diffuser. Obviously, this ensures an increased mixing rate over a wide range of the initial separation region, and thus reduces reverse flow in the time mean.

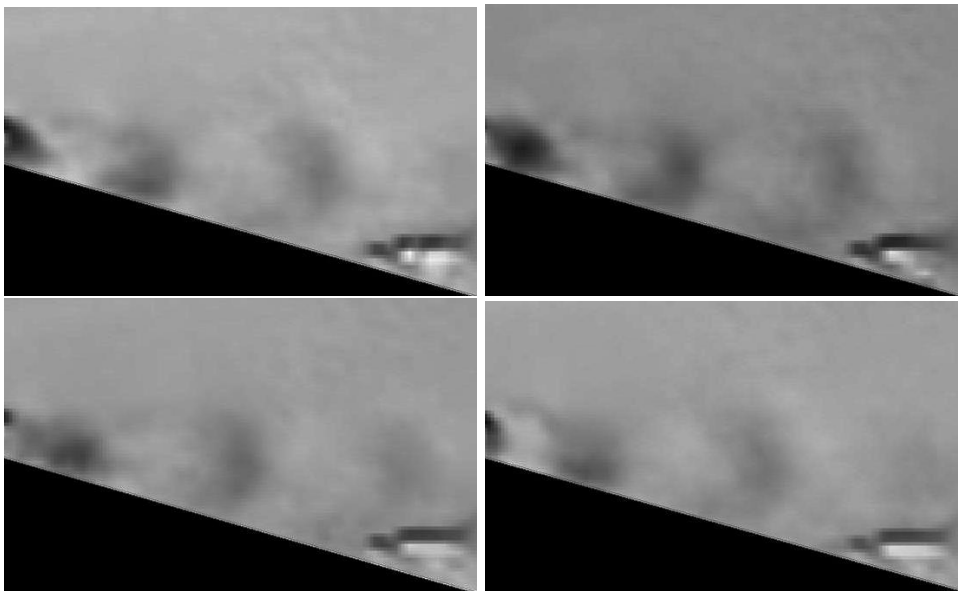

FIGURE 5.6: Phase-averaged PIV measurement of the separation region in a half diffuser with active flow control at phase angles of 90 ° increments. Grey scale corresponds to vorticity. The diffuse pattern in the lower right corner of the pictures is caused by reflections in the test section. $c_p/c_{p_{pot}} = 0.78$, $Re_u = 6.5 \times 10^5$, $2s = 4\,\mathrm{mm}$, $St_{2s} = 0.02$, $\langle c_\mu \rangle = 3.29 \times 10^{-2}$.

List of symbols

c_p	pressure coefficient ($= \Delta p/(\frac{1}{2}\rho U_\infty^2)$)
$c_{p_{\mathrm{pot}}}$	pressure coefficient obtained from potential flow theory
c_μ	momentum coefficient
$\dot{I}$	momentum flux
l_y	height of the actuator cavity
l_z	span of the actuator cavity
L	characteristic length
$\dot{m}$	mass flux
$\underline{n}$	unit outward normal
Re_u	Reynolds number based on unit length (1 m)
s	half-slit width of the actuator neck
St_{2s}	Strouhal number based on streamwise length of actuator neck

t	time
T	cycle duration
$\underline{u}$	velocity vector
u	velocity component in x-direction
U_∞	free-stream velocity
v	velocity component in y-direction
w	spanwise velocity component
x	streamwise coordinate originating at the upstream edge of the slit
y	wall-normal coordinate originating at the wall
ρ	mass density of fluid
$\langle\,\rangle$	phase-averaged value of a quantity

Chapter 6

Flow control using acoustic resonators

After a discussion of general aspects of flow control in chapter 5, it is shown in this chapter that a variety of separation regions can in fact be controlled by the oscillations of an acoustic resonator induced by a grazing flow.

Section 6.1 points out on which parameters the success of the manipulation of a recirculation zone depends when a resonator is employed as a passive flow-control device. Section 6.2 discusses the factors that determine the optimum streamwise actuator location. To understand the resulting processes in the flow downstream of an oscillating resonator, its effect on the boundary-layer properties was investigated at first in a zero pressure-gradient flow (section 6.3). Subsequently, flow-induced resonators were applied to two different flow configurations exhibiting generic examples of separation regions: a planar asymmetric diffuser (section 6.4) and a wing section at high angle of attack (section 6.5).

Both flow configurations differ by several features: In the half-diffuser configuration, the boundary layer was artificially tripped prior to detachment and was turbulent at all Reynolds numbers investigated. The detachment of the flow was then provoked by an abrupt change in geometry at the entrance of the diffuser, where the tunnel started to expand. On the suction side of the wing, the boundary layer upstream of the separation line was laminar. In this case, separation was prompted by the strong adverse pressure gradient in streamwise direction prevailing at the leading edge at high angles of attack. Although the airfoil is actually of the trailing-edge-stall type, the flow separated immediately downstream of the leading edge under these conditions. In the free shear layer downstream transition to turbulence occurred.

The flow in the half diffuser formed a closed recirculation zone, often denoted as separation bubble, allowing to manipulate both the separation and the reattachment line. In contrast, the flow around the wing section

suffered from leading-edge separation in the post-stall regime and formed an open reverse-flow region. Thus, only the separation line could be controlled. According to a classification by Fernholz (1994), the separated diffuser flow is a strong reverse flow, while the stalled airfoil flow is a weak reverse flow. This has some implications for the flow properties which will be discussed in the corresponding sections.

Besides the differences in the respective baseline flows of both configurations, the resonators applied in each situation differed as well. The separated diffuser flow was manipulated by a resonator of rectangular cross-section oscillating in the Helmholtz mode at a frequency of the order of 10^2 Hz. The resonator applied to the airfoil flow had a circular cross-section. The oscillations of the first azimuthal mode were used to control the separation at an excitation frequency of the order of 10^3 Hz. Table 6.1 shows the differences between both configurations.

Configuration	Diffuser	Airfoil
Boundary-layer state prior to separation	turbulent	laminar
Separation induced by	geometry	pressure gradient
Strength of separation region	strong	weak
Shape of separation region	closed	open
Control of separation line	yes	yes
Control of reattachment line	yes	no
Resonator cross-section	rectangular	circular
Mode of resonator oscillations	Helmholtz	azimuthal
Excitation frequency [Hz]	O(10^2)	O(10^3)
Discussion in section	6.4	6.5

TABLE 6.1: Overview of the characteristics of separation control in a diffuser and on a wing section.

6.1 Parameter study

When controlling a separation region by fluidic actuators, the intention is usually to minimize pressure losses. In flow situations associated with diverging channels such as the configuration in section 6.4, this goal is equivalent to maximizing the pressure recovery $p - p_{ref}$. In the investigation of the flow around airfoils (section 6.5), an increase of lift or a reduction of drag are aspired. To quantify the effect of separation control in these flow fields, we, therefore, choose $p - p_{ref}$ as well as the lift and drag forces per unit span, F_l/s_w and F_d/s_w, respectively, as our figures of merit. Both latter quantities refer here to two-dimensional effects only. Independent of the objective, ambient conditions, the characteristics of the separated flow region, and the properties of the excitation all play a role in the success of control.

Thus, the aforementioned parameters are functions[1] $\mathcal{F}$ of the free-stream velocity U_∞, the fluid density ρ, and the kinematic viscosity ν of the fluid. In addition, the characteristic length L of the problem such as the length or height of the reverse-flow region, and the distance between the actuator location x_a and the separation line x_s are relevant (figure 6.1). Finally, as discussed in section 5.2, the excitation is characterized by the fluctuating momentum flux per unit span of the slit $\langle \dot{I} \rangle / l_z$, and the excitation frequency f_e:

$$\left.\begin{matrix} p - p_{ref} \\ F_l / s_w \\ F_d / s_w \end{matrix}\right\} = \mathcal{F}\Big(\underbrace{U_\infty, \rho, \nu}_{\text{ambient conditions}} , \underbrace{L, x_s - x_a}_{\text{separation region}} , \underbrace{\frac{\langle \dot{I} \rangle}{l_z}}_{\text{excitation}}, f_e \Big) \tag{6.1}$$

By performing a dimensional analysis, the number of independent variables can be reduced from seven to four. The resulting non-dimensional parameters have been abbreviated according to common notation: The success of the flow control by fluidic actuators is given in terms of the pressure recovery c_p in a diffuser, or the lift and drag coefficients[2] of an airfoil, c_l and c_d, respectively. The variable S_w denotes the area of the wing:

$$c_p = \frac{2(p - p_{ref})}{\rho U_\infty^2} \tag{6.2}$$

$$c_l = \frac{2F_l}{\rho U_\infty^2 S_w} \tag{6.3}$$

$$c_d = \frac{2F_d}{\rho U_\infty^2 S_w} \tag{6.4}$$

For convenience, we will abbreviate the figure of merit as c_x representing c_p, c_l, or c_d, for example, or similar quantities which describe the performance of a fluidic system. From dimensional analysis, we obtain that the figure of merit depends on the Reynolds number $Re_L = U_\infty L/\nu$, the distance of the actuator location x_a to the separation line x_s with respect to L, the momentum coefficient $\langle c_\mu \rangle = 2\langle \dot{I} \rangle / (l_z L \rho U_\infty^2)$, and the reduced excitation frequency $St_L = f_e L / U_\infty$. Both Re_L and St_L are based on the characteristic length L of the separation region.

$$c_x = \mathcal{F}\left(Re_L, \frac{x_s - x_a}{L}, \langle c_\mu \rangle, St_L \right) \tag{6.5}$$

When the fluidic actuator is of the active type, appropriate values of the characteristic parameters of the excitation, $\langle c_\mu \rangle$ and St_L, can usually be

[1] Again, the symbol $\mathcal{F}$ is used to indicate a relation between variables. However, the mathematical function it represents is different in each equation of this section.

[2] Strictly, the above dimensional analysis yields Ls_w as the area to non-dimensionalize the lift and drag forces F_l and F_d with, respectively. However, in order to comply with common notation, the wing area $S_w = cs_w$ is used in the definition of c_l and c_d, where c represents the chord length.

preset in a simple way. In the case of an acoustic resonator, however, the situation is much more complex as both parameters are determined by how the resonator is induced by the grazing flow. They have to be adjusted to appropriate values depending on the flow conditions by changing the geometry of the resonator. This can be done via a control loop as will be demonstrated in chapter 7. Under these circumstances, the method is denoted as adaptive.

The excitation *required* for the control of a separation region is given in terms of the fluctuating momentum flux $\langle c_\mu \rangle$ in the resonator orifice and the reduced frequency St_L (see equation (6.5)). The excitation *provided* by a resonator, however, is described by the relative amplitude of the flow-induced pressure oscillations p_{cav}/p_{dyn} and the resonance frequency St_{2s} (see equation (3.20)). From this comparison, the question comes up how to relate $\langle c_\mu \rangle$ and St_L with p_{cav}/p_{dyn} and St_{2s}.

The momentum coefficient $\langle c_\mu \rangle$ written as $\langle c_\mu \rangle = (\langle \dot{I} \rangle / l_z)/(L p_{dyn})$ represents a non-dimensional momentum flux through the slit, and is essentially computed from the velocity normal to the exit plane of the aperture (see equation (5.4)). This velocity is related to the pressure within the cavity p_{cav} via the specific acoustic impedance Z defined in equation (1.8). Z is a complex quantity containing phase and amplitude information.

Obviously, both systems, the separated flow field and the flow-induced resonator, have different characteristic length scales, namely L and $2s$, respectively. Consequently, care must be taken to adjust the resonator geometry to the flow conditions in a way that not only a strong resonance occurs and, therefore, an effective $\langle c_\mu \rangle$ is provided, but also that the resonance frequency St_{2s} matches the frequency St_L the separated flow is receptive to.

When considering the resonator and using the slit width $2s$ as the characteristic length scale, both resulting quantities $\langle c_\mu \rangle$ and St_{2s} are functions of the following parameters, in analogy to equation (3.20): the Reynolds number Re_{2s} based on the slit width, the non-dimensional momentum thickness $\delta_2/2s$ and the state of the boundary layer, the relative neck length $l_n/2s$, the dimensionless cross-sectional area of the resonator cavity $A/4s^2$, and the geometry of the resonator neck:

$$\left.\begin{matrix}\langle c_\mu \rangle \\ St_{2s}\end{matrix}\right\} = \mathcal{F}(Re_{2s}, \frac{\delta_2}{2s}, \text{laminar/turbulent}, \frac{l_n}{2s}, \frac{A}{4s^2}, \text{neck shape}) \qquad (6.6)$$

It would go far beyond the scope of the present investigation to study systematically the effect of varying each parameter in equation (6.5) obtained from dimensional analysis. This has been done before by other researchers using conventional, active fluidic actuators (see sections 1.3.3 to 1.3.5). Therefore, it is sufficient to demonstrate by two sample cases that flow control by aerodynamically excited resonators shows virtually identical effects (sections 6.4 and 6.5).

6.2 Streamwise resonator location

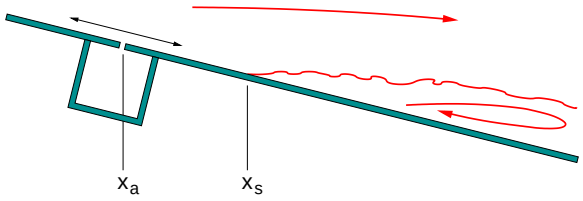

FIGURE 6.1: Schematic flow situation with adverse pressure gradient illustrating the streamwise locations of the actuator x_a and of the separation line x_s.

The result of the parameter study has important consequences regarding the streamwise location x_a of the resonator relative to the separation line x_s in situations governed by an adverse pressure gradient (see figure 6.1). The goal is, of course, to place the resonator such that a maximum change Δc_x in the figure of merit is achieved. The optimum location for an *active* actuator is close to the separation line, while a position further up- or downstream would result in a reduction of the beneficial effects, even when holding $\langle c_\mu \rangle$ constant (red curve in figure 6.2). In contrast to this, when applying a resonator, the momentum coefficient $\langle c_\mu \rangle$ is a function of still other flow parameters (see equation (6.6)). The amplitude of the associated flow-induced oscillations depends, for example, also on the boundary-layer momentum-thickness δ_2 (see section 3.2.9). In situations with a mild adverse pressure gradient, δ_2 increases in downstream direction such that the momentum coefficient $\langle c_\mu \rangle$ produced by the resonator decreases, the further downstream the resonator is situated (black curve in figure 6.2). Obviously, if the resonator location lies

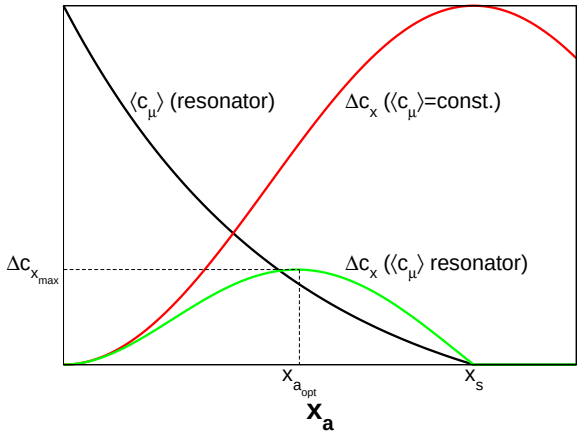

FIGURE 6.2: Schematic to illustrate the behavior of the momentum coefficient $\langle c_\mu \rangle$ and the change Δc_x in the figure of merit depending on the resonator location x_a with respect to the separation line x_s in situations governed by an adverse pressure gradient. The resulting optimum resonator location is denoted by $x_{a_{opt}}$.

downstream of the line where the flow separates from the wall ($x_a \geq x_s$), no aerodynamic excitation occurs. Therefore, the optimum resonator location $x_{a_{opt}}$ is a compromise between sufficient flow induction on the one hand, and proximity to the separation line on the other (green curve in figure 6.2). In non-dimensional form, this location is described by the optimum distance between actuator and separation line $x_s - x_a$ with respect to the characteristic length L.

The application of a resonator, thus, seems promising to control separation induced by geometry, e.g. by a surface discontinuity or edge, or by a strong adverse pressure gradient. When the prevailing pressure gradient is weak, the resonator should be placed far upstream of the separation line to ensure adequate excitation. However, in this case the vortices produced might not persist long enough to significantly manipulate the reverse-flow region.

6.3 Manipulation of zero pressure-gradient turbulent flow

This section examines the impact of the aerodynamically excited oscillations of a resonator on the turbulent boundary layer downstream in a zero pressure-gradient flow. A description of the experimental apparatus was given in section 3.2.2. The velocity data presented were obtained by LDA measurements, while the wall shear-stress used for normalization of the profiles was determined by a Preston tube.

In the following, the baseline-flow conditions will be compared with the case manipulated by the resonant oscillations for a Reynolds number of $Re_u = 6.5 \times 10^5$. An overview of the resulting boundary-layer characteristics is given in table 6.2 for the streamwise location closest to the resonator.

Flow	Re_u [−]	Re_{δ_2} [−]	δ_{99} [mm]	δ_1 [mm]	δ_2 [mm]	H_{12} [−]	c_f [−]
Baseline	6.5×10^5	987	13.54	2.21	1.50	1.47	4.07×10^{-3}
Manipulated	6.5×10^5	1058	13.98	2.44	1.62	1.50	3.96×10^{-3}

TABLE 6.2: Characteristic quantities of the boundary layer in the wake of the resonator ($x - x_{LE} = 18.65$ mm, where x_{LE} denotes the streamwise location of the leading edge of the resonator neck). The data apply to figures 6.3 to 6.8. Case with resonance: $2s = 9$ mm, $l_y = 130$ mm, neck geometry A30/K5, $St_{2s} = 0.19$, $p_{cav}/p_{dyn} = 46\,\%$.

6.3.1 Time-averaged velocity profiles

In the baseline-flow case, the time-averaged profiles of all quantities discussed in the present section show very good agreement with the data review com-

piled by Fernholz & Finley (1996).

As a consequence of the resonator oscillations, however, the normalized profiles of the mean streamwise velocity U show appreciable differences confined to the range between 4 and 40 % of the boundary layer thickness δ_{99}. This is equivalent to the region of the logarithmic law extending from $y^+ = 15$ to 150 (figure 6.3). $U^+ = U/u_\tau$ and $y^+ = yu_\tau/\nu$ denote the mean streamwise velocity component and the distance normal to the wall in inner-law scaling. When the resonator is oscillating, a marked velocity deficit occurs in the abovementioned range. Similar behavior was reported by Flynn *et al.* (1990), whose measurements, however, did not cover the near-wall region at $y^+ < 15$. The resulting momentum deficit associated with the oscillations corresponds to the difference between energy convected into the resonator by the flow, and energy convected out. According to De Metz & Farabee (1977), this difference is radiated out as acoustic energy or dissipated within the resonator by heat conduction and viscous effects.

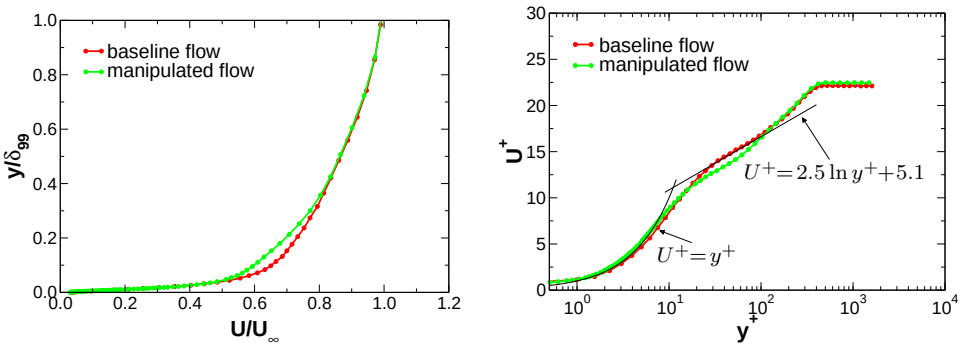

FIGURE 6.3: Mean velocity profiles of the boundary layer in the wake of the resonator. $Re_u = 6.5 \times 10^5$, $x - x_{LE} = 18.65\,\text{mm}$. Case with resonance: $2s = 9\,\text{mm}$, $l_y = 130\,\text{mm}$, neck geometry A30/K5, $St_{2s} = 0.19$, $p_{cav}/p_{dyn} = 46\,\%$.

In case of resonance, the rms-values of the streamwise velocity fluctuations u'_{rms} increase in a range from $y/\delta_{99} = 3$ to 50 %, equivalent to $y^+ = 15$ to 200 (figure 6.4). A very small difference compared to the baseline case even persists beyond the edge of the boundary layer. The location of the maximum of $u'_{rms}/\overline{u_\tau}$ shifts from $y^+ = 13$ to 19. For wall distances $y^+ < 4$, the streamwise velocity fluctuations are slightly less when the resonator oscillates. This might be related to the smaller wall shear-stress measured in the presence of resonance (see table 6.2).

The velocity fluctuations induced by the oscillations of the resonator are most noticeable in the v'_{rms} distribution (figure 6.4). Strong variations between baseline and manipulated flow occur in the range $0.01 < y/\delta_{99} < 0.6$, or $2 < y^+ < 300$, respectively. In particular, the maximum increased by as much as 50 % from $v'_{rms}/\overline{u_\tau} = 1.08$ to 1.62, while it is also moved closer to the wall from $y^+ = 83$ to 62.

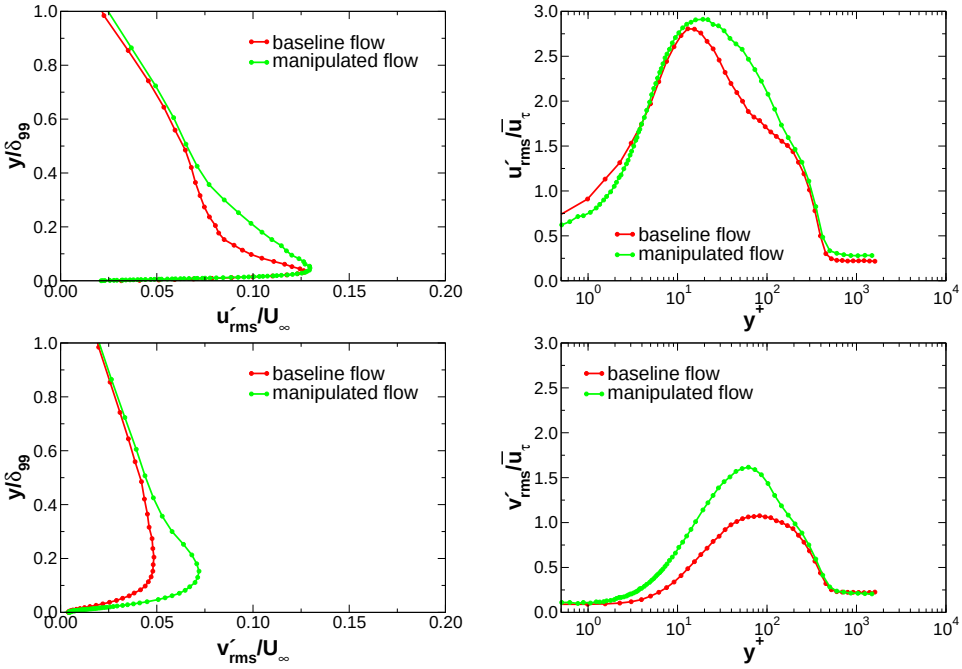

FIGURE 6.4: Profiles of u'_{rms} and v'_{rms} in the wake of the resonator. $Re_u = 6.5 \times 10^5$, $x - x_{LE} = 18.65\,\text{mm}$. Case with resonance: $2s = 9\,\text{mm}$, $l_y = 130\,\text{mm}$, neck geometry A30/K5, $St_{2s} = 0.19$, $p_{cav}/p_{dyn} = 46\,\%$.

The distribution of $\overline{u'v'}$ is given in figure 6.5. While the baseline case corresponds well with values presented in the review by Fernholz & Finley (1996), the data do not show a clear trend in the presence of resonance. In the range $y^+ = 20$ to 350, the Reynolds shear-stress varies strongly and is mostly less than for unperturbed conditions. At $y^+ = 50$, the distribution of $-\overline{u'v'}/\overline{u_\tau}^2$ jumps sharply from rather low values near the wall to higher

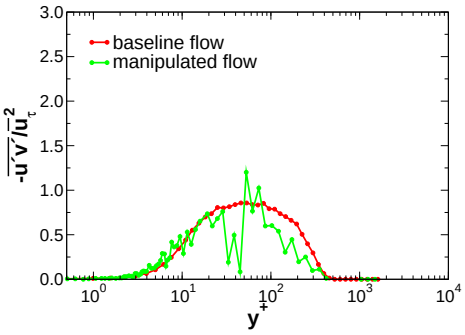

FIGURE 6.5: Profile of $\overline{u'v'}/\overline{u_\tau}^2$ in the wake of the resonator. $Re_u = 6.5 \times 10^5$, $x - x_{LE} = 18.65\,\text{mm}$. Case with resonance: $2s = 9\,\text{mm}$, $l_y = 130\,\text{mm}$, neck geometry A30/K5, $St_{2s} = 0.19$, $p_{cav}/p_{dyn} = 46\,\%$.

values in the outer region of the boundary layer. In view of the large amount of samples averaged for each data point, this behavior is somewhat surprising. The strong distortion might be attributed to highly unsteady processes induced by the vortices ejected from the resonator orifice.

6.3.2 Phase-averaged velocity profiles

The phase-averaged data presented in this section illustrate the variations of both velocity profiles and boundary-layer characteristics during one cycle of the resonator oscillations.

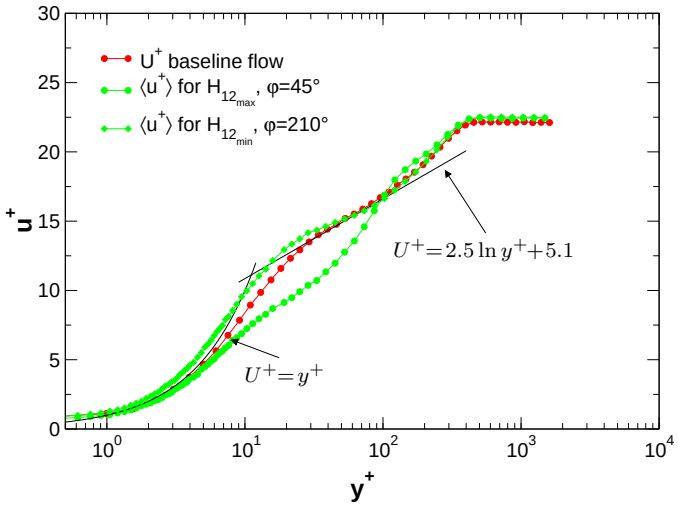

FIGURE 6.6: Phase-averaged velocity profiles of the boundary layer in the wake of the resonator. $Re_u = 6.5 \times 10^5$, $x - x_{LE} = 18.65\,\text{mm}$. Case with resonance: $2s = 9\,\text{mm}$, $l_y = 130\,\text{mm}$, neck geometry A30/K5, $St_{2s} = 0.19$, $p_{cav}/p_{dyn} = 46\,\%$.

Figure 6.6 shows the profiles of the streamwise velocity at phase angles associated with the minimum and maximum instantaneous shape factor $\langle H_{12} \rangle$, respectively, in comparison to the baseline case. Depending on the phase, both profiles vary widely as virtually the entire velocity distribution from $y^+ = 1$ to 300 is affected by the oscillations. The deviations are most pronounced in the range $5 < y^+ < 80$. It is interesting to note that the profile with minimum $\langle H_{12} \rangle$ is even fuller than the unperturbed one.

As a consequence of the strong variations in the mean velocity profile during one cycle, the characteristics of the boundary-layer in terms of its thickness, the shape factor, and the skin friction are altered as well. Each of the boundary-layer thicknesses $\langle \delta_{99} \rangle$, $\langle \delta_1 \rangle$, and $\langle \delta_2 \rangle$ changes by about $\pm 5\,\%$ from their respective time mean throughout one cycle of oscillation (figure 6.7). All three parameters show identical, nearly sinusoidal behavior with the phase angle.

As seen in figure 6.8, the shape factor $\langle H_{12} \rangle$ and the skin-friction coeffi-

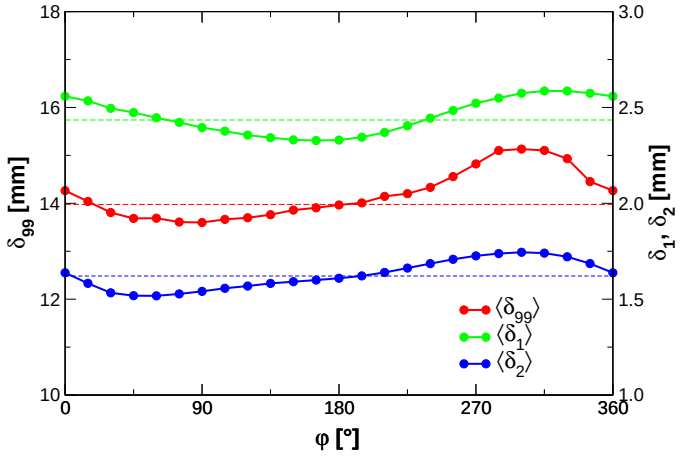

FIGURE 6.7: Phase-averaged boundary layer thicknesses $\langle\delta_{99}\rangle$, $\langle\delta_1\rangle$, and $\langle\delta_2\rangle$ downstream of the resonator as a function of the phase angle φ of the oscillation. $Re_u = 6.5 \times 10^5$, $x - x_{LE} = 18.65\,\text{mm}$, $2s = 9\,\text{mm}$, $l_y = 130\,\text{mm}$, neck geometry A30/K5, $St_{2s} = 0.19$, $p_{cav}/p_{dyn} = 46\,\%$. The dashed lines indicate the respective mean values.

cient $\langle c_f\rangle$ vary in a similar fashion throughout the phase. For the representation of $\langle c_f\rangle$, the phase-averaged values were determined from the wall-normal gradient of the streamwise velocity component as described in appendix B.2. The maximum of the shape factor, $\langle H_{12}\rangle = 1.63$, is obtained at a phase angle of $\varphi = 45°$, while the minimum occurs at $\varphi = 210°$ with a value of 1.45. Correspondingly, the skin friction varies by as much as -18 and $+11\,\%$ from the time mean. Both parameters reflect well how the velocity profiles near

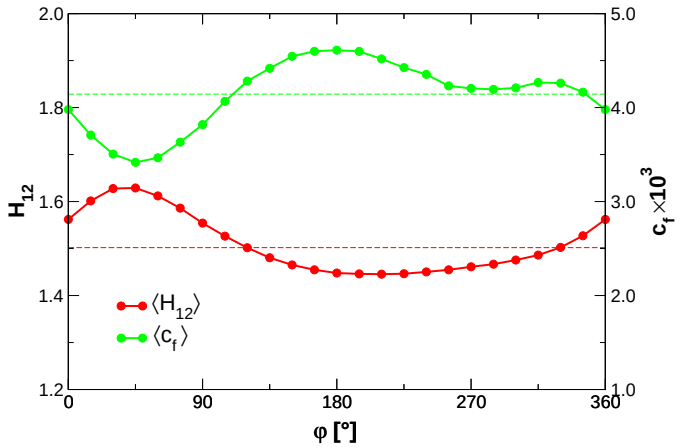

FIGURE 6.8: Phase-averaged shape factor $\langle H_{12}\rangle$ and skin-friction coefficient $\langle c_f\rangle$ downstream of the resonator as a function of the phase angle φ of the oscillation. $\langle c_f\rangle$ was determined from the wall-normal velocity gradient. $Re_u = 6.5 \times 10^5$, $x - x_{LE} = 18.65\,\text{mm}$, $2s = 9\,\text{mm}$, $l_y = 130\,\text{mm}$, neck geometry A30/K5, $St_{2s} = 0.19$, $p_{cav}/p_{dyn} = 46\,\%$. The dashed lines indicate the respective mean values.

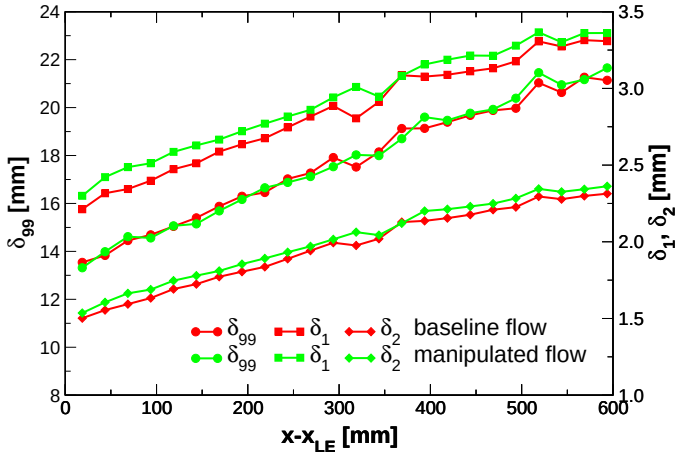

FIGURE 6.9: Downstream development of the 99 %-thickness δ_{99}, the displacement thickness δ_1, and the momentum thickness δ_2 of the boundary layer in the resonator wake. $Re_u = 6.5 \times 10^5$. Case with resonance: $2s = 9\,\text{mm}$, $l_y = 130\,\text{mm}$, neck geometry A30/K5, $St_{2s} = 0.19$, $p_{cav}/p_{dyn} = 46\,\%$.

the wall change with the passage of vortices ejected from the resonator.

6.3.3 Streamwise development of the boundary-layer properties

Figures 6.9 and 6.10 show the variations of δ_{99}, δ_1, δ_2, H_{12}, and c_f in streamwise direction caused by the resonator oscillations. In both plots, the slight irregularities occurring around the location $x - x_{LE} = 320\,\text{mm}$ are due to a link in the measurement surface.

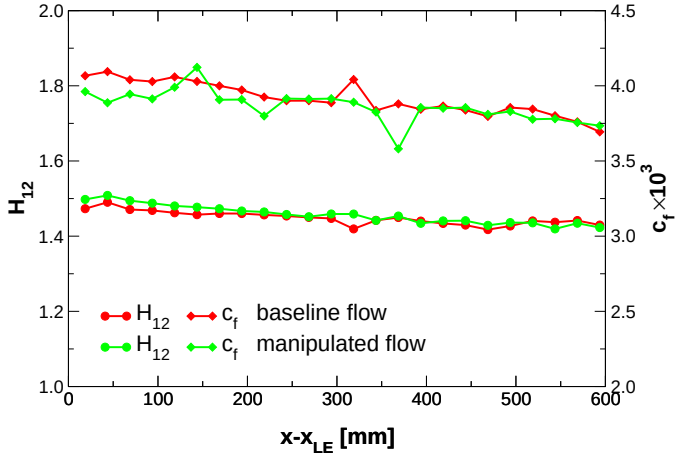

FIGURE 6.10: Downstream development of the shape factor H_{12} and the skin-friction coefficient c_f in the wake of the resonator. $Re_u = 6.5 \times 10^5$. Case with resonance: $2s = 9\,\text{mm}$, $l_y = 130\,\text{mm}$, neck geometry A30/K5, $St_{2s} = 0.19$, $p_{cav}/p_{dyn} = 46\,\%$.

The three quantities characterizing the boundary-layer thickness increase downstream of the resonator in the expected way (figure 6.9). Both the displacement and the momentum thickness display the differences between baseline- and manipulated-flow case clearly, although such a behavior is not seen for the 99 %-thickness. The increase of δ_1 and δ_2 indicates that, in the presence of oscillations, the boundary layer is rearranged directly downstream of the orifice. With further distance, this change persists as a constant increment beyond the end of the test section.

The shape factor and the skin-friction coefficient, however, differ only up to about $x - x_{LE} = 250\,\text{mm}$ downstream of the actuator (figure 6.10). In this region, c_f is reduced when the resonator oscillates, while H_{12} is increased.

6.4 Control of separation in a diffuser

In this section, an aerodynamically excited resonator controls the flow separating in a diffuser. At first, section 6.4.1 discusses the limitations of the applicability of this method in situations governed by a mild adverse pressure gradient. The remainder of section 6.4 deals with a sample case where flow separation is induced by an abrupt change in the wall geometry at the diffuser entrance (Bake, 2002). Under these circumstances, the resonator can be employed advantageously.

6.4.1 Some notes on controlling flow separation induced by a mild adverse pressure gradient

Different flow conditions with varying adverse pressure gradients could be generated by changing the expansion angle of the diffuser (section 5.1). The active actuator associated with this set-up was replaced by a passive resonator for the following experiments.

By enlarging the diffuser expansion angle β, the adverse pressure gradient and the momentum thickness of the boundary layer in the diverging section increased. This had two implications for the manipulation of the flow: First, with increasing angle the amplitude of the flow-induced resonator oscillations deteriorated while the resonance regime became drastically smaller (figure 6.11). For $\beta > 10°$, no resonance could be excited at all. Second, the flow in the diffuser did not separate unless the expansion angle exceeded 10°. The separation line moved upstream, the more aggressively the diffuser expanded. This implies that under flow conditions where the resonator was excited no separation occurred in the diffuser. In turn, once the pressure gradient was strong enough to prompt separation, the conditions were too unfavorable to induce resonator oscillations. This is illustrated in figure 6.12, where a relative location $(x_{DO} - x_s)/(x_{DO} - x_{LE})$ of the separation line of 100 % would indicate that the reverse-flow region reached the resonator slit. x_{DO} and x_{LE} denote the locations of the diffuser outlet and of the leading

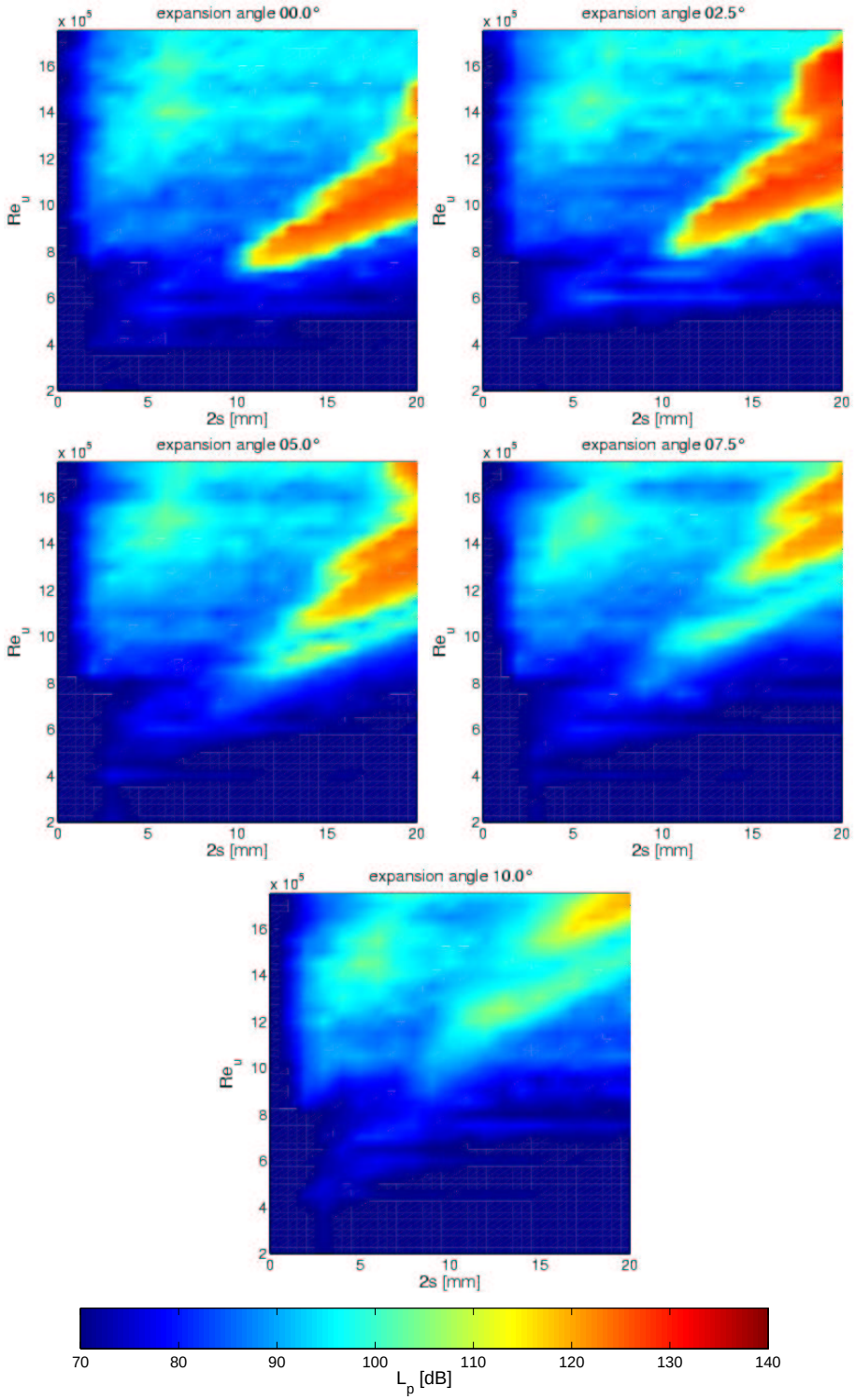

FIGURE 6.11: Sound-pressure level (see color scale) of the resonance peaks depending on Reynolds number and slit width: Diffuser expansion angle β varies from 0° to 10°. Neck geometry A30*/K5*, $l_y = 130\,\text{mm}$, $l_n = 9.35\,\text{mm}$.

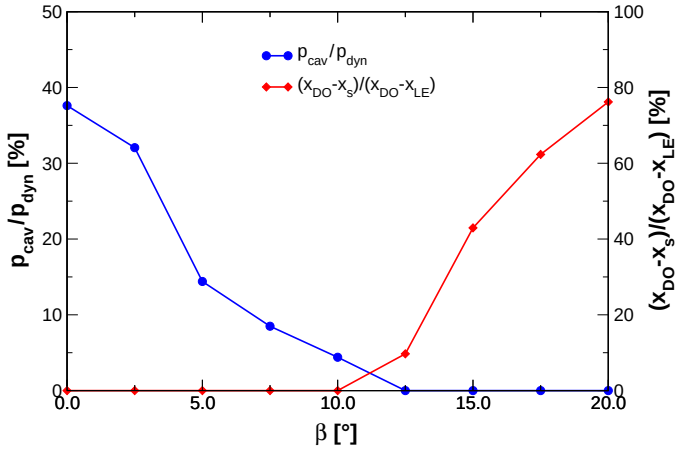

FIGURE 6.12: Relative flow-induced sound pressure p_{cav}/p_{dyn} in the resonator cavity and relative location $(x_{DO} - x_s)/(x_{DO} - x_{LE})$ of the separation line depending on the diffuser expansion angle β. The maxima of p_{cav}/p_{dyn} were obtained from figure 6.11 and are associated with varying Reynolds numbers and slit widths. The separation line is given for $Re_u = 1.5 \times 10^6$. $l_y = 130\,\text{mm}$, neck geometry A30*/K5*.

edge of the resonator neck, respectively, while x_s represents the position of the separation line.

This outcome rendered the described set-up impractical for flow control by a resonator and it had to be altered as specified in section 6.4.2.

6.4.2 Experimental set-up

The experimental set-up used to investigate separation control by means of a resonator was a modification of the planar asymmetric diffuser presented in section 5.1. The flexible joint at the diffuser entrance was replaced by a rigid connection fixing the expansion angle at $\beta = 23°$ (figure 6.13). As a result, the diffuser inlet was located at $x_{DI} = 740\,\text{mm}$ followed by the expanding section of length 340 mm.

In contrast to the previous set-up, the adaptive resonator was positioned

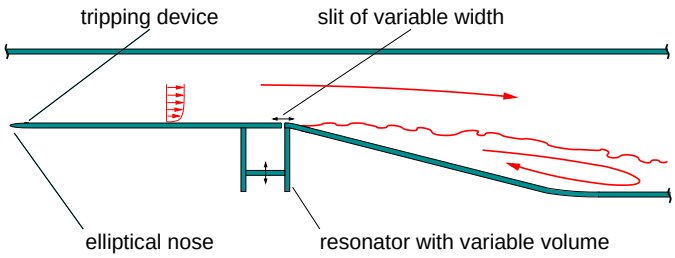

FIGURE 6.13: Schematic of the experimental set-up to control the separation region in a planar asymmetric diffuser by means of a flow-induced resonator.

just upstream of the diffuser entrance ($x_{DI} - x_{LE} = 25\,\text{mm}$), where the flow was still attached. This ensured optimum conditions for the aerodynamic excitation. The resonator featured a cavity of rectangular cross-section (see section 2.1.1) and was equipped with the optimized neck geometry A30*/K5*.

Tufts were attached to the wall opposite to the inclined bottom plate to monitor that the flow would not separate in this region. This is important when applying flow control to ensure that the flow does not just flip unnoticed, therefore staying attached on the diverging wall of the diffuser, but forming a reverse-flow region elsewhere instead.

6.4.3 Baseline flow inside the diffuser

The topology of the baseline flow in the diffuser is illustrated in figures 6.14 and 6.15. Both the velocity vectors and the streamlines imply that the approaching boundary layer separates directly at the entrance to the diffuser and proceeds as a free shear layer downstream. The flow forms a closed reverse-flow region of length $L = 945\,\text{mm}$, according to the wall pulsed-wire measurement shown in figure 6.22. At a Reynolds number of $Re_u = 7.0 \times 10^5$,

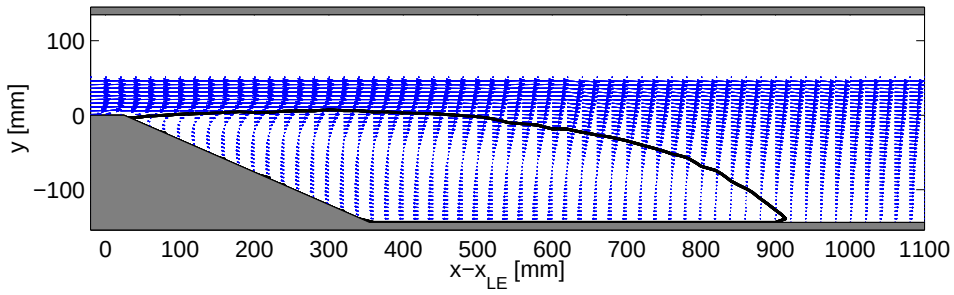

FIGURE 6.14: Time mean velocities of the baseline flow field in the center plane of the diffuser. The black curve indicates where the stream function vanishes. $Re_u = 7.0 \times 10^5$.

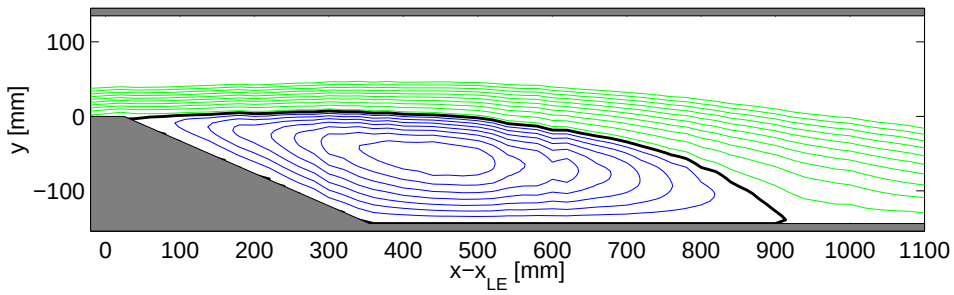

FIGURE 6.15: Time mean streamlines computed from the baseline velocity field in the center plane of the diffuser. Depending on its value, the stream function is represented in green ($\Psi > 0$), black ($\Psi = 0$), or blue ($\Psi < 0$). $Re_u = 7.0 \times 10^5$.

the pressure recovery amounts to $c_p = 0.315$, equivalent to $c_p/c_{p_{\text{pot}}} = 0.410$.

The free shear layer downstream of the diffuser inlet is governed by large-scale vortices that are averaged out in figures 6.14 and 6.15. Although the process is highly stochastic, in the time mean a preferred frequency of the vortex shedding can be observed depending on the Reynolds number. It is worthwhile to determine these frequencies, e.g. via the power spectral density of the streamwise velocity fluctuations, since they are effective excitation frequencies when controlling the flow (Huppertz & Fernholz, 2002).

For this purpose, spectra at the outer edge of the free shear layer were recorded (figure 6.16). The measurement position ($x - x_{DI} = 375\,\text{mm}$, $y = 32\,\text{mm}$) was chosen according to Huppertz & Fernholz (2002).

The reduced frequency St_L based on the characteristic length L of the separation region was determined at the peak of the power spectral density distribution of the streamwise velocity fluctuations. St_L varies only slightly with unit Reynolds number Re_u. Between $Re_u = 5.0 \times 10^5$ and 10.0×10^5, it shifts from $St_L = 1.55$ to 1.90, while it remains constant for higher Reynolds numbers.

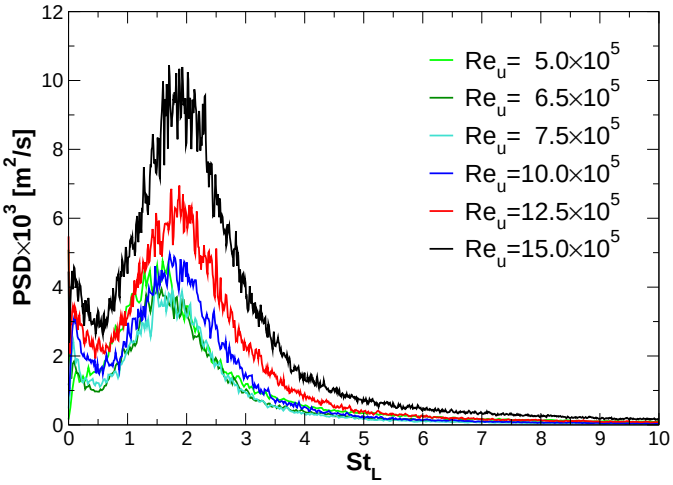

FIGURE 6.16: Power spectral density (PSD) distribution of the streamwise velocity fluctuations at the outer edge of the unperturbed shear layer.

6.4.4 Resonator output

The fluctuating velocity field in the neck of the aerodynamically excited resonator used to control the separation region in the diffuser is characterized in figure 6.17 during one cycle of oscillation. The data correspond to the case of most efficient control, which will be investigated in detail in section 6.4.5.

It can be seen that the reciprocating fluid motion in the neck is not homogeneous in x-direction. Instead, the streamwise location of the maximum in $\langle v \rangle$ varies with the phase as a consequence of a vortex being convected across

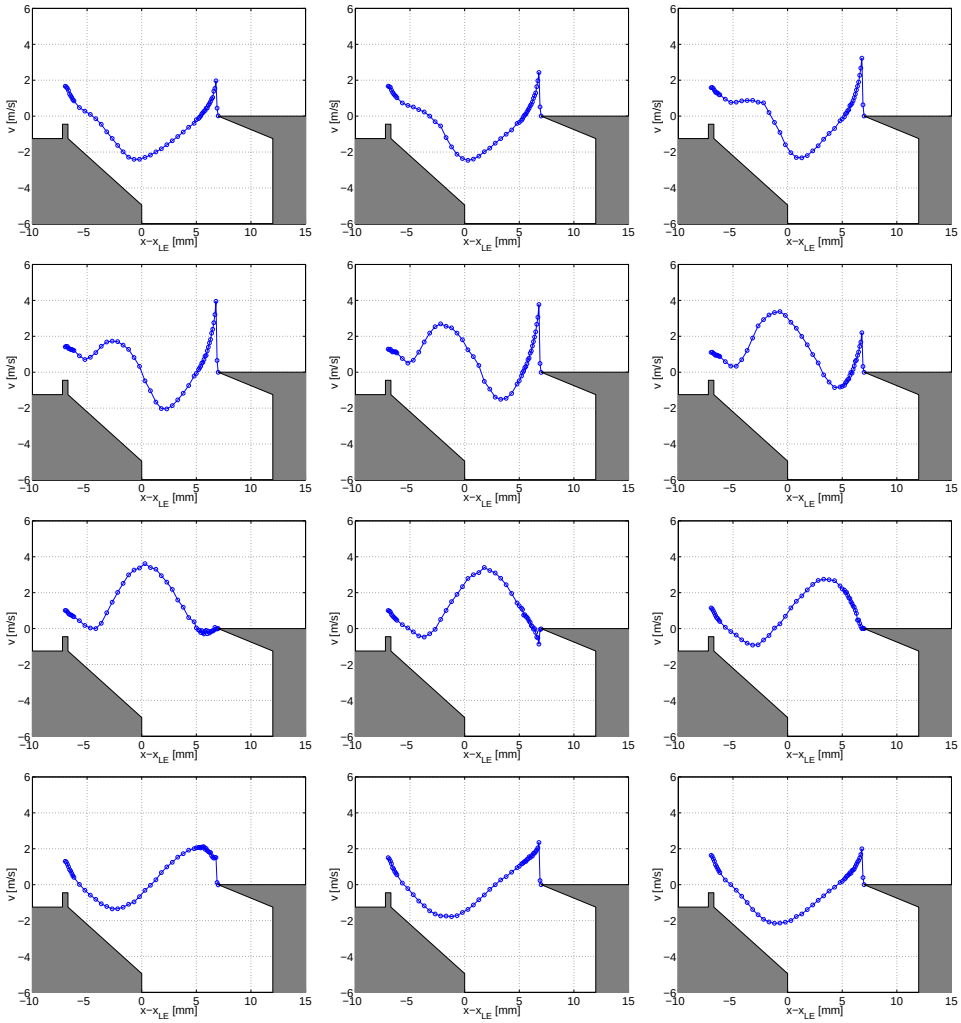

FIGURE 6.17: Phase-averaged vertical velocity component v in resonator orifice at different phase angles ($\Delta\varphi = 30°$). $Re_u = 7.0 \times 10^5$, $2s = 12\,\text{mm}$, $l_n = 9.35\,\text{mm}$, $l_y = 130\,\text{mm}$, neck geometry A30*/K5*, $St_{2s} = 0.22$, $\langle c_\mu \rangle = 4.4 \times 10^{-4}$.

the opening. The interaction of this vortex with the downstream edge causes a sharp, time-dependent peak in the v-component in this region. Generally, the absolute value of the velocities associated with local outflow are higher by as much as a factor two than those associated with local inflow.

LDA measurements of this kind served to provide the data basis for a very accurate computation of $\langle c_\mu \rangle$ according to equations (5.4) and (5.5), which involve both integration in time and in streamwise direction.

6.4.5 Results obtained with a single resonator

The pressure fluctuations generated by the flow-induced resonator located at the diffuser entrance are shown in figure 6.18 (top) depending on Reynolds number and slit width. For every Reynolds number above $Re_u = 4.0 \times 10^5$, a corresponding slit width can be found such that strong resonance occurs. Under all resonant flow conditions, the Helmholtz mode of oscillation was excited. In conjunction with figure 6.18 (bottom), it can be seen that the pressure recovery in the diffuser was enhanced whenever the resonator was set oscillating by the cross-flow. Below $Re_u = 4.5 \times 10^5$, no improvement could be achieved. In this Reynolds-number regime, the flow at the diffuser entrance was still laminar.

At each Reynolds number, an optimum slit width can be chosen such

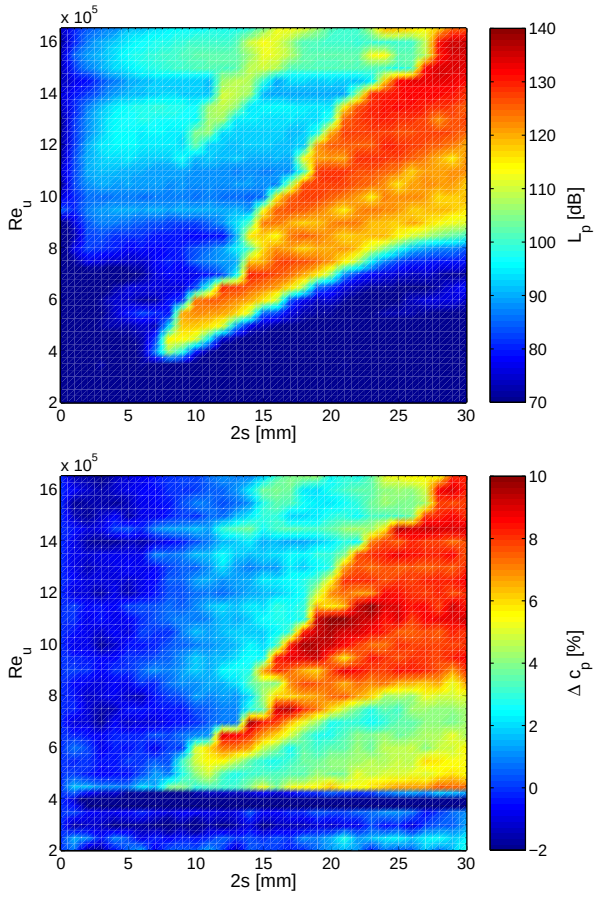

FIGURE 6.18: Sound-pressure level L_p generated by the flow-induced resonator (top) along with the resulting change of the pressure recovery Δc_p in the diffuser (bottom) depending on Reynolds number Re_u and slit width $2s$. $l_n = 9.35\,\text{mm}$, $l_y = 130\,\text{mm}$, neck geometry A30*/K5*.

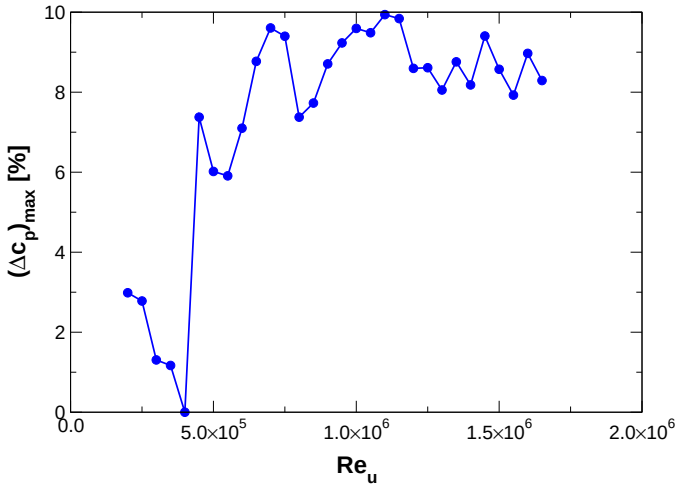

FIGURE 6.19: Improvement of the pressure recovery Δc_p in the diffuser resulting from the resonator oscillations as a function of the Reynolds number Re_u. Data extracted from figure 6.18 (bottom) for the respective optimum choice of slit width. $l_n = 9.35\,\text{mm}$, $l_y = 130\,\text{mm}$, neck geometry A30*/K5*.

that the induced resonator oscillations maximize the pressure recovery. The associated values of Δc_p extracted from figure 6.18 (bottom) are shown in figure 6.19. For all Reynolds numbers greater than $Re_u = 4.0 \times 10^5$, the pressure recovery was enhanced by 6 to 10 %.

When hysteresis effects were exploited (see figure 3.42), c_p could be improved by as much as 13 % at $Re_u = 7.0 \times 10^5$. The associated slit width of the resonator was 12 mm in this case, and the oscillations provided a momentum coefficient of $\langle c_\mu \rangle = 4.4 \times 10^{-4}$ at a reduced frequency of $St_{2s} = 0.22$. Scaled with the characteristic length of the separated flow region, the frequency measured $St_L = 17.33$, which was an order of magnitude above the natural frequency of the vortex shedding in the free shear layer (see section 6.4.3). This case of most effective separation control was investigated in greater detail.

A comparison of the reverse-flow factor χ throughout the flow field within the diffuser is shown in figure 6.20 for the baseline flow and for the case of optimum pressure recovery. In spite of the noticeable change in c_p, however, the differences in the flow fields are relatively small. Besides a sparse overall reduction of χ, they are confined to the area directly downstream of the inlet and around the end of the separation region.

A better perception of the variation of the recirculation zone due to the manipulation, can be obtained by calculating the line where the stream function Ψ vanishes: Figure 6.21 implies that, in the time mean, the improvement of the pressure recovery is a result of the slight reduction in height and length of the separation region.

A quantitative assessment of the changes caused by the resonator oscilla-

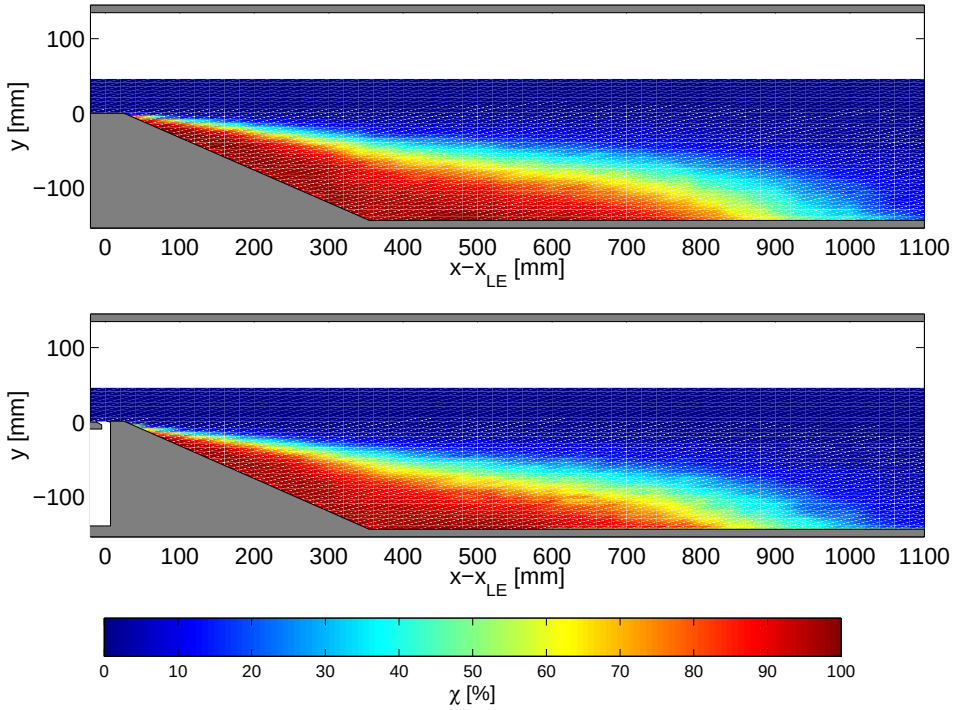

FIGURE 6.20: Time mean reverse-flow factor χ computed from the velocity field in the center plane of the diffuser for the baseline flow (top) and with separation control by a resonator (bottom). $Re_u = 7.0 \times 10^5$. Controlled case: $2s = 12\,\text{mm}$, $l_n = 9.35\,\text{mm}$, $l_y = 130\,\text{mm}$, neck geometry A30*/K5*, $St_{2s} = 0.22$, $\langle c_\mu \rangle = 4.4 \times 10^{-4}$.

tions is given by the reverse-flow-factor χ_w and the skin-friction coefficient c_f along the bottom wall of the diffuser (figure 6.22). The differences between baseline and manipulated case were most pronounced in the region downstream of the diffuser inlet and near the reattachment line. In both areas,

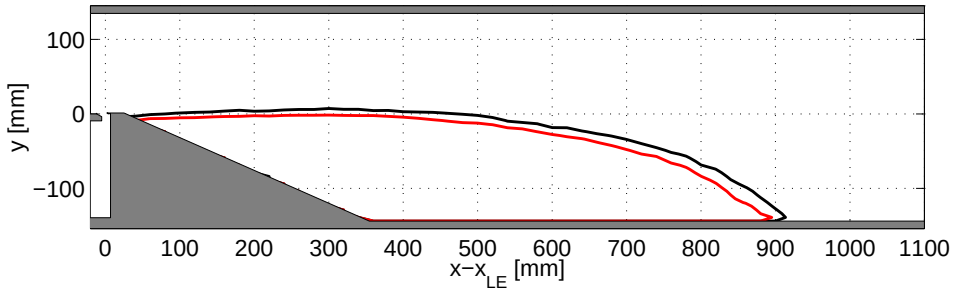

FIGURE 6.21: Streamlines with $\Psi = 0$ computed from the velocity field in the center plane of the diffuser for the baseline flow (black) and with separation control by a resonator (red). $Re_u = 7.0 \times 10^5$. Controlled case: $2s = 12\,\text{mm}$, $l_n = 9.35\,\text{mm}$, $l_y = 130\,\text{mm}$, neck geometry A30*/K5*, $St_{2s} = 0.22$, $\langle c_\mu \rangle = 4.4 \times 10^{-4}$.

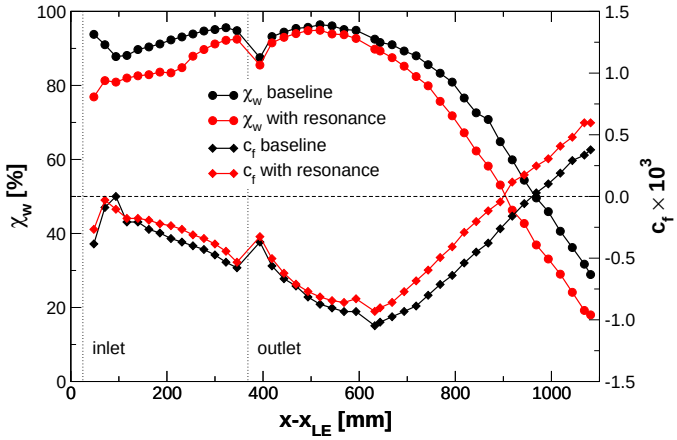

FIGURE 6.22: Reverse-flow factor χ_w and skin-friction coefficient c_f along the bottom wall of the diffuser from wall pulsed-wire measurement. The dotted vertical lines mark the diffuser inlet and outlet, respectively. $Re_u = 7.0 \times 10^5$. Controlled case: $2s = 12\,\text{mm}$, $l_n = 9.35\,\text{mm}$, $l_y = 130\,\text{mm}$, neck geometry A30*/K5*, $St_{2s} = 0.22$, $\langle c_\mu \rangle = 4.4 \times 10^{-4}$.

the reverse-flow factor was reduced by about 10 % as a result of the actuation. In contrast, the skin-friction coefficient remained nearly unaffected throughout the expanding section, while it was increased in the last third of the reverse-flow region. Both χ_w and c_f indicate that the length of the recirculation zone was reduced by 62 mm, i.e. 6.5 %, due to the flow control.

6.4.6 Results obtained with systems of adjacent resonators

While the maximum improvement of the pressure recovery in the diffuser amounted to 13 % with control by a single flow-induced resonator, a system of two adjacent resonators oscillating in anti-phase caused c_p to increase by as much as 18 %. The superposition of the oscillation modes of three resonators showed no advantage over a single resonator, as the pressure recovery was equally enhanced by 13 %. An overview of the results for the different resonator configurations is given at the end of this section in table 6.3.

In order to capture the effects of systems of adjacent resonators on the flow field, LDA measurements in the x,z-plane of the diffuser were performed. In particular, the reverse-flow factor χ at a wall distance of 1 mm was determined throughout the upstream half of the recirculation zone. The measurement was restricted to the inner 80 % of the diffuser width to exclude the influence of the decelerated flow in the corners. A small region that was optically inaccessible by the LDA probe is left blank in the corresponding figures 6.23 to 6.25.

The reverse-flow factor associated with the baseline flow field is represented in figure 6.23 at $Re_u = 7.0 \times 10^5$ (left) and 1.6×10^6 (right). Both plots exemplify that the flow separated abruptly at the diffuser inlet and did

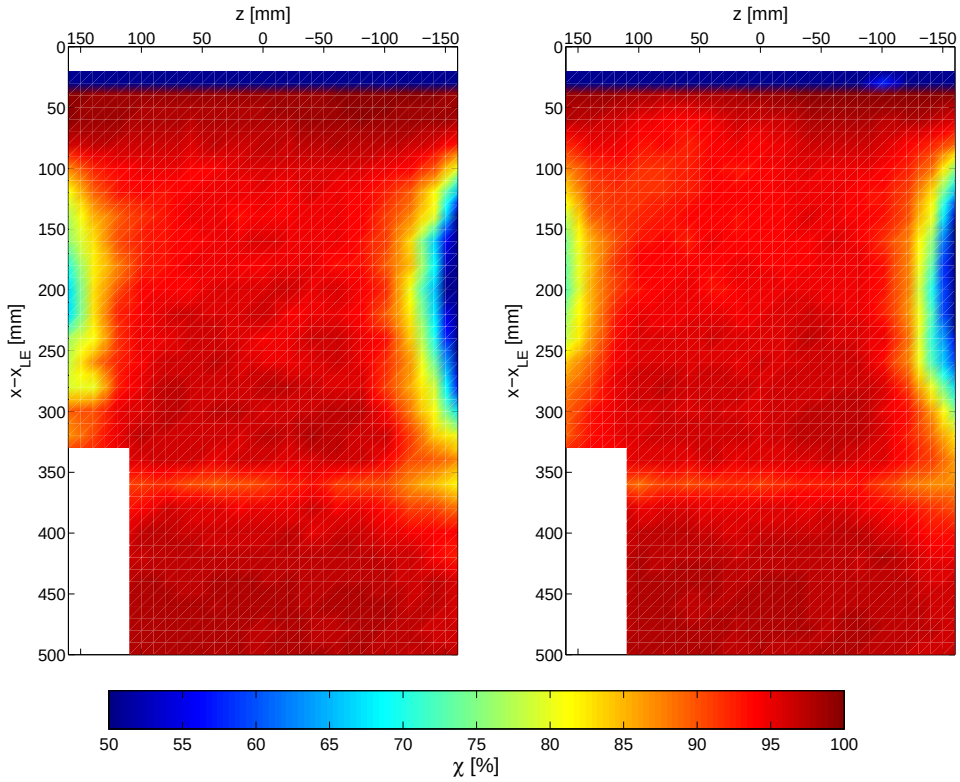

FIGURE 6.23: LDA measurement of the reverse-flow factor χ in the x,z-plane of the diffuser at a wall distance of 1 mm. Baseline flow at $Re_u = 7.0 \times 10^5$ (left) and at $Re_u = 1.6 \times 10^6$ (right). Upstream half of diffuser shown, free-stream is from top to bottom.

not reattach within the area investigated. The influence of the flow in the corners can be identified by small domains of reduced χ near the sidewalls of the expanding section. Since no significant differences are apparent, this implies that the separation region was not Reynolds-number dependent in the range of interest.

Figure 6.24 (left) shows how the flow field at $Re_u = 7.0 \times 10^5$ differed when it was manipulated by a single resonator compared to the baseline case of figure 6.23 (left): The effects of the control were mainly confined to the region directly downstream of the resonator extending up to $x - x_{LE} \approx 60\,\text{mm}$, where χ was noticeably reduced. This case of control achieved an improvement of 13 % in c_p by applying a momentum coefficient of $\langle c_\mu \rangle = 4.4 \times 10^{-4}$.

The corresponding flow fields manipulated by a single resonator (figure 6.24, left) and by a set of two resonators that oscillated in phase (figure 6.24, right) exhibited no significant differences. The pressure recovery (13 and 14 %, respectively) was virtually identical in both cases, although the

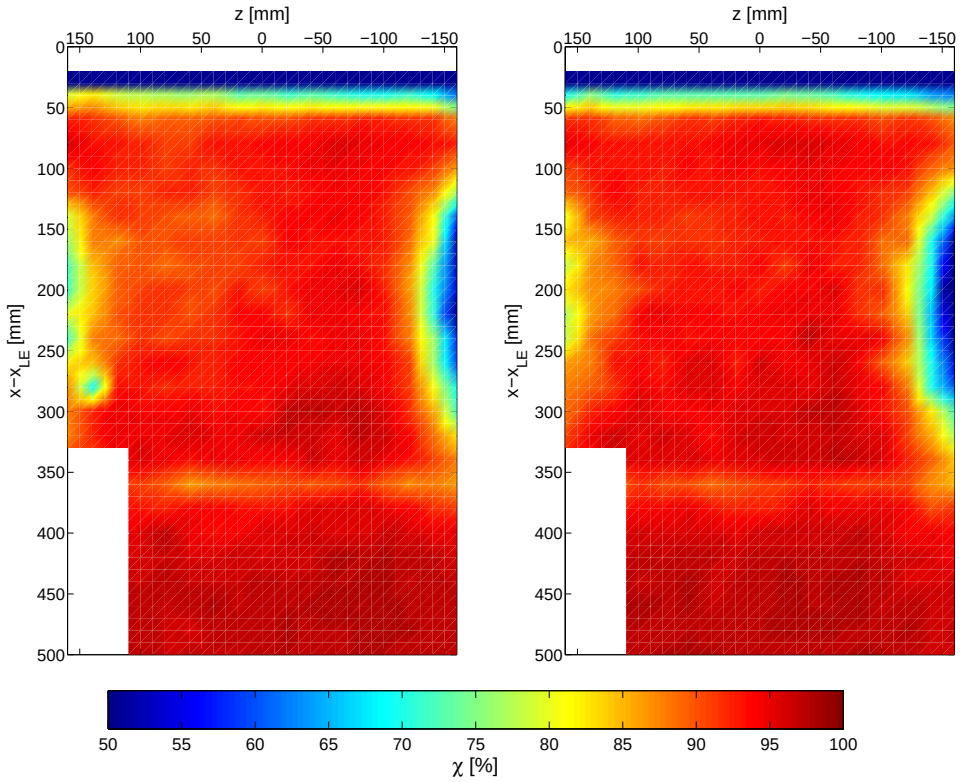

FIGURE 6.24: LDA measurement of the reverse-flow factor χ in the x,z-plane of the diffuser at a wall distance of 1 mm. $Re_u = 7.0 \times 10^5$, $l_n = 9.35$ mm, neck geometry A30*/K5*. Left: 1 resonator, $2s = 12$ mm, $l_y = 130$ mm, $St_{2s} = 0.22$, $\langle c_\mu \rangle = 4.4 \times 10^{-4}$, $\Delta c_p = 13\,\%$. Right: 2 resonators oscillating in phase ($\varphi_{12} = 0°$), $2s = 12$ mm, $l_y = 125$ mm, $St_{2s} = 0.23$, $\langle c_\mu \rangle = 2.5 \times 10^{-4}$, $\Delta c_p = 14\,\%$. Upstream half of diffuser shown, free-stream is from top to bottom.

momentum coefficients produced were unequal (4.4×10^{-4} and 2.5×10^{-4}, respectively).

In contrast, a change in the mode from *in-phase* oscillations of two adjacent resonators at $Re_u = 7.0 \times 10^5$ (figure 6.24, right) to *anti-phase* behavior at $Re_u = 1.6 \times 10^6$ (figure 6.25, left) prompted pronounced variations in the separation region. In the latter case, the effect of the control was drastic and persisted until far downstream. The asymmetry in the χ-distribution might have resulted from the phase difference φ_{12} being 160° instead of an exact anti-phase, as no asymmetries could be observed in the initial conditions or in the oscillatory behavior of both resonators involved. With an improvement of the pressure recovery by as much as 18 %, this case represented the most effective control of separation. It is interesting to note that the momentum coefficient $\langle c_\mu \rangle = 4.5 \times 10^{-4}$ was almost identical to the case of the single resonator.

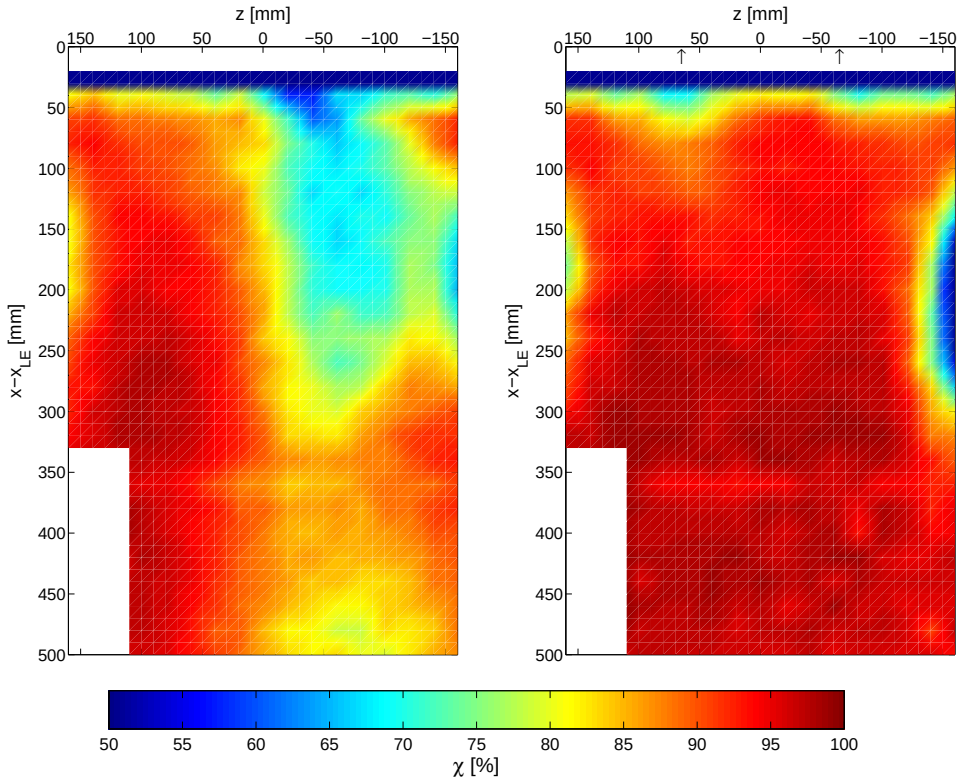

FIGURE 6.25: LDA measurement of the reverse-flow factor χ in the x,z-plane of the diffuser at a wall distance of 1 mm. $Re_u = 1.6 \times 10^6$, $l_n = 9.35$ mm, neck geometry A30*/K5*. Left: 2 resonators oscillating in anti-phase ($\varphi_{12} = 160°$), $2s = 28$ mm, $l_y = 125$ mm, $St_{2s} = 0.34$, $\langle c_\mu \rangle = 4.5 \times 10^{-4}$, $\Delta c_p = 18\,\%$. Right: 3 resonators oscillating with superimposing modes, $2s = 28$ mm, $l_y = 125$ mm, $St_{2s} = 0.32$, $\langle c_\mu \rangle = 6.6 \times 10^{-4}$, $\Delta c_p = 13\,\%$. Upstream half of diffuser shown, free-stream is from top to bottom.

The flow control case which employed three resonators characterized by the superposition of two modes of oscillation (figure 6.25, right) was not quite as effective as the previous configuration. Still, a reduction of the reverse-flow factor could be observed downstream of the diffuser inlet, and in particular in the wake of the dividing walls. However, the Δc_p of 13 % implied that there were no advantages over the case with just one resonator, besides an attenuation of the radiated sound pressure (see table 6.3).

6.4.7 Concluding remarks on the control of separation in a diffuser

The experiments to control the separated flow in a diffuser by aerodynamically excited resonators show the following results:

- In situations, where a mild adverse pressure gradient prevails, the res-

No. of resonators	1	2	2	3
φ_{12} [°]	—	0	160	—
Re_u	7.0×10^5	7.0×10^5	1.6×10^6	1.6×10^6
Neck geometry	A30*/K5*	A30*/K5*	A30*/K5*	A30*/K5*
$2s$ [mm]	12	12	28	28
l_n [mm]	9.35	9.35	9.35	9.35
l_y [mm]	130	125	125	125
St_{2s}	0.22	0.23	0.34	0.32
p_{rad}/p_{cav} [%]	19	19	8	14
$\langle c_\mu \rangle$	4.4×10^{-4}	2.5×10^{-4}	4.5×10^{-4}	6.6×10^{-4}
Δc_p [%]	13	14	18	13

TABLE 6.3: Overview of the parameters and results of separation control in a planar asymmetric diffuser applying different systems of resonators.

onator might not be sufficiently excited by the cross-flow to manipulate a reverse-flow region. A resonator location that ensures appropriate flow induction tends to lie too far upstream of the recirculation zone.

- Flow separation prompted by an abrupt change in geometry can readily be manipulated by a passive resonator.
- The resonator geometry can be chosen such that the pressure recovery in the diffuser is enhanced in a wide range of Reynolds numbers.
- A system of two resonators oscillating in anti-phase provided optimum results regarding both pressure recovery ($\Delta c_p = 18\,\%$) and attenuation of radiated sound pressure ($p_{rad}/p_{cav} = 8\,\%$).

6.5 Control of separation on a stalled airfoil

Another situation where an aerodynamically excited resonator was employed to manipulate a separation region was the flow around a stalled airfoil at high angle of attack (Müller, 2001, 2002). In this case, the flow separated due to a strong adverse pressure gradient. In contrast to the previous experiments, a resonator with circular cavity cross-section was applied.

6.5.1 Experimental set-up

For the control of separation on an airfoil by flow-induced resonators, a wing model with FX 61-184 laminar-flow profile and 18.4 % thickness ratio was used. The model was designed during a former project, and is described in detail in the thesis of Erk (1997). The coordinates of the profile, which is often applied on sailplanes, were made available by Althaus & Wortmann (1981). The wing span s_w and the chord length c of the airfoil section

measured 900 and 450 mm, respectively. In order to reduce three-dimensional effects caused by vortices induced at the tips, the airfoil was equipped with end plates of diameter 840 mm. The experiments presented in this section were conducted in the closed-return wind-tunnel described in section 2.2.2.

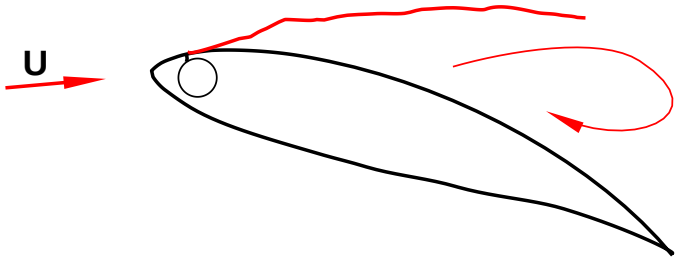

FIGURE 6.26: Schematic of the FX 61-184 airfoil model with resonator of circular cavity cross-section at a streamwise position of $x/c = 1.9\,\%$. At high angle of attack, the flow separated shortly downstream of the leading edge.

A resonator of cylindrical cavity cross-section was located on the suction side of the airfoil at a streamwise position of $x/c = 1.9\,\%$, and extended along the entire span. The neck geometry could be modified by exchanging several parts to yield upstream edges of types R0, R2, and A30 and downstream edges of types K0, K1, K2, S1, and S2. In analogy to the notation in figures 3.25 and 3.26, R and A represent the radius of curvature and the inclination angle of the leading edge, respectively, while K denotes how far the horizontal blade at the trailing edge protrudes into the neck. S differed from K in that the blade featured a sharp edge. More details on the resonator are given in section 2.1.2.

For the measurement of aerodynamic forces and moments, the airfoil model was mounted on a six-component wind-tunnel balance by three streamlined supports such that it was variable in pitch. A rotary encoder monitored the angle of attack. Velocity profiles and the flow through the resonator neck were determined using LDA. In addition, pressure distributions as well as spectra of the sound pressure in the resonator cavity were taken. The reverse-flow factor along the centerline of the wing was measured by wall pulsed-wire anemometry. For this purpose, one probe was mounted at a fixed position in close vicinity to the resonator, while a second one was installed on a belt traverse further downstream. Complementary information on the measurement techniques involved is given in section 2.3.2.

6.5.2 Baseline flow around the airfoil

The wing section investigated was of the trailing-edge-stall type (see McCullough & Gault, 1951): It was characterized by the occurrence of flow separation starting out from the trailing edge on the suction side of the airfoil. As the angle of attack α was increased, the separation line moved gradually

upstream while the open recirculation zone grew in size. The smooth course of the lift polar near its maximum lift coefficient reflects this behavior (see figure 6.31). Beyond $\alpha = 23°$, however, the flow detached from the leading edge resulting in a drastic breakdown of lift. In this case, the characteristic streamwise length of the separated flow region was $L = 437\,\mathrm{mm}$. At such high angles of attack, three-dimensional structures evolved in the flow on the suction side: During flow visualizations, the formation of a so-called stall cell was detected, which was marked by a reverse-flow region with typical "owl's eye" pattern bounded by domains of attached flow near both end plates. This phenomenon had been observed before by other researchers, and a review is given, for example, in Boiko *et al.* (1996). The spanwise number of stall cells depends on the aspect ratio s_w/c of the wing. For $s_w/c = 2$, Yon & Katz (1997) report the formation of a single cell, as seen in the present case.

Under post-stall conditions, the separating boundary layer was laminar. However, the flow could not be kept attached by simply applying a tripping device to the airfoil at the location of the resonator slit. This was verified for the entire Reynolds-number range investigated. As a consequence, it can be ruled out that the effects of the flow control described in the following were the result of promoting laminar-turbulent transition.

Data of the lift and drag polar diagrams of the FX 61-184 profile obtained in the Stuttgart laminar wind-tunnel can be found in Althaus & Wortmann (1981) for comparison.

6.5.3 Resonance regime

Spectra of the sound pressure induced in the resonator cavity were taken at angles of attack ranging from 0° to 24°, and at Reynolds numbers Re_c based on the airfoil chord length from 1×10^5 to 1×10^6. Under certain flow conditions, strong resonances occurred. Figure 6.27 shows a synopsis of resonance peaks from these spectra in comparison to the natural acoustic frequencies obtained from the analytical computations discussed in sections 3.1.1 and 3.1.4 (see figure 3.16). At these natural acoustic frequencies, a concentration of aerodynamically excited resonances can be observed. This implies that both the Helmholtz mode and higher cavity modes were induced by the cross-flow. Taking into account the oscillation amplitude, however, the first azimuthal mode $j'_{1,0}$ was clearly dominant.

The spectra compiled in figure 6.28 show how the excitation of the different modes varied with the Reynolds number: Starting at $Re_c = 7.2 \times 10^5$, the first azimuthal mode ($f_0 = 7.3\,\mathrm{kHz}$) was induced and persisted up to $Re_c = 9.5 \times 10^5$. As the Reynolds number was increased further, each of the remaining azimuthal and radial modes was excited, associated with higher resonance frequencies. Although Helmholtz-mode oscillations could be detected at $f_0 \approx 900\,\mathrm{Hz}$, their low amplitude rendered them insignificant.

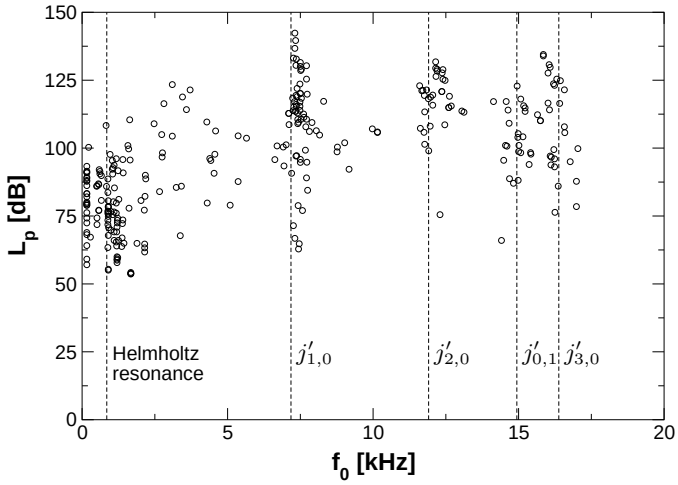

FIGURE 6.27: Synopsis of resonances excited by the cross-flow for angles of attack from 0° to 24° and for Reynolds numbers from 1×10^5 to 1×10^6. The vertical lines indicate the purely acoustic resonance frequencies obtained analytically according to section 3.1.1. $2s = 1.6\,\text{mm}$, neck geometry R0/K0, $n_z = 1$.

When cavity modes are induced by the cross-flow, slit width and neck geometry do not affect the resonance frequency. Therefore, the configuration for the subsequent investigation of one sample case was chosen on the basis of optimum oscillation amplitude: $\alpha = 23.0°$, $Re_c = 8.5 \times 10^5$, $2s = 2.6\,\text{mm}$, neck geometry A30/S2.

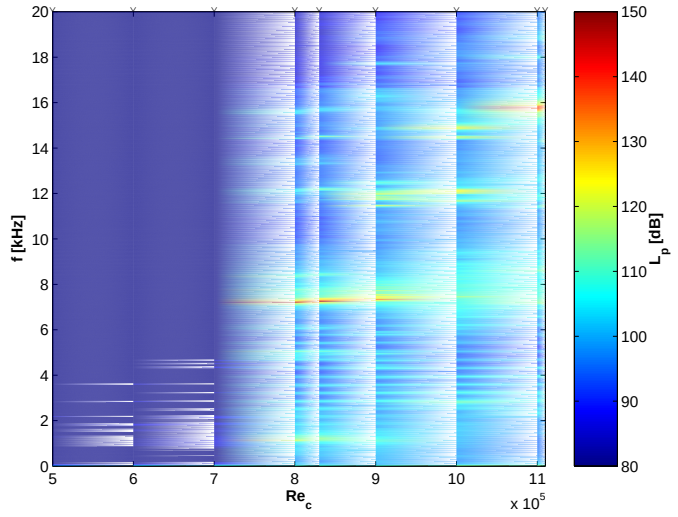

FIGURE 6.28: Spectra of the flow-induced sound-pressure level inside the resonator cavity as a function of Re_c. $\alpha = 24.0°$, $2s = 2.6\,\text{mm}$, neck geometry A30/K2, $n_z = 1$.

6.5.4 Resonator output

The fluctuating velocity field in the neck of the aerodynamically excited resonator used to control the separation region on the suction side of the stalled airfoil is characterized in figure 6.29 during one cycle of oscillation. The data shown correspond to the case of most effective control, which will be investigated in detail in sections 6.5.6 and 6.5.7.

Similar to the resonator used to control the separated diffuser flow, the reciprocating fluid motion in the neck is not homogeneous in x-direction. Instead, the streamwise location of the maximum outflow velocity varies with the phase as a consequence of a vortex being convected across the opening. The fact that the flow is barely directed into the resonator implies that the fluid motion in the neck must vary in spanwise direction. Section 6.5.5 will address the three-dimensionality of the resonator oscillations.

As before, this kind of LDA measurements provided the data for the computation of the momentum coefficient $\langle c_\mu \rangle$ according to equations (5.4) and (5.5), based on the streamwise length $L = 437\,\mathrm{mm}$ of the baseline separation region.

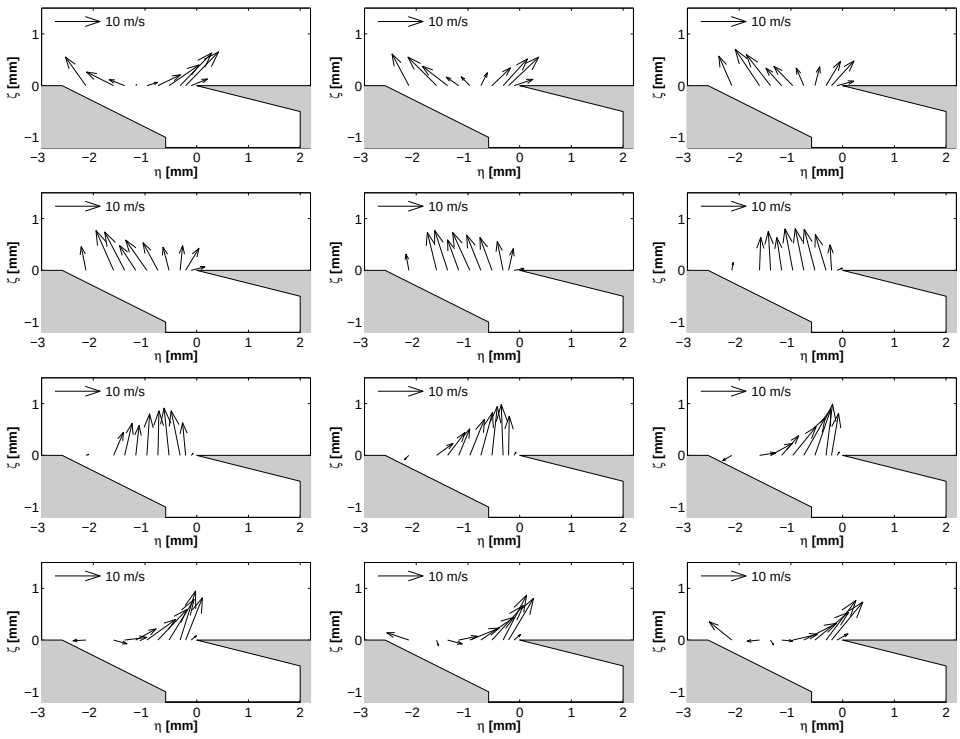

FIGURE 6.29: Phase-averaged velocity field within the resonator orifice at different phase angles ($\Delta\varphi = 30°$). η and ζ denote local coordinates parallel and normal to the slit exit plane, respectively, originating at the trailing edge of the slit. $\alpha = 23.0°$, $Re_c = 8.5 \times 10^5$, $2s = 2.6\,\mathrm{mm}$, neck geometry A30/S2, $n_z = 1$, $St_{2s} = 0.66$, $\langle c_\mu \rangle = 4.2 \times 10^{-4}$.

6.5.5 Spanwise coherence of resonator oscillations

In view of the small acoustic wavelength of the induced oscillations relative to the spanwise resonator dimensions, the coherence $\gamma^2(f)$ and phase relation $\Delta\varphi(f)$ of the sound pressure in z-direction were investigated. Using a traversable microphone, both quantities were measured along one half of the span with respect to the reference microphone at the spanwise center of the resonator cavity. The resulting functions are shown in figure 6.30 evaluated for the resonance frequency of the first azimuthal mode $f_0 = 7360\,\mathrm{Hz}$.

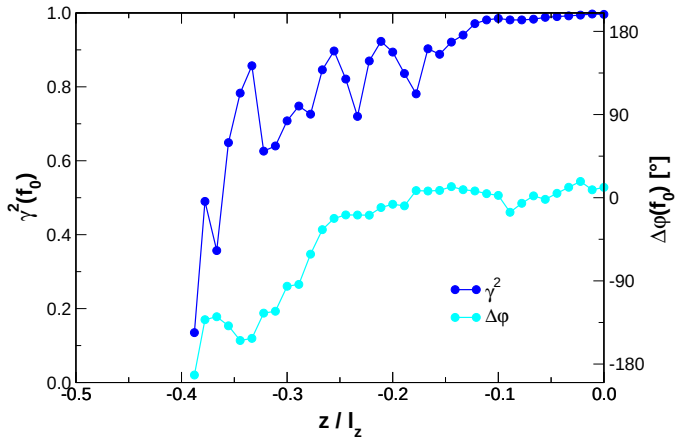

FIGURE 6.30: Coherence γ^2 and phase difference $\Delta\varphi$ of the resonator oscillations along the half span of the wing with respect to the reference microphone at the center of the resonator cavity. The centerline is located at $z/l_z = 0$. $\alpha = 23.0°$, $Re_c = 8.4 \times 10^5$, $2s = 2.6\,\mathrm{mm}$, neck geometry A30/S2, $n_z = 1$, $St_{2s} = 0.66$, $\langle c_\mu \rangle = 4.2 \times 10^{-4}$.

The coherence function provides a tool to determine how correlated two signals are, and represents a normalized cross-spectral density function $G_{ab}(f)$ between two time-history records $a(t)$ and $b(t)$ (Bendat & Piersol, 1993):

$$\gamma^2_{ab}(f) = \frac{|G_{ab}(f)|^2}{G_{aa}(f)G_{bb}(f)} \qquad 0 \leq \gamma^2_{ab}(f) \leq 1. \tag{6.7}$$

$G_{aa}(f)$ and $G_{bb}(f)$ denote the power spectral density function of $a(t)$ and $b(t)$, respectively. For an ideal correlation, one obtains $\gamma^2_{ab} = 1$, while $\gamma^2_{ab} = 0$ in cases where both signals are completely uncorrelated. When the coherence is greater than zero but less than unity, this indicates extraneous noise, resolution bias errors, a non-linear relationship between the two signals, or that the output of the one signal is due to other inputs besides the second signal (Bendat & Piersol, 1993).

Due to the microphone dimensions, the measurement could not be continued to $z/l_z = -0.5$. The spacing $\Delta z = 10\,\mathrm{mm}$ of the measurement points in spanwise direction was sufficiently small to detect possible standing waves up to a frequency of 17150 Hz. Assuming symmetry about the centerline,

it can be seen that the coherence of the resonator oscillations was greater than 0.7 along the inner 60 % of the wing span. In this region, the phase difference did not exceed 96° which implies that no standing wave pattern occurred. With decreasing coherence tending to zero towards the wing tip, the phase difference reached values close to 180°. Assuming symmetric conditions, again, it can be concluded that a standing wave with one node was present in the resonator cavity. The resulting spanwise sound-pressure gradient was negligible, however, such that the generation of longitudinal vortices was very unlikely.

The data scatter seen in the coherence function was reproduceable independent of averaging time. It might, therefore, be attributed to small variations in the cavity geometry along the span, caused, for example, by the embedded tubes required for the measurement of the static-pressure distribution.

6.5.6 Effect of resonator oscillations on lift

As discussed in section 6.5.2, the lift polar of the baseline case behaved smoothly for angles of attack α in a wide range from 10.0° to 22.5° associated with maximum lift conditions (figure 6.31). Beyond $\alpha = 22.5°$, however, the lift dropped sharply.

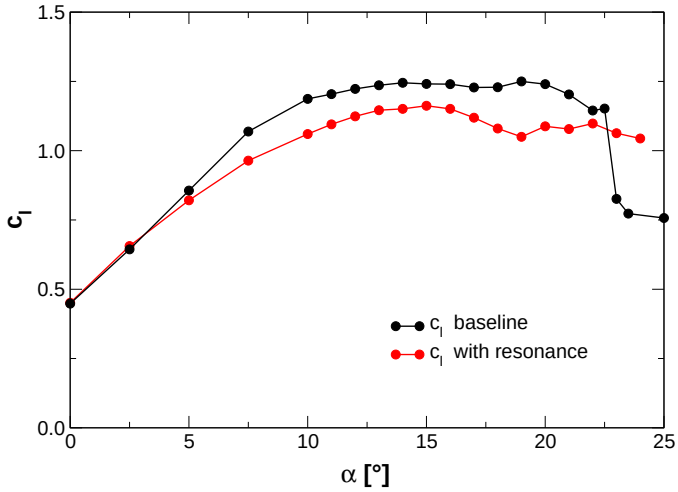

FIGURE 6.31: Lift polars obtained from balance measurement. $Re_c = 5.0 \times 10^5$. Controlled case: $2s = 2.6$ mm, neck geometry A30/S2, $n_z = 10$.

When an aerodynamically excited resonator manipulated the flow, the lift performance at $5.0° \leq \alpha \leq 22.5°$ was inferior to the baseline case. This was not surprising, since at low angles of attack, the resonator was likely to trigger premature transition on the suction side of the laminar-flow profile. Also at higher, but still moderate angles of attack, the perturbations produced by

the resonator were detrimental to the performance, as long as they did not interact with the separated flow region. This was a result of the strong mixing processes induced downstream of the resonator. The large vortical structures increased the displacement thickness of the boundary layer and, thus, effectively reduced the camber of the airfoil.

At $\alpha \geq 23.0°$, when the separation line was located far upstream in the vicinity of the leading edge, the vortices generated by the resonator oscillations had a beneficial effect, and maintained high-lift conditions. Compared to the baseline case, lift was up by 36 % at an angle of attack of $\alpha = 24.0°$, for example. As a consequence of the losses involved in the actuation process, however, the corresponding lift coefficient was slightly less than in the baseline case just before the breakdown of lift.

The observed behavior implies that a resonator must be adaptive (see chapter 7) to ensure that no flow-induced oscillations occur under flow conditions which are not supposed to be controlled.

In situations where the wing was strongly inclined versus the free-stream ($\alpha \geq 23°$), the flow on the suction side separated directly at the leading edge. As a consequence, a constant pressure distribution formed along the upper side of the airfoil (figure 6.32).

When the flow was manipulated by an aerodynamically excited resonator, separation was delayed such that the suction peak in the pressure distribution was partially restored. In the case presented in figure 6.32, this resulted in an increase of lift by $\Delta c_l = 23\,\%$ and in a reduction of pressure drag by $\Delta c_{d_p} = -27\,\%$ compared to the baseline case.

Figure 6.33 shows a comparison of the lift coefficients obtained from bal-

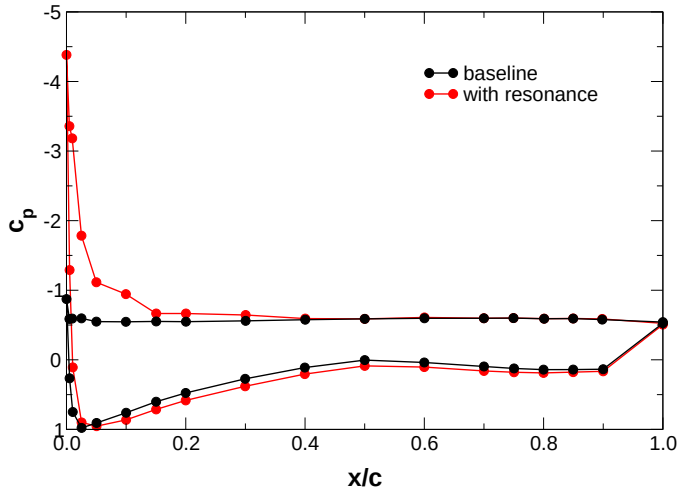

FIGURE 6.32: Pressure distribution around the airfoil. $\alpha = 24.5°$, $Re_c = 8.4 \times 10^5$. Controlled case: $2s = 2.6\,\text{mm}$, neck geometry A30/S2, $n_z = 1$, $St_{2s} = 0.66$, $\langle c_\mu \rangle = 4.2 \times 10^{-4}$, $\Delta c_l = 23\,\%$, $\Delta c_{d_p} = -27\,\%$.

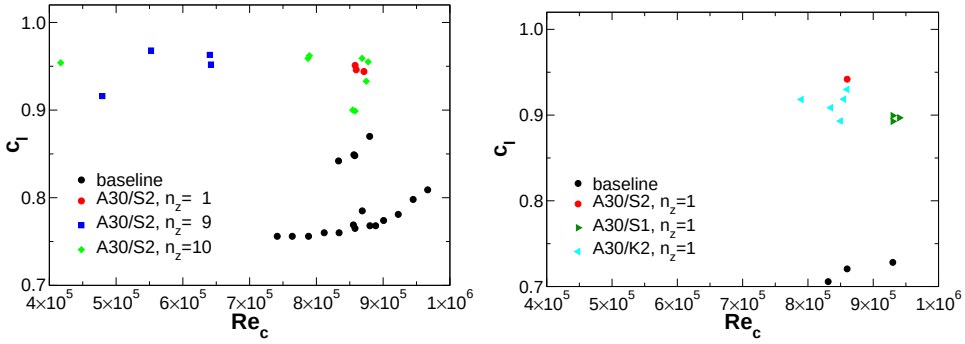

FIGURE 6.33: Lift coefficients c_l computed from balance measurements (left) and from pressure distributions around the airfoil (right) for different neck geometries. $\alpha = 24.0°$. Controlled cases: $2s = 2.6\,\text{mm}$.

ance measurements and from the integration of static-pressure distributions. In general, the values computed from the pressure measurements are below the balance data for both the baseline and the manipulated case. This might be a consequence of the three-dimensionality of the separated flow field pointed out in section 6.5.2, since the wind-tunnel balance integrated the lift forces over the entire wing area, whereas the pressure distributions represent the flow conditions in a single cross-section. The results from the pressure distributions, however, exhibit a more consistent behavior.

According to the balance measurements, the maximum increase in lift due to the resonator oscillations was $\Delta c_l = 27\,\%$ at a Reynolds number of $Re_c = 7.9 \times 10^5$. The corresponding increase calculated from the pressure distributions was $\Delta c_l = 31\,\%$ at $Re_c = 8.6 \times 10^5$. Both optimum results were obtained with the neck geometry A30/S2.

6.5.7 Effect of resonator oscillations on the flow field

The results of LDA measurements of the global velocity field on the suction side of the airfoil are depicted in figures 6.34 to 6.36. The data were taken in a cross-section close to the centerline at a relative span of $z/s_w = 4.7\,\%$.

The velocity vectors in the measurement plane showed a drastic difference between the baseline flow and the flow manipulated by the aerodynamically excited resonator (figure 6.34). The effect of the control reached deep into the flow field. Velocity profiles downstream of the oscillating resonator exhibited a noticeable increase of momentum near the wall. Thus, the boundary layer in this region was rearranged in a way that it stayed attached over a much longer distance. This demonstrated the enhanced mixing process induced by the spanwise vortices generated at the resonator orifice. As a result, both the streamwise and the vertical extension of the reverse-flow region were largely reduced.

The size of the recirculation zone can be assessed more accurately by

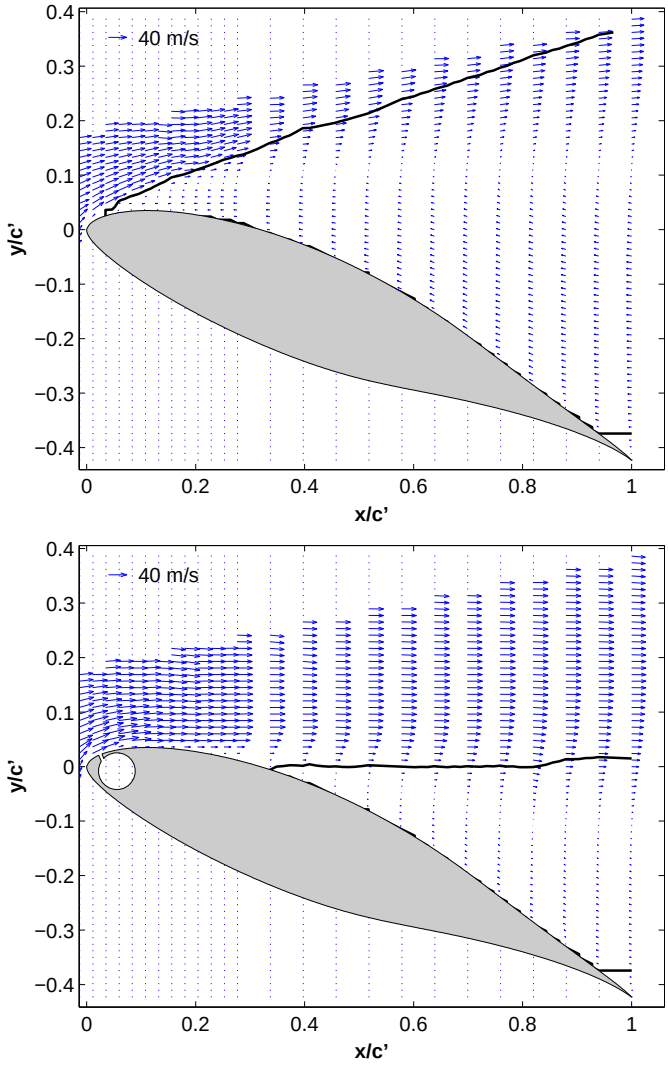

FIGURE 6.34: Velocity-vector field on the suction side of the airfoil for the baseline flow (top) and with separation control by a resonator (bottom). The black line indicates the streamline where $\Psi = 0$. $\alpha = 23.0°$, $Re_c = 8.4 \times 10^5$. Controlled case: $2s = 2.6\,\mathrm{mm}$, neck geometry A30/S2, $n_z = 1$, $St_{2s} = 0.66$, $\langle c_\mu \rangle = 4.2 \times 10^{-4}$.

considering the curve along which the stream function vanishes (figure 6.35): Under the influence of resonance, the separation line moved from $x/c \approx 5\,\%$ to about $34\,\%$. The vertical extension of the reverse-flow region decreased by roughly $50\,\%$, which significantly reduced the wake and, therefore, the associated pressure drag of the airfoil.

The representation of the streamwise velocity component in figure 6.36 shows that, with resonance, high local velocities occurred near the leading edge. This corresponded to the restoration of the suction peak of the static-

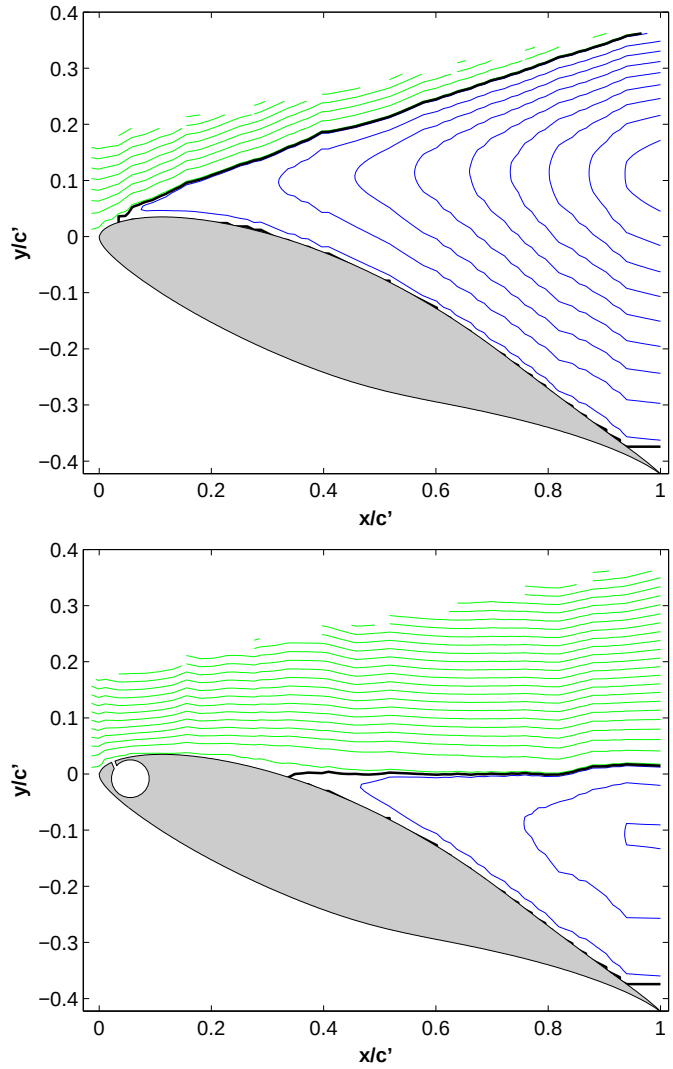

FIGURE 6.35: Streamlines computed from the velocity field on the suction side of the airfoil for the baseline flow (top) and with separation control by a resonator (bottom). Depending on its value, the stream function is represented in green ($\Psi > 0$), black ($\Psi = 0$), or blue ($\Psi < 0$). $\alpha = 23.0°$, $Re_c = 8.4 \times 10^5$. Controlled case: $2s = 2.6\,\mathrm{mm}$, neck geometry A30/S2, $n_z = 1$, $St_{2s} = 0.66$, $\langle c_\mu \rangle = 4.2 \times 10^{-4}$.

pressure distribution (see figure 6.32) in this region.

The shift of the separation line could also be observed in the behavior of the reverse-flow factor χ_w obtained from wall pulsed-wire anemometry (figure 6.37). In this context, the inception of separation was characterized by χ_w exceeding 50 %. While in the baseline case separation was prompted upstream of the first measurement position ($x/c = 6.9\,\%$), the flow detached as far downstream as $x/c = 30\,\%$ when the resonator was oscillating. This

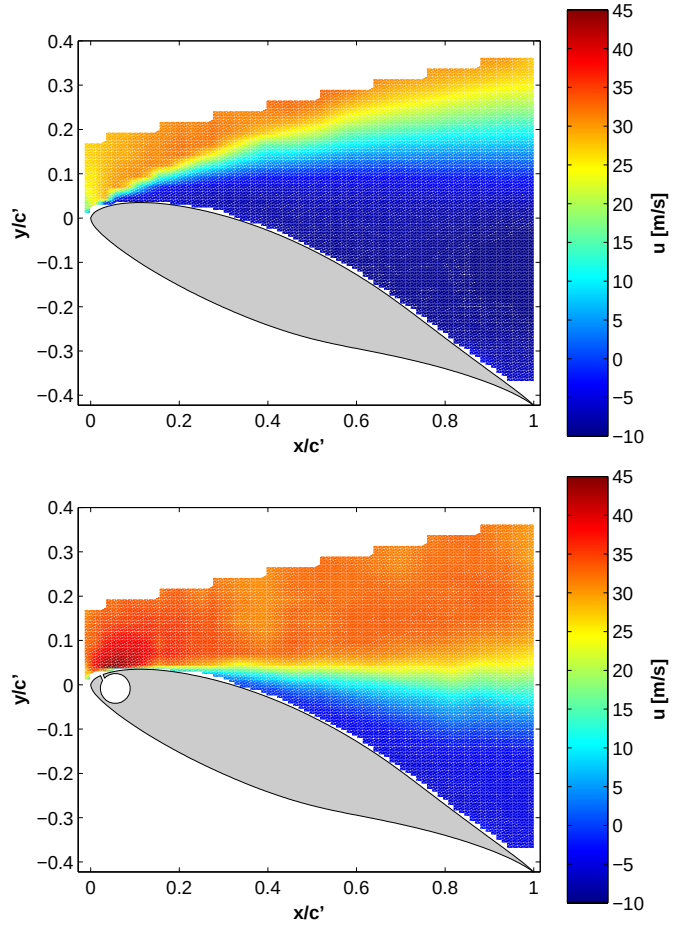

FIGURE 6.36: u-component of the velocity field on the suction side of the airfoil for the baseline flow (top) and with separation control by a resonator (bottom). $\alpha = 23.0°$, $Re_c = 8.4 \times 10^5$. Controlled case: $2s = 2.6\,\text{mm}$, neck geometry A30/S2, $n_z = 1$, $St_{2s} = 0.66$, $\langle c_\mu \rangle = 4.2 \times 10^{-4}$.

agrees well with the previous results of the LDA measurements. Moreover, χ_w was significantly reduced throughout the entire streamwise range investigated. Near the leading edge, the reverse-flow factor decreased from values close to 100 % to 0 %. This pronounced reduction in χ_w deteriorated with increasing distance from the resonator. At a location of $x/c = 70\,\%$, a difference of 10 % in the reverse-flow factor could still be measured indicating a larger portion in time of instantaneously attached flow.

6.5.8 Additional notes on the control of separation on an airfoil by a resonator

At angles of attack beyond 25°, the separation line was located upstream of the resonator. As a consequence, no energetic boundary layer grazed across

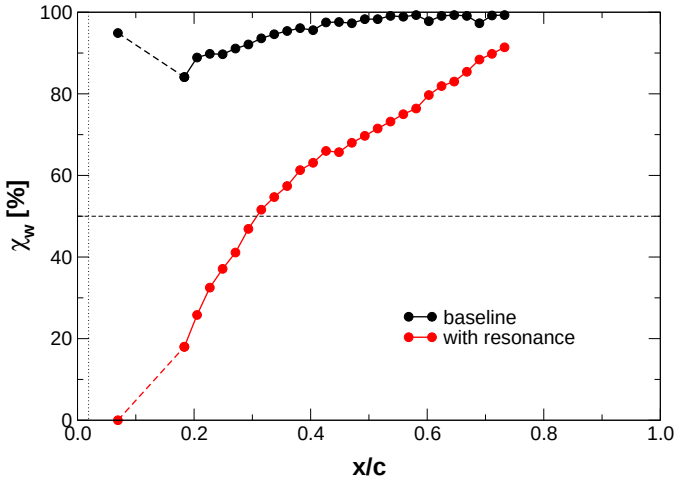

FIGURE 6.37: Reverse-flow factor χ_w along the centerline on the suction side of the airfoil. The dotted vertical line marks the location of the resonator neck. $\alpha = 23.7°$, $Re_c = 8.5 \times 10^5$. Controlled case: $2s = 2.6\,\text{mm}$, neck geometry A30/S2, $n_z = 1$, $St_{2s} = 0.66$, $\langle c_\mu \rangle = 4.2 \times 10^{-4}$.

the resonator opening such that oscillations could not be excited. A short initial impulse generated actively by loudspeakers was sufficient in this situation to cause the flow to reattach at the orifice. The frequency of this impulse was not required to coincide with any of the natural frequencies of the resonator. Subsequently, the cross-flow was able to sustain the resonator oscillations rearranging the flow field downstream in the way described before.

To control the separated flow around the airfoil, systems of $n_z = 1$, 9, and 10 resonators were applied. Regarding the increase in lift, however, the results obtained with the various configurations did not differ much (see figure 6.33). Both systems consisting of several adjacent resonators were beneficial in providing strictly symmetric flow conditions on the airfoil suction side.

Finally, it should be noted that hysteresis effects regarding the oscillation amplitude occurred when the Reynolds number was varied.

6.5.9 Concluding remarks on the control of separation on a stalled airfoil

The results of separation control on an airfoil by means of a flow-induced resonator can be summarized as follows:

- The flow separating near the leading edge of an airfoil at high angle of attack was manipulated by aerodynamically excited cavity-mode oscillations of a resonator.

- The induced oscillations were coherent over a long portion of the span while showing only a weak three-dimensional character.
- Under flow conditions that were not supposed to be controlled, resonator oscillations were detrimental to the airfoil performance.
- Under post-stall conditions, separation was delayed from $x/c \approx 5\,\%$ to $30\,\%$ by the control such that the suction peak in the pressure distribution was partially restored. As a consequence, lift was increased and pressure drag was reduced.
- The control success was a result of enhanced momentum transfer into the near-wall region by large-scale vortices, rather than of promoting laminar-turbulent transition.

List of symbols

$a(t)$	time history record
A	cross-sectional area of the resonator cavity
$b(t)$	time history record
c	airfoil chord length
c_d	drag coefficient
c_{d_p}	pressure drag coefficient
c_f	skin-friction coefficient
c_l	lift coefficient
c_p	pressure coefficient ($= \Delta p/(\frac{1}{2}\rho U_\infty^2)$)
$c_{p_{\mathrm{pot}}}$	pressure coefficient obtained from potential flow theory
c_x	figure of merit
c_μ	momentum coefficient
f	frequency
f_0	resonance frequency
f_e	excitation frequency
$\mathcal{F}$	arbitrary function
F_d	drag force
F_l	lift force
$G_{aa}(f)$	power spectral density function of $a(t)$
$G_{ab}(f)$	cross-spectral density function between $a(t)$ and $b(t)$
H_{12}	velocity-profile form-parameter
$\dot{I}$	momentum flux
$j'_{m,n}$	$(n+1)$st positive zero of $J'_m(g)$
$J'_m(g)$	derivative of the Bessel function with respect to g
l_n	neck length of a resonator
l_y	height of the actuator cavity
l_z	span of the actuator cavity

L	characteristic length
L_p	sound-pressure level
n_z	number of adjacent resonators
p	static pressure
p_{cav}	rms sound-pressure within the resonator cavity
p_{dyn}	free-stream dynamic pressure
p_{rad}	radiated rms sound-pressure
p_{ref}	static reference pressure
Re_{2s}	Reynolds number based on streamwise length of resonator neck
Re_c	Reynolds number based on airfoil chord length
Re_L	Reynolds number based on characteristic length L
Re_u	Reynolds number based on unit length (1 m)
Re_{δ_2}	Reynolds number based on boundary-layer momentum-thickness
s	half-slit width of the resonator neck
s_w	wing span
S_w	wing area
St_{2s}	Strouhal number based on streamwise length of resonator neck
St_L	Strouhal number based on characteristic length L
u	velocity component in x-direction
u'	fluctuating streamwise velocity
u'_{rms}	rms-value of the fluctuating streamwise velocity
u_τ	skin-friction velocity
U	time-averaged streamwise velocity component
U_∞	free-stream velocity
U^+	streamwise velocity component in inner-law scaling
v	velocity component in y-direction
v'	fluctuating wall-normal velocity
v'_{rms}	rms-value of the fluctuating wall-normal velocity
x	streamwise coordinate originating at entrance of test section; airfoil: chordwise coordinate originating at nose
x_a	streamwise position of the actuator
$x_{a_{opt}}$	optimum streamwise position of the actuator
x_{DI}	streamwise location of the diffuser intlet
x_{DO}	streamwise location of the diffuser outlet
x_{LE}	streamwise location of the leading edge of the resonator neck
x_s	streamwise location of the separation line
y	wall-normal coordinate originating at the wall
y^+	distance from wall in inner-law scaling
z	spanwise coordinate originating at centerline of test section, airfoil, or resonator
Z	specific acoustic impedance
α	angle of attack
β	diffuser expansion angle
$\gamma^2(f)$	coherence function

$\gamma_{ab}^2(f)$	coherence function between $a(t)$ and $b(t)$
δ_1	displacement thickness of the boundary layer
δ_2	momentum thickness of the boundary layer
δ_{99}	99 %-thickness of the boundary layer
Δ	variation of a quantity
ζ	local coordinate normal to the slit exit plane
η	local coordinate parallel to the slit exit plane
ν	kinematic viscosity of the fluid
ρ	mass density of fluid
φ	phase
χ	reverse-flow factor
χ_w	reverse-flow factor at the wall
Ψ	stream function
$\overline{}$	time-averaged value of a quantity
$\langle\,\rangle$	phase-averaged value of a quantity

Chapter 7

Closed-loop control scheme employing a resonator

In both sample configurations discussed in sections 6.4 and 6.5 in the context of separation control, it would have been desirable to automatically adapt the resonator to the flow conditions: In the half diffuser, this would have helped in detecting the optimum slit width of the resonator according to the Reynolds number. The airfoil performance could have been maximized by opening or shutting the resonator slit depending on whether the flow needed to be manipulated or not, when varying the angle of attack.

To this end, a closed-loop control concept based on an extremum-seeking strategy was implemented, which managed to tune the resonator such that the figure of merit was optimized. The control loop was applied to the diffuser configuration described in section 6.4.2 (Darmadi, 2002).

7.1 Concept of extremum seeking feed-back

Adaptive controller concepts are derived from low-dimensional approximations of the non-linear behavior of fluidic systems. The method of extremum-seeking feed-back is used to maximize or minimize the output of a non-linear plant that can be characterized by a static map with an extremum.

As shown in figure 7.1, the controller consists of a low- and a high-pass filter, an integrator, an amplifier, and a waveform generator providing a sinusoidal signal (e.g. Garwon *et al.*, 2003). The input $u(t)$ to the plant results from a superposition of an initial value u_0, the actual controller output $\Delta u(t)$, and a sine signal $a_s \sin(\omega_s t)$. Under the condition that the cycle duration of the sine is greater than the one of the controlled process, the dynamics of the plant can be neglected. The goal of the feed-back is to optimize the input $u(t)$ such that a minimum or maximum output $y(t)$ is achieved. The measured output $y(t)$ is passed through a high-pass filter to remove a time-mean offset and extract the periodic portion of the signal.

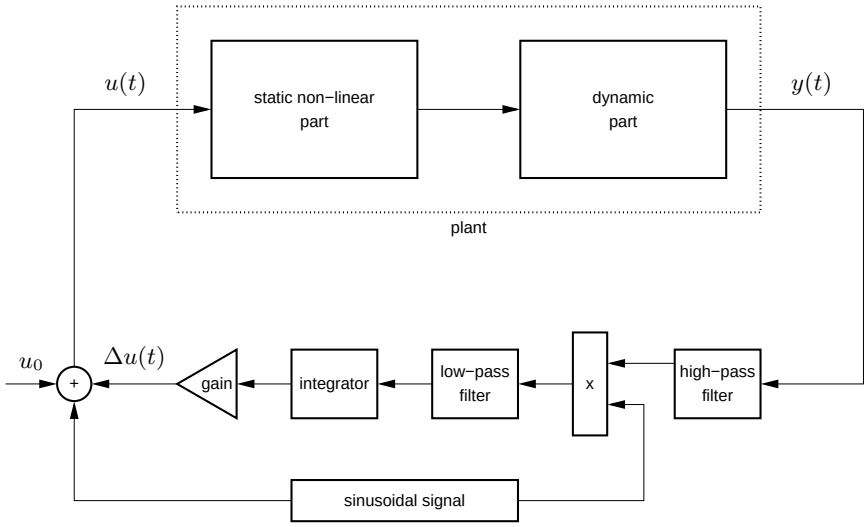

FIGURE 7.1: Scheme of the extremum seeking feed-back (e.g. Garwon *et al.*, 2003). $u(t)$ and $y(t)$ represent the input and output variables, respectively, while u_0 denotes an initial value.

Depending on whether the actual input $u(t)$ is below or above the desired optimum input, this periodic portion of the output is in phase or in anti-phase to the generated sine wave. The multiplication of the high-pass filtered output with the sine wave yields another periodic signal with a constant component, which is non-zero as long as the output $y(t)$ is not extremal. The mean value is extracted by a low-pass filter, and its sign determines whether the new input decreases or increases. A subsequent integration provides a variation $\Delta u(t)$, and ensures that the actual input $u(t)$ converges towards the optimum value with time.

Depending on the properties of the plant, five variables have to be chosen when implementing this method: both cut-off frequencies of the filters, the amplitude a_s and the frequency ω_s of the sine signal, and the gain of the controller. The frequencies of both filters and of the sine wave can be set equal, but must be much less than the natural frequency of the controlled process. The remaining parameters can be obtained from simulations.

7.2 Customization for the diffuser test-case

In order to minimize the separation region in the diffuser, both manipulated variables, the slit width and the cavity height of the resonator, were controlled separately. For this purpose, two extremum-seeking feed-back loops were applied (Darmadi, 2002). The first, outer loop maximized the pressure recovery c_p in the diffuser by varying the cavity height l_y. This loop was characterized by a comparatively long cycle duration. The second, inner

loop maximized the rms sound-pressure p_{cav} inside the resonator cavity by adjusting the slit width $2s$. The corresponding cycle duration was much shorter than the one of the first loop. By choosing two different time scales, both interdependent control loops were almost entirely decoupled. In this way, the second loop worked on the basis of quasi-stationary conditions and, thus, provided a maximum sound pressure according to the instantaneous cavity height.

Two static maps represented the behavior of c_p and p_{cav} as functions of both $2s$ and l_y. The existence of an optimum value in each of the maps allowed for the application of the extremum-seeking feed-back method in either case. However, the presence of a number of local maxima complicated the detection of the respective global optimum. For this reason, the strategy was modified by varying the amplitude a_s of the sine signal depending on the controlled variables c_p and p_{cav}: Under conditions far away from the global optimum, relatively large amplitudes a_s were permitted, and vice versa. This amplitude modulation also helped in dealing with the hysteresis effects pointed out in section 3.2.10.

7.3 Results of the closed-loop control

The application of the extremum-seeking strategy to obtain an optimum pressure recovery in the diffuser was successful. Near-optimal values of c_p and p_{cav} were found by the controller independent of the initial conditions.

Two samples of the various cases tested are shown in figures 7.2 and 7.3: The path taken by the feed-back loops within the static maps is illustrated for different sets of initial conditions at a Reynolds number of $Re_u = 6.5 \times 10^5$. For the two cases, initial values of $2s$ and l_y from opposed regions of the static maps were chosen such that the pressure recovery in the diffuser and the sound pressure produced by the resonator started out at low levels. In all situations, the controller found the respective global optimum straightforward.

7.4 Robustness of the controllers

The robustness of both extremum-seeking controllers to changing flow conditions was checked by varying the Reynolds number Re_u by 20 % (figure 7.4). In the test case shown, Re_u was abruptly increased after $t = 150\,\mathrm{s}$ such that new stationary conditions were reached after about another 3 s.

It could be observed how, in a first reaction, both the pressure recovery c_p and the sound pressure p_{cav} dropped sharply as a consequence of the new, non-optimum conditions. Subsequently, this was compensated by both feed-back loops by varying the slit width $2s$ and the cavity height l_y. As a result, the pressure recovery was restored to its optimum value after a short

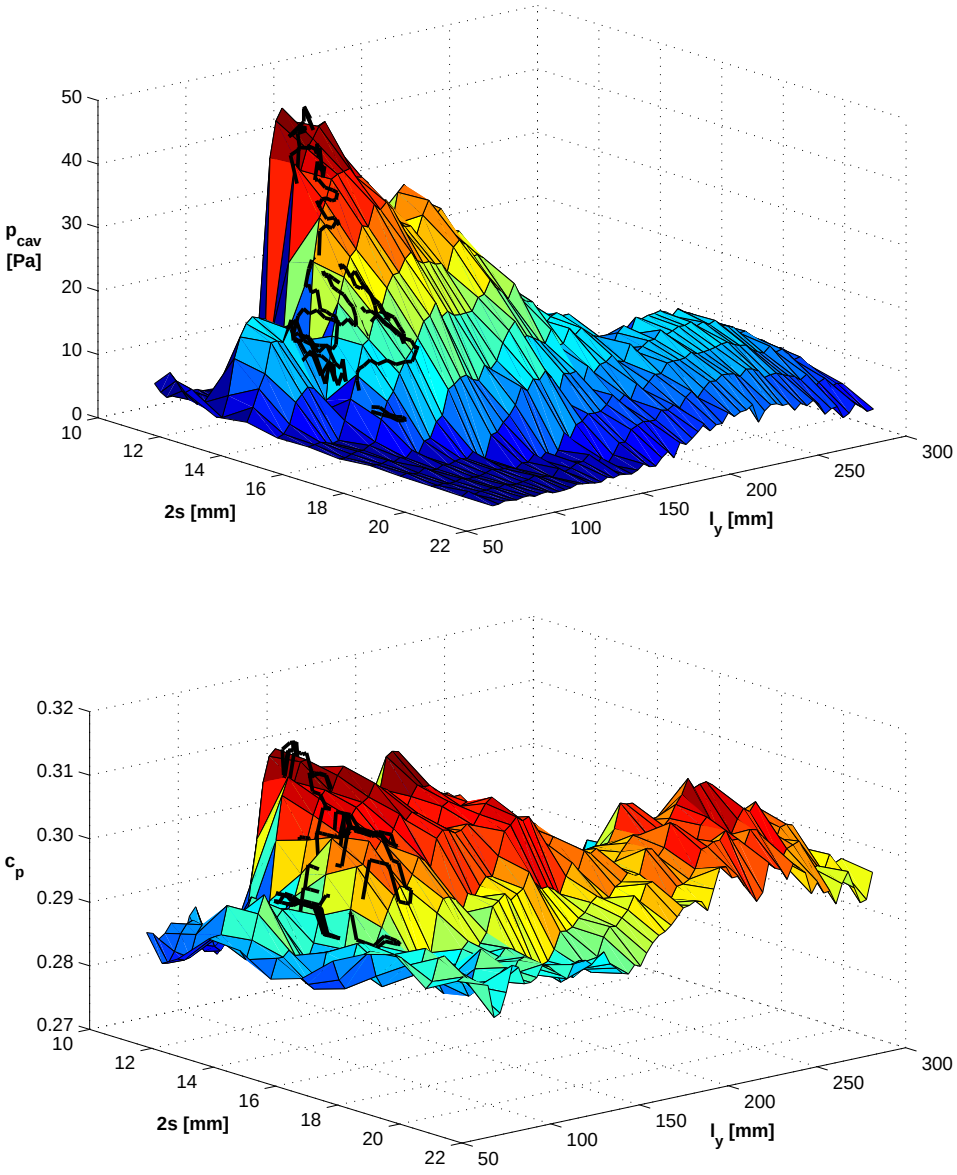

FIGURE 7.2: Path of the control algorithm (black) in the static maps of the cavity sound-pressure p_{cav} (top) and of the pressure recovery c_p (bottom). $Re_u = 6.5 \times 10^5$. Initial conditions: $2s = 16\,\mathrm{mm}$, $l_y = 100\,\mathrm{mm}$.

duration. This implies that the implemented control scheme is unsusceptible to perturbations in the free-stream velocity as high as 20 %.

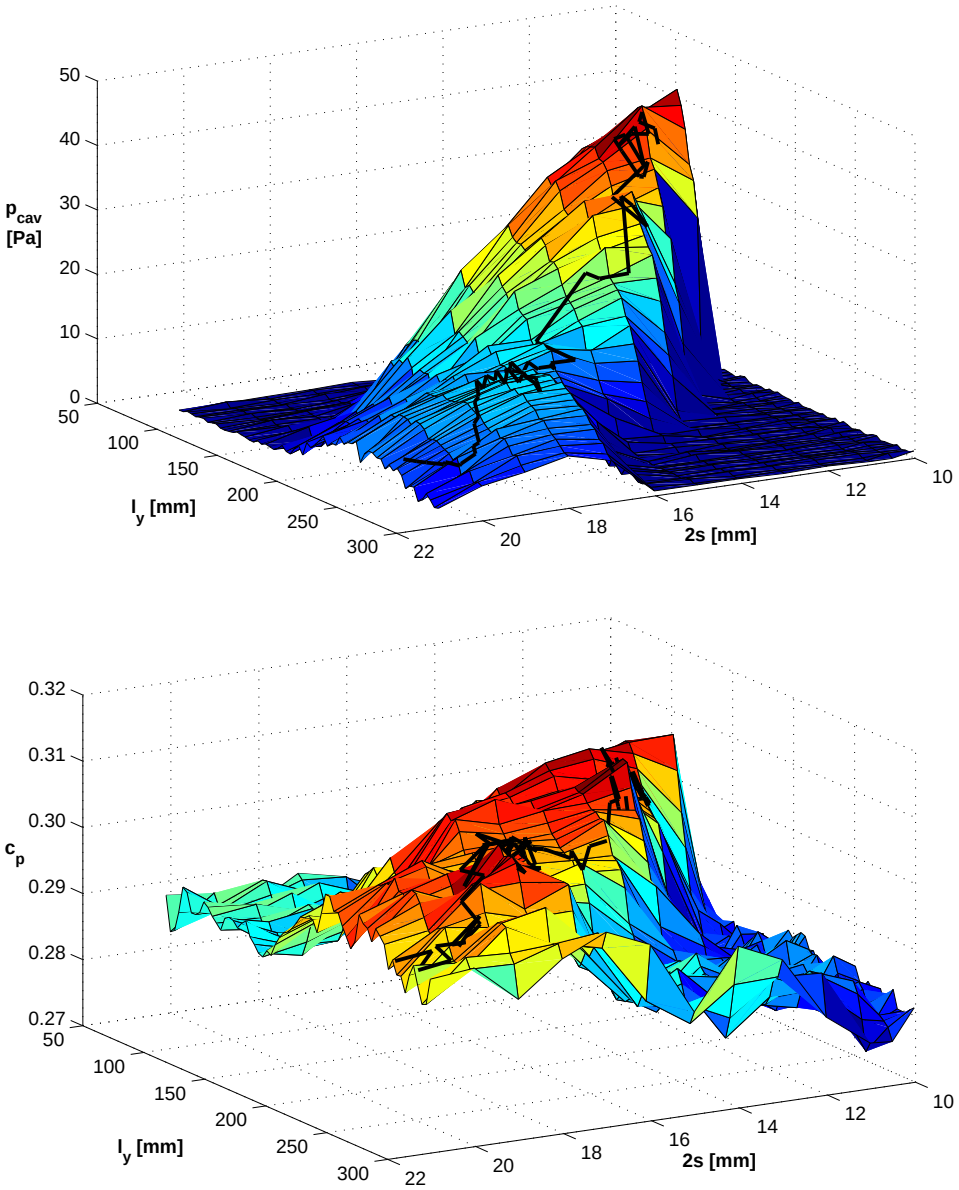

FIGURE 7.3: Path of the control algorithm (black) in the static maps of the cavity sound-pressure p_{cav} (top) and of the pressure recovery c_p (bottom). $Re_u = 6.5 \times 10^5$. Initial conditions: $2s = 21\,\text{mm}$, $l_y = 270\,\text{mm}$.

List of symbols

a_s	amplitude of the sine signal
c_p	pressure coefficient $(= \Delta p/(\frac{1}{2}\rho U_\infty^2))$
l_y	height of the actuator cavity

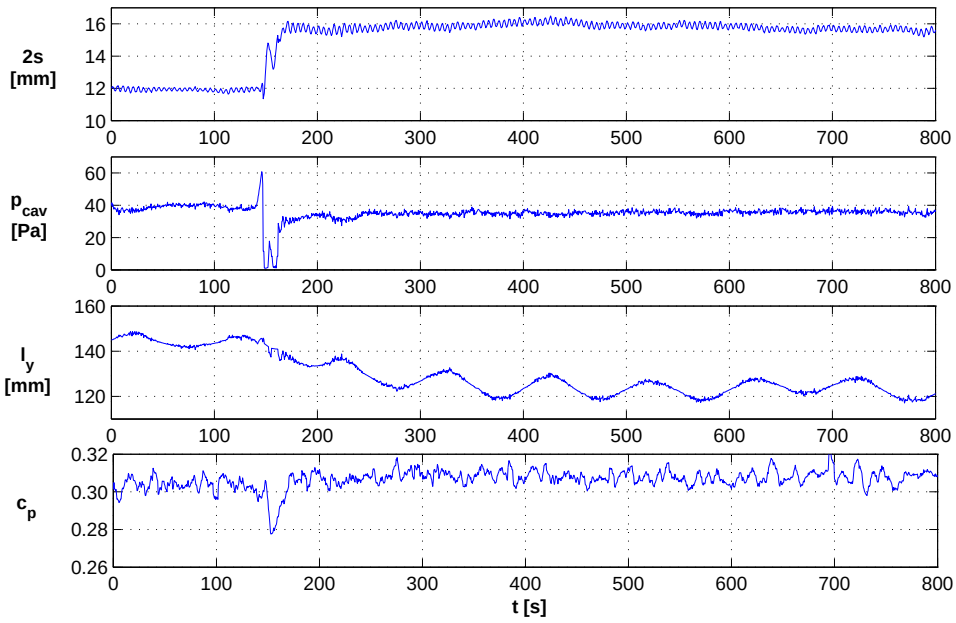

FIGURE 7.4: Response to a 20 % change in Reynolds number ($Re_u = 6.5\times10^5 \rightarrow 8.0\times10^5$) at $t = 150\,\mathrm{s}$ in the context of testing the robustness of the controllers.

p_{cav}	rms sound-pressure within the resonator cavity
Re_u	Reynolds number based on unit length (1 m)
s	half-slit width of the resonator neck
t	time
u_0	initial value of the input variable
$u(t)$	input variable of the plant
$y(t)$	output variable of the plant
Δ	variation of a quantity
ω_s	angular frequency of the sine signal

Chapter 8

Conclusions

Aerodynamically excited acoustic resonators were successfully applied as adaptive passive devices to manipulate separation regions in two different flow situations: The flow in a half diffuser and the flow around an airfoil at high angle of attack. No external energy input was required as the fluid in the resonators oscillated by interaction with the cross-flow. Vortices generated at the orifice rearranged the flow downstream of the resonators such that additional momentum from the energetic outer flow was transported into the near-wall region reducing reverse flow in the time mean. Using a resonator of variable geometry controlled by a feed-back loop, the characteristic parameters of the actuation (fluctuating momentum flux in the orifice and frequency of the aeroacoustic resonance) could be adjusted to changing flow conditions.

Some concluding remarks follow in the form of a step-by-step guideline on when and how to effectively apply this method of flow control:

1. *Consideration of the flow conditions*
   In order to decide, whether a reverse-flow region can be effectively manipulated by an aerodynamically excited resonator, it is vital to identify the causes of flow detachment. If the separation is prompted by an abrupt change in geometry or by a strong adverse pressure gradient, a flow-induced resonator can be applied successfully (sections 6.4 and 6.5, respectively). In situations where a mild adverse pressure gradient prevails, it might be easier and more effective to use other methods of control (section 6.4.1). This is a consequence of the sensitivity of the flow-induction process to the momentum thickness δ_2 of the approaching boundary layer (section 3.2.9). As δ_2 increases in downstream direction due to the adverse pressure gradient, the flow does not carry enough momentum near the wall to sufficiently excite the resonator for the manipulation of a reverse-flow region. This problem is closely linked with the most suitable streamwise location of the resonator.

2. *Determination of the actuator location*
   The optimum streamwise resonator location is a compromise between sufficient flow induction and proximity to the separation line (section 6.2). The first criterion is best met far upstream where the boundary layer is relatively thin. In contrast, an actuator position as close as possible to, but still upstream of the separation line would be best with regard to the impact of perturbations on the reverse-flow region. In situations where separation is caused by geometry, both conditions are usually satisfied directly upstream of the separation line. Otherwise, the strength of the adverse pressure gradient dictates the balance between the two aforementioned requirements.

3. *Determination of the optimum actuation frequency*
   The question which actuation frequency is best to manipulate a separation region must be posed whenever periodic actuation is applied, and is not just specific to this method of flow control. The answer boils down to the determination of the frequency range to which a reverse-flow region is particularly receptive. The result will be a reduced frequency St_L based on a characteristic length L of the recirculation zone (section 6.4.3).

4. *Design of the resonator dimensions*
   In the next step, the resonator has to be designed such that it oscillates at the natural frequency prescribed by the result given above: The reduced frequency based on L is governed by the properties of the separation region. Likewise, it must be ensured that the resonance frequency, when reduced on the basis of the slit width $2s$, lies in the range where flow induction occurs: $0.1 \leq St_{2s} \leq 0.7$. Matching both requirements yields the condition $St_L/L = St_{2s}/(2s)$. Depending on the flow situation, this might not be easy to satisfy, and occasionally a sub-optimal actuation frequency will have to be chosen.
   Flow-induced resonance occurs, if the frequency of the vortex shedding in the neck described by St_{2s} lies close to one of the acoustic natural frequencies of the resonator. These frequencies along with the corresponding modes can be computed by the analytical and numerical methods presented in this study (sections 3.1.1 and 3.1.2, respectively). Based on this, suitable resonator dimensions can be derived. Both the Helmholtz mode and cavity modes can be taken into account as all of them were shown to be effective in manipulating a separation region (sections 6.4 and 6.5).

5. *Application of a system of adjacent resonators*
   Systems of adjacent flow-induced resonators exhibit properties superior to a single resonator. Depending on the number of resonators involved, such a system can oscillate in phase, in anti-phase, or by superimposing

several modes (section 4.2). In both latter cases, alternating longitudinal vortices are generated in the wake of the separating walls between the individual resonators. These vortices occur in addition to the spanwise vortices produced along the neck, and enhance the mixing process in the shear layer downstream (section 4.5). Thus, they increase the wall-shear stress in this region and contribute to a further reduction of a downstream separation region. Compared with a single resonator, the radiated sound pressure is reduced by about an order of magnitude (section 4.4).

6. *Selection of the neck geometry*
   The geometry of the neck is the most influential parameter for maximizing the resonator output. A small vertical fence followed by a beveled leading edge (30°) in combination with a sharp, slightly elevated trailing edge protruding into the orifice provides the best results (section 3.2.6). This configuration has to be scaled according to the resonator slit width. The amplitude of the induced oscillations is then sufficiently high to eject the vortices generated in the neck which subsequently enhance the mixing downstream. In this way, a maximum amount of energy is returned to the flow as periodic perturbations.
   In the context of separation control, the output of a fluidic actuator is characterized by the oscillating momentum coefficient $\langle c_\mu \rangle$ based on a characteristic length L of the baseline reverse-flow region (section 5.2).

7. *Definition of efficiency*
   Finally, a quantity has to be chosen which represents the efficiency of the separation control. For the diffuser, such a quantity is the pressure recovery coefficient, whereas for the airfoil the lift coefficient is more appropriate. If measurement techniques permit, these parameters can be used as the controlled variable in the context of a feed-back loop.

8. *Implementation of closed-loop control*
   If varying flow conditions occur, a closed-loop control scheme must be implemented to adapt the resonator geometry accordingly. A combination of two extremum-seeking feed-back loops manipulating the resonator volume and the slit width proved to be suitable to maximize the pressure recovery in a diffuser independent of the initial conditions (section 7.3).

Appendix A

Flow characteristics of the open-return wind-tunnel

In the following, data on the flow conditions in the test section of the open-return wind-tunnel described in section 2.2.1 will be given.

A.1 Turbulence level

The turbulence level Tu at the spanwise center of the entrance to the measurement section was determined by hot-wire anemometry (see section 2.3.1). Tu was less than 0.15 % over the entire range of flow speeds (figure A.1).

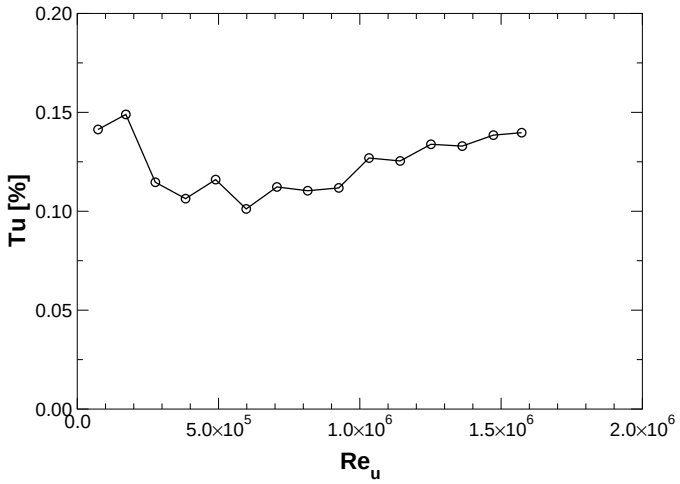

FIGURE A.1: Turbulence level Tu of the u-component of the free-stream at the entrance to the measurement section as a function of unit Reynolds number Re_u ($x = 0\,\text{mm}$, $y = 60\,\text{mm}$, $z = 0\,\text{mm}$).

A.2 Profiles of the free-stream velocity

The profiles of the mean velocity U in the free-stream direction were obtained from LDA measurements. U varied by less than $\pm 0.5\,\%$ over $95\,\%$ of the height H of the test section in a wide range of Reynolds numbers (figure A.2).

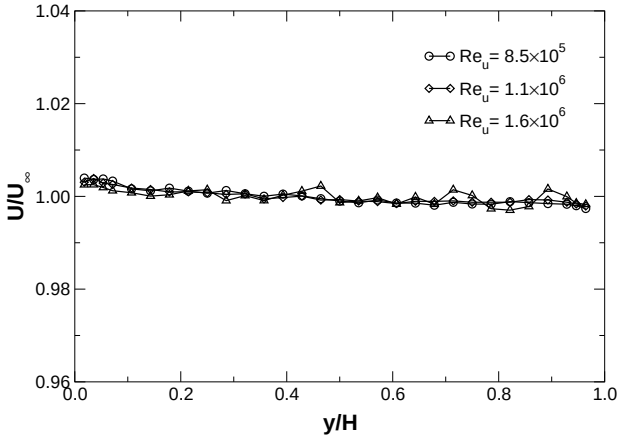

FIGURE A.2: Vertical profiles of the u-component of the flow in the test section normalized with the free-stream velocity U_∞ ($x = 188\,\text{mm}$, $z = 0\,\text{mm}$).

A.3 Spanwise skin-friction distribution

The spanwise distribution of the skin friction c_f along the flat plate in the set-up of section 3.2.2 was determined by a Preston-tube. At a distance 400 mm downstream of the entrance to the test section, the time mean of c_f

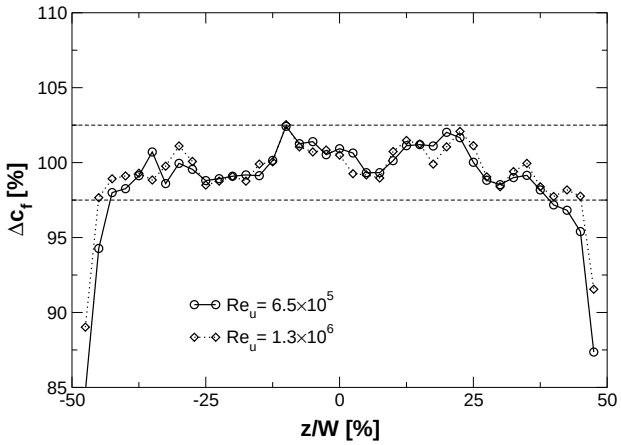

FIGURE A.3: Spanwise variation of the skin-friction coefficient c_f at $x = 400\,\text{mm}$. The dashed lines indicate a range deviating $\pm 2.5\,\%$ from the mean.

varied by ±2.2 % in the inner 75 % of the span W (figure A.3).

A.4 Boundary-layer properties upstream of the resonator

Boundary-layer profiles at distances $x - x_{LE} = -7.35$ and -26.35 mm upstream of the resonator were determined by LDA, where x_{LE} denotes the location of the leading edge of the neck. To avoid the induction of oscillations, the resonator slit was shut. The measurements were taken on a flat plate in the set-up of section 3.2.2 where the pressure gradient was nominally zero. A Preston tube was used to determine the wall-shear stress at the respective location of the profiles.

Re_u [–]	Re_{δ_2} [–]	δ_{99} [mm]	δ_1 [mm]	δ_2 [mm]	H_{12} [–]	c_f [–]
0.5×10^6	774	13.80	2.32	1.54	1.50	4.33×10^{-3}
1.0×10^6	1417	12.48	2.03	1.41	1.44	3.79×10^{-3}
1.5×10^6	2018	11.80	1.94	1.36	1.43	3.46×10^{-3}

TABLE A.1: Properties of the boundary layer upstream of the resonator ($x - x_{LE} = -26.35$ mm). Data refer to figures A.4 to A.7.

Table A.1 gives an overview of the boundary-layer properties at various Reynolds numbers. The profiles of the mean velocity and the Reynolds stresses (figures A.4 to A.6) are in excellent agreement with data reviewed by Fernholz & Finley (1996). Skewness and flatness distributions are shown in figure A.7 and the variation of the boundary-layer properties with unit Reynolds number is illustrated in figures A.8 to A.10.

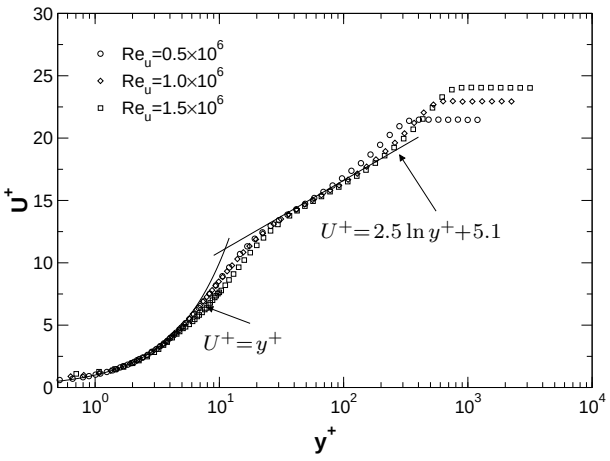

FIGURE A.4: Mean velocity profiles of the boundary layer at $x - x_{LE} = -26.35$ mm.

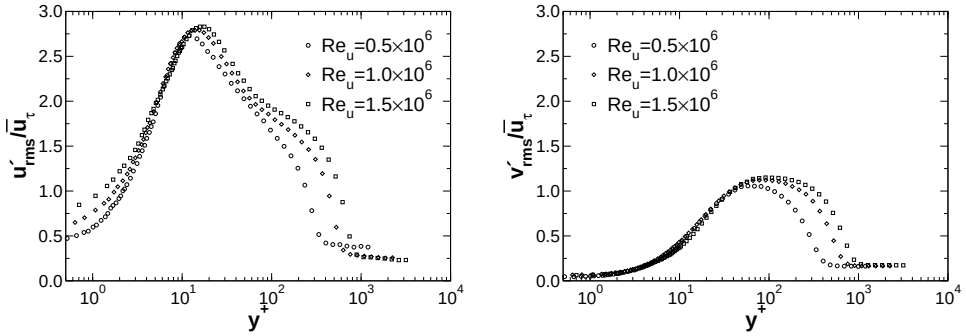

FIGURE A.5: Profiles of u'_{rms} and v'_{rms} upstream of the resonator ($x - x_{LE} = -26.35\,\text{mm}$).

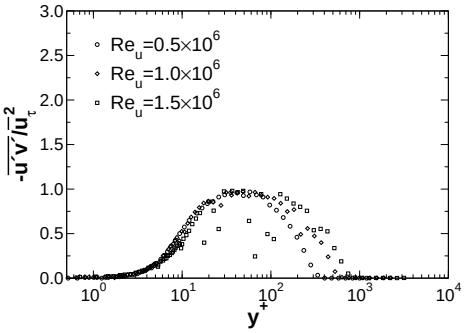

FIGURE A.6: Profile of $\overline{u'v'}/\overline{u_\tau}^2$ upstream of the resonator ($x - x_{LE} = -26.35\,\text{mm}$).

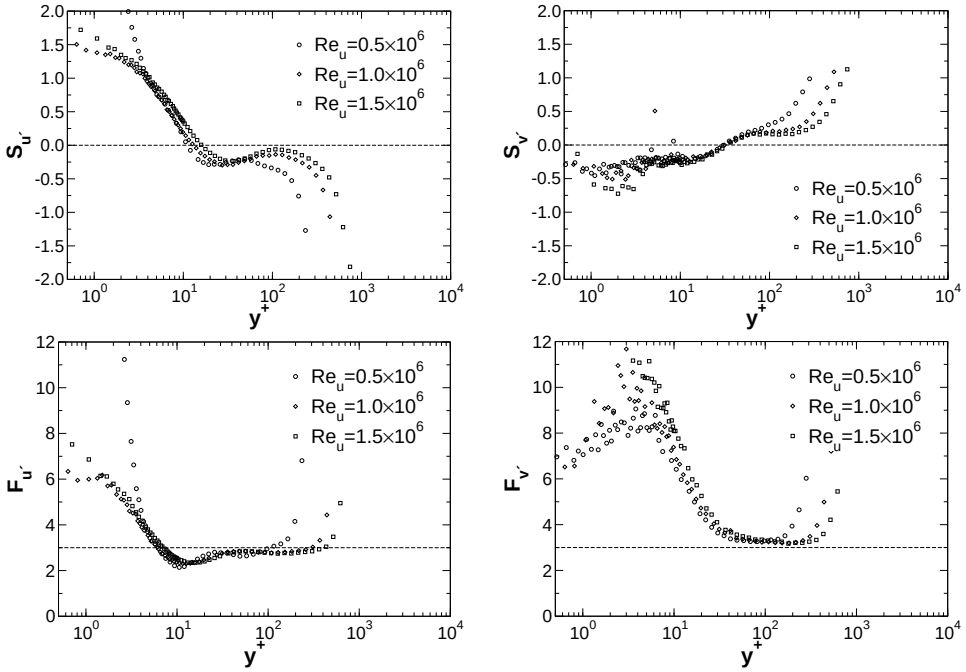

FIGURE A.7: Skewness and flatness distributions of u and v at $x - x_{LE} = -26.35\,\text{mm}$.

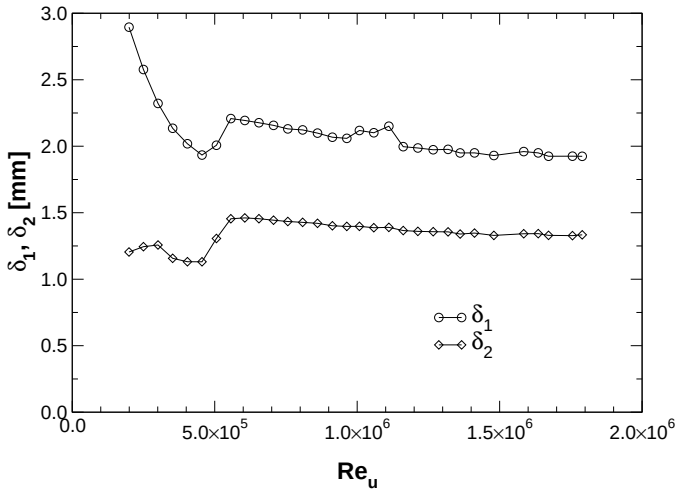

FIGURE A.8: Displacement and momentum thickness δ_1 and δ_2, respectively, upstream of the resonator ($x - x_{LE} = -7.35\,\mathrm{mm}$) as a function of unit Reynolds number Re_u.

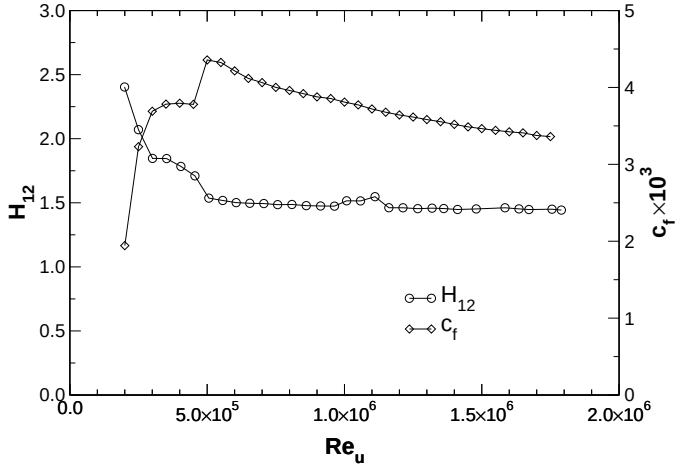

FIGURE A.9: Shape factor H_{12} and skin-friction coefficient c_f upstream of the resonator ($x - x_{LE} = -7.35\,\mathrm{mm}$) as a function of unit Reynolds number Re_u.

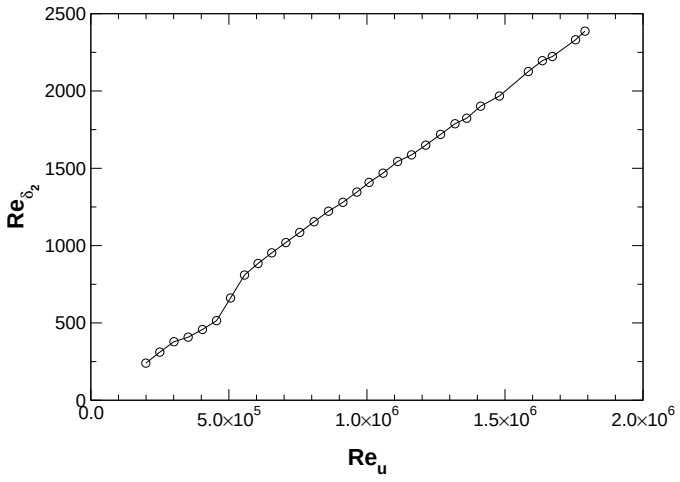

FIGURE A.10: Reynolds number Re_{δ_2} based on momentum thickness upstream of the resonator ($x - x_{LE} = -7.35\,\mathrm{mm}$) as a function of unit Reynolds number Re_u.

Appendix B

Determination of wall distance and wall shear-stress from LDA measurements

In the LDA measurements, both the exact wall distance of the boundary-layer profiles and the wall shear-stress could be determined by post-processing the velocity data. As a prerequisite, the data had to be acquired over a highly reflective surface which, in this case, consisted of glass blackened at the back. When traversing the measurement volume from the outer flow close to and finally into the wall, the samples were mirrored at the surface. To ensure good spatial resolution, a very fine measurement grid was used with steps in wall-normal direction as little as $\Delta y = 5\,\mu\text{m}$.

B.1 Wall distance

Since close to the wall the velocity complies with the linear law of the wall, a straight line was fitted through appropriate data points to determine the wall distance. For this purpose, the least-squares method was applied and the wall distance was then found by extrapolation. The data points were chosen individually for each profile as the samples nearest to the wall were biased once the measurement volume touched the surface. In this case, the velocity was measured too high as can be observed in figure B.1.

B.2 Wall shear-stress

From the wall-normal gradient of the streamwise velocity component $\partial u/\partial y$ at the wall obtained by extrapolating the data, the wall shear-stress τ_w can

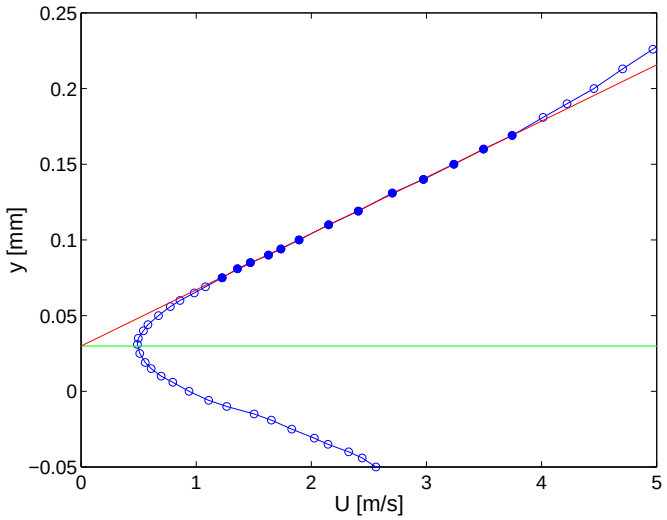

FIGURE B.1: Close-up of a mirrored velocity profile measured by LDA. The filled symbols represent data points considered for the curve fit, the red line indicates the fitted curve, and the green line is the resulting position of the wall suggesting a correction of the wall distance of 29.87 µm in this measurement.

be computed with η being the dynamic viscosity of the fluid:

$$\tau_w = \eta \frac{\partial u}{\partial y}\bigg|_{\text{wall}} \tag{B.1}$$

The reliability of this method was shown by comparison with Preston tube measurements and oil-film interferometry in a zero-pressure-gradient boundary layer (Bake, 2002). The three methods were completely independent of each other and showed excellent agreement: The maximum relative deviation in the skin-friction coefficient was ±1.2 %.

It should be noted that this method was only tested in zero-pressure-gradient boundary layers, and that difficulties might be expected when adverse pressure gradients prevail.

Bibliography

Abramowitz, M. & Stegun, I. A., ed. 1965 *Handbook of Mathematical Functions*. New York: Dover.

Ahuja, K. K. & Burrin, R. H. 1984 Control of flow separation by sound. *AIAA Paper 84-2298* AIAA / NASA 9th Aeroacoustics Conference.

Ahuja, K. K., Whipkey, R. R. & Jones, G. S. 1983 Control of turbulent boundary layer flows by sound. *AIAA Paper 83-0726* AIAA 8th Aeroacoustics Conference.

Althaus, D. & Wortmann, F. X. 1981 *Stuttgarter Profilkatalog I*. Braunschweig: Vieweg.

Amitay, M. & Glezer, A. 2002 Role of actuation frequency in controlled flow reattachment over a stalled airfoil. *AIAA J.* **40** (2), 209–216.

Amitay, M., Smith, D. R., Kibens, V., Parekh, D. E. & Glezer, A. 2001 Aerodynamic flow control over an unconventional airfoil using synthetic jet actuators. *AIAA J.* **39** (3), 361–370.

Bader, V. & Grosche, F.-R. 1999 Control of leading-edge separation from an airfoil by internal acoustic excitation and self-induced resonances. In *Mechanics of Passive and Active Flow Control* (ed. G. E. A. Meier & P. R. Viswanath), *Fluid Mechanics and its Applications*, vol. 53, pp. 299–304. Dordrecht: Kluwer Acad. Publ., proceedings of the IUTAM Symposium, 7.–11.9.98, Göttingen, Germany.

Bake, F. 2002 Einsatz eines optimierten akustischen Resonators zur Strömungsbeeinflussung in einem Halbdiffusor. Diplomarbeit, Technische Universität Berlin, Hermann-Föttinger-Institut für Strömungsmechanik.

Batchelor, G. K. 1967 *An Introduction to Fluid Dynamics*. Cambridge: Cambridge University Press.

Bendat, J. S. & Piersol, A. G. 1993 *Engineering Applications of Correlation and Spectral Analysis*, 2nd edn. New York: John Wiley & Sons, Inc.

Béraud, F. 1994 Experimental study of the receptivity of a separated boundary layer on an airfoil at high angles of attack and low Reynolds numbers. Diplomarbeit, Technische Universität Berlin, Hermann-Föttinger-Institut für Strömungsmechanik.

Blake, W. K. 1986 *Mechanics of Flow-Induced Sound and Vibration*, *Applied Mathematics and Mechanics*, vol. 17-I. Orlando: Academic Press, Inc.

Boiko, A. V., Dovgal, A. V., Zanin, B. Y. & Kozlov, V. V. 1996 Three-dimensional structure of separated flows on wings (review). *Thermophysics and Aeromechanics* **3** (1), 1–13.

Bruggeman, J. C. 1987 The propagation of low-frequency sound in a two-dimensional duct system with T joints and right angle bends: Theory and experiment. *J. Acoust. Soc. Am.* **82** (3), 1045–1051.

Bruggeman, J. C., Hirschberg, A., van Dongen, M. E. H., Wijnands, A. P. J. & Gorter, J. 1989 Flow-induced pulsations in gas transport systems: Analysis of the influence of closed side branches. *J. Fluids Eng.* **111**, 484–491, Transactions of the ASME.

Bruggeman, J. C., Hirschberg, A., van Dongen, M. E. H., Wijnands, A. P. J. & Gorter, J. 1991 Self-sustained aero-acoustic pulsations in gas transport systems: Experimental study of the influence of closed side branches. *J. Sound Vib.* **150** (3), 371–393.

Clara, C. 1996 Akustische Beeinflussung einer abgelösten Tragflügelumströmung. Diplomarbeit, Technische Universität Berlin, Hermann-Föttinger-Institut für Strömungsmechanik.

Cohen, H., Rogers, G. F. C. & Saravanamuttoo, H. I. H. 1987 *Gas Turbine Theory*, 3rd edn. Singapore: Longman Scientific & Technical.

Coller, B. D., Noack, B. R., Narayanan, S., Banaszuk, A. & Khibnik, A. I. 2000 Reduced-basis model for active separation control in a planar diffuser flow. *AIAA Paper 2000-2562* Fluids 2000 Conference and Exhibit.

Crowder, J. P. 1989 Tufts. In *Handbook of Flow Visualization* (ed. W.-J. Yang), pp. 125–175. New York: Hemisphere Pub.

Currle, J. 1990 Numerische Untersuchung instationärer Strömungsphänomene bei einer Cavityumströmung. Dissertation, Universität Stuttgart.

Darmadi, L. H. H. 2002 Adaptive Regelung eines Helmholtz-Resonators mit dem Maximum-Such-Verfahren. Diplomarbeit, Technische Universität Berlin, Institut für Meß- und Regelungstechnik und Hermann-Föttinger-Institut für Strömungsmechanik.

De Metz, F. C. & Farabee, T. M. 1977 Laminar and turbulent shear flow induced cavity resonances. *AIAA Paper 77-1293* AIAA 4th Aeroacoustics Conference.

DeGraaff, D. B. 1999 Reynolds number scaling of the turbulent boundary layer on a flat plate and on swept and unswept bumps. PhD thesis, Stanford University.

Dowling, A. P. 1998 Private communication.

Dowling, A. P. & Ffowcs Williams, J. E. 1983 *Sound and Sources of Sound*. Chichester: Ellis Horwood Ltd.

Eaton, D. C. G. 1997 An overview of structural acoustics and related high-frequency-vibration activities. *ESA Bulletin* **92**.

Ehrenfried, K. & Meier, G. E. A. 1995 Ein Finite-Volumen-Verfahren zur Berechnung von instationären, transsonischen Strömungen. DLR-Forschungsbericht 94-33. Institut für Strömungsmechanik der DLR, Göttingen, Germany.

Elder, S. A. 1978 Self-excited depth-mode resonance for a wall-mounted cavity in turbulent flow. *J. Acoust. Soc. Am.* **64** (3), 877–890.

Eriksson, L. J. 1980 Higher order mode effects in circular ducts and expansion chambers. *J. Acoust. Soc. Am.* **68** (2), 545–550.

Erk, P. P. 1997 *Separation Control on a Post-Stall Airfoil Using Acoustically Generated Perturbations*. *Fortschr.-Ber. VDI Reihe 7* 328. Düsseldorf: VDI Verlag.

Fernholz, H.-H. 1994 Near-wall phenomena in turbulent separated flows. *Acta Mech. Suppl.* **4**, 57–67.

Fernholz, H.-H. & Finley, P. J. 1996 The incompressible zero-pressure gradient turbulent boundary layer: An assessment of the data. *Prog. Aerospace Sci.* **32**, 245–311.

Fernholz, H.-H., Janke, G., Schober, M., Wagner, P. M. & Warnack, D. 1996 New developments and applications of skin-friction measuring techniques. *Meas. Sci. Technol.* **7**, 1396–1409.

Fernholz, H.-H., Zhou, M. d., Cheng, X. & Dengel, P. 1993 The manipulation of open and closed reverse-flow regions on a wedge-like body. In *Turbulente Strömungen in Forschung und Praxis* (ed. A. Leder), pp. 123–130. Aachen: Shaker.

Fiedler, H. E. & Fernholz, H.-H. 1990 On management and control of turbulent shear flows. *Prog. Aerospace Sci.* **27**, 305–387.

Fletcher, N. H. & Rossing, T. D. 1991 *The Physics of Musical Instruments*. New York: Springer.

Flynn, K. P. & Panton, R. L. 1990 The interaction of Helmholtz resonators in a row when excited by a turbulent boundary layer. *J. Acoust. Soc. Am.* **87** (4), 1482–1488.

Flynn, K. P., Panton, R. L. & Bogard, D. G. 1990 Effect of Helmholtz resonators on boundary-layer turbulence. *AIAA J.* **28** (11), 1857–1858.

Franke, M. E. & Carr, D. L. 1975 Effect of geometry on open cavity flow-induced pressure oscillations. *AIAA Paper 75-492* AIAA 2nd Aeroacoustics Conference.

Gad-el-Hak, M. & Bushnell, D. M. 1991 Separation control: Review. *J. Fluids Eng.* **113**, 5–29, Transactions of the ASME.

Garwon, M., Darmadi, L. H. H., Urzynicok, F., Bärwolff, G. & King, R. 2003 Adaptive control of separated flows. Submitted to the European Control Conference, Cambridge, UK.

Gasch, R., ed. 1996 *Windkraftanlagen: Grundlagen und Entwurf*, 3rd edn. Stuttgart: Teubner.

Goetz, M. 2000 Effektivitätssteigerung der Strömungsbeeinflussung durch mehrere Störquellen an einem Flügelprofil. Diplomarbeit, Technische Universität Berlin, Hermann-Föttinger-Institut für Strömungsmechanik.

Graps, A. 1995 An introduction to wavelets. *IEEE Computational Sciences and Engineering* **2** (2), 50–61.

Greenblatt, D. & Wygnanski, I. J. 2000 The control of flow separation by periodic excitation. *Prog. Aerospace Sci.* **36**, 487–545.

Hancock, P. E. 1980 The effect of free-stream turbulence on turbulent boundary layers. PhD thesis, Imperial College of Science and Technology, University of London.

Heckl, M. & Müller, H. A., ed. 1994 *Taschenbuch der technischen Akustik*, 2nd edn. Berlin: Springer.

Heller, H. H. & Bliss, D. B. 1975 The physical mechanism of flow-induced pressure fluctuations in cavities and concepts for their suppression. *AIAA Paper 75-491* AIAA 2nd Aeroacoustics Conference.

Helmholtz, H. 1860 Theorie der Luftschwingungen in Röhren mit offenen Enden. *Crelle* **57**, 1–72.

Hoffmann, D., Laitko, H. & Gockel, E. 1997 *Hermann von Helmholtz: Klassiker an der Epochenwende - Zum 175. Geburtstag des Universalgelehrten*, 2nd edn. Bonn: Hermann von Helmholtz-Gemeinschaft Deutscher Forschungszentren, Physikalisch-Technische Bundesanstalt Braunschweig.

Howe, M. S. 1976 On the Helmholtz resonator. *J. Sound Vib.* **45** (3), 427–440.

Hsiao, F.-B., Shyu, R.-N. & Chang, R. C. 1994 High angle-of-attack airfoil performance improvement by internal acoustic excitation. *AIAA J.* **32** (3), 655–657.

Huang, L. S., Bryant, T. D. & Maestrello, L. 1988 The effect of acoustic forcing on trailing edge separation and near wake development of an airfoil. *AIAA Paper 88-3531* AIAA, ASME, SIAM, and APS 1st National Fluid Dynamics Congress.

Hughes, I. J. 1988 The scattering of sound from some practical surfaces. PhD thesis, Downing College, Cambridge.

Huppertz, A. 2001 Aktive Beeinflussung der Strömung stromab einer rückwärtsgewandten Stufe. Dissertation, Technische Universität Berlin, http://edocs.tu-berlin.de/diss/2001.

Huppertz, A. & Fernholz, H.-H. 2002 Active control of the turbulent flow over a swept fence. *Eur. J. Mech. B/Fluids* **21**, 429–446.

Ingard, K. U. 1994 *Notes on Sound Absorption Technology*. Poughkeepsie, NY: Noise Control Foundation.

Jaroch, M. & Dengel, P. 1983 Messungen am GroWiKa in der Zeit zwischen dem 23.09.1982 und 04.03.1983. Tech. rep. Hermann-Föttinger-Institut für Strömungsmechanik, Technische Universität Berlin.

Johnston, J. P. & Nishi, M. 1990 Vortex generator jets - means for flow separation control. *AIAA J.* **28** (6), 989–994.

Kalter, M. 2001 Beeinflussung einer stark gestörten Grenzschicht mit Druckanstieg durch die Turbulenzstruktur der Außenströmung. Dissertation, Technische Universität Berlin.

Kalter, M. & Fernholz, H.-H. 2001 The reduction and elimination of a closed separation region by free-stream turbulence. *J. Fluid Mech.* **446**, 271–308.

Kegerise, M. A., Cattafesta, L. N. & Ha, C. 2002 Adaptive identification and control of flow-induced cavity oscillations. *AIAA Paper 2002-3158* AIAA 1st Flow Control Conference.

Kinsler, L. E. & Frey, A. R. 1962 *Fundamentals of Acoustics*, 2nd edn. New York: John Wiley & Sons, Inc.

Kwong, A. H. M. & Dowling, A. P. 1994 Active boundary-layer control in diffusers. *AIAA J.* **32** (12), 2409–2414.

Lachmann, G. V., ed. 1961*a* *Boundary Layer and Flow Control, Its Principles and Application*, vol. 1. Oxford: Pergamon Press.

Lachmann, G. V., ed. 1961*b* *Boundary Layer and Flow Control, Its Principles and Application*, vol. 2. Oxford: Pergamon Press.

Lamb, H. 1932 *Hydrodynamics*, 6th edn. Cambridge: Cambridge University Press.

Lamp, A. M. & Chokani, N. 1999 Control of cavity resonance using steady and oscillatory blowing. *AIAA Paper 99-0999* AIAA 37th Aerospace Sciences Meeting and Exhibit.

Lin, J. C. 1999 Control of turbulent boundary-layer separation using microvortex generators. *AIAA Paper 99-3404* AIAA 30th Fluid Dynamics Conference.

Lin, J. C., Howard, F. G. & Bushnell, D. M. 1990 Investigation of several passive and active methods for turbulent flow separation control. *AIAA Paper 90-1598* AIAA 21st Fluid Dynamics, Plasma Dynamics and Lasers Conference.

Mattingly, J. D., Heiser, W. H. & Daley, D. H. 1987 *Aircraft Engine Design*. New York: AIAA.

McCullough, G. B. & Gault, D. E. 1951 Examples of three representative types of airfoil-section stall at low speed. *Tech. Rep.* NACA TN 2502. Ames Aeronautical Laboratory, Moffett Field, California.

McGregor, O. W. & White, R. A. 1970 Drag of rectangular cavities in supersonic and transonic flow including the effects of cavity resonance. *AIAA J.* **8** (11), 1959–1964.

McManus, K. R., Legner, H. H. & Davis, S. J. 1994 Pulsed vortex generator jets for active control of flow separation. *AIAA Paper 94-2218* AIAA 25th Fluid Dynamics Conference.

McMichael, J. M. 1996 Progress and prospects for active flow control using microfabricated electro-mechanical systems (MEMS). *AIAA Paper 96-0306* AIAA 34th Aerospace Sciences Meeting and Exhibit.

Meirovitch, L. 1986 *Elements of Vibration Analysis*, 2nd edn. New York: McGraw-Hill, Inc.

Merzkirch, W. 1987 Techniques of flow visualization. In *AGARD-AG-302* (ed. K. Gersten). Neuilly sur Seine, France: North Atlantic Treaty Organization.

Meyer, R. K. J. 2000 Experimentelle Untersuchungen von Rückstromklappen auf Tragflügeln zur Beeinflussung von Strömungsablösungen. Dissertation, Technische Universität Berlin.

Miau, J. J., Lee, K. C., Chen, M. H. & Chou, J. H. 1991 Control of separated flow by a two-dimensional oscillating fence. *AIAA J.* **29** (7), 1140–1148.

Miles, J. B. & Watson, G. H. 1971 Pressure waves for flow induced acoustic resonance in cavities. *AIAA J.* **9** (7), 1402–1404.

Miles, J. W. & Lee, Y. K. 1975 Helmholtz resonance of harbors. *J. Fluid Mech.* **67** (3), 445–464.

Morse, P. M. 1948 *Vibration and Sound*, 2nd edn. New York: McGraw-Hill, Inc.

Müller, M. 2001 Einsatz eines optimierten akustischen Resonators zur Strömungsbeeinflussung an einem Tragflügel. Diplomarbeit, Technische Universität Berlin, Hermann-Föttinger-Institut für Strömungsmechanik.

Müller, M. 2002 LDA-Messung des Strömungsfeldes um ein Flügelprofil bei Beeinflussung durch einen akustischen Resonator. Studienarbeit, Technische Universität Berlin, Hermann-Föttinger-Institut für Strömungsmechanik.

Neise, W. 1975 Theoretical and experimental investigations of microphone probes for sound measurements in turbulent flow. *J. Sound Vib.* **39** (3), 371–400.

Nelson, P. A., Halliwell, N. A. & Doak, P. E. 1981 Fluid dynamics of a flow excited resonance, part I: Experiment. *J. Sound Vib.* **78** (1), 15–38.

Nelson, P. A., Halliwell, N. A. & Doak, P. E. 1983 Fluid dynamics of a flow excited resonance, part II: Flow acoustic interaction. *J. Sound Vib.* **91** (3), 375–402.

Obi, S., Ohizumi, H., Aoki, K. & Masuda, S. 1993 Turbulent separation control in a plane asymmetric diffuser by periodic perturbation. In *Eng. Turbulence Modelling and Expts. 2* (ed. W. Rodi & F. Martelli), pp. 633–642. Amsterdam: Elsevier Sci. Publ.

Panton, R. L. 1990 Effect of orifice geometry on Helmholtz resonator excitation by grazing flow. *AIAA J.* **28** (1), 60–65.

Panton, R. L. & Miller, J. M. 1975*a* Excitation of a Helmholtz resonator by a turbulent boundary layer. *J. Acoust. Soc. Am.* **58** (4), 800–806.

Panton, R. L. & Miller, J. M. 1975*b* Resonant frequencies of cylindrical Helmholtz resonators. *J. Acoust. Soc. Am.* **57** (6), 1533–1535.

Park, J. & Choi, H. 1999 Effects of uniform blowing or suction from a spanwise slot on a turbulent boundary layer flow. *Phys. Fluids* **11** (10), 3095–3105.

Patel, V. C. 1965 Calibration of the Preston tube and limitations on its use in pressure gradients. *J. Fluid Mech.* **23** (1), 185–208.

Pearcey, H. H. 1961 Shock-induced separation and its prevention by design and boundary layer control. In *Boundary Layer and Flow Control. Its Principles and Application* (ed. G. V. Lachmann), vol. 2, pp. 1166–1344. Oxford: Pergamon Press.

Perrier, V., Philipovitch, T. & Basdevant, C. 1995 Wavelet spectra compared to Fourier spectra. *J. Math. Phys.* **36**, 1506–1519.

Poisson-Quinton, P. & Lepage, L. 1961 Survey of French research on the control of boundary layer and circulation. In *Boundary Layer and Flow Control. Its Principles and Application* (ed. G. V. Lachmann), vol. 1, pp. 21–73. Oxford: Pergamon Press.

Prandtl, L. 1905 Über Flüssigkeitsbewegung bei sehr kleiner Reibung. In *Verh. III Int. Math.-Kongr., Heidelberg 1904*, pp. 484–491. Leipzig: Teubner.

Raman, G., Raghu, S. & Bencic, T. J. 1999 Cavity resonance suppression using miniature fluidic oscillators. *AIAA Paper 99-1900* AIAA / CEAS 5th Aeroacoustics Conference.

Rathnasingham, R. & Breuer, K. S. 1996 Characteristics of resonant actuators for flow control. *AIAA Paper 96-0311* AIAA 34th Aerospace Sciences Meeting and Exhibit.

Rayleigh, J. W. S. 1896 *The Theory of Sound*, 2nd edn., vol. 2. London: Macmillan.

Rockwell, D. & Naudascher, E. 1978 Review - self-sustaining oscillations of flow past cavities. *J. Fluids Eng.* **100**, 152–165, Transactions of the ASME.

Rossiter, J. E. 1964 Wind-tunnel experiments on the flow over rectangular cavities at subsonic and transonic speeds. Reports and Memoranda 3438. Royal Aircraft Establishment.

Ruck, B. 1990 Einfluß der Tracerteilchengröße auf die Signalinformation in der Laser-Doppler-Anemometrie. *tm - Technisches Messen* **57** (7/8), 284–295.

Seifert, A., Bachar, T., Koss, D., Shepshelovich, M. & Wygnanski, I. 1993 Oscillatory blowing: A tool to delay boundary-layer separation. *AIAA J.* **31** (11), 2052–2060.

Seifert, A., Eliahu, S., Greenblatt, D. & Wygnanski, I. 1998 Use of piezoelectric actuators for airfoil separation control. *AIAA J.* **36** (8), 1535–1537.

Seifert, A. & Pack, L. G. 1999 Oscillatory control of separation at high Reynolds numbers. *AIAA J.* **37** (9), 1062–1071.

Siller, H. 1999 Reduction of the recirculation length downstream of a fence by an oscillating cross-flow. Dissertation, Technische Universität Berlin.

Siller, H. A. & Fernholz, H.-H. 1999 Active separation control on an aerofoil by a periodic cross-flow. In *New Results in Numerical and Experimental Fluid Mechanics II* (ed. W. Nitsche, H.-J. Heinemann & R. Hilbig), *Notes on Numerical Fluid Mechanics*, vol. 72, pp. 450–457. Braunschweig: Vieweg.

Skudrzyk, E. 1954 *Die Grundlagen der Akustik*. Wien: Springer.

Sondhauss, G. 1850*a* Über den Brummkreisel und das Schwingungsgesetz der kubischen Pfeifen. *Pogg. Ann.* **81**, 235–257, 347–373.

Sondhauss, G. 1850*b* Über die Schallschwingungen der Luft in erhitzten Glasröhren und in gedeckten Pfeifen von ungleicher Weite. *Pogg. Ann.* **79**, 1–34.

Sonnenberger, R. 1997 Laser Doppler measurements of high-frequent oscillatory flow. Diplomarbeit, Technische Universität Berlin, Hermann-Föttinger-Institut für Strömungsmechanik.

Steinwand, M. 2002 Untersuchung des Impulsstroms eines überströmten Resonators. Diplomarbeit, Technische Universität Berlin, Hermann-Föttinger-Institut für Strömungsmechanik.

Timmel, T., Goubergrits, L. & Affeld, K. 2001 Optimization and investigation of a novel cardiac assist valve with a purge flow. *Int. J. Artif. Organs* **24** (11), 777–783.

Torrence, C. & Compo, G. P. 1998 A practical guide to wavelet analysis. *Bulletin of the American Meteorological Society* **79** (1), 61–78.

Turns, S. R. 1996 *An Introduction to Combustion: Concepts and Applications*. New York: McGraw-Hill, Inc.

Urzynicok, F. 1997 Separation control on an airfoil under post-stall conditions using low-frequency acoustic and low-frequency mechanical excitation. Diplomarbeit, Technische Universität Berlin, Hermann-Föttinger-Institut für Strömungsmechanik.

Urzynicok, F. & Dowling, A. P. 1999 Natural frequencies of a resonator consisting of a cylindrical tube with axial slit. Tech. rep. Hermann-Föttinger-Institut für Strömungsmechanik, Technische Universität Berlin.

Vagt, J.-D. & Fernholz, H.-H. 1977 Wall interference effects of static pressure probes in an incompressible turbulent boundary layer. *Aeronaut. Quart.* **27**, 176–184.

Williams, D. R. & Fabris, D. 2000 Experiments on controlling multiple acoustic modes in cavities. *AIAA Paper 2000-1903* AIAA / CEAS 6th Aeroacoustics Conference.

Wu, J.-Z., Lu, X.-Y., Denny, A. G., Fan, M. & Wu, J.-M. 1998 Post-stall flow control on an airfoil by local unsteady forcing. *J. Fluid Mech.* **371**, 21–58.

Wygnanski, I. 1997 Boundary layer and flow control by periodic addition of momentum. *AIAA Paper 97-2117* AIAA 4th Shear Flow Control Conference.

Wygnanski, I. & Seifert, A. 1994 The control of separation by periodic oscillations. *AIAA Paper 94-2608* AIAA 18th Aerospace Ground Testing Conference.

Yon, S. & Katz, J. 1997 Study of the unsteady flow features on a stalled wing. *AIAA Paper 97-1927* AIAA 28th Fluid Dynamics Conference.

Zhang, X., Chen, X. X., Rona, A. & Edwards, J. A. 1999 Attenuation of cavity flow oscillation through leading edge flow control. *J. Sound Vib.* **221** (1), 23–47.

Zhou, M. d., Fernholz, H.-H., Ma, H. Y., Wu, J. Z. & Wu, J. M. 1993 Vortex capture by a two-dimensional airfoil with a small oscillating leading-edge flap. *AIAA Paper 93-3266* AIAA Shear Flow Conference.